Development of a High-Order Implicit Discontinuous Galerkin Method on Unstructured Meshes for Turbomachinery Flow



Min Yao

Worcester College

University of Oxford

A thesis submitted for the degree of

Doctor of Philosophy

Michaelmas 2018

To My Grandfather

Acknowledgements

First and foremost, the most sincere thank you must go to my supervisor, Professor L. He, for giving me this opportunity to work on this project under his supervision. I am deeply grateful for his continuous support on my research work. Prof. He is always keen to discuss with me on the method development, formulation derivations, CFD code implementation and results validation. His comprehensive understanding of the sophisticated theories always gives me the insightful ideas in this research work.

I would also like to express my gratitude to Dr Liwei Chen and Dr Junsok Yi, for their help in my CFD development.

Many thanks also go to all the colleagues at Osney Lab: Penghao Duan, Francesco Ornano, Dr Mai Zhang, Dr Yuewen Jiang, Dr Haiteng Ma, Maxwell Adamas, Marios Kapsis, Alexander Murray, Alexander Bucknell, Michael Mair, Amir Ibrahim, Andrew Pilkington, Anna Bru Revert, Anton Glazkov, Nathan Donaldson, Olufemi Awe and Dr Peter Forsyth, for their advices and encouragement.

Finally, my special thanks go to my wife and daughter for bringing the great joy to my life. To my parents and brother who have always supported and encouraged me.

Development of a High-Order Implicit Discontinuous Galerkin Method on Unstructured Meshes for Turbomachinery Flow

Min Yao

Worcester College
Supervised by Prof. L. He

A thesis submitted for the degree of Doctor of Philosophy

Michaelmas 2018

Abstract

There is a continued need to further capabilities of turbomachinery flow design and analysis method tools, both in terms of the flow modeling fidelity (e.g. moving towards DES/LES) and temporal and spatial accuracy of the numerical discretization methods. To enhance solution accuracy with high-order methods, an implicit solver using the Discontinuous Galerkin (DG) discretization on unstructured meshes has been developed. The DG scheme is favored chiefly due to its distinctive feature that a higher-order accuracy being achieved through simple internal sub-divisions of a given mesh cell. It thus can considerably relieve the burden of mesh generation for local refinement of complex configurations. The implicit formulation is well suited for an unstructured mesh solver, for which some well-established solution techniques for explicit methods (e.g. multigrid methods) are less effective.

The RANS equations in conjunction with the Sparlart-Allmaras one equation turbulence model are discretized using a high-order DG method on unstructured meshes. The all-speed AUSM$^+$-up scheme is applied for the inviscid flux calculations and the BR2 scheme is implemented for the viscous flux discretization. An implicit time integration is adopted and the system linear equations are solved at each time step by using a preconditioned GMRES iterative algorithm with the ILU0. A modification of the turbulence model is also adopted to enhance the robustness for high-order turbulent flow simulations.

The validity and effectiveness of the present developed method have been examined in several test cases, for both validating the method implementation and illustrating salient features and characteristics of the methodology. The flows around a cylinder solved up to 5th-order of accuracy on an extremely coarse mesh illustrate the need for high-order geometrical representation in relation to the high-order flow field discretization. A laminar boundary layer and the vortex shedding after a cylinder validate both the steady and unsteady modelling capabilities with the implicit time integration method. A calculated turbulent boundary layer on flat plate demonstrates the capability of a high-order DG in capturing the laminar sub-layer in a coarse mesh (y^+>20) without a wall function, in a clear contrast to a conventional 2nd-order scheme. The all-speed flows past an airfoil show the distinct capability of AUSM$^+$-up scheme on solving a wide range of flow regimes.

A main focal test case of the present work is a high pressure turbine cascade, where the flow losses are strongly influenced by the boundary layer transition on the blade surface and the secondary flow development in the endwall region. In this case the RANS solutions consistently over-predict the losses, prompting further modelling considerations. A higher-order solution does indicate higher resolution for more detailed 3D secondary flow structures. It is however more remarkable that both overall and distributed losses of the unsteady laminar solutions on a coarse mesh are consistently better than the RANS solutions. The results indicate that for the turbine blade flows similar to the one presently tested, a direct unsteady laminar solution on a coarse mesh (far coarser than those typically required for LES) may be further explored.

Contents

List of Figures **ix**

List of Tables **xvi**

1 Introduction **1**

1.1 Background 1

1.2 Challenges for CFD in Turbomachinery 3

1.2.1 Low-order of Accuracy 4

1.2.2 Mesh Generation for Complex Geometries 4

1.2.3 Limit of Temporal Discretization 6

1.2.4 A Wide Range of Flow Speed 7

1.3 Objectives of Present Work 9

1.4 Outline of Thesis 10

2 Literature Review **12**

2.1 Brief Overview of Turbomachinery CFD 12

2.2 High-order CFD Method 14

2.2.1 Demands for High-Order Schemes 14

2.2.2 High-Order Construction from Conventional CFD 16

2.2.3 Development of High-Order DG Method 19

2.2.4 Features of High-Order DG Method 23

2.2.5 High-Order DG Methods in Turbomachinery 24

2.3 Unstructured Meshing Technique 28

2.4 Implicit Time Integration Method 29

2.5 All-Speed Scheme 31

2.6 Summary Notes to Underline Main Objectives of Present Work . . . 34

3 Discontinuous Galerkin Discretization **36**
3.1 Conservative Equations 36
3.2 DG Discretization in Space 38
3.2.1 Weak Formulation 39
3.2.2 Convective Flux Discretization with AUSM$^+$-up Scheme . . 41
3.2.3 Viscous Flux Discretization with BR2 Method 43
3.3 Modification of SA Turbulence Model 46
3.4 Boundary Conditions 50
3.4.1 Subsonic Inflow 50
3.4.2 Subsonic Outflow 51
3.4.3 No-slip Wall 51
3.4.4 Slip Wall 52
3.4.5 Farfield 52

4 Time Integration **53**
4.1 Ordinary Differential Equations 53
4.2 Implicit Time Integration 55

5 Validation Studies **60**
5.1 Inviscid Flow around a Cylinder 61
5.2 Laminar Flows 68
5.2.1 Vortex Shedding after a Cylinder 68
5.2.2 Laminar Boundary Layer over a Flat Plate 76
5.3 Turbulent Flow over a Flat Plate 86
5.4 All-Speed Flow past an Airfoil 92
5.4.1 Subsonic Flow with a Mach Number of 0.5 94
5.4.2 Transonic Flow with a Mach Number of 0.8 99
5.4.3 Supersonic Flow with a Mach Number of 2 104
5.4.4 Low-Speed Flow with a Mach Number of 0.01 108
5.5 Summary 112

6 RANS Solution for High Pressure Turbine Cascade **114**
6.1 Durham HPT Cascade 114
6.2 Definition of Secondary Flow Quantities 117
6.3 3D RANS Solution 119
6.3.1 Traverse Plots 120
6.3.2 Pitch-Averaged Results 141
6.4 Summary and Discussion 148

7 Unsteady Laminar Solution for High Pressure Turbine Cascade 150
7.1 Some Further Modelling Considerations 150
7.2 Sensitivity Study on Temporal Resolution of Unsteady Laminar Solution 153
7.3 3D Unsteady Laminar Solution of Durham Cascade 165
7.3.1 Traverse Plots 165
7.3.2 Pitch-Averaged Results 185
7.3.3 Further Comparison between Unsteady Laminar and RANS 192
7.4 Summary 196

8 Conclusions and Recommendations 198
8.1 Conclusions 198
8.1.1 Method Implementation 198
8.1.2 Validation Work 199
8.1.3 Turbomachinery Application 200
8.2 Recommendations for Future work 201
8.2.1 Further Methodology Development 201
8.2.2 Future Applications 202

Bibliography 204

List of Figures

1.1 Unstructured mesh for computation of low pressure turbine blades by Zheng and He (2001) 5
1.2 Sample engine pressure, temperature and velocity (see Cast, 1997) . 7

4.1 2D triangular elements with different orders of internally divided sub-cells (indicated by dash lines) 54
4.2 DG discretization and implicit time integration process 59

5.1 2D schematic of Flow past a cylinder 62
5.2 3D mesh for an inviscid flow around a cylinder 63
5.3 High-order representations of cylinder with 12 base-mesh points for inviscid solution 64
5.4 Static pressure coefficient contours with streamlines for an inviscid flow around cylinder of DG representations with corresponding orders of boundary geometrical representation 65
5.5 Static pressure coefficient distributions around cylinder ($\theta = 0$: leading edge; $\theta = 180^0$: trailing edge) 66
5.6 Static pressure coefficient contours for an inviscid flow around cylinder with linear boundary representation (BP1) 67
5.7 High-order representations of cylinder with 12 base-mesh points for unsteady laminar solution 69
5.8 Instantaneous entropy contours [exp(-S/R)] for a laminar flow around cylinder of DG representations with corresponding orders of boundary geometrical representation 70
5.9 Instantaneous static pressure coefficient contours for a laminar flow around cylinder of DG representations with corresponding orders of boundary geometrical representation 71
5.10 Time-averaged static pressure coefficient contours for a laminar flow around cylinder 73
5.11 Time-averaged axial velocity contours for a laminar flow around cylinder 74

5.12 Time-averaged static pressure coefficients on cylinder surface ($\theta = 0$: leading edge; $\theta = 180^0$: trailing edge), compared to experiment data of Thom (1933) 75
5.13 Laminar boundary layer over a flat plate 77
5.14 Computed mesh and boundary condition for laminar flat plate . . . 78
5.15 Velocity contours around the leading edge of the flat plate 80
5.16 Comparison between computed and analytical tangential velocity profiles at the 20% and 51% sections of plate 81
5.17 Comparison between computed and analytical tangential velocity profiles at the 77% and 95% sections of plate 82
5.18 Comparison between computed and analytical normal velocity profiles at the 20% and 51% sections of plate 83
5.19 Comparison between computed and analytical normal velocity profiles at the 77% and 95% sections of plate 84
5.20 Computed skin friction coefficient along a flat plate 85
5.21 Flow past the flat plate 87
5.22 Computed turbulent viscosity over the flat plate 89
5.23 Computed velocity profiles 90
5.24 Computed skin friction coefficient along a flat plate, compared to the theoretical distribution of Schlichting (1979) 91
5.25 Mesh around the NACA0012 airfoil 93
5.26 Static pressure coefficient contours for a subsonic flow near the leading edge of a NACA0012 airfoil of DG representations with corresponding orders of boundary geometrical representation (Mach=0.5, Re=5000, incidence = 0^0) 96
5.27 Mach number contours around the NACA0012 airfoil from the 2nd-order DG1 to the 4th-order DG3 solutions, compared to that of the 2nd-order FVM solution by Mavriplis and Jameson (1990) (Mach=0.5, Re=5000, incidence = 0^0) 97
5.28 Computed distributions on the NACA0012 airfoil surface from the DG3 solutions, compared to that of the DG3 solutions by Bassi and Rebay (1997a) (Mach=0.5, Re=5000, incidence = 0^0) (a) static pressure coefficient; (b) skin friction coefficient 98
5.29 Static pressure coefficient contours around the NACA0012 airfoil with a close up near the leading edge (Mach=0.8, Re=73, incidence = 10^0) 101

5.30 Mach number contours around the NACA0012 airfoil from the 2nd-order DG1 to the 4th-order DG3 solutions, compared to that of the 2nd-order FVM solution by Mavriplis and Jameson (1990) (Mach=0.8, Re=73, incidence = 10^0) 102
5.31 Computed distributions on the NACA0012 airfoil surface from the DG3 solutions, compared to that of the DG3 solutions by Bassi and Rebay (1997a) (a) static pressure coefficient; (b) skin friction coefficient (Mach=0.8, Re=73, incidence = 10^0) 103
5.32 Static pressure coefficient contours around the NACA0012 airfoil with a close up near the leading edge (Mach=2, Re=106, incidence = 10^0) 105
5.33 Density contours around the NACA0012 airfoil from the 2nd-order DG1 to the 4th-order DG3 solutions, compared to that of the 2nd-order FVM solution by Mavriplis and Jameson (1990) (Mach=2, Re=106, incidence = 10^0) 106
5.34 Computed distributions on the NACA0012 airfoil surface from the DG3 solutions, compared to that of the DG3 solutions by Bassi and Rebay (1997a) (a) static pressure coefficient; (b) skin friction coefficient (Mach=2, Re=106, incidence = 10^0) 107
5.35 Static pressure coefficient contours for an incompressible flow around the leading edge of a NACA0012 airfoil of DG representations with corresponding orders of boundary geometrical representation (Mach=0.01, Re=100, incidence = 0^0) 109
5.36 Mach number contours around the NACA0012 airfoil from the 2nd-order DG1 to the 4th-order DG3 solutions (Mach=0.01, Re=100, incidence = 0^0) 110
5.37 Computed distributions along the NACA0012 airfoil from the DG3 solutions (Mach=0.01, Re=100, incidence = 0^0) 111

6.1 Axial positions of measurement for Durham cascade 116
6.2 Schematic of flow regimes through the blade passage 117
6.3 Secondary flow vectors 118
6.4 Mesh for RANS simulations 124
6.5 Secondary vectors at axial chord position of C_{ax}=-9% (a) Experiment by Hartland (2001); (b) RANS DG1; (c) RANS DG2 125
6.6 Total pressure loss coefficient contours at axial chord position of C_{ax}=-9% (a) Experiment by Hartland (2001); (b) RANS DG1; (c) RANS DG2 126

6.7 Yaw angles contours at axial chord position of C_{ax}=-9% (a) Experiment by Hartland (2001); (b) RANS DG1; (c) RANS DG2 127
6.8 Secondary kinetic energy coefficient contours at axial chord position of C_{ax}=-9% (a) Experiment by Hartland (2001); (b) RANS DG1; (c) RANS DG2 128
6.9 Secondary vectors at axial chord position of C_{ax}=71% (a) Experiment by Hartland et al. (2000); (b) RANS DG1; (c) RANS DG2 129
6.10 Total pressure loss coefficient contours at axial chord position of C_{ax}=71% (a) Experiment by Hartland et al. (2000); (b) RANS DG1; (c) RANS DG2 130
6.11 Yaw angles contours at axial chord position of C_{ax}=71% (a) Experiment by Hartland (2001); (b) RANS DG1; (c) RANS DG2 131
6.12 Secondary kinetic energy coefficient contours at axial chord position of C_{ax}=71% (a) Experiment by Hartland (2001); (b) RANS DG1; (c) RANS DG2 132
6.13 Secondary vectors at axial chord position of C_{ax}=97% (a) Experiment by Hartland et al. (2000); (b) RANS DG1; (c) RANS DG2 133
6.14 Total pressure loss coefficient contours at axial chord position of C_{ax}=97% (a) Experiment by Hartland et al. (2000); (b) RANS DG1; (c) RANS DG2 134
6.15 Yaw angles contours at axial chord position of C_{ax}=97% (a) Experiment by Hartland (2001); (b) RANS DG1; (c) RANS DG2 135
6.16 Secondary kinetic energy coefficient contours at axial chord position of C_{ax}=97% (a) Experiment by Hartland (2001); (b) RANS DG1; (c) RANS DG2 136
6.17 Secondary vectors at axial chord position of C_{ax}=128% (a) Experiment by Hartland et al. (2000); (b) RANS DG1; (c) RANS DG2 . . 137
6.18 Total pressure loss coefficient contours at axial chord position of C_{ax}=128% (a) Experiment by Hartland et al. (2000); (b) RANS DG1; (c) RANS DG2 138
6.19 Yaw angles contours at axial chord position of C_{ax}=128% (a) Experiment by Hartland (2001); (b) RANS DG1; (c) RANS DG2 139
6.20 Secondary kinetic energy coefficient contours at axial chord position of C_{ax}=128% (a) Experiment by Hartland (2001); (b) RANS DG1; (c) RANS DG2 140
6.21 Pitch-averaged data at axial chord position of C_{ax}=-9% (a) Total pressure loss coefficient; (b) Yaw angle; (c) Secondary kinetic energy coefficient (Experiment denotes the measured data by Hartland, 2001) 144

6.22 Pitch-averaged data at axial chord position of C_{ax}=71% (a) Total pressure loss coefficient; (b) Yaw angle; (c) Secondary kinetic energy coefficient (Experiment denotes the measured data by Hartland, 2001) 145
6.23 Pitch-averaged data at axial chord position of C_{ax}=97% (a) Total pressure loss coefficient; (b) Yaw angle; (c) Secondary kinetic energy coefficient (Experiment denotes the measured data by Hartland, 2001; Experiment[1] denotes the measured data by Moore, 1995) 146
6.24 Pitch-averaged data at axial chord position of C_{ax}=128% (a) Total pressure loss coefficient; (b) Yaw angle; (c) Secondary kinetic energy coefficient (Experiment denotes the measured data by Hartland, 2001) 147

7.1 Entropy contour of the steady laminar solution from DG1: (a) overall domain and (b) close-up of suction surface near trailing edge 152
7.2 Mesh for direct unsteady laminar simulations 154
7.3 Instantaneous entropy contours from DG1 on CFL_m = 2000, 1000, 500 and 250 155
7.4 Instantaneous entropy contours from DG1 on CFL_m = 2000, 1000, 500 and 250 close-up of suction surface and trailing edge 156
7.5 Instantaneous entropy contours from DG2 on CFL_m = 2000, 1000, 500 and 250 157
7.6 Instantaneous entropy contours from DG2 on CFL_m = 2000, 1000, 500 and 250, close-up of suction surface and trailing edge 158
7.7 Comparison of steady and unsteady time-averaged static pressure contours around trailing edge from DG1 162
7.8 Comparison of steady and unsteady time-averaged static pressure contours around trailing edge from DG2 163
7.9 Time-averaged Mach contours from steady and unsteady on CFL_m=500 164
7.10 Secondary vectors at axial chord position of C_{ax}=-9% (a) Experiment by Hartland (2001); (b) Time-averaged unsteady laminar DG1; (c) Time-averaged unsteady laminar DG2 169
7.11 Total pressure loss coefficient contours at axial chord position of C_{ax}=-9% (a) Experiment by Hartland (2001); (b) Time-averaged unsteady laminar DG1; (c) Time-averaged unsteady laminar DG2 . 170
7.12 Yaw angles contours at axial chord position of C_{ax}=-9% (a) Experiment by Hartland (2001); (b) Time-averaged unsteady laminar DG1; (c) Time-averaged unsteady laminar DG2 171

7.13 Secondary kinetic energy coefficient contours at axial chord position of C_{ax}=-9% (a) Experiment by Hartland (2001); (b) Time-averaged unsteady laminar DG1; (c) Time-averaged unsteady laminar DG2 . 172
7.14 Secondary vectors at axial chord position of C_{ax}=71% (a) Experiment by Hartland et al. (2000); (b) Time-averaged unsteady laminar DG1; (c) Time-averaged unsteady laminar DG2 173
7.15 Total pressure loss coefficient contours at axial chord position of C_{ax}=71% (a) Experiment by Hartland et al. (2000); (b) Time-averaged unsteady laminar DG1; (c) Time-averaged unsteady laminar DG2 174
7.16 Yaw angles contours at axial chord position of C_{ax}=71% (a) Experiment by Hartland (2001); (b) Time-averaged unsteady laminar DG1; (c) Time-averaged unsteady laminar DG2 175
7.17 Secondary kinetic energy coefficient contours at axial chord position of C_{ax}=71% (a) Experiment by Hartland (2001); (b) Time-averaged unsteady laminar DG1; (c) Time-averaged unsteady laminar DG2 . 176
7.18 Secondary vectors at axial chord position of C_{ax}=97% (a) Experiment by Hartland et al. (2000); (b) Time-averaged unsteady laminar DG1; (c) Time-averaged unsteady laminar DG2 177
7.19 Total pressure loss coefficient contours at axial chord position of C_{ax}=97% (a) Experiment by Hartland et al. (2000); (b) Time-averaged unsteady laminar DG1; (c) Time-averaged unsteady laminar DG2 178
7.20 Yaw angles contours at axial chord position of C_{ax}=97% (a) Experiment by Hartland (2001); (b) Time-averaged unsteady laminar DG1; (c) Time-averaged unsteady laminar DG2 179
7.21 Secondary kinetic energy coefficient contours at axial chord position of C_{ax}=97% (a) Experiment by Hartland (2001); (b) Time-averaged unsteady laminar DG1; (c) Time-averaged unsteady laminar DG2 . 180
7.22 Secondary vectors at axial chord position of C_{ax}=128% (a) Experiment by Hartland et al. (2000); (b) Time-averaged unsteady laminar DG1; (c) Time-averaged unsteady laminar DG2 181
7.23 Total pressure loss coefficient contours at axial chord position of C_{ax}=128% (a) Experiment by Hartland et al. (2000); (b) Time-averaged unsteady laminar DG1; (c) Time-averaged unsteady laminar DG2 182

7.24 Yaw angles contours at axial chord position of C_{ax}=128% (a) Experiment by Hartland (2001); (b) Time-averaged unsteady laminar DG1; (c) Time-averaged unsteady laminar DG2 183
7.25 Secondary kinetic energy coefficient contours at axial chord position of C_{ax}=128% (a) Experiment by Hartland (2001); (b) Time-averaged unsteady laminar DG1; (c) Time-averaged unsteady laminar DG2 . 184
7.26 Pitch-averaged data at axial chord position of C_{ax}=-9% (a) Total pressure loss coefficient; (b) Yaw angle; (c) Secondary kinetic energy coefficient (Experiment denotes the measured data by Hartland, 2001) 188
7.27 Pitch-averaged data at axial chord position of C_{ax}=71% (a) Total pressure loss coefficient; (b) Yaw angle; (c) Secondary kinetic energy coefficient (Experiment denotes the measured data by Hartland, 2001) 189
7.28 Pitch-averaged data at axial chord position of C_{ax}=97% (a) Total pressure loss coefficient; (b) Yaw angle; (c) Secondary kinetic energy coefficient (Experiment denotes the measured data by Hartland, 2001) 190
7.29 Pitch-averaged data at axial chord position of C_{ax}=128% (a) Total pressure loss coefficient; (b) Yaw angle; (c) Secondary kinetic energy coefficient (Experiment denotes the measured data by Hartland, 2001) 191
7.30 Comparison of total pressure loss coefficient contours at axial chord position of C_{ax}=128% (a) Experiment by Hartland et al. (2000); (b) DG2 RANS; (c) DG2 time-averaged unsteady laminar 194
7.31 Comparison of pitch-averaged total pressure loss coefficient at axial chord positions of (a) C_{ax}=97% (b) C_{ax}=128% (Experiment denotes the measured data by Hartland, 2001) 195

List of Tables

2.1 Features compared among DG method and other conventional CFD methods 24

6.1 Geometrical and flow parameters of Durham cascade 115
6.2 Traverse slot locations 115
6.3 RANS overall mass-averaged Cp_0 and C_{ske} at planes 97% and 128% C_{ax} 143

7.1 Number of time steps per period and calculated Strouhal numbers for trailing edge vortex shedding 159
7.2 Laminar overall mass-averaged Cp_0 and C_{ske} at planes 97% and 128% C_{ax} 187
7.3 Overall mass-averaged Cp_0 at planes 97% and 128% C_{ax} 193

Nomenclature

Roman

$\hat{\mathcal{F}}^c$	numerical convective flux
$\hat{\mathcal{G}}$	numerical viscous flux
$\mathbf{M}$	global mass matrix
$\mathbf{n}$	normal vector to element boundary
$\mathbf{R}$	global residual vector
$\mathbf{r}$	auxiliary variables
$\mathbf{U}$	solution vector
$\mathbf{U}_h$	approximate solution vector
$\mathbf{v}_h$, $\mathbf{w}_h$	test functions
$\mathbf{x}$	spatial coordinates
$\mathcal{A}$	Jacobian matrix of viscous flux
$\mathcal{F}^c$	convective flux
$\mathcal{F}^v$	viscous flux
$\mathcal{S}$	source term
$\mathcal{V}_h$, $\mathcal{W}_h$	finite element space
a	speed of sound
b	basis shape function
c_p	specific heat for constant pressure
c_v	specific heat for constant volume

C_{ax} axial chord

Cp static pressure loss coefficient

Cp_0 total pressure loss coefficient

d dimension of space

E spefic total energy

H total enthalpy

h measure of cell spacing

k thermal conductivity

M Mach number

m dimension of conservative variables

N number of degrees of freedom

p order of accuracy

R Riemann invariants

S Sutherland temperature

T temperature

t time

u, v, w velocity componets in x, y, z directions

V velocity normal to element interface

Greek

β yaw angle

δ Kronecker delta

η_f stability constant

γ ratio of specific heats

κ local elments

μ dynamic viscosity

ν kinematic viscosity

ν_t turbulent eddy viscosity

Ω computational element

$\partial\Gamma$ interior faces

$\partial\Omega$ boundary faces

ρ density

τ viscous stress tensor

$\tilde{\nu}$ turbulence working variable

ε solution errors

Superscripts

$+, -$ outward, inward vectors

$\hat{}$ numerical approximate values

b boundary faces

n time step

Subscripts

0 stagnation

∞ freestream condition

f local faces

h finite element approximations

L, R left and right states

x, y, z directions in Cartesian coordinates

Abbreviations

1D one-dimensional

2D two-dimensional

3D three-dimensional

AUSM$^+$-up advection upstream splitting method plus-up

BR2 second Bassi Rebay method

CFD computational fluid dynamics

CFL Courant–Friedrichs–Lewy

DNS direct numerical simulation

FDM finite difference method

FEM finite element method

FR flux reconstruction

FVM finite volume method

GMRES generalized minimal residual

GS Gauss-Seidel

HPT high pressure turbine

ILU0 incomplete lower–upper factorizations with zero fill-in

LES large eddy simulation

LPT low pressure turbine

PDE partial differential equations

RANS Reynolds-Average Navier-Stokes

Re Reynolds number

SA Spalart-Allmaras

T.E. trailing edge

1 Introduction

The first chapter will start with an introduction of computational fluid dynamics in Section 1.1, followed by some statements on the current challenges of computational fluid dynamics in turbomachinery in Section 1.2. Section 1.3 will describe the objectives of present work and finally an outline of the thesis will be described in Section 1.4.

1.1 Background

Fluid dynamics is a subject which studies the physical laws governing various kinds of flow, normally divided into three branches: theoretical analysis, experimental investigation and computational fluid dynamics (CFD). The theoretical method aims for simplifying the flow model and obtaining the analytical solutions of the simplified governing equations. However, since most of the governing equations are non-linear, only few cases can reach the analytical solutions and it is impossible to seek the theoretical results when coming to the complex flow applications. The experiments

can quantitatively describe the physical phenomena of the flow using measurements. Still there are limitations of experimental tests, such as limited test points and time instants, measurement errors, expensive test facilities and limited laboratory-scaling.

In the past three decades, the enhancement of computer speed and growth in memory stimulate the tremendous development of CFD, which employs numerical algorithms to solve the governing equations for fluid mechanics. For the CFD process, the truncated region of the target problems is first defined and subdivided into discrete mesh points, then appropriate boundary conditions are specified and initial conditions are given as well for transient problems. Finally, the simulations start and iteratively solve the governing equations until a set of values satisfy the equations at each point. Thus, CFD is capable of efficiently and reliably predicting the flow patterns with high resolutions both in space and time and it has enormous applications in academic research and industry.

Currently, most of the workhorse schemes for CFD are 2nd-order finite volume method, which can both robustly and efficiently predict the detailed flow patterns and resultant performance parameters with engineering accuracy (e.g. 5% error, see Wang et al., 2013). Nevertheless, there are still problems that are out of reach for conventional 2nd-order CFD scheme. For example, the vortex dominated problems are difficult in preserving the vortices long distance after the solid body since second-order scheme numerically dissipates very fast. Similarly, the aeroacoustic problems require the capability of CFD scheme in propagating the acoustic wave with extremely low numerical dissipation, where the first- or second-order schemes always struggle. Moreover, the turbomachinery flow is inherently unsteady with

complex physical features and a wide range of flow regimes, both in terms of the speed, and in terms of the laminar, transitional and turbulent, where the 2nd-order scheme tend to be dissipative and often inadequate when pursuing the high resolution of complex problems involving turbomachinery design and analysis.

In order to capture and resolve the complex interactions in turbomachinery configurations more accurately and effectively, a CFD scheme higher than 2nd-order with remarkably low numerical dissipation are of great interest. Then it comes to a term of 'high-order scheme', normally defined as a numerical scheme which has 3rd or higher orders of accuracy in the CFD community, which has been undergoing a prosperous development and applications in external aerodynamics in recent decade.

The primary practical interest of the author's present work is to focus in development and application of a CFD method for turbomachinery design and analysis, where some key challenges and limitations of conventional turbomachinery CFD methods can be addressed.

1.2 Challenges for CFD in Turbomachinery

The challenging issues existing in CFD for turbomachinery will be described in the following four subsections. One is the low-order of accuracy of numerical discretization, another issue comes from mesh generation for the complex geometries of turbomachines, one further restriction is the limited time step size for unsteady turbulent flows, the final concern is that there is lack of unified schemes/solvers for a wide flow speed range (e.g. from an incompressible flow regime to a supersonic one as experienced in a realistic turbomachine).

1.2.1 Low-order of Accuracy

Turbomachinery flow is inherently unsteady, multi-scale in both time and space with complex geometries, which tends to be more complicated than those many other fundamental aerodynamic devices. These disturbances tend to be too expensive to be resolved inclusively and some are even out of reach by conventional CFD methods on current supercomputers, such as unsteady turbulent flows of multi-physics and multi-scales (e.g. multi-component interactions, heat transfer, turbulent combustion, etc.). For instance, the capability of predicting the aero-thermal interactions of turbomachinery plays a significant role in the design and optimization of turbomachines. However, the simulations are very expensive and the solutions can be too dissipative for current conventional 2nd-order discretization schemes, whereas the researches seek high resolutions for aero-thermal performance. Hence, the need of developing and applying high-order schemes has been highlighted in pursuing solutions with high resolution for practical design and optimization of multi-scale turbomachine systems.

1.2.2 Mesh Generation for Complex Geometries

Mesh generation has been an essential part in CFD simulations and good quality meshes can produce accurate solution, robust computation and fast convergence rate. Structured mesh is arranged in a regularly specified pattern called block without the need of storing the connectivity information of elements and nodes, which normally consumes less CPU memory and computing time. The typical choices of structured elements are quadrilaterals in two-dimensional (2D) space

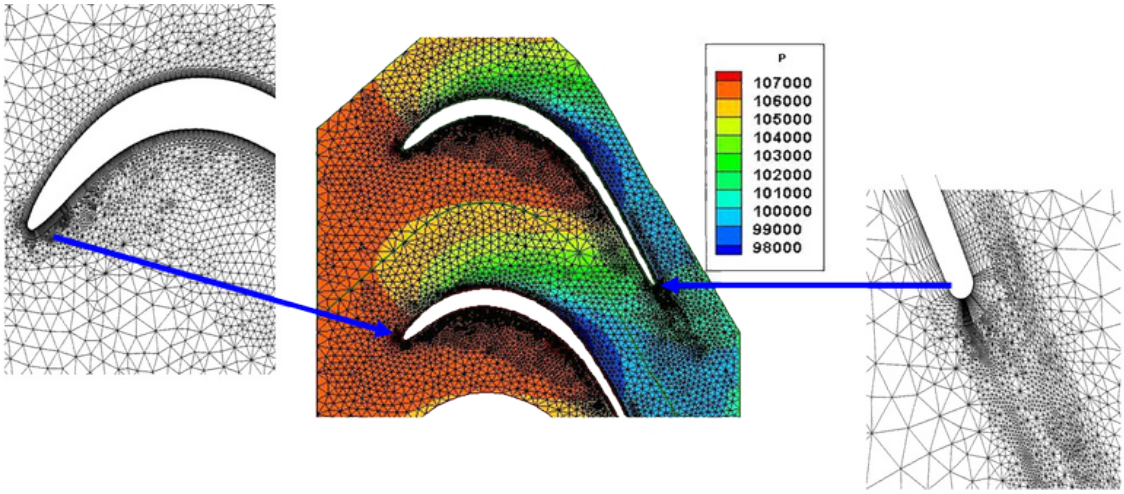


Figure 1.1: Unstructured mesh for computation of low pressure turbine blades by Zheng and He (2001)

and hexahedrons in three-dimensional (3D) space. The structured mesh also allows high degree of control in positioning the elements and nodes, but it is very time-consuming for generating the meshes for complex geometrical configurations. For example, generation of structured or multi-block structured meshes might need a few days or even weeks for complex geometry of turbomachinery flows.

On the contrary, unstructured mesh is laid out in an indiscernible pattern with irregular connectivity of elements and nodes. The typical unstructured elements in 2D are triangles and tetrahedrons in 3D. One advantage of unstructured mesh is the automated grid generation without need of specifying the block structures whereas it might take considerable effort in meshing the boundary. Therefore, it easily handles the complex geometry and delivers fast grid generation comparing to structured one. For turbomachinery flows, unstructured mesh provides an efficient approach to the complex geometry and also gives much more freedom of refining different regions. Figure 1.1 illustrates unstructured meshes with adaptive refinement for prediction of wake and large scale separation of low pressure turbine cascade at

negative incidence by Zheng and He (2001), which provides flexibility of effectively computing turbulent flows through complex configurations.

1.2.3 Limit of Temporal Discretization

The spatially discretized equations can be integrated easily in time using an explicit time marching scheme (e.g. a multi-stage Runge-Kutta method). It is typically an adequate approach for flow problems spatially discretized on relatively isotropic meshes. But it is worth noting that for very complex geometry configurations of high Reynolds (Re) number turbomachinery flow, highly anisotropic meshes might have to be generated. The eminently high aspect ratio (e.g. up to 10^4, see Wang, 2014) of near wall meshes imposes severe bounds of time step size due to numerical stability requirement. The time step limit set by the minimum mesh size of an extremely non-uniform and also highly skewed mesh can be too restrictive, particularly for unsteady flow solutions where a uniform time step needs to be taken for the temporal consistency. For example, the time step size of a Runge-Kutta method is restricted by the corresponding smallest Courant–Friedrichs–Lewy (CFL) number, normally less than 1, which makes this explicit scheme inefficient for unsteady simulations of turbomachinery flows. Note that a standard CFL is only for for Euler solver/inviscid flow convection, and an extended expression should also include the restriction caused by the viscous diffusion part.

Given the challenges in developing effective multi-grid methods to accelerate the time marching for explicit schemes on unstructured meshes, the implicit time integration with the advantage of using very large time steps can alleviate this

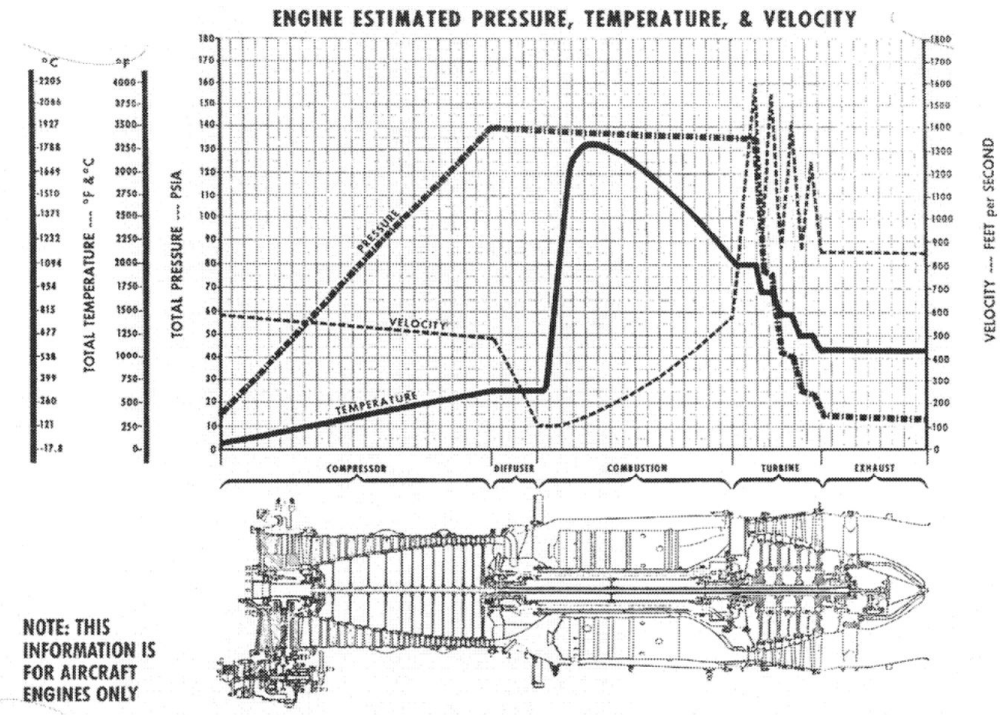


Figure 1.2: Sample engine pressure, temperature and velocity (see Cast, 1997)

issue. The implicit formulation has proven to be stale over a wide range of CFL numbers, sometimes unconditionally stable, and has shown to be an important way of accelerating solutions for both steady and unsteady flows.

1.2.4 A Wide Range of Flow Speed

Turbomachinery flow is subject to a wide flow regime ranging from a low speed equivalently incompressible flow to a high speed transonic flow, thus a unified CFD algorithm can be employed for both incompressible and compressible flows is significantly urgent. Figure 1.2 gives an estimated flow pressure, temperature and velocity variations through an engine as reported in Cast (1997), it clearly reveals a wide flow speed range from 30 m/s (incompressible) up to 500 m/s (supersonic). The internal air systems of gas turbines are a mix of all-speed flows, such as turbine passage flows, leakage flows, cavity flows and film cooling flows.

Turbine Flows Accurate and efficient prediction of the flow and heat transfer through turbine blades and passages is the key point to improve the design and performance of turbomachinery. The flow pattern can vary from incompressible to compressible flows from the first turbine stage to the last one, it would be of great significance to have a flow solver to simulate the flows through turbines at any given Mach number of practical interest.

Leakage Flows The interaction between the leakage and mainstream flows in shrouded turbomachines has caused the energy losses, thus many studies have been focusing on reducing the losses, such as the geometry optimization of arrangements of sealing, shroud and casing. Since the flow simulations to investigate the leakage flow on the rotor blade tip in shrouded turbomachines may vary from incompressible, subsonic, transonic to supersonic, a unified solver that is capable of accurately and efficiently simulating the relevant Mach regime is needed.

Cavity Flows The flow simulations of axisymmetric rotor-rotor and rotor-stator with cavities are also widely studied. These rotating cavity flows and interactions between cavities and main flows also raise interest in developing an accurate and efficient CFD solver to simulate both the main passage high speed flows and cavity flows which tend to be of a very low speed. The capability of simulating a wide range of flow characteristics is also highly addressed here.

Cooling Flows At the design process of a gas turbine, both the efficiency and reliability need to be improved by conducting the heat transfer study on the metal

vane surfaces. As commonly known, the coolant inside an internal path is usually in a low-Mach regime but the simulations can over-predict the velocity field in the cooling holes using a conventional compressible solver, which will result in the poorer performance of cooling holes than designed. Hence, a flow solver capable of simulating the mix of incompressible and compressible flows can greatly improve the design and performance of film cooling.

1.3 Objectives of Present Work

Given the current challenges of CFD simulations of turbomachinery flows, the present research aims to develop a CFD method with the following four key features:

- easily extended to a high-order spatial discretization;
- time marched using implicit techniques for both steady and unsteady flows;
- based on unstructured mesh for complex geometry;
- suited for both incompressible and compressible flows.

Although each or some combination of above was pursed in some previous efforts, it has been unknown to the present author that a combination of all four desired features has been so far put into a single turbomachinery solver development. The development of a distinctive solver with combined characteristics of implicit time integration, high-order discretization, unstructured meshes and all-speed flows is thus regarded as a novel approach to simulations of complex turbomachines with greatly enhanced accuracy for a wide flow speed range (from an incompressible flow

regime to a supersonic one), which can be potentially developed further into an essential CFD tool for next generation turbomachinery design and analysis.

1.4 Outline of Thesis

The subsequent Chapter 2 will review the literature first on the state of the art of turbomachinery CFD, then various high-order schemes in general CFD and recent development of high-order schemes in turbomachinery. In addition, it will also compare the merits and drawbacks of unstructured mesh with structured one, investigate the implicit time integration strategy and review the present schemes applied for all-speed flows.

Chapter 3 will detail the numerical methodology consisting of spatial discretization of conservation equations, application of all-speed convective flux scheme, employment of a compact viscous flux discretization strategy, modification of one equation turbulence model.

Chapter 4 will describe the implicit time integration strategy.

Chapter 5 will present the validation studies, first for some simple canonic cases. These include the inviscid flow past a cylinder, a laminar cylinder vortex shedding, a laminar boundary layer through flat plate, a turbulent boundary layer over the flat plate and a subsonic, transonic and supersonic flow over an airfoil.

Chapter 6 will describe Reynolds-Average Navier Stokes (RANS) validation studies for a high pressure turbine (HPT) cascade.

Chapter 7 will present further modelling considerations and subsequent case studies for the HPT cascade using a unsteady laminar approach.

Chapter 8 will conclude the work which has been conducted, presenting major conclusions and some recommendations on future work.

2
Literature Review

This literature review chapter will start with a brief overview of the turbomachinery CFD development in Section 2.1. Then the literature on the four challenging issues as discussed in Chapter 1 will be covered. The review of the state-of-the-art high-order CFD methods will be described in Section 2.2. The following Section 2.3 will compare the pros and cons of both structured and unstructured meshing strategies. The subsequent Section 2.4 will discuss the available time integration schemes including representative explicit and implicit methods. Section 2.5 will deal with current methodologies, with certain restraints, in achieving the unified solver with capability of solving a mix of compressible and incompressible flows. Finally, Section 2.6 will summarize the characteristics of present work.

2.1 Brief Overview of Turbomachinery CFD

The blade passage-to-passage periodicity in turbomachinery has significant influences on the blade design analysis. The time-marching methods for the inviscid Euler

equations pioneered by Denton (1975, 1983) remarkably enhanced the predictability of 3D unsteady flows in the blade passage. The calculations of stator-rotor interaction in both low-speed and high-speed turbines using the time-marching solution of the unsteady Euler were carried out by Giles (1988, 1990).

The extension to a 3D viscous calculation for the multi-stage machine flows was established by Denton (1992). The Naver-Stokes viscous flow solver was also developed by Dawes (1988, 1992) with mixing planes and applied to efficiently simulate multi-stage blade rows. The turbulent calculations of the turbomachinery flows with an implicit relaxation method were carried out by Hah (1987). The multi-grid acceleration methods developed by He (1993, 2000) significantly speeded up the calculations for 3D unsteady viscous flows in turbomachines. The computations of 3D rotor flows using the multi-grid method were also performed by Arnone (1994) and Arnone et al. (1995) with enhanced efficiency.

Giles (1992) put forward an asymptotic formulation based on the nonlinear steady flow for the calculation of the unsteadiness in multi-stage turbomachinery. Furthermore, the simultaneously coupled method between the time-averaged flow and the harmonic unsteady perturbations for the unsteady viscous turbine flows was developed by He and Ning (1998). An overall detailed overview of the temporal Fourier modelling approach in the past two decades was conducted by He (2010).

Overall, the CFD methods developed in the past three decades greatly improve the predicability of the turbomachinery blade flows, but there is continuous need to further enhance the accuracy and efficiency for the turbomachinery simulations.

2.2 High-order CFD Method

To solve the real world applications introduces many challenges, more advanced CFD algorithms are required. The requirement for new CFD methods corresponds to increased efficiency of computing performance, enhanced high-order accuracy of discretization errors, improved robustness to reach convergence and raised flexibility for complex geometries. Here, it needs to be stressed that a consistent definition is taken that only the order of spatial discretization equal to or greater than third-order is called high-order. There tend to be different assumptions and expectations regarding 'higher order accuracy', because many tend to expect the concern that 'high-order' means increasing computational costs and memories, complexity in code implementation, less robustness and slow convergence, difficulties in coping with complex geometry and requirement of high-order meshes. Some of questions/concerns are certainly debatable and are also research and development topics for CFD modellers. For example, with regard to the concern on computational efficiency, Wang et al. (2013) suggested a fair way is to compare the computational cost upon reaching the same order of accuracy between high-order and 2nd-order schemes. In this context, high-order schemes might not always mean to be expensive.

2.2.1 Demands for High-Order Schemes

In a recent series of American Institute of Aeronautics and Astronautics (AIAA) CFD drag prediction workshop from 2001 to 2016 (Laflin et al. (2005), Levy et al. (2003, 2014), Tinoco et al. (2018), and Vassberg et al. (2007, 2014)), researchers have accounted the discretization errors as the dominant sources of errors for the

state-of-the-art CFD methods. Many efforts are focusing on providing a high-quality and parametrically consistent family of grids for accurate drag prediction. However, whether the required accuracy can be obtained by 2nd-order spatial discretization schemes with grid refinement is still uncertain. Furthermore, Mavriplis et al. (2009) found that increasing the grid resolutions has trivial effect on improving accuracy of local quantities like surface pressure coefficients and skin frictions. The numerical solution errors ε for a 2nd-order scheme in CFD is defined as $\varepsilon \propto h^2$, where h denotes the measure of mesh cell spacing. Then, the solution errors ε for high-order scheme can be delivered in a similar manner, $\varepsilon \propto h^p$, $p \geq 3$ and represents the order of discretization accuracy, which implies, for a high-order method, the discretization errors can be decreased to third-order or higher-order. Therefore, researchers put more efforts on seeking for the potential of high-order schemes in reducing the spatial descretization errors.

Moreover, the computational aeroacoustic (CAA) modelling remains challenging for the conventional 2nd-order scheme since extremely fine grid resolution is needed for preserving the acoustic wave propagation, whereas the high-order schemes with much less numerical dissipation are more capable of solving the CAA problems. Karabasov and Goloviznin (2007, 2009) developed an efficient high-resolution CABARET method applied in aeroacoustic simulations. Faranosov et al. (2013) further extended this methodology with the 4th-order velocity corrections for the prediction of jet noise using a large eddy simulation (LES) solver. More recently, Elnaz Naghibi et al. (2019) applied the spectral Galerkin method to solve the double-gyre turbulent flows with a two-scale approach.

The present author admits that whether there exists certain flow problems that high-order schemes are capable of solving whist low-order ones completely can not tackle with may be debatable. However, it is of the present interest to explore the prospect of high-order CFD methods in obtaining enhanced accuracy with increased efficiency and simplicity.

2.2.2 High-Order Construction from Conventional CFD

Consequently, the question arises as how high-order accuracy of spatial discretization can be achieved within the scope of conventional CFD methods. The present author will first review these predominant discretization schemes, including Finite Difference Method (FDM), Finite Volume Method (FVM) and Finite Element Method (FEM) or Continuous Galerkin Method (CGM), and identify their basic properties in order to construct possible high-order implementations.

For FDM, the derivatives in partial differential equations (PDE) are approximated by finite difference at discrete points. The corresponding discretization errors are determined by the difference between true values and approximate solutions. FDM is not only easy for code implementation and efficient in computing, but also easy to be used to construct high-order extensions. Lele (1992) put forward compact approximations for third- and higher-order derivatives constructed on narrow stencils and obtained the high-order accuracy through the high-order approximations of local discrete derivatives. The extension of high-order compact finite difference schemes from Euler to Navier-Stokes equations on the stretched, curvilinear and deforming meshes were developed by Visbal and Gaitonde (2002). In contrast to

its simplicity in obtaining high-order accuracy, its restriction of only fitting for structured meshes impedes the further applications. The implementation of FDM on unstructured meshes is not as straightforward as on structured ones, hence FDM lacks of flexibility for complex geometries.

In the context of FVM, the governing equations are integrated over the discretized mesh elements with the fluxes through element interfaces evaluated by either central differencing schemes introducing numerical dissipations, e.g. by Jameson et al. (1981) or upwind schemes based on the nature of wave propagation, such as flux-vector splitting scheme by van Leer (1982) and flux-vector differencing scheme by Roe (1981). And more recently, Liou (1996) and Liou and Steffen (1993) put forward a new family of schemes, called Advection Upstream Splitting Method (AUSM), combined both features of the flux spitting and flux differencing scheme. FVM is well suited for the conservation laws and applicable for unstructured grids, which holds the key to complex geometries. Barth (1993) proposed a high-order reconstruction scheme incorporated into the upwind schemes applied for Euler and Navier-Stokes equations. However, this reconstruction was conducted with the adjacent elements, where these reconstruction stencils became extremely complex for three-dimension unstructured meshes. In addition, it was not efficient in parallelization because of the increased reconstruction stencils, which carried a large amount of information when communicating with parallel nodes. Thus, conventional FVM still remains under developed when extending to higher-order discretization on unstructured meshes.

Unlike FVM, FEM owns the ability of achieving a high-order easily by increasing the degree of piece-wise polynomials. For FEM, the integrated governing equations

are first multiplied by arbitrary test functions, a subsequent variational statement is obtained from integration by parts and the final discrete solutions are approximated by a combination of basis functions. Babuska et al. (1981) established the p-version of FEM (p denotes the degree of approximate polynomials) for 2D elasticity problems. FEM is easy to be used to construct high-order approximation since the accuracy is simply obtained by the degree of basis approximate polynomials without any reconstruction. Another merit is its flexibility for complex boundaries. Still there are shortcomings that FEM may not be stable for convection-dominated problems. Hence, various research has been focusing on adding artificial dissipative terms to stabilize the standard FEM schemes. Hughes et al. (1986) introduced a new streamline upwind Petrov-Galerkin (SUPG) method to stabilize the FEM for solving the Stokes equation, and in the meanwhile, Johnson and Saranen (1986) presented a generalization of stabilized FEM including a streamline diffusion method for incompressible inviscid and viscous flows. Hughes et al. (1989) and Shakib et al. (1991) built a new framework of finite element formulations to solve the compressible Euler and Navier-Stokes equations by adding a least-square operator and a discontinuity-capturing operator to guarantee the required stability. Masud and Khurram (2004) investigated the multiscale stabilized FEM in advection-diffusion problems and examined on simple 2D flows reaching a desired convergence rate. However, it has not yielded wide-ranging applications and needs further development under the framework of stabilized methods.

On account of the various drawbacks of current conventional discretization schemes, a scheme called Discontinuous Galerkin (DG) method or Discontinuous

Finite Element Method (DFEM) that combines the capabilities of local high-order extension of FEM (or CGM) and local flux discretization maintaining the conservation laws from FVM has been recently proposed.

The distinct difference between the DG method and CGM is that the DG discretization is local to an element without any continuity requirement on the boundary with the neighbouring elements whereas the CGM forces the continuity across the element interfaces. Therefore, the DG method is more capable of resolving the problems with large discontinuity.

2.2.3 Development of High-Order DG Method

Due to the combination of both advantages of FEM and FVM, the DG method has gained tremendous interest from researchers in recent two decades. For a DG method, the high-order accuracy is simply achieved by increasing the order of approximate piece-wise polynomials without depending on the stencils as in the conventional FVM. In addition, since the approximate solutions are represented by the piece-wise polynomials without inter-element continuity restrictions, the upwind flux schemes from Liou and Steffen (1993), Roe (1981), and van Leer (1982) initially developed for FVM or FDM are also adopted to compute the numerical flux through the element interfaces.

The DG method was first introduced by Reed and Hill (1973) to solve the neutron transport problems. Furthermore, LaSaint and Raviart (1974) constructed the extension to solve linear hyperbolic problems, estimated the priori errors and proved the corresponding convergence rates. However, the DG scheme still has

yet enjoyed many practical applications.

The breakthrough from dealing with the linear hyperbolic problems to non-linear hyperbolic applications was established by Cockburn and Shu (1989, 1991, 1998a) and Cockburn et al. (1989, 1990). They implemented the Runge-Kutta Discontinuous Galerkin (RKDG) method to solve the system of non-linear hyperbolic conservative laws in a general framework, particularly for the compressible Euler equations, which employed explicit Total Variation Diminishing (TVD) Runge-Kutta method by Shu and Osher (1988) to achieve high-order accuracy for temporal discretization. The RKDG method is essentially based on the framework of FEM whilst evaluating the numerical flux by Riemann solvers originally applied in FVM.

Bassi and Rebay (1997b) carried out the application of RKDG method to 2D steady state flows on unstructured grids with a high-order representation of curved boundaries. The extension from Euler to Navier-Stokes equations using the DG discretization was pioneered by Bassi and Rebay (1997a, 2002). They introduced Bassi and Rebay first (BR1) scheme of a mixed formulation to spatially discretize the viscous flux and further presented the Bassi and Rebay second (BR2) scheme that eliminates the extended stencils and only includes the nearest neighbour stencils for the treatment of viscous terms. Cockburn and Shu (1998b, 2001) and Cockburn et al. (2002, 2005) also extended the RKDG method for purely hyperbolic systems to a Local Discontinuous Galerkin (LDG) method for convection-diffusion systems. The LDG method handles the second-order viscous terms by rewriting them into first-order equations and then employs then DG discretization for these first-order systems. Apart from this, the LDG method introduces extended stencils, similar to

BR1, and increases the computational cost in the multidimensional applications. Thereafter, Peraire and Persson (2008) developed a compact Discontinuous Galerkin (CDG) method for the elliptic problems. The proposed CDG scheme remains to have compact stencils and reduces sparsity pattern while retaining the advantages of LDG method. Another hybridizable DG (HDG) method with the global coupled unknowns significantly reduced by approximating traces of conservative variables was put forward by Nguyen et al. (2009, 2011) and Peraire et al. (2010). In addition, the HDG method provides the optimal convergence rate for all approximate solutions whereas the LDG method partially yields the optimal convergence.

Moreover, Huynh (2007) proposed a flux reconstruction (FR) scheme to reach robust and efficient high-order methods. A new families of energy-stable FR schemes can recover various high-order schemes comprising of the DG method and spectral difference method in a single unified framework were developed in 1D space by Vincent et al. (2011) and 2D space by Castonguay et al. (2012) for linear advection problems. The energy stable FR schemes were further extended to advection-diffusion problems in 2D space by Williams et al. (2013) and in 3D space by Williams and Jameson (2014). Notwithstanding that FR schemes were provably stable and efficient, the aliasing non-linear stability problems which manifest if the flux function is non-linear were addressed by Jameson et al. (2012). Another reconstructed DG method to efficiently discretize viscous and heat fluxes based on arbitrary grids was constructed by Luo et al. (2010, 2011) and Xia et al. (2014), where strong interpolations on the facing-neighbouring cells were solved in the least-square method. This reconstruction method has not been performed above

3rd-order of accuracy and the choice of a reconstruction operator is specially vital to the robustness, accuracy and efficiency of this method.

The DG method has also been evolved to discretize Reynolds-Average Navier-Stokes (RANS) equations closure with turbulence models. Bassi et al. (2005) implemented the DG discretization of compressible RANS equations with $k-\omega$ turbulence model (Wilcox, 1988) equations. Bassi et al. (2009) and Crivellini and Bassi (2011) carried out the subsequent numerical validation through steady state turbulent flows. Hartmann (2013) and Hartmann et al. (2011) further gave an artificial viscosity term to complement an adaptive DG discretization of RANS and $k-\omega$ turbulence model equations in solving turbulent flows with the large discontinuities (e.g. shock). Meanwhile, Moro et al. (2011) and Nguyen et al. (2007) conducted the DG discretization of RANS equations with a modified Spalart-Allmaras (SA) turbulence model (Spalart and Allmaras, 1992) that prevents the negative working variable and creates an improved convergence. Analogously, Oliver (2008) altered the eddy viscosity to be non-negative that avoids the divergence of high-order DG simulations of turbulent flows. Burgess and Mavriplis (2012a,b) inherited the modification of turbulence working variable in the SA equation to retain positivity and performed the turbulent simulations of high-lift multi-element airfoil configurations. Similarly, Landmann (2008) included a limitation procedure of turbulence variables to augment the robustness of high-order DG discretizations of the RANS equations with SA and $k-\omega$ turbulence models.

On the whole, the high-order DG method has been steadily developed from its first occurrence, in solving the Euler, Navier-Stokes and RANS equations with

remarkably enhanced robustness and efficiency owing to the enrichment of various schemes have been established in literature, and so far, the DG discretization has been gradually applied in aerodynamic study and analysis.

2.2.4 Features of High-Order DG Method

As described above, the DG method is a numerical scheme that achieves local high-order accuracy by simply increasing the degree of approximate piece-wise polynomials from FEM and maintains conservative properties at element interfaces by an approximate Riemann solver from FVM. In addition, due to its flexibility and adaptability to the unstructured meshes, the DG method is well suited for complex geometries. Moreover, the DG method maintains the compactness, regardless of the order of accuracy, owing to that the required stencils are only confined to the neighbouring elements. The compactness also allows for structured and simplified implementation of the DG discretization. On account of this advantageous property, the DG discretization can be highly parallelizable and easily handle adaptive mesh strategies, since coursing and refining a grid can be obtained without considering the continuity restrictions related to the conforming elements. Consequently, the DG method can be easily implemented for the hp-refinement. Note that a h-refinement is to subdivide a mesh cell while keeping the degree of piece-wise polynomials fixed and a p-refinement is to increase the degree of piece-wise polynomials within the same mesh cell, thus the hp-refinement is the combination of these two approaches (see Karniadakis and Sherwin, 1999). Based on the aforementioned features of the DG method, a detailed comparison among the DG method and other conventional

Table 2.1: Features compared among DG method and other conventional CFD methods

	FDM	FVM	FEM	DG
High-order accuracy	√	×	√	√
Complex geometries	×	√	√	√
Conservation laws	√	√	×	√
Compactness of scheme	×	×	×	√
hp-adaptivity	×	×	√	√

×: not work √: work

CFD methods is illustrated in Table 2.1.

In contrast to these favourable features, high-order methods have been criticized for slow convergence rate as a result of the decrease of numerical dissipations by Wang et al. (2013). In addition, the requirement for computer memory is demanding due to the enormous number of degrees of freedom from a high-order DG discretization and more severe if employing an implicit integration scheme. On top of that, the high-order curved meshes are not straightforwardly generated comparing to the straight-sided meshes. Despite these deficiencies, the high-order DG method is still a promising scheme with enhanced accuracy with potential to become a working method for future CFD for aeronautical applications.

2.2.5 High-Order DG Methods in Turbomachinery

CFD has played a significant role in the design and evaluation of performance of turbomachinery both in academic and industrial applications. These applications in the single- and multi-blade row design, leakage flows, cavity flows and heat transfer have demanded even more accurate predictive capability, which requires a high resolution scheme due to the presence of some small-scale flow features.

However, the conventional CFD codes as widely applied in industry are mostly based on 2nd-order FVM or FEM discretization schemes, which tend to be very dissipative and inadequate when pursuing high resolution of complex problems involving turbomachinery design and analysis.

The recent trend in applications of high fidelity flow models in turbomachinery has increasingly highlighted the requirement for developing and applying new high-order schemes. High-order schemes based on the finite difference upwind-biased weighted essentially non-oscillatory (WENO) to simulate the flow through a turbine blade cascade by Jimbo et al. (2012), though showing great promises in enhanced accuracy, tended to be limited to structured grids and required rather large neighboring stencils for higher-order discretization. Another high-order FVM using an upwind flux scheme with Monotonic Upstream-Centered Scheme for Conservative Law (MUSCL) reconstruction was applied to predict the transitional flow over a LPT cascade and the tip leakage flow in a high pressure compressor by Marty et al. (2015) while the extension to high-orders was also restrictive.

The DG approach has been extensively applied to external aerodynamics, and also started to be developed and applied to internal flows, though to a much less extent. For turbomachinery field, the development and applications of DG based solvers are relatively more recent. The DG method solving the RANS with the $k-\omega$ equations were employed to simulate the vortex shedding developed behind the trailing edge of a turbine blade by Bassi et al. (2005), to predict the main flow features of the transitional turbulent flow through T106A (designed by Hoheisel, 1981) low pressure turbine cascade by Ghidoni et al. (2013) and Bassi

et al. (2016), and to examine the flow characteristics of turbulent flow through a National Aeronautics and Space Administration (NASA) Rotor 37 (designed by Moore and Reid, 1980) by Bassi et al. (2016).

Turbulence eddy resolved (instead of modelled) simulations have also been conducted more recently using the DG based methods, typically at relatively low Reynolds numbers. The direct numerical simulation (DNS) using a DG discretization was lately applied to low pressure turbine (LPT) cascade to capture the flow separation and transition at low Reynolds number by de Wiart et al. (2012) and Hillewaert et al. (2014), on a 2D geometry with a small spanwise length without considering the end wall effects. Another preliminary study of large eddy simulation of a full-span T106C LPT cascade with a DG solver by introducing an extra wall-resolved model was carried out by de Wiart et al. (2015), but only the benchmark test case of a turbulent channel flow was validated. Garai et al. (2015, 2016) constructed the entropy-stable DG spectral-element method to simulate a LPT cascade with elevated inflow turbulence where good agreement on computed surface pressure profile with experimental one was achieved, but the transition characteristics on the suction side still did not match well with experimental data. In addition, the downstream loss in this study only took into account of profile loss due to lack of end wall effects.

It is worth pointing out that most of the previous high-order DG studies for turbomachinery have been confined to 2D (quasi 3D) configurations. It is well known than a major source of flow losses in a blade passage is the endwall region dominated by secondary flows as pointed out by Denton (1993). To the

present author's knowledge the endwall secondary flow development is yet to be studied by a high-order scheme.

Furthermore, it is of interest to examine a 3D turbine configuration where flow losses are influenced by both secondary flow in the endwall region and blade surface laminar to turbulence transition. The laminar separation is followed by instabilities of separated shear-layer, which subsequently leads to a transition to a turbulent state followed by a reattachment. For a RANS based flow solver, the boundary layer transition can be modelled by a 2D boundary layer based transition model, e.g. a very simple separation bubble length correlated model by He (1998), and those more recent developed four-equation transitional turbulence models by Langtry and Menter (2009). The presence of strong secondary flow effects in the endwall region would challenge those boundary layer based transition models. A LES/DNS approach should be naturally more suitable in resolving a laminar separation, the initiation and development of associated shear layer instabilities and the subsequent transition to turbulence. The challenge would arise from the need to fully resolve the 3D endwall region as well as the blade surface boundary. A typical LES mesh count per blade passage would be in the range of 2 orders of magnitude more than that for a RANS solution. For a blade design environment where multiple fast solutions are needed, the present author would wonder if there is any other option.

Given the background as introduced above, the present work has been initiated to develop a high-order DG solver for turbomachinery applications. More specifically, flow losses in a HPT cascade subject to the influences of secondary flow and the laminar separation induced transition will be examined using high-order DG solver

and compared to the corresponding experimental data.

2.3 Unstructured Meshing Technique

A computational domain is normally discretized into a finite set of mesh cells to obtain the discrete approximation of governing equations. There are a few discretization schemes as reviewed in Section 2.2, such as FDM, FVM, FEM or DG. For the meshing techniques, the two representative approaches are the structured and unstructured meshes.

Some early studies by Thompson et al. (1985) summarized the numerical schemes of generating structured meshes and constructed a mesh generation system with a mapping from the physical region to the transformed (computational) domain. Castillo (1991) further produced a robust and efficient variational mesh generation technique by controlling the spacing, area and orthogonality of structured grids. A structured mesh is quite appealing owing to its regular connectivity, utilized spacial efficiency and high degree of control with the typical 2D quadrilateral elements and 3D hexahedral elements. However, one non-negligible drawback of the structured mesh is that the required experience and time for optimally laying out the block structure and positioning the nodes and points are too demanding for complex turbomachinery geometry.

On the contrast, George et al. (1991) and George (1991) developed an automatic unstructured mesh generator applied in the FEM computation for both 2D and 3D flows. Mavriplis (1995) further performed the unstructured mesh generation and adaptivity for complex geometries. Zheng and He (2001) lately constructed

the unstructured meshing technique with an adaptive refinement for predicting the turbomachinery flows. Unstructured mesh is distinctively attractive for problems with complex geometrical configurations due to its capability of automatic mesh generation. The main disadvantage arises from lack of control especially involving the treatment of near wall boundary meshes.

Given the aforementioned pros and cons of meshing techniques, the present author would like to adopt the unstructured mesh for turbomachinery applications on the basis of its great efficiency and flexibility for complex geometry.

2.4 Implicit Time Integration Method

The spatial discretization of governing equations can be integrated in time using either an explicit or an implicit scheme. An explicit scheme calculates the approximate solutions of next time step based on the ones of the current time step, whereas an implicit scheme approaches the approximate solutions by solving the equations involving solutions at both current and next time steps.

One representative explicit scheme is the multi-stage Runge-Kutta method that has been applied in time integration of discrete flow equation with a high-order DG discretization by Cockburn and Shu (1989, 1991, 1998a) and Cockburn et al. (1989, 1990). One major drawback of the explicit scheme is that the permissible time step size is particularly restrictive due to the numerical stability requirement. It is much worse for time-dependent calculations, where a uniform time step is confined by the smallest CFL number, and it consequently leads to an excessive number of temporal iterations. Thence, a multi-grid technique has been put forward to alleviate the

time step restriction. He (1993) developed a time-consistent two-grid time-marching scheme to favourably relax the time step limitation (speeding up by a factor of 20) for unsteady airfoil flow calculations. He and Denton (1994) further employed this time-consistent two-grid scheme for the 3D unsteady simulations of blade flutter. Furthermore, He (2000) implemented the time-consistent multi-grid scheme in a full 3D Navier-Stokes method and applied for calculations of unsteady stator–rotor interaction in axial-flow turbines. Although these multi-grid techniques considerably speed up the time-marching with an explicit scheme, developing effective multi-grid methods for unstructured meshes still remains challenging.

On the other hand, the main merit of an implicit scheme is that large time steps can be adopted with the consequence of speeding up the time-marching for both steady and unsteady flows on either structured or unstructured meshes. The DG discretization was implicitly integrated in time with Euler backward differencing by Bassi and Rebay (2000) and Bassi et al. (2005, 2007) and the subsequent linear system equations were solved using the preconditioned Generalized minimal residual (GMRES) iterative method. Similarly, Burgess and Mavriplis (2012a,b) implemented the Newton-GMRES iterative method with the line Gauss-Seidel (GS) preconditioning in a DG solver. Another comprehensive comparison of performance of various preconditioning techniques of Newton-GMRES method, such as the block Jacobi, block GS and block incomplete lower–upper factorizations with zero fill-in (ILU0), for the DG discretization of the Navier-Stokes equations was carried out by Persson and Peraire (2008) and the block ILU0 preconditioner with minimum discarded fill was shown to be remarkably robust and efficient over

a wide range of problems on highly anisotropic meshes. Diosady and Darmofal (2009) further introduced a reordering technique for the block-ILU0 to reduce the number of iterations to reach convergence. A more recent matrix free Newton-GMRES method to save the memory for implicit DG scheme was introduced by Crivellini and Bassi (2011).

Given the features as discussed above, an implicit temporal integration scheme using the Newton-GMRES iterative method with several preconditioning options will be developed as a primary solution method in the present work because that very large time steps can be used on unstructured meshes.

2.5 All-Speed Scheme

The need of a unified CFD algorithm capable of solving both incompressible and compressible (or called All-Speed) flows has been addressed in Section 1.2. There are different approaches for conventional flow solvers (e.g. pressure-based and density based ones) to simulate flows with a wide speed range. For the pressure based method, a pressure correction equation extracted from the continuity and momentum equations is normally solved to obtain the pressure field. Staggered grids as such are needed to remove the oscillations in the solutions of pressure itself from the correction terms. One approach is to extend the pressure based solver to compressible flows, that is originally designed for an incompressible flow. Politis and Giannakoglou (1997) extended the pressure based method to simulate the transonic turbomachinery flows and integrated with a fully implicit scheme to improve the efficiency.

The density-based algorithm has been primarily applied for the steady and

transient solutions of transonic, supersonic and hypersonic flows, where density is computed from the continuity equation, the velocity field is solved from the momentum equations and pressure is calculated from the equation of state. However, the density based method consistently encounters with deficiencies of accuracy, efficiency and stability if the Mach number is close to 0. For instance, the severe numerical stability requirement of explicit schemes restricts time step size and leads to an excessive computing cost if the velocity is approaching 0. Similarly, the implicit schemes also endure stiffness problems due to the disparity in eigenvalues of the system matrix and the subsequent time-marching scheme becomes extremely slow as a result of the ill-conditioned algebraic system matrix.

To tackle these issues, researchers have developed the preconditioning scheme and asymptotic method for the solver capability of simulating with a wide flow speed range (Keshtiban et al., 2004). van Leer et al. (1991) added a local preconditioning matrix to the time derivatives of the governing equations for accelerating the convergence of steady-state solution for both compressible and incompressible inviscid flows. Turkel et al. (1997) defined a preconditioning matrix and artificial dissipation terms to obtain steady-state solution for the low-speed viscous flows. However, the preconditioning method lacks robustness at some stagnation points and the selection of appropriate preconditioners for complex problems is not straightforward. For asymptotic method, a perturbation term is typically introduced to reduce the stiffness of system matrix. Although the perturbation method is comparatively robust for inviscid and viscous flows, the nature of perturbation limits its application, especially for a mix of incompressible and compressible

flows. Given the existence of non-negligible shortcomings in the extensions of both pressure-based and density-based solvers, the present author would wonder if there is any other approach to the unified robust numerical scheme applicable for flows at a wide range of Mach numbers.

The present approach stems from a paper by Liou (2006), in which an upwind flux scheme, called AUSM$^+$-up flux, with characteristics of all-speed was applied in FVM. Liou and Steffen (1993) first introduced the AUSM flux and Liou (1996) further developed it into AUSM$^+$ flux, with combined efficiency from flux-vector splitting method and accuracy from flux-difference splitting method. This family of AUSM methods has enjoyed improved accuracy, efficiency and robustness over other upwind flux schemes. All previous AUSM development and applications mostly seem to be based on 2nd-order schemes. To the present author's knowledge, there has not been previous effort combining the all-speed AUSM$^+$-up scheme with a higher-order DG. The all-speed AUSM$^+$-up flux is constructed by combining a numerical speed of sound to the flux formulas and adding a cut-off Mach number to the pressure splitting function, which will be described in detail in Chapter 3. It has been validated that the convergence rates are independent of the Mach number and solutions remain stable without a local preconditioning matrix added in the time derivative terms in a low Mach regime. In addition, the solutions maintain desirable accuracy at all-speeds.

Given the characteristics as mentioned above, an AUSM$^+$-up flux will be implemented and further modified into the present high-order DG discretization scheme for the favour of unified robust all-speeds.

2.6 Summary Notes to Underline Main Objectives of Present Work

The major challenges for CFD methods in turbomachinery point to the need of high-order accuracy, mesh generation for complex geometry, relaxation of time step limit for unsteady simulations and applicability to a wide flow speed range. Based on the literature reviewed above, a few distinctive approaches to handle these four issues are pertinent to the present work.

First and foremost, a class of high-order methods with the features of internal sub-division have shown a distinctive approach to high-order accuracy using piecewise polynomials instead of relying on extended neighbouring stencils. Among these methods, the DG discretization has both gained high-order accuracy and maintained the conservation laws. To discretize the viscous terms in the DG scheme, a BR2 method is one of those that reserve the compactness with only considering the nearest neighbouring stencils. Towards the discretization of RANS equations, modifying the turbulence working variables in either SA or $k-\omega$ equations provides a choice of a high-order scheme in robustly simulating turbulent flows.

In addition, the DG discretization on unstructured mesh delivers much flexibility for mesh generation for complex geometry. Moreover, an implicit time integration relaxes the time step size limitation for unsteady calculations, and a Newton-GMRES method with the ILU0 preconditioner solving the subsequent linear system equations further reduces the number of iterations per time step. On top of these, an AUSM$^+$-up flux scheme gives an approach to a unified algorithm applicable for all-speed flows. In short, an implicit DG discretization using the AUSM$^+$-up flux

on an unstructured mesh will be developed in the present work to provide an option for tackling with those aforementioned challenges in turbomachinery flows.

The key novel approach of the present work is the implementation of the all-speed AUSM$^+$-up scheme in the framework of a standard higher-order DG. Another general novelty of the present work is the combination of all four major features including the high-order discretization, implicit time integration, unstructured meshes and all-speed upwind schemes to obtain the high-order accuracy, temporal efficiency, flexibility for complex geometry and applicability to all-speeds under a unified development in a single flow solver. To the best knowledge of the present author, there has not been any other unified CFD method including all of those four features applied in turbomachinery. The implementation, validation and application of the unified DG will be described in the remaining parts of this thesis.

3

Discontinuous Galerkin Discretization

In this chapter, the conservative law will be first introduced in Section 3.1 and the DG discretization of this governing law will be given in Section 3.2, followed by the detailed convective and viscous flux discretization in Sections 3.2.2 and 3.2.3, respectively. Next, a modification of SA turbulence model will be presented in Section 3.3. Finally, Section 3.4 will provide some typical boundary conditions implemented in the present DG solver.

3.1 Conservative Equations

The governing law of 3D Navier-Stokes equations in the conservative form are given by,

$$\frac{\partial \mathbf{U}}{\partial t} + \nabla \cdot (\mathcal{F}^c(\mathbf{U}) - \mathcal{F}^v(\mathbf{U}, \nabla \mathbf{U})) = \mathbf{0} \tag{3.1.1}$$

within the domain Ω, where $\mathbf{U}$ is the conservative variables, $\mathcal{F}^c(\mathbf{U})$ is the convective flux function of the conservative variables and $\mathcal{F}^v(\mathbf{U}, \nabla \mathbf{U})$ is the viscous flux function of the conservative variables and the gradients of the conservative variables. The

conservative variables $\mathbf{U}$, convective fluxes $\mathcal{F}^c$ and viscous fluxes $\mathcal{F}^v$ are given by,

$$\mathbf{U} = \begin{bmatrix} \rho \\ \rho u \\ \rho v \\ \rho w \\ \rho E \end{bmatrix}, \tag{3.1.2}$$

$$\mathcal{F}_x^c = \begin{bmatrix} \rho u \\ \rho u^2 + p \\ \rho uv \\ \rho uw \\ u(\rho E + p) \end{bmatrix}, \mathcal{F}_y^c = \begin{bmatrix} \rho v \\ \rho vu \\ \rho v^2 + p \\ \rho vw \\ v(\rho E + p) \end{bmatrix}, \mathcal{F}_z^c = \begin{bmatrix} \rho w \\ \rho wu \\ \rho wv \\ \rho w^2 + p \\ w(\rho E + p) \end{bmatrix},$$

$$\mathcal{F}_x^v = \begin{bmatrix} 0 \\ \tau_{xx} \\ \tau_{xy} \\ \tau_{xz} \\ u\tau_{xx} + v\tau_{xy} + w\tau_{xz} + k\frac{\partial T}{\partial x} \end{bmatrix},$$

$$\mathcal{F}_y^v = \begin{bmatrix} 0 \\ \tau_{yx} \\ \tau_{yy} \\ \tau_{yz} \\ u\tau_{yx} + v\tau_{yy} + w\tau_{yz} + k\frac{\partial T}{\partial y} \end{bmatrix}, \tag{3.1.3}$$

$$\mathcal{F}_z^v = \begin{bmatrix} 0 \\ \tau_{zx} \\ \tau_{zy} \\ \tau_{zz} \\ u\tau_{zx} + v\tau_{zy} + w\tau_{zz} + k\frac{\partial T}{\partial z} \end{bmatrix}$$

where ρ, u, v, w, p and E denote the density, velocity components, pressure and specific total energy, respectively. In addition, the equation of the state of an ideal gas is given by

$$p = (\gamma - 1)\rho(E - \frac{1}{2}(u^2 + v^2 + w^2)) \tag{3.1.4}$$

where γ is the ratio of specific heats, normally taken as 1.4 for ideal gas, and is calculated by $\gamma = c_p/c_v$, where c_p is the specific heat for the constant pressure and

c_v is that for the constant volume. The speed of sound can then be calculated by $a = \sqrt{\gamma p/\rho}$. Furthermore, the thermal conductivity k is calculated as $k = c_p\mu/P_r$, where P_r is the Prandtl number, generally set as 0.72, μ is the dynamic viscosity obtained via the Sutherland's law,

$$\mu = \mu_{ref}\left(\frac{T}{T_{ref}}\right)^{3/2}\frac{T_{ref}+S}{T+S} \tag{3.1.5}$$

where T_{ref} is the reference temperature, μ_{ref} is the reference dynamic viscosity and S is the Sutherland temperature, usually set as 110.4.

The viscous stress tensor is defined by

$$\begin{aligned}\tau_{ij} &= \mu(\frac{\partial u_i}{\partial x_j}+\frac{\partial u_j}{\partial x_i}-\frac{2}{3}\frac{\partial u_k}{\partial x_k}\delta_{ij})\\ i &= 1,2,3\ j = 1,2,3\ k = 1,2,3\end{aligned} \tag{3.1.6}$$

where the Kronecker delta is

$$\delta_{ij} = \begin{cases}1 & i = j\\ 0 & i \neq j\end{cases} \tag{3.1.7}$$

Finally, the components of 3D viscous stress tensors are

$$\begin{aligned}&\tau_{xx} = \mu\left(\frac{4}{3}\frac{\partial u}{\partial x}-\frac{2}{3}\frac{\partial v}{\partial y}-\frac{2}{3}\frac{\partial w}{\partial z}\right), \tau_{xy} = \mu\left(\frac{\partial u}{\partial y}+\frac{\partial v}{\partial x}\right), \tau_{xz} = \mu\left(\frac{\partial u}{\partial z}+\frac{\partial w}{\partial x}\right),\\ &\tau_{yx} = \mu\left(\frac{\partial v}{\partial x}+\frac{\partial u}{\partial y}\right), \tau_{yy} = \mu\left(\frac{4}{3}\frac{\partial v}{\partial y}-\frac{2}{3}\frac{\partial u}{\partial x}-\frac{2}{3}\frac{\partial w}{\partial z}\right), \tau_{yz} = \mu\left(\frac{\partial v}{\partial z}+\frac{\partial w}{\partial y}\right),\\ &\tau_{zx} = \mu\left(\frac{\partial w}{\partial x}+\frac{\partial u}{\partial z}\right), \tau_{zy} = \mu\left(\frac{\partial w}{\partial y}+\frac{\partial v}{\partial z}\right), \tau_{zz} = \mu\left(\frac{4}{3}\frac{\partial w}{\partial z}-\frac{2}{3}\frac{\partial u}{\partial x}-\frac{2}{3}\frac{\partial v}{\partial y}\right)\end{aligned} \tag{3.1.8}$$

3.2 DG Discretization in Space

The computational domain Ω is partitioned into a set of non-overlapping elements Ω_k with boundary $\partial\Omega$. The boundary $\partial\Omega$ is composed of Dirichlet and Neumann

boundaries, noted as $\partial\Omega_D$ and $\partial\Omega_N$. The solutions $\mathbf{U}_h(\mathbf{x}, t)$ in 3D space $\mathbf{x} \in \Omega$ and time space $t \in [0, T]$ can be achieved by

$$\frac{\partial \mathbf{U}}{\partial t} + \nabla \cdot \mathcal{F}^c(\mathbf{U}) - \nabla \cdot \mathcal{G} = 0 \tag{3.2.1a}$$

$$\mathcal{G} - \mathcal{A}\nabla\mathbf{U} = 0 \tag{3.2.1b}$$

where an auxiliary equation (3.2.1b) is included to obtain the first-order system equations. Here, a new vector $\mathcal{G}$ to reformulate the viscous flux $\mathcal{F}^v(\mathbf{U}, \nabla\mathbf{U})$ is defined as an form of the conservative variables and the gradients of conservative variables, $\mathcal{G} = \mathcal{A}\nabla U$, where $\mathcal{A} = \frac{\partial \mathcal{F}^v(\mathbf{U}, \nabla\mathbf{U})}{\partial \nabla\mathbf{U}}$ is the Jacobian matrix of viscous flux (see Landmann, 2008).

3.2.1 Weak Formulation

Here, some notations are introduced to discretize domain into finite dimensional space. The spatial domain Ω is partitioned into meshes $\mathcal{T}_h$ consisting of tetrahedral elements κ. Given that each two adjacent elements $\kappa^+, \kappa^- \in \mathcal{T}_h$, $\mathbf{n}^+$ and $\mathbf{n}^-$ are denoted as the outward and inward normal vector to the element boundary $\partial\kappa$. Next, the finite element spaces $\mathcal{V}_h$ and $\mathcal{W}_h$ are represented as

$$\mathcal{V}_h = \mathcal{V}_h^p = \{\mathbf{v} \in [L^2(\Omega_h)]^m : \mathbf{v}|_\kappa \in [\mathcal{P}^p(\kappa)]^m, \forall\kappa \in \mathcal{T}_h\} \tag{3.2.2}$$

$$\mathcal{W}_h = \mathcal{W}_h^p = \{\mathbf{w} \in [L^2(\Omega_h)]^{md} : \mathbf{w}|_\kappa \in [\mathcal{P}^p(\kappa)]^{md}, \forall\kappa \in \mathcal{T}_h\} \tag{3.2.3}$$

where $\mathcal{P}^p(\kappa)$ represents the space of polynomials of degree at most p in element κ, m denotes the dimension of conservative variables $\mathbf{U}$ and d is the dimension of space.

In order to achieve the approximate solutions $\mathbf{U}_h$, a weak formulation is first obtained by multiplying the governing equations (3.2.1) with arbitrary test functions

$\mathbf{v}_h \in \mathcal{V}_h$ and $\mathbf{w}_h \in \mathcal{W}_h$ and integrated over the element κ, then integrated by parts, the DG formulation of the governing equation (3.2.1) is finally reached as follows: Find $\mathbf{U}_h \in \mathcal{V}_h$ and $\mathcal{G}_h \in \mathcal{W}_h$, such that for all $\mathbf{v}_h \in \mathcal{V}_h$ and $\mathbf{w}_h \in \mathcal{W}_h$:

$$\sum_{\kappa \in T_h} \int_\kappa \mathbf{v}_h^T \frac{\partial \mathbf{U}_h}{\partial t} d\mathbf{x} + \int_{\partial\kappa} \mathbf{v}_h^T \hat{\mathcal{F}}^c ds - \int_\kappa \nabla \mathbf{v}_h^T \cdot \mathcal{F}^c d\mathbf{x} - \int_{\partial\kappa} \mathbf{v}_h^T \hat{\mathcal{G}} ds + \int_\kappa \nabla \mathbf{v}_h^T \cdot \mathcal{G}_h d\mathbf{x} = 0 \tag{3.2.4a}$$

$$\sum_{\kappa \in T_h} \int_\kappa \mathbf{w}_h^T \mathcal{G}_h d\mathbf{x} - \int_{\partial\kappa} (\mathbf{w}_h^T \mathcal{A}) \mathbf{U}_h ds + \int_\kappa \nabla \cdot (\mathbf{w}_h^T \mathcal{A}) \mathbf{U}_h d\mathbf{x} = 0 \tag{3.2.4b}$$

where the above DG discretization equations can be further re-written into,

$$\sum_{\kappa \in T_h} \int_\kappa \mathbf{v}_h^T \frac{\partial \mathbf{U}_h}{\partial t} d\mathbf{x} + \int_{\partial\kappa} \mathbf{v}_h^T \hat{\mathcal{F}}^c(\mathbf{U}_h^+, \mathbf{U}_h^-, \mathbf{n}) ds - \int_\kappa \nabla \mathbf{v}_h^T \cdot \mathcal{F}^c(\mathbf{U}_h) d\mathbf{x} - \int_{\partial\kappa} (\mathbf{v}_h^T)^+ \hat{\mathcal{G}}(\mathcal{G}_h^+, \mathcal{G}_h^-) \cdot \mathbf{n}^+ ds + \int_\kappa \nabla \mathbf{v}_h^T \cdot \mathcal{G}_h d\mathbf{x} = 0 \tag{3.2.5a}$$

$$\sum_{\kappa \in T_h} \int_\kappa \mathbf{w}_h^T \mathcal{G}_h d\mathbf{x} - \int_{\partial\kappa} (\mathbf{w}_h^T \mathcal{A})^+ \hat{\mathbf{U}} \cdot \mathbf{n}^+ ds + \int_\kappa \nabla \cdot (\mathbf{w}_h^T \mathcal{A}) \mathbf{U}_h d\mathbf{x} = 0 \tag{3.2.5b}$$

where $(\cdot)^+$ and $(\cdot)^-$ denote the variables from two sides of the element interface and the numerical fluxes $\hat{\mathbf{U}}$, $\hat{\mathcal{F}}^c$ and $\hat{\mathcal{G}}$ are introduced as the approximations to the $\mathbf{U}$, $\mathcal{F}^c$ and $\mathcal{G}$, respectively.

Here, the numerical flux functions from the approximate Riemann solver commonly used in FVM can be used to evaluate inviscid flux here. In the present work, a family of upwind flux scheme called AUSM (see Liou and Steffen, 1993) is considered. In order to ensure the solver works for both the incompressible and compressible flow, the type of numerical flux, called AUSM$^+$-up flux (see Liou, 2006), based on the framework of AUSM scheme for the all-speed flows is chosen. The details of the AUSM$^+$-up scheme are presented in the next section.

3.2.2 Convective Flux Discretization with AUSM$^+$-up Scheme

Here, the numerical inviscid flux $\hat{\mathcal{F}}^c$ based on the algorithm of AUSM, including AUSM$^+$ and AUSM$^+$-up flux, are employed in the present solver. The more specific AUSM$^+$-up scheme for the all-speed flow regimes is defined as follows (see Liou, 2006; Scandaliato and Liou, 2010).

For 3D discretization, the velocities normal to the element interface, denoted as $V_{L/R}$, are given by,

$$V_{L/R} = u_{L/R}n_x + v_{L/R}n_y + w_{L/R}n_z \tag{3.2.6}$$

where u, v and w are the velocity components in x, y and z directions, the subscripts L and R represent left and right states of the interface, n_x, n_y and n_z are the unit normal vectors in x, y and z directions, respectively.

Note that the shock can be captured through the two discontinuous states at the element interface, where the numerical speed of sound $a_{1/2}$ is given by,

$$a_{1/2} = \min\left(\frac{a_L^{*2}}{\max(a_L^*, V_L)}, \frac{a_R^{*2}}{\max(a_R^*, -V_R)}\right) \tag{3.2.7}$$

where the critical speed of sound $a_{L/R}^*$ is defined by,

$$a_{L/R}^* = \sqrt{H_{L/R}\left(\frac{2(\gamma-1)}{\gamma+1}\right)}, \tag{3.2.8}$$

where the total enthalpy $H_{L/R}$ is,

$$H_{L/R} = \frac{\gamma p_{L/R}}{(\gamma-1)\rho_{L/R}} + \frac{u_{L/R}^2 + v_{L/R}^2 + w_{L/R}^2}{2} \tag{3.2.9}$$

The left and right state Mach numbers are then calculated by,

$$M_{L/R} = \frac{V_{L/R}}{a_{1/2}} \tag{3.2.10}$$

The interface Mach number $M_{1/2}$ dependent on $M_{L/R}$ is then given by,

$$M_{1/2} = \mathscr{M}^{+}_{(4)}(M_L) + \mathscr{M}^{-}_{(4)}(M_R) + M_p \tag{3.2.11}$$

where the split Mach number polynomials $\mathscr{M}^{\pm}_{(d)}$ of degree $d = (1, 2, 4)$ are defined by

$$\begin{aligned}
\mathscr{M}^{\pm}_{(1)} =& \frac{1}{2}(M \pm |M|) \\
\mathscr{M}^{\pm}_{(2)} =& \pm \frac{1}{4}(M \pm 1)^2 \\
\mathscr{M}^{\pm}_{(4)} =& \begin{cases} \mathscr{M}^{\pm}_{(1)} & if\ |M| \geq 1 \\ \mathscr{M}^{\pm}_{(2)}(1 \mp 16\beta \mathscr{M}^{\mp}_{(2)}) & otherwise \end{cases}
\end{aligned} \tag{3.2.12}$$

with a given parameter $\beta = 0.125$, and M_p is a pressure diffusion term introduced as the numerical dissipation for improving the robustness of the simulations of the low Mach number flow, which is given by,

$$M_p = -\frac{K_p}{f_a} \max(1 - \sigma \bar{M}^2, 0) \frac{p_R - p_L}{\rho_{1/2} a^2_{1/2}} \tag{3.2.13}$$

where $0 \leq K_p \leq 1$, $\sigma \leq 1$, the average density is $\rho_{1/2} = (\rho_L + \rho_R)/2$, the average Mach number is $\bar{M}^2 = (V_L^2 + V_R^2)/(2a^2_{1/2})$ and the scaling function is defined by $f_a(M_o) = M_o(2 - M_o) \in [0, 1]$, where scaling factor is $M_o^2 = \min(1, \max(\bar{M}^2, M^2_\infty)) \in [0, 1]$.

The mass flux is then obtained,

$$\dot{m}_{1/2} = a_{1/2} M_{1/2} \begin{cases} \rho_L & if\ M_{1/2} > 0 \\ \rho_R & otherwise \end{cases} \tag{3.2.14}$$

and the pressure flux is also reached,

$$P_{1/2} = \mathscr{P}^{+}_{(5)}(M_L) P_L + \mathscr{P}^{-}_{(5)}(M_R) P_R + P_u \tag{3.2.15}$$

where the polynomials $\mathscr{P}^{\pm}_{(5)}$ are defined in terms of $\mathscr{M}^{\pm}_{(d)}$,

$$\mathscr{P}^{\pm}_{(5)} = \begin{cases} \frac{1}{M} \mathscr{M}^{\pm}_{(1)} & if\ |M| \geq 1 \\ \mathscr{M}^{\pm}_{(2)}[(\pm 2 - M) \mp 16\alpha M \mathscr{M}^{\mp}_{(2)})] & otherwise \end{cases} \tag{3.2.16}$$

with the parameter $\alpha = \frac{3}{16}(-4 + 5f_a^2) \in [-\frac{3}{4}, \frac{3}{16}]$, and P_u is the velocity diffusion term given by,

$$P_u = -K_u \mathscr{P}^+_{(5)} \mathscr{P}^-_{(5)} (\rho_R + \rho_L)(f_a a_{1/2})(V_R - V_L) \tag{3.2.17}$$

where $0 \leq K_u \leq 1$. In the present implementation, the above constant values are set as, $K_p = 0.25$, $K_u = 0.75$ and $\sigma = 1.0$, in line with the recommended ones by Liou (2006).

Finally, the numerical upwind flux is achieved,

$$\hat{\mathcal{F}}^c = \dot{m}_{1/2} \begin{cases} q_L & if\ \dot{m}_{1/2} > 0 \\ q_R & otherwise \end{cases} + P_{1/2} \cdot \mathbf{n} \tag{3.2.18}$$

where $q_{L/R} = [1, u_{L/R}, v_{L/R}, w_{L/R}, H_{L/R}]^T$. Note that the AUSM$^+$-up scheme turns into AUSM$^+$ scheme when setting scaling factor $f_a = 1$.

3.2.3 Viscous Flux Discretization with BR2 Method

Here, the BR method (see Bassi and Rebay, 1997a, 2002) is chosen to discretize the viscous terms and the implementation will be described in the following details.

First, equation (3.2.5b) can be further derived after the second integration by parts,

$$\sum_{\kappa \in T_h} \int_\kappa \mathbf{w}_h^T \mathcal{G}_h d\mathbf{x} - \int_\kappa \mathbf{w}_h^T \mathcal{A} \nabla \mathbf{U}_h d\mathbf{x} + \int_{\partial\kappa} (\mathbf{w}_h^T \mathcal{A})^+ (\mathbf{U}_h^+ - \hat{\mathbf{U}}) \cdot \mathbf{n}^+ ds = 0 \tag{3.2.19}$$

Next, moving the second and third terms from left hand side to right hand side in equation (3.2.19),

$$\sum_{\kappa \in T_h} \int_\kappa \mathbf{w}_h^T \mathcal{G}_h d\mathbf{x} = \sum_{\kappa \in T_h} \int_\kappa \mathbf{w}_h^T \mathcal{A} \nabla \mathbf{U}_h d\mathbf{x} + \int_{\partial\kappa} (\mathbf{w}_h^T \mathcal{A})^+ (\hat{\mathbf{U}} - \mathbf{U}_h^+) \cdot \mathbf{n}^+ ds = 0 \tag{3.2.20}$$

Here, letting $\mathbf{w}_h = \nabla \mathbf{v}_h$ in equations (3.2.20) (see Barter, 2008; Hartmann, 2008),

$$\sum_{\kappa \in T_h} \int_\kappa \nabla \mathbf{v}_h^T \cdot \mathcal{G}_h d\mathbf{x} = \sum_{\kappa \in T_h} \int_\kappa \nabla \mathbf{v}_h^T \cdot \mathcal{A} \nabla \mathbf{U}_h d\mathbf{x} + \int_{\partial\kappa} (\nabla \mathbf{v}_h^T \mathcal{A})^+ (\hat{\mathbf{U}} - \mathbf{U}_h^+) \cdot \mathbf{n}^+ ds = 0 \tag{3.2.21}$$

Furthermore, with substitution of equation (3.2.21) into equation (3.2.5a), the following weak formulation is further obtained: Find $\mathbf{U}_h \in \mathcal{V}_h$, such that for all $\mathbf{v}_h \in \mathcal{V}_h$:

$$\begin{aligned} \sum_{\kappa \in T_h} & \int_\kappa \mathbf{v}_h^T \frac{\partial \mathbf{U}_h}{\partial t} d\mathbf{x} + \int_{\partial\kappa} \mathbf{v}_h^T \hat{\mathcal{F}}^c(\mathbf{U}_h^+, \mathbf{U}_h^-, \mathbf{n}) ds - \int_\kappa \nabla \mathbf{v}_h^T \cdot \mathcal{F}^c(\mathbf{U}_h) d\mathbf{x} \\ & + \int_\kappa \nabla \mathbf{v}_h^T \cdot \mathcal{A} \nabla \mathbf{U}_h d\mathbf{x} + \int_{\partial\kappa} (\nabla \mathbf{v}_h^T \mathcal{A})^+ (\hat{\mathbf{U}} - \mathbf{U}_h^+) \cdot \mathbf{n}^+ ds \\ & - \int_{\partial\kappa} (\mathbf{v}_h^T)^+ \hat{\mathcal{G}}(\mathcal{G}_h^+, \mathcal{G}_h^-) \cdot \mathbf{n}^+ ds = 0 \end{aligned} \tag{3.2.22}$$

There are a few options for the approximation of the numerical fluxes $\hat{\mathbf{U}}$ and $\hat{\mathcal{G}}$, the BR2 method is chosen in the present work owing to its compactness and consistency (see Landmann, 2008).

Before performing the BR2 discretization, some notations for the operators across the element interface will be first introduced. The average operator is noted as $\{\cdot\} = 1/2\Big((\cdot)^+ + (\cdot)^-\Big)$ and the jump operator is defined as $[\![\cdot]\!] = (\cdot)\mathbf{n}^+ + (\cdot)\mathbf{n}^-$, where $\mathbf{n}$ is the normal vector of the element. For example, the average operators for scalar and vector variables are given by,

$$\begin{aligned} \{s\} &= \frac{1}{2}(s^+ + s^-) \\ \{\mathbf{v}\} &= \frac{1}{2}(\mathbf{v}^+ + \mathbf{v}^-) \end{aligned} \tag{3.2.23}$$

and jump operators are represented by

$$\begin{aligned} [\![s]\!] &= (s^+\mathbf{n}^+ + s^-\mathbf{n}^-) \\ [\![\mathbf{v}]\!] &= (\mathbf{v}^+ \cdot \mathbf{n}^+ + \mathbf{v}^- \cdot \mathbf{n}^-) \end{aligned} \tag{3.2.24}$$

Note that the scalar changes into a vector when adopting a jump operator, whereas a vector turns into a scalar if applying the jump operator. Given these notations,

the numerical fluxes for the interior faces are expressed as,

$$\begin{aligned} \hat{\mathbf{U}} &= \{\mathbf{U}_h\} \\ \hat{\mathcal{G}} &= \{\mathcal{G}_h\} = \{\mathcal{A}\nabla\mathbf{U}_h\} - \eta_f\{\mathbf{r}_f\} \end{aligned} \tag{3.2.25}$$

and for the boundary faces are,

$$\begin{aligned} \hat{\mathbf{U}} &= \mathbf{U}^b \\ \hat{\mathcal{G}} &= \mathcal{G}^b = (\mathcal{A}\nabla\mathbf{U}_h)^b - \eta_f\mathbf{r}_f^b \end{aligned} \tag{3.2.26}$$

where the $\mathbf{r}_f$ and $\mathbf{r}_f^b$ are the auxiliary variables for the interior and boundary faces, respectively, the subscript f is used for the local face, the superscript b represents the boundary state, and η_f is the stability constant, normally set as $\eta_f > N_f$, where N_f is the number of faces for each element. Note that the constant η_f is set to 6 in the present implementation, which satisfies the stability requirement for the tetrahedral elements in the BR2 discretization.

The auxiliary variables are defined as: Find $\mathbf{r}_f, \mathbf{r}_f^b \in \mathcal{W}_h$, such that for all $\mathbf{w}_h \in \mathcal{W}_h$:

$$\int_\kappa \mathbf{w}_h^T \cdot \mathbf{r}_f d\mathbf{x} = \int_{\partial\Gamma} \{\mathbf{w}_h^T\mathcal{A}\} \cdot [\![\mathbf{U}_h]\!] ds \tag{3.2.27a}$$

$$\int_\kappa \mathbf{w}_h^T \cdot \mathbf{r}_f^b d\mathbf{x} = \int_{\partial\Omega} (\mathbf{w}_h^T\mathcal{A})^b(\mathbf{U}_h^+ - \mathbf{U}^b) \cdot \mathbf{n}^+ ds \tag{3.2.27b}$$

where the $\partial\Gamma$ denotes for the interior faces and $\partial\Omega$ represents the boundary faces.

Finally, given the discretization of the viscous term using the BR2 method, the discretization of the governing law can be derived from equation (3.2.22) and

expressed as: Find $\mathbf{U}_h \in \mathcal{V}_h$, such that for all $\mathbf{v}_h \in \mathcal{V}_h$,

$$\begin{aligned}
&\sum_{\kappa \in T_h} \int_\kappa \mathbf{v}_h^T \frac{\partial \mathbf{U}_h}{\partial t} d\mathbf{x} - \int_\kappa \nabla \mathbf{v}_h^T \cdot \mathcal{F}^c(\mathbf{U}_h) d\mathbf{x} + \int_\kappa \nabla \mathbf{v}_h^T \cdot \mathcal{A} \nabla \mathbf{U}_h d\mathbf{x} \\
&\quad + \int_{\partial\Gamma} \mathbf{v}_h^T \hat{\mathcal{F}}^c(\mathbf{U}_h^+, \mathbf{U}_h^-, \mathbf{n}) ds + \int_{\partial\Omega} \mathbf{v}_h^T (\hat{\mathcal{F}}^c)^b(\mathbf{U}_h^+, \mathbf{U}^b, \mathbf{n}) ds \\
&\quad - \int_{\partial\Gamma} \{\nabla \mathbf{v}_h^T \mathcal{A}\} \cdot [\![\mathbf{U}_h]\!] ds - \int_{\partial\Omega} \nabla (\mathbf{v}_h^T)^+ \mathcal{A}^b (\mathbf{U}_h^+ - \mathbf{U}^b) \cdot \mathbf{n}^+ ds \\
&\quad - \int_{\partial\Gamma} [\![\mathbf{v}_h^T]\!] \cdot \Big(\{\mathcal{A} \nabla \mathbf{U}_h\} - \eta_f \{\mathbf{r}_f\} \Big) ds \\
&\quad - \int_{\partial\Omega} (\mathbf{v}_h^T)^+ \Big((\mathcal{A} \nabla \mathbf{U}_h)^b - \eta_f \mathbf{r}_f^b \Big) \cdot \mathbf{n}^+ ds = 0
\end{aligned} \tag{3.2.28}$$

Overall, the BR2 method maintains the compactness of the DG method since the local auxiliary variables only depend on the two adjacent elements connected to the element interface. Thus, this BR2 method is capable of obtaining the high-order solutions without relying on the extended stencils.

3.3 Modification of SA Turbulence Model

In this section, a modification of the one-equation Spalart-Allmaras turbulence model by Moro et al. (2011) will be introduced. The original form of this turbulence model is defined by Spalart and Allmaras (1992),

$$\frac{\partial \tilde{\nu}}{\partial t} + u_j \frac{\partial \tilde{\nu}}{\partial x_j} = c_{b1} \tilde{S} \tilde{\nu} + \frac{1}{\sigma} \Big\{ \nabla \cdot [(\nu + \tilde{\nu}) \nabla \tilde{\nu}] + c_{b2} |\nabla \tilde{\nu}|^2 \Big\} - c_{w1} f_w [\frac{\tilde{\nu}}{d}]^2 \tag{3.3.1}$$

In the present study, the trip terms are excluded in the above model transport equations since it is of present interest to simulate the fully turbulent flows with the large Reynolds number. The eddy viscosity ν_t is calculated by,

$$\nu_t = \tilde{\nu} f_{v1}, \quad f_{v1} = \frac{\chi^3}{\chi^3 + c_{v1}^3}, \quad \chi = \frac{\tilde{\nu}}{\nu}$$

where $\tilde{\nu}$ is the turbulence working variable and ν is the kinematic viscosity. The

production and wall destruction terms in the model equation are,

$$P = c_{b1}\tilde{S}\tilde{\nu}, \quad D = c_{w1}f_w[\frac{\tilde{\nu}}{d}]^2$$

where $\tilde{S}$ is given by,

$$\tilde{S} = S + \frac{\tilde{\nu}}{\kappa^2 d^2}f_{v2}, \quad S = \sqrt{2\Omega_{ij}\Omega_{ij}}, \quad f_{v2} = 1 - \frac{\chi}{1+\chi f_{v1}}$$

where S is the magnitude of the vorticity, Ω_{ij} is the rotation tensor given by $\Omega_{ij} = 1/2(\partial u_i/\partial x_j - \partial u_j/\partial x_i)$ and d denotes the distances to the closest wall. In addition, the function f_w is defined by

$$f_w = g\left[\frac{1+c_{w3}^6}{g^6+c_{w3}^6}\right]^{1/6}, \quad g = r + c_{w2}(r^6 - r), \quad r = \frac{\tilde{\nu}}{\tilde{S}\kappa^2 d^2}$$

where the parameters are given by, $\sigma = 2/3$, $\kappa = 0.41$, $c_{b1} = 0.1355$, $c_{b2} = 0.622$, $c_{w1} = c_{b1}/\kappa^2 + (1 + c_{b2})/\sigma$, $c_{w2} = 0.3$, $c_{w3} = 2$, $c_{v1} = 7.1$.

Burgess and Mavriplis (2012b) have demonstrated that a high-order DG discretization for the mean flow with a low-order finite volume discretization for the SA turbulence model can lead to the discretization errors discrepancy between the mean flow and the turbulence model, whereas, a tightly coupled RANS equations with the SA turbulence model discretized using high-order DG method is capable of obtaining the equivalent resolution between the mean flow and turbulence model. However, the high-order methods solving the coupled RANS-SA equations normally meet with the stiffness problems due to the non-smooth behaviour of the SA turbulence model. In particular, the diffusion term $\nabla \cdot (\tilde{\nu}\nabla\tilde{\nu})$ in a laminar region is discontinuous in the first derivatives, which leads to the oscillations when applying a high-order discretization across the discontinuity. In addition, the negative working

variable $\tilde{\nu}$ can result in the unbounded function f_{v1} and failure of the computation. Therefore, a simple modification of the function χ has been made to avoid the negative values (see Moro et al., 2011),

$$\chi = \psi = 0.05 \log(1 + e^{20\chi})$$

Given this modification function χ, the SA model equation then turns into,

$$\frac{\partial \tilde{\nu}}{\partial t} + u_j \frac{\partial \tilde{\nu}}{\partial x_j} = c_{b1}\tilde{S}\psi\nu + \frac{1}{\sigma}\Big\{\nabla \cdot [(\nu + \psi\nu)\nabla\tilde{\nu}] + c_{b2}|\nabla\tilde{\nu}|^2\Big\} - c_{w1} f_w [\frac{\psi\nu}{d}]^2 \quad (3.3.2)$$

where all the modified terms are expressed as,

$$\nu_t = \psi\nu f_{v1}, \quad f_{v1} = \frac{\psi^3}{\psi^3 + c_{v1}^3},$$

$$P = c_{b1}\tilde{S}\psi\nu, \quad D = c_{w1} f_w [\frac{\psi\nu}{d}]^2,$$

$$\tilde{S} = S + \frac{\psi\nu}{\kappa^2 d^2} f_{v2}, \quad S = \sqrt{2\Omega_{ij}\Omega_{ij}}, \quad f_{v2} = 1 - \frac{\psi}{1 + \psi f_{v1}},$$

$$f_w = g\left[\frac{1 + c_{w3}^6}{g^6 + c_{w3}^6}\right]^{1/6}, \quad g = r + c_{w2}(r^6 - r), \quad r = \frac{\psi\nu}{\tilde{S}\kappa^2 d^2}$$

Finally, the tightly coupled RANS equations with the modified SA turbulence model are expressed in the system equations,

$$\frac{\partial \mathbf{U}}{\partial t} + \nabla \cdot (\mathcal{F}^c(\mathbf{U}) - \mathcal{F}^v(\mathbf{U}, \nabla\mathbf{U})) = \mathcal{S} \quad (3.3.3)$$

$$\mathbf{U} = \begin{bmatrix} \rho \\ \rho u \\ \rho v \\ \rho w \\ \rho E \\ \rho\tilde{v} \end{bmatrix}, \quad (3.3.4)$$

$$\mathcal{F}_x^c = \begin{bmatrix} \rho u \\ \rho u^2 + p \\ \rho uv \\ \rho uw \\ u(\rho E + p) \\ \rho u\tilde{v} \end{bmatrix}, \mathcal{F}_y^c = \begin{bmatrix} \rho v \\ \rho vu \\ \rho v^2 + p \\ \rho vw \\ v(\rho E + p) \\ \rho v\tilde{v} \end{bmatrix}, \mathcal{F}_z^c = \begin{bmatrix} \rho w \\ \rho wu \\ \rho wv \\ \rho w^2 + p \\ w(\rho E + p) \\ \rho w\tilde{v} \end{bmatrix},$$

$$\mathcal{F}_x^v = \begin{bmatrix} 0 \\ \tau_{xx} \\ \tau_{xy} \\ \tau_{xz} \\ u\tau_{xx} + v\tau_{xy} + w\tau_{xz} + c_p(\frac{\mu}{Pr} + \frac{\mu_T}{Pr_T})\frac{\partial T}{\partial x} \\ \frac{1}{\sigma}(\mu + \mu\psi)\frac{\partial(\psi\nu)}{\partial x} \end{bmatrix},$$

$$\mathcal{F}_y^v = \begin{bmatrix} 0 \\ \tau_{yx} \\ \tau_{yy} \\ \tau_{yz} \\ u\tau_{yx} + v\tau_{yy} + w\tau_{yz} + c_p(\frac{\mu}{Pr} + \frac{\mu_T}{Pr_T})\frac{\partial T}{\partial y} \\ \frac{1}{\sigma}(\mu + \mu\psi)\frac{\partial(\psi\nu)}{\partial y} \end{bmatrix},$$

$$\mathcal{F}_z^v = \begin{bmatrix} 0 \\ \tau_{zx} \\ \tau_{zy} \\ \tau_{zz} \\ u\tau_{zx} + v\tau_{zy} + w\tau_{zz} + c_p(\frac{\mu}{Pr} + \frac{\mu_T}{Pr_T})\frac{\partial T}{\partial z} \\ \frac{1}{\sigma}(\mu + \mu\psi)\frac{\partial(\psi\nu)}{\partial z} \end{bmatrix},$$

$$\mathcal{S} = \begin{bmatrix} 0 \\ 0 \\ 0 \\ 0 \\ 0 \\ c_{b_1}\tilde{S}\mu\psi + \frac{1}{\sigma}\Big[c_{b_2}\rho\nabla(\psi\nu)\cdot\nabla(\psi\nu)\Big] - c_{w_1}\rho f_w(\frac{\psi\nu}{d})^2 \end{bmatrix}$$

where the production and destruction terms in the SA model equation are moved into the source terms $\mathcal{S}$ in the system equations. Note that the source terms are discretized with the direct calculations of the gradient $\nabla\mathbf{U}_h$ in the present implementation. In order to maintain the consistency with the discretization of the diffusion terms and improve the robustness of the scheme, the BR2 discretization of the source terms with consideration of the jumps of $\mathbf{U}_h$ will be performed in the future work. Overall, this modified approach improves the robustness of high-order DG discretization for the coupled RANS-SA equations.

3.4 Boundary Conditions

The boundary conditions are applied through the inviscid and viscous flux across the physical boundary in a weak manner. These fluxes are computed based on the interior states, gradients of the states and constructed exterior boundary states. Some of the typical physical boundary conditions are presented as follows (see Carlson, 2011; Landmann, 2008; Oliver, 2008).

3.4.1 Subsonic Inflow

A subsonic inflow boundary condition can be specified by four incoming Riemann invariants, e.g. total pressure p_t, total temperature T_t and inflow angle α, with one extrapolated outgoing Riemann invariants. The flow across the boundary is assumed to be adiabatic with consistent total enthalpy,

$$H_t = \frac{a^2}{\gamma - 1} + \frac{U^2}{2} \tag{3.4.1}$$

The outgoing Riemann invariants R^+ is defined as,

$$R^+ = U + \frac{2a}{\gamma - 1} \tag{3.4.2}$$

By combing Eqn. (3.4.1) and Eqn.(3.4.2), a quadric equation is obtained as,

$$H_t = \frac{a^2}{\gamma - 1} + \frac{1}{2}\Big(R^+ - \frac{2a}{\gamma - 1}\Big)^2 \tag{3.4.3}$$

where the sonic speed a is achieved by solving this quadric equation. The velocity U and Mach number are then computed as,

$$U = R^+ - \frac{2a}{\gamma - 1}, \quad M = \frac{U}{a} \tag{3.4.4}$$

The static pressure p and temperature T are computed from the isentropic relations,

$$\begin{aligned} p &= p_t\Big(1+\frac{\gamma-1}{2}M^2\Big)^{-\frac{\gamma}{\gamma-1}} \\ T &= T_t\Big(1+\frac{\gamma-1}{2}M^2\Big)^{-1} \end{aligned} \tag{3.4.5}$$

Therefore, the boundary state variables are reached as,

$$q = \begin{bmatrix} p/RT \\ Un_x \\ Un_y \\ Un_z \\ p \\ \tilde{\nu}_{set} \end{bmatrix} \tag{3.4.6}$$

Note that a SA turbulence working variable $\tilde{\nu}_{set}$ also needs to be set here if running turbulent simulations.

3.4.2 Subsonic Outflow

A subsonic outflow boundary condition is specified using one incoming Riemann invariants with four outgoing Riemann invariants. The static pressure p_{set} is specified whilst other state variables are extrapolated from interior states. The boundary state variables are then defined as,

$$q = \begin{bmatrix} p/RT \\ u \\ v \\ w \\ p_{set} \\ \tilde{\nu} \end{bmatrix} \tag{3.4.7}$$

3.4.3 No-slip Wall

For the no-slip wall, the velocity and eddy viscosity are all prescribed to zero and an adiabatic condition is also imposed here requiring that the viscous flux is set

to zero in the energy equation. The state variables are,

$$q = \begin{bmatrix} \rho \\ 0 \\ 0 \\ 0 \\ p \\ 0 \end{bmatrix} \tag{3.4.8}$$

3.4.4 Slip Wall

The slip wall boundary condition enforces the flow is tangential to the wall, implying that interior states extracted by the normal velocity are given to the slip wall. The state variables are,

$$q = \begin{bmatrix} \rho \\ u - Un_x \\ v - Un_y \\ w - Un_z \\ p \\ \tilde{\nu} \end{bmatrix} \tag{3.4.9}$$

3.4.5 Farfield

The far field boundary conditions in the numerical domains investigated are 1D non-reflecting, it is necessary to place the far field boundary far away from the solid body, for example, it is common that the far field is placed at least 20 chord length away for the simulations of an airfoil. The boundary states are prescribed by the freestream variables,

$$q = \begin{bmatrix} \rho_\infty \\ u_\infty \\ v_\infty \\ w_\infty \\ p_\infty \\ \tilde{\nu}_\infty \end{bmatrix} \tag{3.4.10}$$

4 Time Integration

This chapter will start with an introduction of the expansions of approximate solutions and test functions using the basis shape functions, followed by the derivations that lead to a global system of ordinary differential equations. Furthermore, the process of the implicit integration scheme using the preconditioned Newton-GMRES method will be presented.

4.1 Ordinary Differential Equations

The approximate solutions $\mathbf{U}_h(\mathbf{x}, t)$ and test functions $\mathbf{v}_h(\mathbf{x})$ are represented as the expansions of p-th order polynomials (see Solin et al., 2003),

$$\begin{aligned} \mathbf{U}_h(\mathbf{x}, t) &= \sum_{i=1}^{N} \hat{\mathbf{U}}_i(t) b_i(\mathbf{x}) \\ \mathbf{v}_h(\mathbf{x}) &= \sum_{j=1}^{N} \hat{\mathbf{v}}_j b_j(\mathbf{x}) \end{aligned} \tag{4.1.1}$$

where t is the time and $\mathbf{x}$ is the spatial coordinates, $\hat{\mathbf{U}}_i(t)$ and $\hat{\mathbf{v}}_j$ denote the expansion coefficients, $b_i(\mathbf{x})$ and $b_j(\mathbf{x})$ are the basis shape functions with $i, j = \{1, ..., N\}$, where N is the number of degrees of freedom. For example, Figure 4.1 shows the

node sets constructed to cover the 2D finite element space.

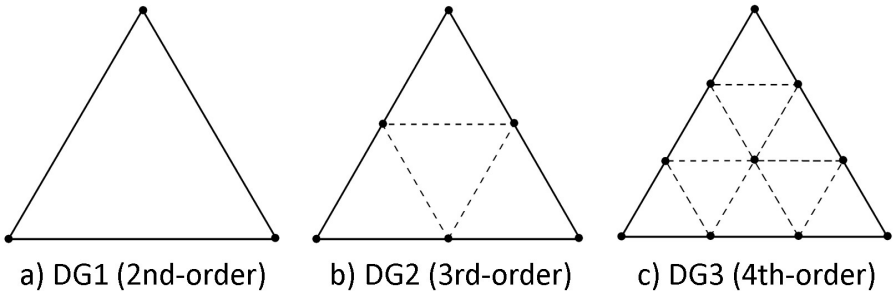


Figure 4.1: 2D triangular elements with different orders of internally divided sub-cells (indicated by dash lines)

Note that the expansions are performed within each element without any continuity constraints on the boundary with adjacent elements, which distinguishes DG method from standard Galerkin method. In addition, the basis function $b_j(\mathbf{x})$ in the physical elements κ is transformed from the basis function in the computational elements $\hat{\kappa}$ through the mapping functions.

After substituting the approximate solutions and test functions of Equation (4.1.1) into the DG discretization of the governing equations in Equation (3.2.28), the discretization equation in a compact form in the elements κ can be written as,

$$\sum_{\kappa \in \mathcal{T}_h} M_{ji} \frac{d\hat{\mathbf{U}}_i}{dt} + R_j = 0 \tag{4.1.2}$$

where M_{ji} and R_j denote the mass matrix and the vector of residual, respectively.

$$M_{ji} = \int_{\kappa} b_j b_i d\mathbf{x} \tag{4.1.3}$$

$$R_j = S_j + V_j \tag{4.1.4}$$

where S_j and V_j are the surface and cell integrals, respectively.

$$\begin{aligned} S_j = & \int_{\partial\Gamma} b_j \hat{\mathcal{F}}^c(\mathbf{U}_h^+, \mathbf{U}_h^-, \mathbf{n}) ds + \int_{\partial\Omega} b_j (\hat{\mathcal{F}}^c)^b(\mathbf{U}_h^+, \mathbf{U}^b, \mathbf{n}) ds \\ & - \int_{\partial\Gamma} \{\nabla b_j \mathcal{A}\} \cdot [\![\mathbf{U}_h]\!] ds - \int_{\partial\Omega} \nabla (b_j)^+ \mathcal{A}^b (\mathbf{U}_h^+ - \mathbf{U}^b) \cdot \mathbf{n}^+ ds \\ & - \int_{\partial\Gamma} [\![b_j]\!] \cdot \Big(\{\mathcal{A}\nabla \mathbf{U}_h\} - \eta_f \{\mathbf{r}_f\} \Big) ds \\ & - \int_{\partial\Omega} (b_j)^+ \Big((\mathcal{A}\nabla \mathbf{U}_h)^b - \eta_f \mathbf{r}_f^b \Big) \cdot \mathbf{n}^+ ds \end{aligned} \tag{4.1.5}$$

$$V_j = - \int_\kappa \nabla b_j \mathcal{F}^c(\mathbf{U}_h) d\mathbf{x} + \int_\kappa \nabla b_j \mathcal{A} \nabla \mathbf{U}_h d\mathbf{x} \tag{4.1.6}$$

Given a combination of the discretization equation in each element through the whole computational domain, a global system of ordinary differential equations can be finally obtained,

$$\mathbf{M} \frac{d\hat{\mathbf{U}}}{dt} + \mathbf{R} = \mathbf{0} \tag{4.1.7}$$

where $\mathbf{M}$ is the global block-diagonal mass matrix including all the mass matrices of elements, $\hat{\mathbf{U}} = (U_1, U_2, ..., U_k, ...)^T$ is the global vector of expansion coefficients, where U_k represents the expansion coefficients vector of k-th element, and $\mathbf{R} = (R_1, R_2, ..., R_k, ...)^T$ denotes the global vector of residuals, where R_k is the residual vector of k-th element.

4.2 Implicit Time Integration

The spatially discretized equations can be integrated easily in time using an explicit scheme using multi-stage Runge-Kutta (see Cockburn and Shu, 1998a). The time step size of the explicit scheme is restricted by the corresponding small CFL, normally less than 1, due to numerical stability requirement.

An implicit temporal integration scheme is developed as a primary solution method in the present work. The implicit scheme has an advantage of using

very large time steps (CFL $\sim \mathcal{O}(10^3)$ in the present work). Given the challenges of developing effective multi-grid methods for unstructured meshes, the implicit formulation proves to be an important way of accelerating solutions for both steady and unsteady flows. It is worth noting that for very complex geometry configuration, highly non-uniform meshes might be generated. The time step limit set by the minimum mesh size of a highly non-uniform and also highly skewed unstructured mesh can be too restrictive, particularly for unsteady flow solutions where a uniform time step needs to be taken for the temporal consistency.

Here, the Euler backward method is employed to solve the system of ordinary differential equations (4.1.7) in time,

$$\mathbf{M}\frac{\mathbf{U}^{n+1}-\mathbf{U}^{n}}{\Delta t}+\mathbf{R}(\mathbf{U}^{n+1})=\mathbf{0} \tag{4.2.1}$$

where the superscript n represents the time step. Since residuals are non-linear terms in the governing equations, Equation (4.2.1) is a non-linear system of algebraic equations. For the sake of resolving this kind of non-linear system equations, the linearization of residuals is performed,

$$\mathbf{R}(\mathbf{U}^{n+1})=\mathbf{R}(\mathbf{U}^{n})+\frac{\partial \mathbf{R}(\mathbf{U}^{n})}{\partial \mathbf{U}^{n}}(\mathbf{U}^{n+1}-\mathbf{U}^{n}) \tag{4.2.2}$$

Note that the global Jacobian matrix $\frac{\partial \mathbf{R}(\mathbf{U})}{\partial \mathbf{U}}$ is a $N_e \times N_e$ block matrix, where N_e is the number of total elements in the whole computational domain. For the local element κ, the local block matrix is a $mN \times mN$ Jacobian matrix, where m is the number of conservative variables and N is the number of degrees of freedom. For example, a

local $6N \times 6N$ Jacobian matrix for the 3D RANS-SA discretization can be given by,

$$\frac{\partial r_i}{\partial U_j} = \begin{bmatrix} \frac{\partial r_1(1)}{\partial \rho_1} & \frac{\partial r_1(1)}{\partial (\rho u)_1} & \cdots & \frac{\partial r_1(1)}{\partial (\rho \tilde{\nu})_1} & \cdots & \cdots & \frac{\partial r_1(1)}{\partial \rho_N} & \frac{\partial r_1(1)}{\partial (\rho u)_N} & \cdots & \frac{\partial r_1(1)}{\partial (\rho \tilde{\nu})_N} \\ \frac{\partial r_1(2)}{\partial \rho_1} & \frac{\partial r_1(2)}{\partial (\rho u)_1} & \cdots & \frac{\partial r_1(2)}{\partial (\rho \tilde{\nu})_1} & \cdots & \cdots & \frac{\partial r_1(2)}{\partial \rho_N} & \frac{\partial r_1(2)}{\partial (\rho u)_N} & \cdots & \frac{\partial r_1(2)}{\partial (\rho \tilde{\nu})_N} \\ \vdots & \vdots & & \vdots & \cdots & \cdots & \vdots & \vdots & & \vdots \\ \frac{\partial r_1(6)}{\partial \rho_1} & \frac{\partial r_1(6)}{\partial (\rho u)_1} & \cdots & \frac{\partial r_1(6)}{\partial (\rho \tilde{\nu})_1} & \cdots & \cdots & \frac{\partial r_1(6)}{\partial \rho_N} & \frac{\partial r_1(6)}{\partial (\rho u)_N} & \cdots & \frac{\partial r_1(6)}{\partial (\rho \tilde{\nu})_N} \\ \vdots & \vdots & & \vdots & \cdots & \cdots & \vdots & \vdots & & \vdots \\ \vdots & \vdots & & \vdots & \cdots & \cdots & \vdots & \vdots & & \vdots \\ \frac{\partial r_N(1)}{\partial \rho_1} & \frac{\partial r_N(1)}{\partial (\rho u)_1} & \cdots & \frac{\partial r_N(1)}{\partial (\rho \tilde{\nu})_1} & \cdots & \cdots & \frac{\partial r_N(1)}{\partial \rho_N} & \frac{\partial r_N(1)}{\partial (\rho u)_N} & \cdots & \frac{\partial r_N(1)}{\partial (\rho \tilde{\nu})_N} \\ \frac{\partial r_N(2)}{\partial \rho_1} & \frac{\partial r_N(2)}{\partial (\rho u)_1} & \cdots & \frac{\partial r_N(2)}{\partial (\rho \tilde{\nu})_1} & \cdots & \cdots & \frac{\partial r_N(2)}{\partial \rho_N} & \frac{\partial r_N(2)}{\partial (\rho u)_N} & \cdots & \frac{\partial r_N(2)}{\partial (\rho \tilde{\nu})_N} \\ \vdots & \vdots & & \vdots & \cdots & \cdots & \vdots & \vdots & & \vdots \\ \frac{\partial r_N(6)}{\partial \rho_1} & \frac{\partial r_N(6)}{\partial (\rho u)_1} & \cdots & \frac{\partial r_N(6)}{\partial (\rho \tilde{\nu})_1} & \cdots & \cdots & \frac{\partial r_N(6)}{\partial \rho_N} & \frac{\partial r_N(6)}{\partial (\rho u)_N} & \cdots & \frac{\partial r_N(6)}{\partial (\rho \tilde{\nu})_N} \end{bmatrix} \tag{4.2.3}$$

where $r_i(l), l = 1, \ldots, 6$ are the local element residuals and $U_j = (\rho, \rho u, \rho v, \rho w, \rho E, \rho \tilde{\nu})_j$ are the conservative variables with subscripts i or $j = 1, \ldots, N$.

The non-linear system Equation (4.2.1) can be solved using a Newton method as the following iterative steps,

1. Newton time step $k = 0,\ \mathbf{U}^{(0)} = \mathbf{U}^n$

2. For $k = 1, \ldots, \infty$

$$\underbrace{\left(\frac{\mathbf{M}}{\Delta t} + \frac{\partial \mathbf{R}(\mathbf{U}^{(k)})}{\partial \mathbf{U}^{(k)}}\right)}_{\mathbf{A}} \underbrace{(\mathbf{U}^{(k+1)} - \mathbf{U}^{(k)})}_{\mathbf{x}} = \underbrace{-\left(\frac{\mathbf{M}}{\Delta t}(\mathbf{U}^{(k)} - \mathbf{U}^n) + \mathbf{R}(\mathbf{U}^{(k)})\right)}_{\mathbf{b}} \tag{4.2.4}$$

3. $\mathbf{U}^{n+1} = \mathbf{U}^{(k)}|_{k \to \infty}$

At time level $n + 1$, the Newton iteration is initialized with a previous time level solution U^n and following iterations are performed to reach the sufficient small convergence tolerance as $\mathbf{U}^{n+1} = \mathbf{U}^{(k)}|_{k \to \infty}$. In each Newton iteration, $\mathbf{Ax} = \mathbf{b}$ is solved using a preconditioned GMRES iterative algorithm with a block incomplete LU factorization with zero fill-in (see Persson and Peraire, 2008). Comparing to other preconditioning schemes like block Jacobi or block Gauss-Seidel (GS), ILU0 is the most robust one with a smaller number of iterations especially when applied

to the low Mach flows on highly stretched meshes. However, the memory storage for ILU0 is larger than those for either block Jacobi or block GS with only diagonal blocks or blocks above the diagonal are stored.

An overall DG discretization and implicit temporal integration process has been illustrated in Figure 4.2, where three nested loops are included. The outermost loop is time step loop, following by the inner Newton iterations, while GMRES iterative scheme sits in the innermost loop.

Here, some further considerations for the present DG solver need to be addressed. First, more types of grids, like the quadrilateral in 2D and the hexahedron and pyramid in 3D, need to be included for the practical turbomachinery applications with complex geometry. In addition, the high-order near wall meshes with multiple layers of curved elements are necessary to resolve the thin boundary layer for the high Reynolds number turbulent flows. Therefore, it will be of practical interest to reconstruct the multi-layer curved near wall meshes in the present solver or rely on the alternative software to generate the high-order meshes. Furthermore, there is a burden of computing and storing the Jacobian matrix for the implicit high-order calculations. Thus, the Jacobian matrix free scheme should be considered to further alleviate the storage requirement in the present solver.

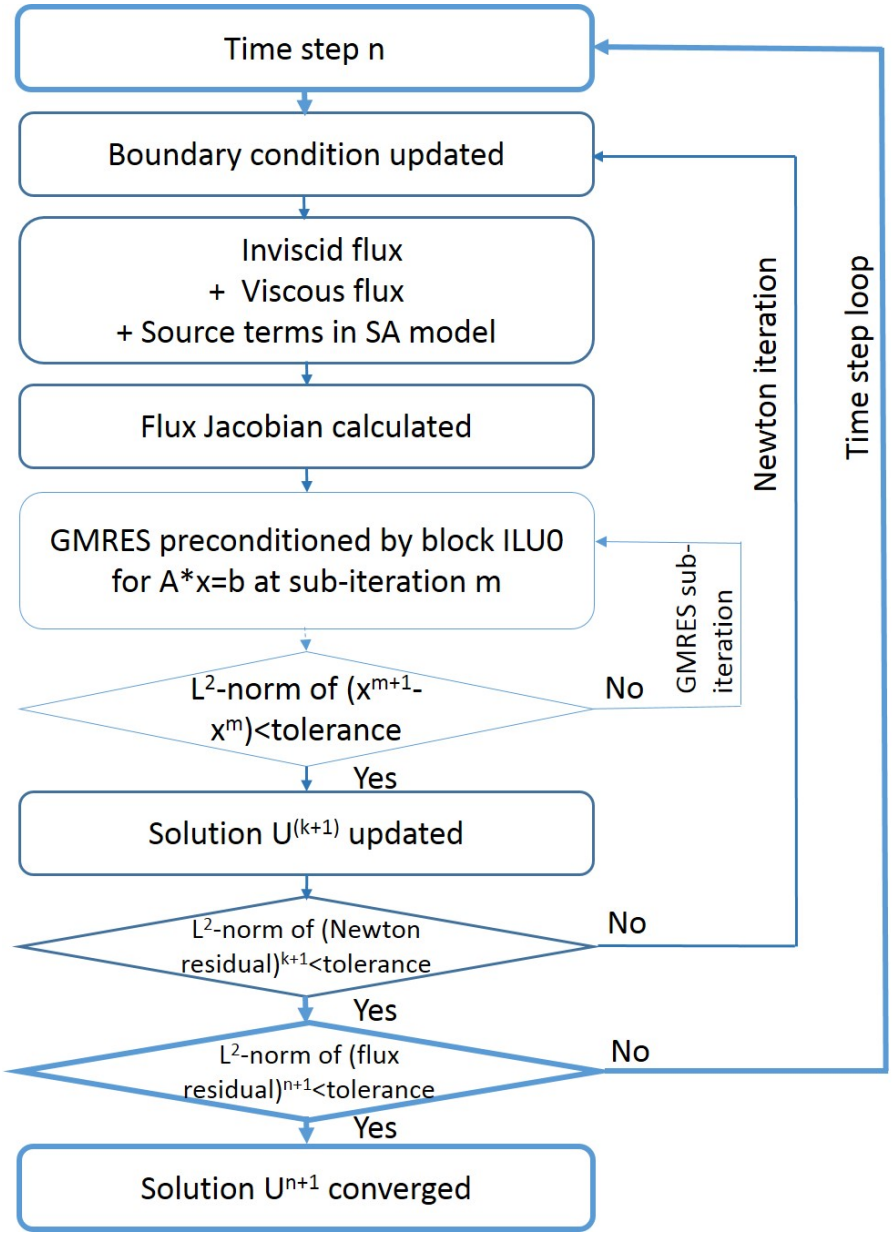


Figure 4.2: DG discretization and implicit time integration process

5

Validation Studies

This chapter will present the numerical studies for some simple canonic cases to validate the numerical methods implementation. The first test case of an inviscid flow around a cylinder described in Section 5.1 will be performed to firstly examine the effectiveness of a high-order geometrical representation. The subsequent Section 5.2 will present the test cases for validating the implementation of a high-order DG discretization of the viscous terms and an implicit time integration. These includes the laminar vortex shedding after a cylinder and the laminar boundary layer over a flat plate. Next, the test case of a turbulent boundary layer over a flat plate described in Section 5.3 will be examined to demonstrate the necessity of modifying the SA turbulence model for the high-order turbulent simulations. Section 5.4 will detail the test case of the flow past an airfoil at any given Mach number of practical interest to validate the capability of simulating with a wide flow speed range for the current DG solver. Finally, a summary of the validation studies will be given in Section 5.5.

5.1 Inviscid Flow around a Cylinder

Since the viscous terms $\mathcal{F}^v$ are eliminated for the simulations of the inviscid flow, the governing laws are turned into the Euler equations, and will be spatially discretized and temporally integrated in due course using the strategies that have been described in Chapter 3 and 4.

Figure 5.1 exhibits the 2D schematic of an inviscid, incompressible flow around a cylinder with a radius R. The uniform flow with a velocity of U_∞ comes from the far field and has no vorticity, which can be modelled as a potential flow. The stagnation points S are located at the leading edge ($\theta = 0$) and the trailing edge ($\theta = 180^0$) and the maximum velocity points are placed at $\theta = 90^0$, 270^0. The stream function of this potential flow field in the polar (r-θ) coordinates can be written as (see Batchelor, 2000),

$$\psi = U_\infty r\left(1 - \frac{R^2}{r^2}\right)\sin\theta \tag{5.1.1}$$

The velocity components are obtained from the differential of ψ,

$$\begin{aligned} U_r &= \frac{1}{r}\frac{\partial\psi}{\partial\theta} = U_\infty\left(1 - \frac{R^2}{r^2}\right)\cos\theta \\ U_\theta &= -\frac{\partial\psi}{\partial r} = -U_\infty\left(1 + \frac{R^2}{r^2}\right)\sin\theta \end{aligned} \tag{5.1.2}$$

With a substitution of $r = R$ into Equation 5.1.2, the velocity components at the cylinder surface are,

$$\begin{aligned} U_{r_R} &= 0 \\ U_{\theta_R} &= -2U_\infty\sin\theta \end{aligned} \tag{5.1.3}$$

The surface static pressure p_R can be derived from the Bernoulli equations,

$$p_\infty + \frac{1}{2}\rho U_\infty^2 = p_R + \frac{1}{2}\rho(U_{r_R}^2 + U_{\theta_R}^2) \tag{5.1.4}$$

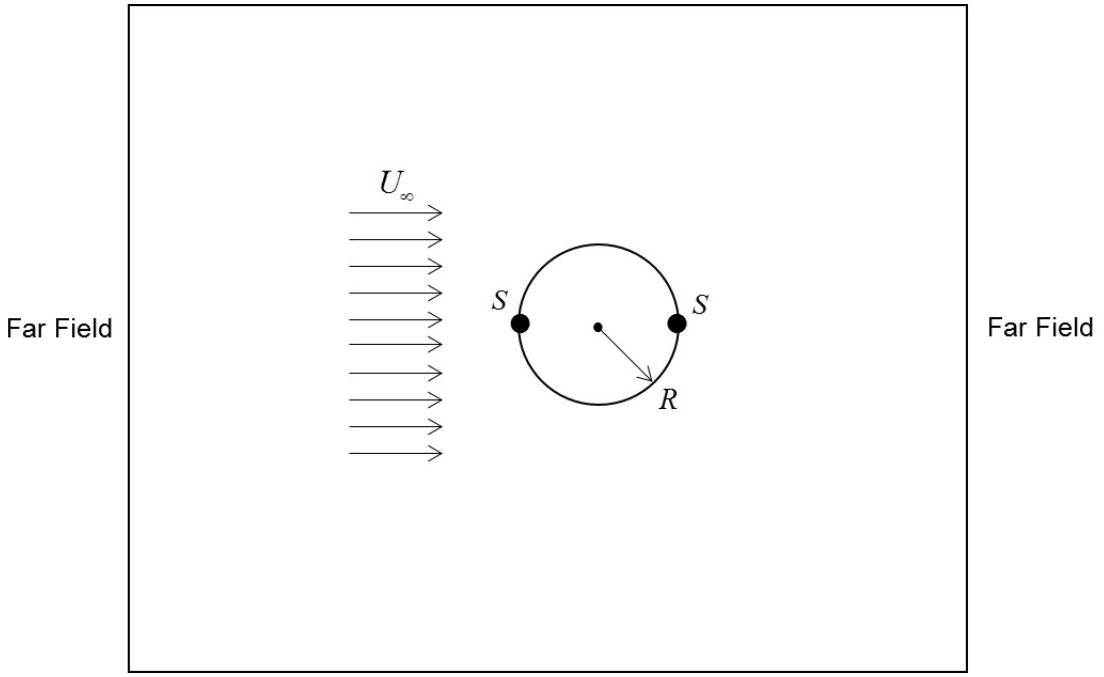


Figure 5.1: 2D schematic of Flow past a cylinder

and the subsequent static pressure coefficients are expressed as,

$$C_p = \frac{p_R - p_\infty}{\frac{1}{2}\rho U_\infty^2} = 1 - 4\sin^2\theta \tag{5.1.5}$$

Although the geometry of the cylinder is 2D, a 3D mesh is generated by extruding the 2D geometry a layer in the third direction to accommodate the current 3D solver. The extremely coarse meshes are generated in the computational domain by Gmsh as shown in Figure 5.2, but problems arise when these straight-sided mesh cells meet with the curved boundary. The mesh cells near the cylinder surface are shown in Figure 5.3(a) and there are only 12 node points to represent the geometry of the cylinder, which may produce inadequate numerical results due to the inaccurate linear representation of the physical boundary. One solution is to refine the meshes at the cylinder surface, however, it conflicts with the interest of high-order schemes in obtaining the flow solutions on relatively coarse meshes. Instead, a

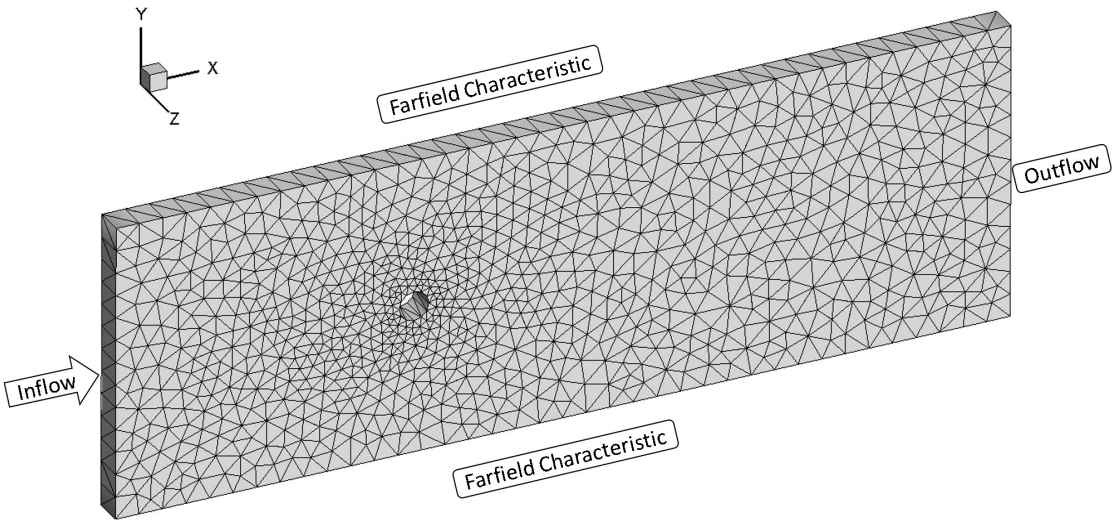


Figure 5.2: 3D mesh for an inviscid flow around a cylinder

high-order geometrical representation for the curved boundary has been performed. Figures 5.3(b), 5.3(c) and 5.3(d) exhibit high-order curved boundaries with iso-parametric elements represented by corresponding p-th order polynomials as adopted in the spatial discretization. The p-th order of the boundary polynomials is denoted by 'BPp'. The DG flow field simulations by p-th order polynomials are denoted as 'DGp', where the corresponding order of the DG discretization accuracy is p+1.

An inflow free stream velocity U_∞ is taken as 35 m/s, and angle of attack α is 0^0, which can be treated as an incompressible flow. The simulations have been conducted at the degrees of piece-wise polynomials from $p = 1$ to $p = 4$. The static pressure coefficient Cp contours with streamlines from the high-order curved boundary representations consistent with the DG discretization orders are given in Figure 5.4. It clearly shows that flow region is better resolved as the order of accuracy increases with corresponding order of polynomials representing the boundary.

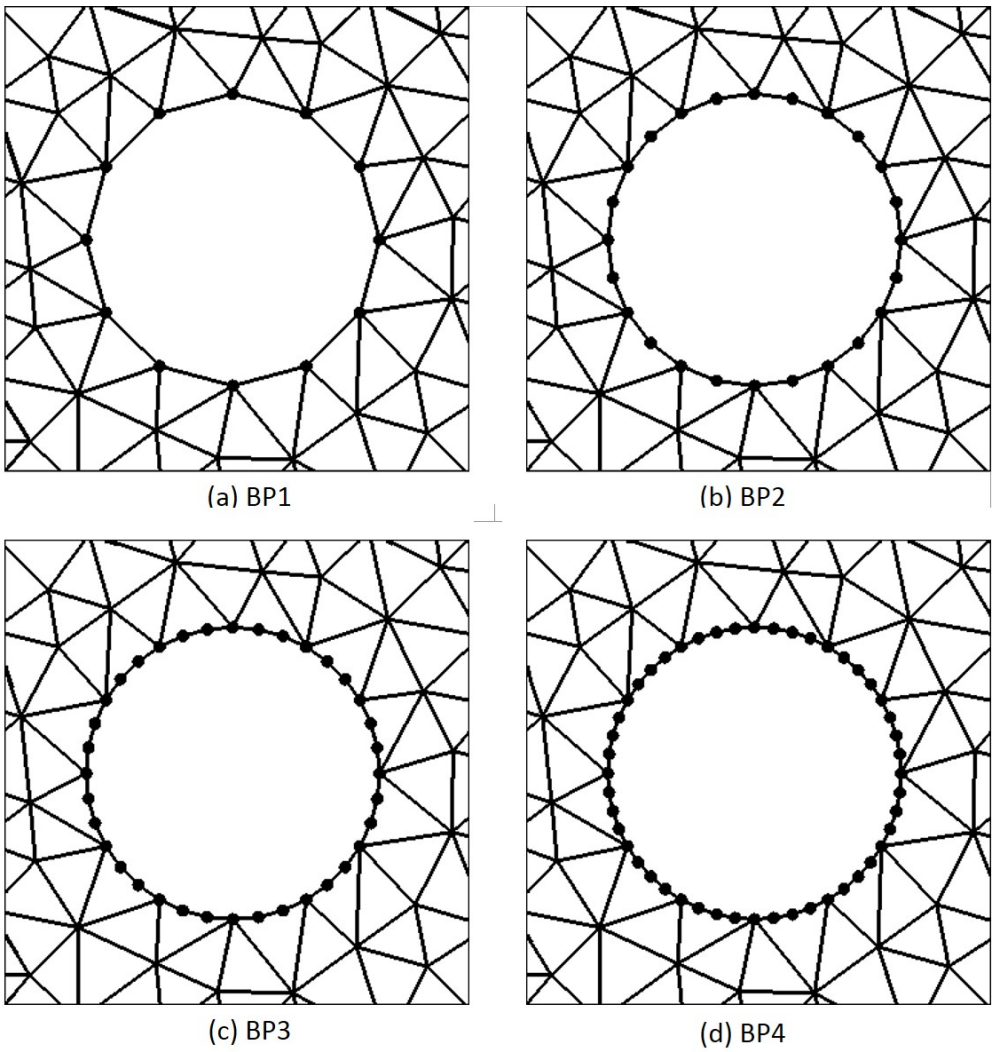


Figure 5.3: High-order representations of cylinder with 12 base-mesh points for inviscid solution

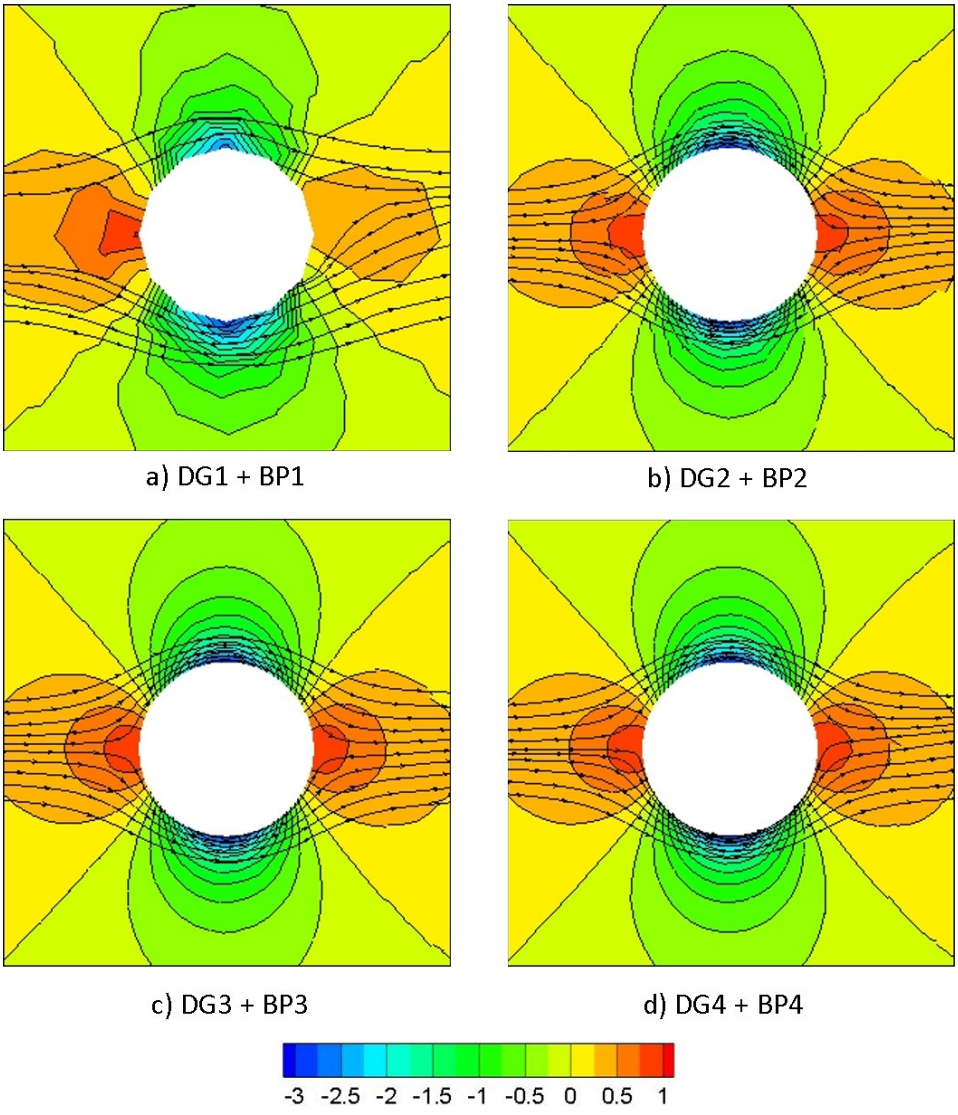


Figure 5.4: Static pressure coefficient contours with streamlines for an inviscid flow around cylinder of DG representations with corresponding orders of boundary geometrical representation

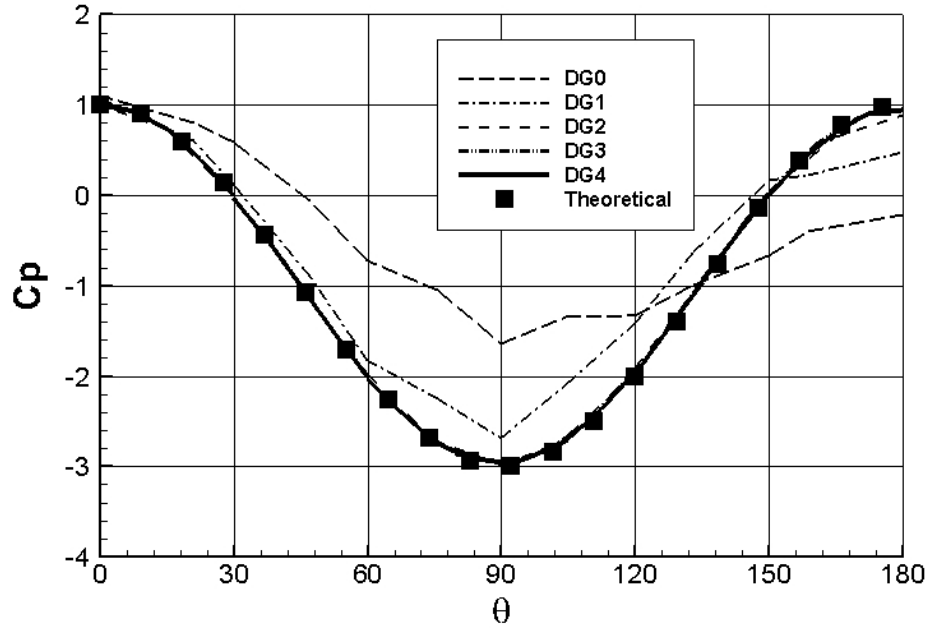


Figure 5.5: Static pressure coefficient distributions around cylinder ($\theta = 0$: leading edge; $\theta = 180^0$: trailing edge)

The computed Cp is also compared with the theoretical exact solution in Figure 5.5. For this mesh, the DG0 and DG1 solutions are unable to match the theoretical one whilst all other results of higher-order than DG2 have agreed well with the exact solution.

As a contrast, a test with a linear boundary representation (BP1) combined with different DG orders of the discretization is also conducted. The corresponding pressure contours are shown in Figure 5.6. The lower-order DG (DG1 and DG2) solutions tend to converge to a steady state, though not fully, and the results are very poor. The higher-order (DG3 and DG4) solutions on the other hand, are clearly not converging to a steady solution. The main difference between the low-order and high-order results of the geometry with edges is that the flow starts separated after the edges from the high-order solutions. This is due to the high-resolution

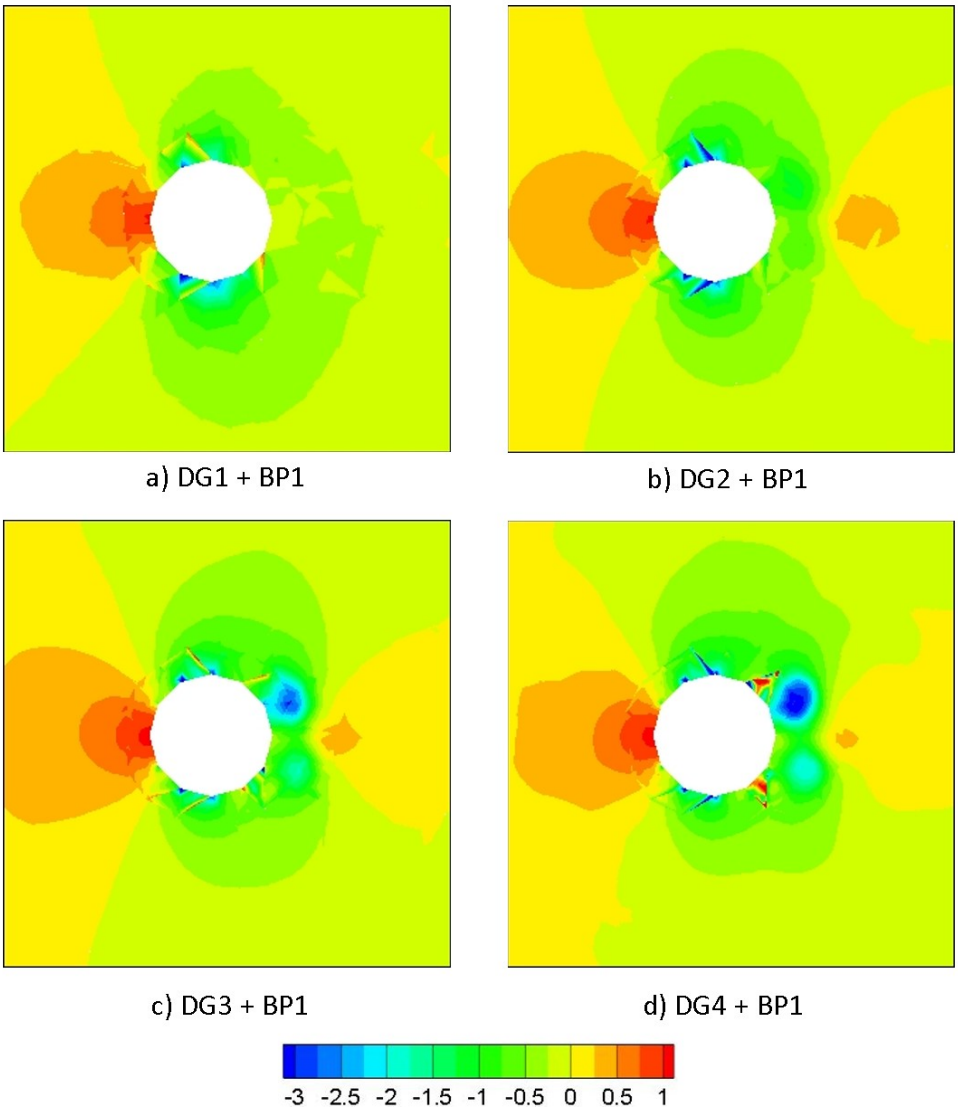


Figure 5.6: Static pressure coefficient contours for an inviscid flow around cylinder with linear boundary representation (BP1)

from high-order solutions, which can resolve the shear layer instability on the geometry with edges and the subsequent separation, whereas the the resolution from low-order solutions is too poor to resolve the shear layer instability. Thus, a high-order field discretization may not be very meaningful without a corresponding high-order boundary geometrical representation.

5.2 Laminar Flows

For the simulations of viscous flow, there are two test cases chosen for validation, one is the vortex shedding after a cylinder and the other one is a laminar boundary layer over a flat plate.

5.2.1 Vortex Shedding after a Cylinder

The laminar flow past a cylinder is a fundamental test case for validating the unsteady viscous flow modelling capability. A low speed inflow velocity is given as 55 m/s, and the Reynolds number is 174 based on the free stream velocity and the diameter of cylinder. For this case the experimental data are available from the early work of Thom (see Thom, 1933), which is also recently used for validation purposes by He (2018).

The mesh taken from the Section 5.1 and refined in the near wall region for capturing the laminar boundary layer is shown in Figure 5.7. There are still only 12 node points to represent the geometry of cylinder and so the high-order boundary representation is also adopted for conducting high-order DG simulations. The high-order curved boundaries, termed as BPp, are represented by the corresponding p-th order of polynomials as performed in the spatial discretization. The unsteady simulations for the laminar flow past a cylinder have been carried out from a 2nd-order DG1 with a BP1 boundary to a 5th-order DG4 with a BP4 boundary. Note that each unsteady simulation needs to be time marched with a constant time step size for the time consistence of a time accurate unsteady solution.

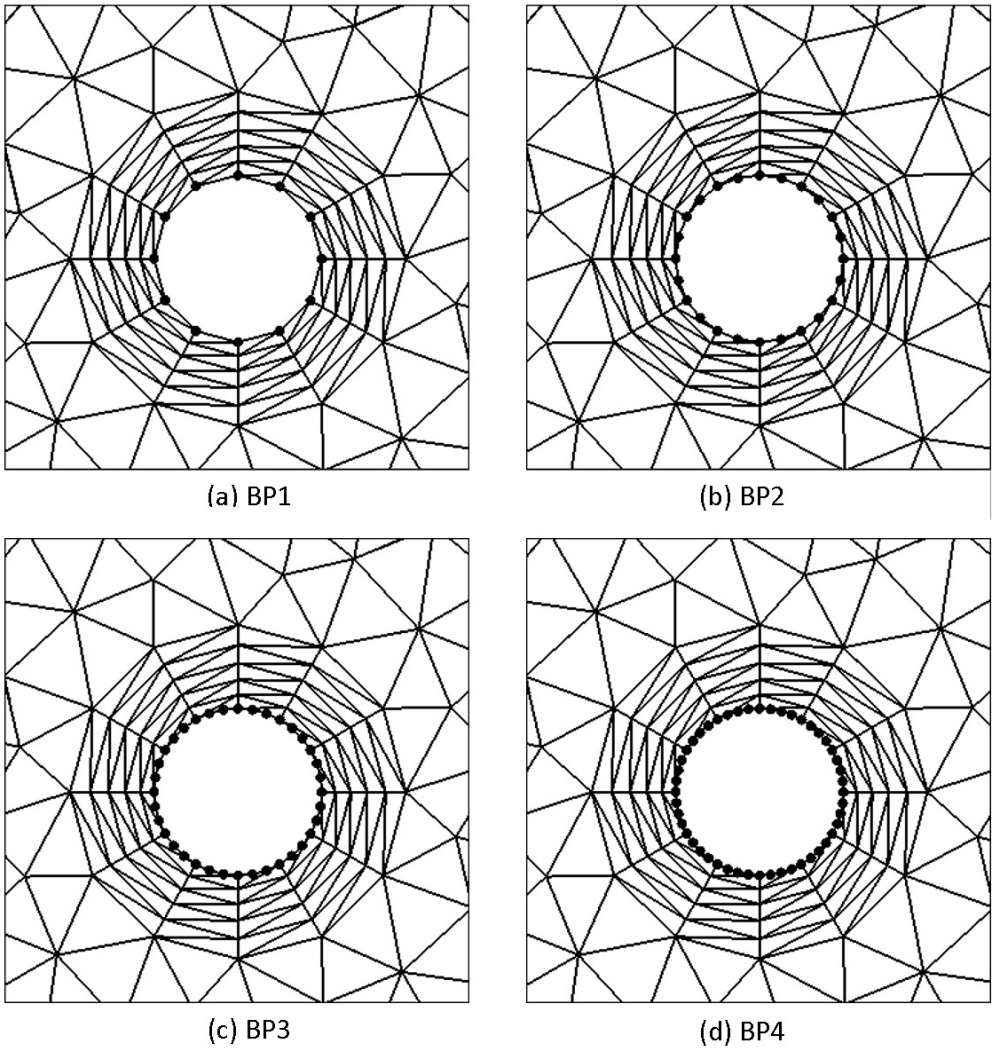


Figure 5.7: High-order representations of cylinder with 12 base-mesh points for unsteady laminar solution

In Figures 5.8 and 5.9, the instantaneous entropy and static pressure coefficient contours from the 2nd-order DG1 to the 5th-order DG4 solutions are presented respectively. Note that all the four boundaries (lef, right, top and bottom) are placed at 20 diameters away from the cylinder in order to apply the non-reflecting farfield characteristic boundary condition. As clearly shown in Figures 5.8 and 5.9, the shed vortices tend to be much less dissipated and better resolved as the order of accuracy is increased.

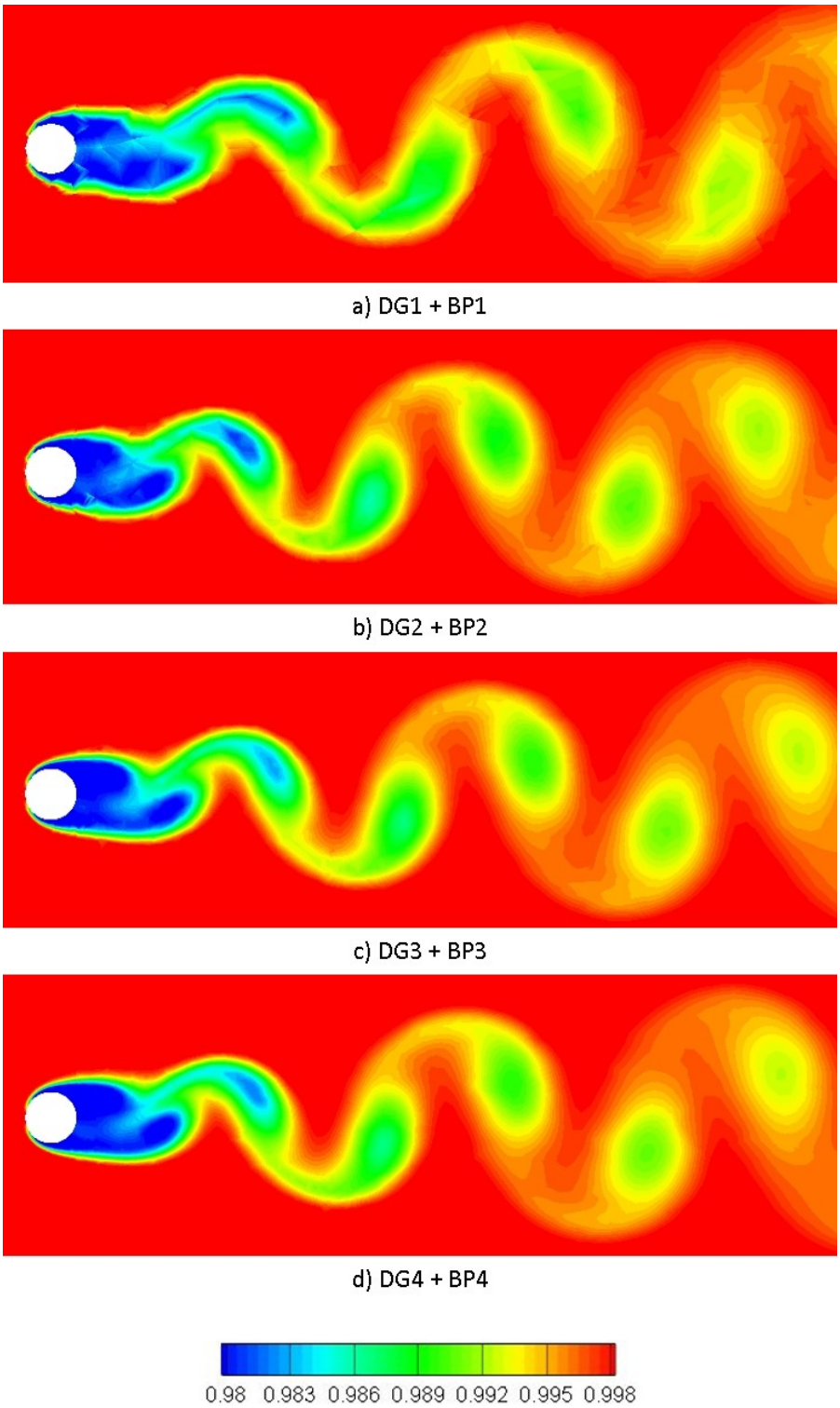


Figure 5.8: Instantaneous entropy contours [exp(-S/R)] for a laminar flow around cylinder of DG representations with corresponding orders of boundary geometrical representation

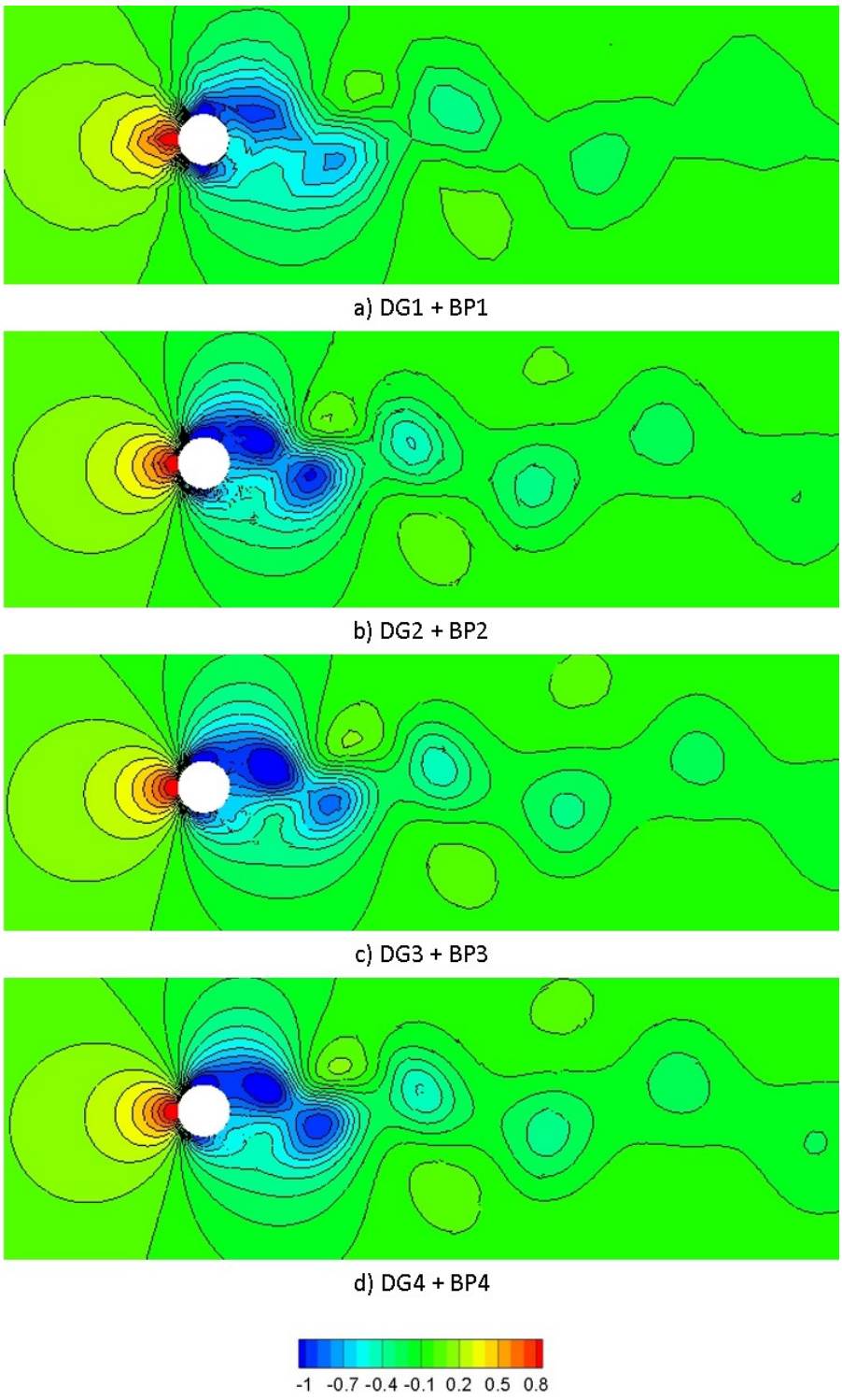


Figure 5.9: Instantaneous static pressure coefficient contours for a laminar flow around cylinder of DG representations with corresponding orders of boundary geometrical representation

It should be pointed out the number of time steps in one vortex shedding period is chosen over 80 in the present simulations and constant temporal time step size is consistently reduced as the discretization order increases because of the subdivision nature of DG scheme. Except for the DG1, the calculated Strouhal (St.) numbers from the DG2 to the DG4 are consistent with an approximate value of 0.186, in agreement with the empirical value around 0.19 for this Reynolds number.

After reaching the periodic shedding vortex, the instantaneous flow field is time averaged over approximately 50 shedding periods to achieve the time-averaged results. Fig. 5.10 and Fig. 5.11 exhibit the time-averaged static pressure coefficients and x-velocities around the cylinder, which are symmetric along the wake centreline.

The time-averaged surface pressure coefficients from the DG1 to the DG4 solutions are plotted in Fig. 5.12. The higher-order DG solutions do tend to show improved results in good agreement with the experimental data.

Overall, the consistent match between the obtained DG results and the reference data has validated the unsteady viscous flow modelling capability for the current DG solver.

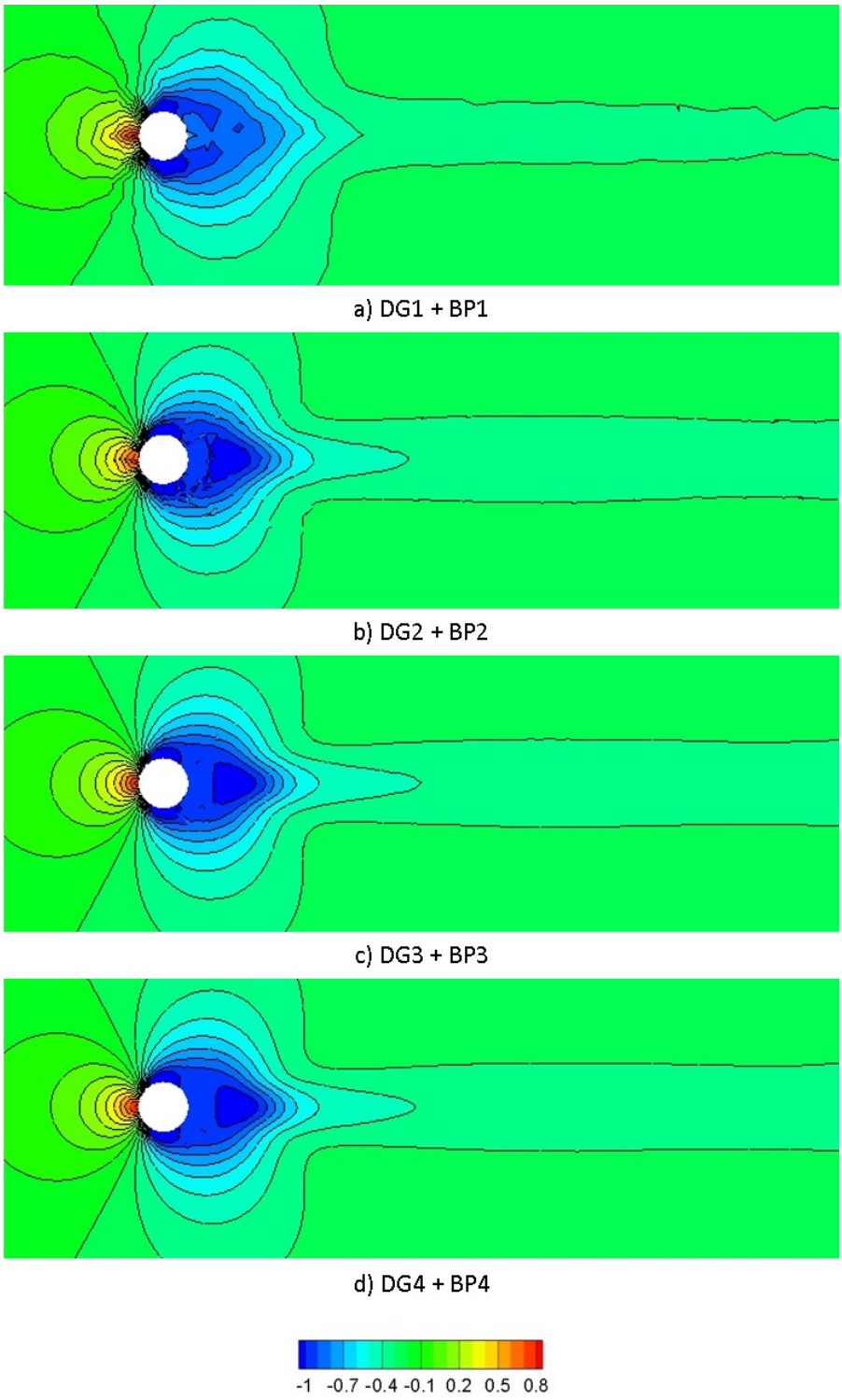


Figure 5.10: Time-averaged static pressure coefficient contours for a laminar flow around cylinder

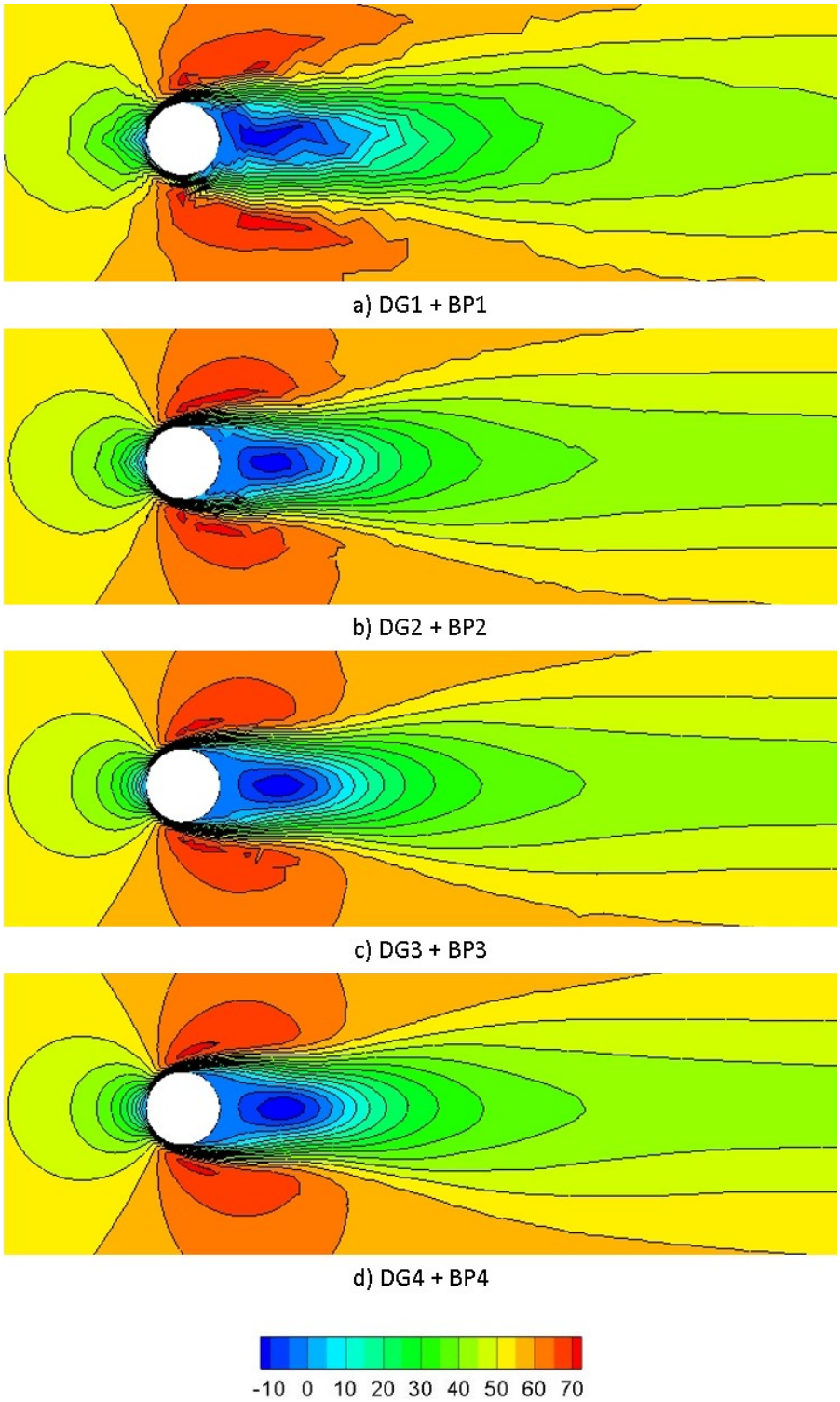


Figure 5.11: Time-averaged axial velocity contours for a laminar flow around cylinder

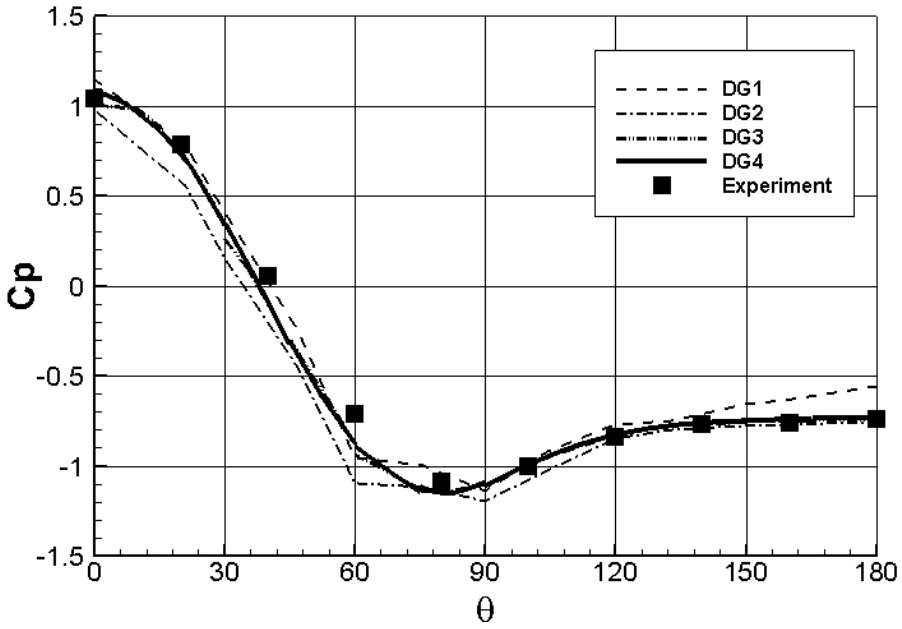


Figure 5.12: Time-averaged static pressure coefficients on cylinder surface ($\theta = 0$: leading edge; $\theta = 180^0$: trailing edge), compared to experiment data of Thom (1933)

5.2.2 Laminar Boundary Layer over a Flat Plate

In order to further validate the discretization and implementation of the viscous terms, an incompressible viscous flow over a flat plate is chosen as the second test case, which is also widely known as the Blasius solution for the laminar boundary layer discovered by Blasius (1950). The Blasius equation for the incompressible laminar boundary layer over a flat plate can be expressed as,

$$2\frac{d^3f}{d\eta^3} + f\frac{d^2f}{d\eta^2} = 0 \tag{5.2.1}$$

with a boundary condition specified as follows,

$$\begin{aligned} f(\eta) = 0, \quad \frac{df}{d\eta} &= 0, \quad when \quad \eta = 0 \\ \frac{df}{d\eta} &\to 1, \quad when \quad \eta \to \infty \end{aligned} \tag{5.2.2}$$

where η is a non-dimensional similarity variable and it is defined as $\eta = y\sqrt{U_\infty/\nu x}$. To approximate the laminar boundary layer profile, this non-linear third-order ordinary differential Equation 5.2.1 can be solved numerically using a shooting method (see Press et al., 2007). The skin friction coefficient C_f over the flat plate can also be derived from this semi-analytical solution,

$$C_f = \frac{0.664}{\sqrt{Re_x}} \tag{5.2.3}$$

where Re_x represents the Reynolds number at the location x on the flat plate.

Figure 5.13 exhibits the setup of a laminar flow past a flat plate with an incompressible inflow velocity U_∞ of 34.6 m/s and a Reynolds number of 2×10^5. In Figure 5.14, a 3D computed mesh (31×31×3, the numbers of mesh points in x, y, z directions) is extruded from a 2D one with a periodic boundary condition in the

third direction. The first element space normal to the wall is $\Delta y/L = 6.9 \times 10^{-4}$ with L denoting as the length of flat plate and a mesh spacing ratio is taken to be 1.2. The first element from the leading edge along the wall is $\Delta x/L = 5.4 \times 10^{-3}$ and a mesh spacing ratio is chosen as 1.2. This near-wall mesh is relatively coarse for a typical 2nd-order spatial discretization, as seen in Figure 5.15(a), it can however be applied for the high-order DG computations.

The computed velocity contours near the leading edge of the flat plate from the 2nd-order DG1 to the 5th-order DG4 solutions are shown in Figure 5.15. The velocity field from a 2nd-order DG1 solution tends to be slightly under-resolved, as observed in Figure 5.15(a), while that from a 3rd-order DG2 solution is better resolved as presented in Figure 5.15(b). Furthermore, the fourth-order DG3 and the fifth-order DG4 solutions, as shown in Figure 5.15(c) and 5.15(d) respectively, are capable of resolving the flow region fairly well owing to the increased order of accuracy.

In order to further quantitatively validate the computed velocity profile over a flat plate from the DG solutions, the non-dimensional similarity variable η as introduced above is plotted against the non-dimensional tangential and normal velocity variables,

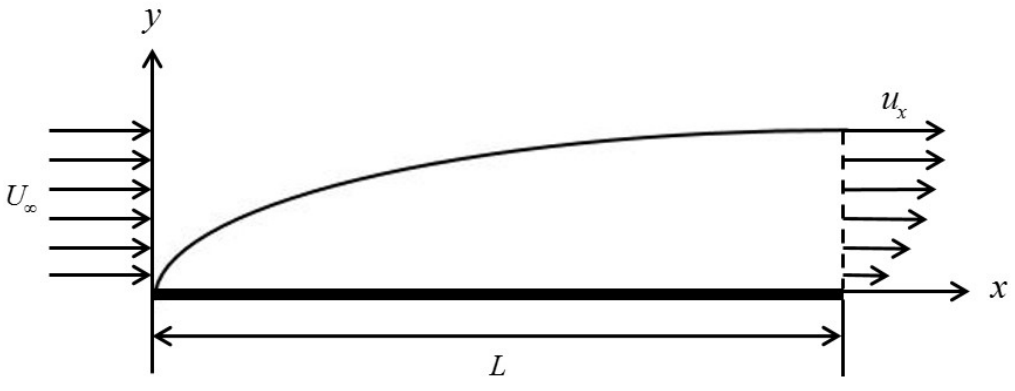


Figure 5.13: Laminar boundary layer over a flat plate

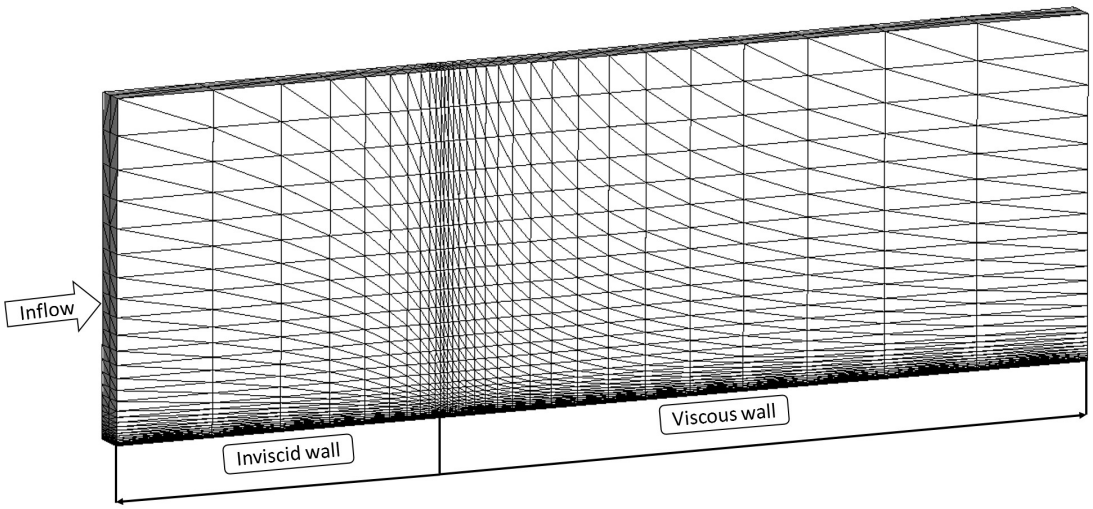


Figure 5.14: Computed mesh and boundary condition for laminar flat plate

which are defined as u/U_∞ and $v/U_\infty\sqrt{Re_x}$ respectively. Figure 5.16 displays the computed tangential velocity profiles from the DG1 to the DG4 solutions compared to the analytical ones from the Blasius solution at the locations of 20% and 51% length of plate (i.e. x/L=20% and 51%) and Figure 5.17 presents the same comparisons at the locations of 77% and 95% length of plate. Results presented in Figure 5.16 and 5.17 clearly show that the computed tangential velocity profiles from all DG solutions exhibit the similarity nature of the tangential velocity profiles and show a very good agreement with the analytical Blasius solutions at all four locations along the flat plate.

Figure 5.18 and 5.19 display the comparisons between computed and analytical normal velocity profiles at the same four locations as described before. For the 2nd-order DG1 solutions, some slight difference compared to the analytical ones are observed in Figure 5.18(a) and 5.18(b) at the locations of 20% and 51% length of plate, and the difference tends to be quite remarkable at the locations of 77% and

95% length of plate, as seen in Figure 5.19(a) and 5.19(b). This increased difference between the DG1 results and analytical ones might be attributed to the growth of Reynolds number (Re_x) along the flat plate without the corresponding refinement of near wall mesh. However, this difference tend to be reduced when the discretization order increased to a 3rd-order of accuracy (DG2), which is equivalent to subdividing the mesh cells and results in a similar effect to that of a mesh refinement. Moreover, the normal velocity profiles from the higher-order (DG3 and DG4) solutions along the flat plate show overall good agreement with the analytical Blasius ones.

The skin friction coefficient C_f from the DG solutions over the flat plate can be calculated by,

$$C_f = \frac{\tau_w}{\frac{1}{2}\rho_\infty {U_\infty}^2} \tag{5.2.4}$$

where τ_w is the plate wall shear stress and defined by,

$$\tau_w = \mu\Big(\frac{\partial u}{\partial y}\Big)_{y=0} \tag{5.2.5}$$

where μ is the dynamic viscosity, u is the velocity component parallel to the plate and y is the distance to the plate.

As shown in Figure 5.20, the skin friction coefficients over a flat plate from the DG1 to the DG4 solutions are compared to the analytical Blasius one (see Equation 5.2.3). The skin friction C_f is calculated using Equation 5.2.4 at Gaussian integration points (see Solin et al., 2003) in the local boundary faces at the no-slip wall $y = 0$. Clearly the computed DG distributions are in good agreement with the Blasius solution.

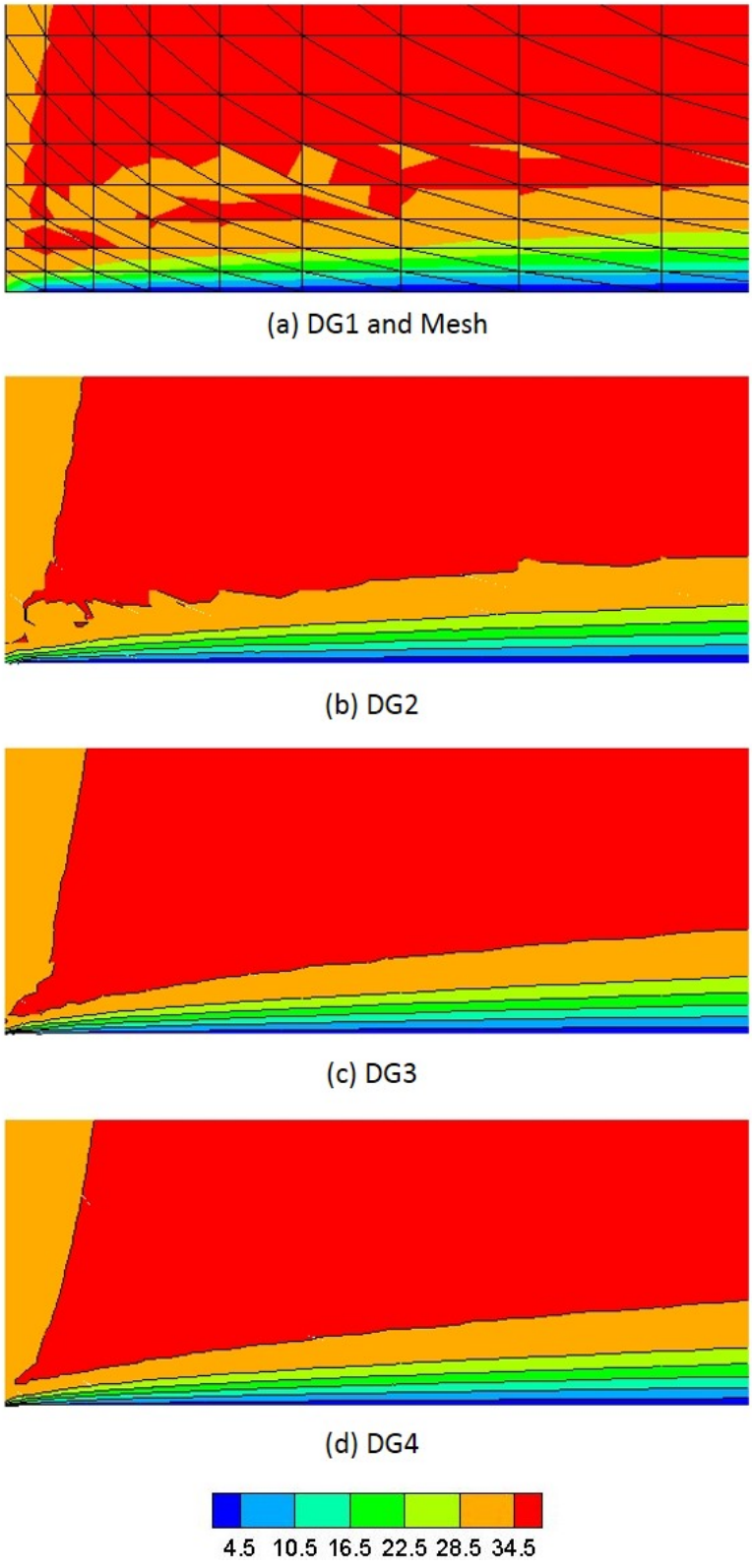


Figure 5.15: Velocity contours around the leading edge of the flat plate

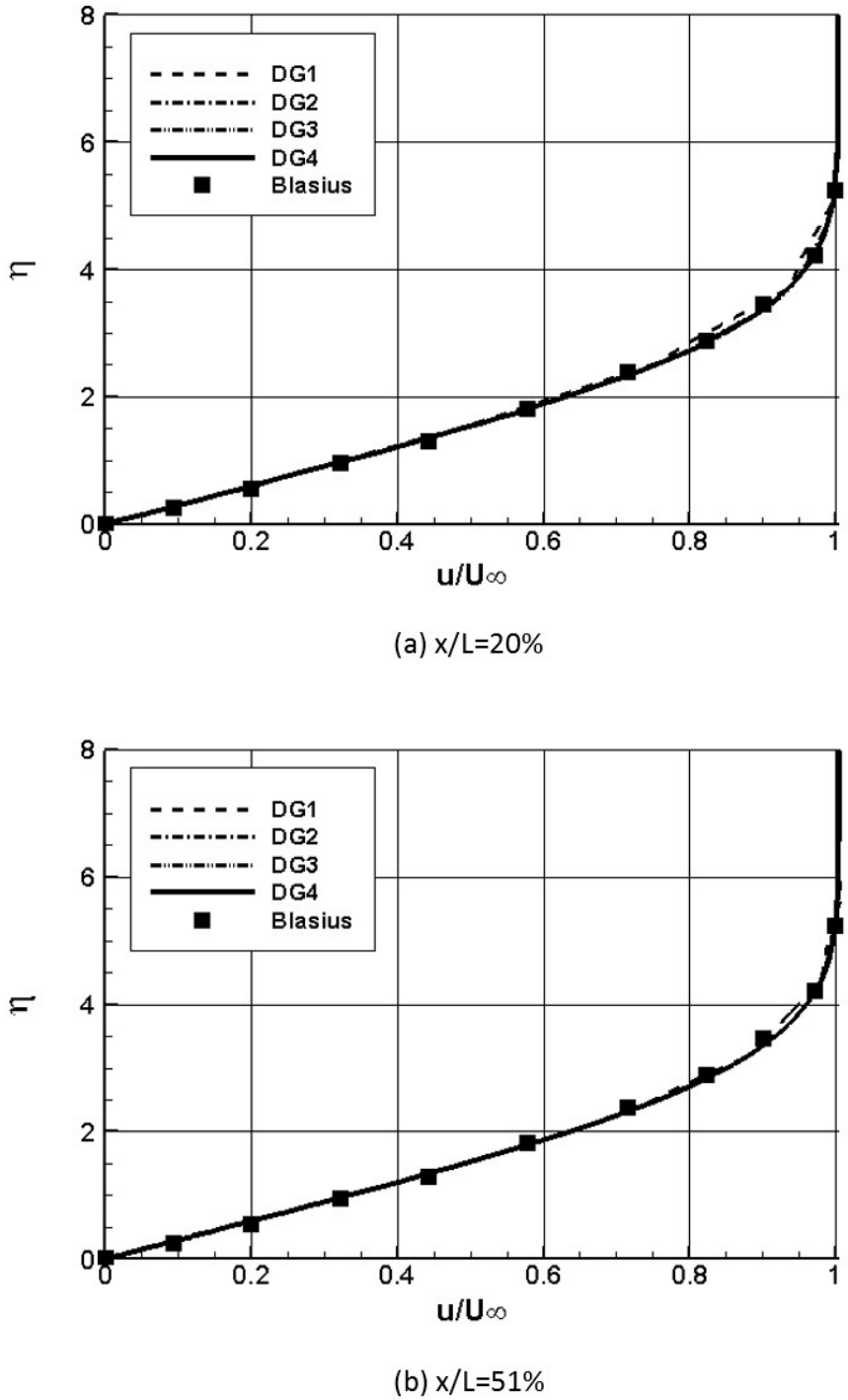


Figure 5.16: Comparison between computed and analytical tangential velocity profiles at the 20% and 51% sections of plate

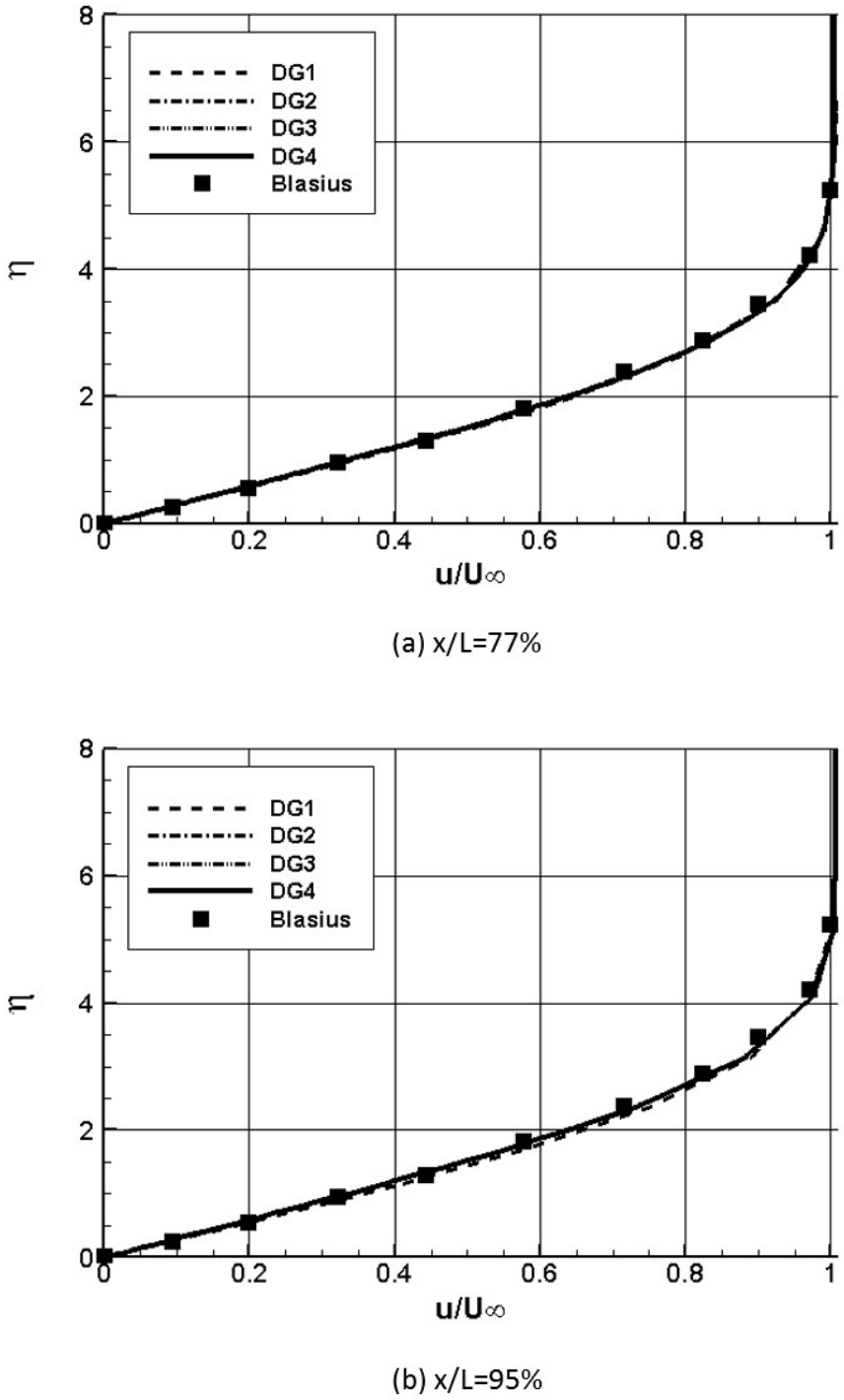
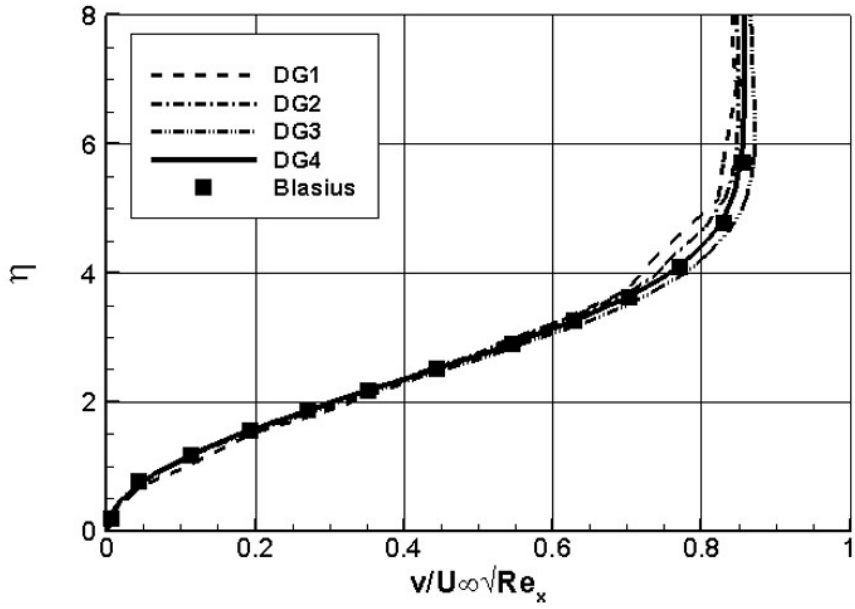
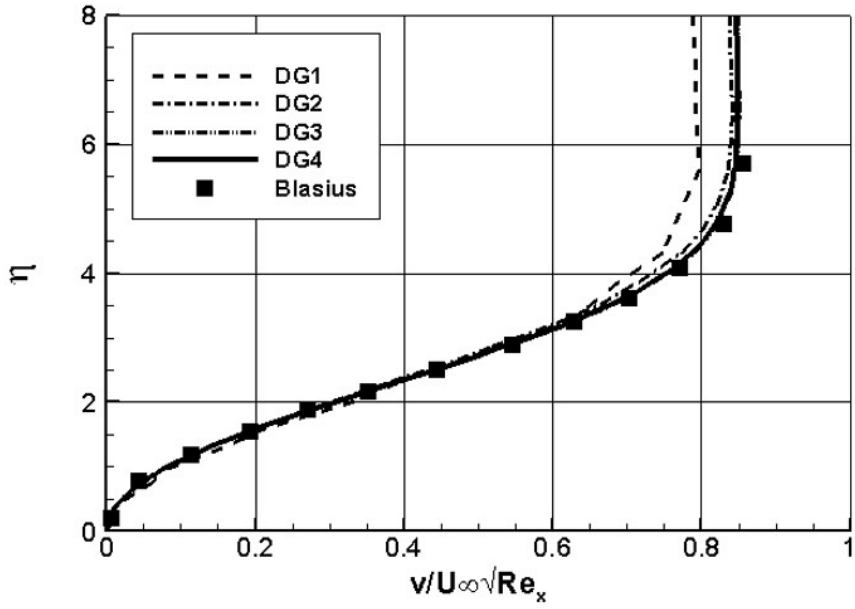


Figure 5.17: Comparison between computed and analytical tangential velocity profiles at the 77% and 95% sections of plate

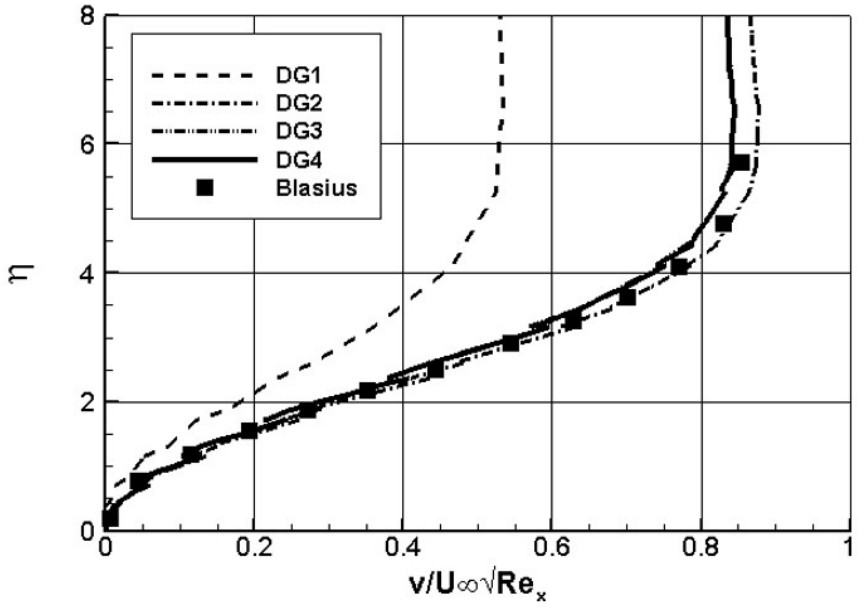


(a) x/L=20%

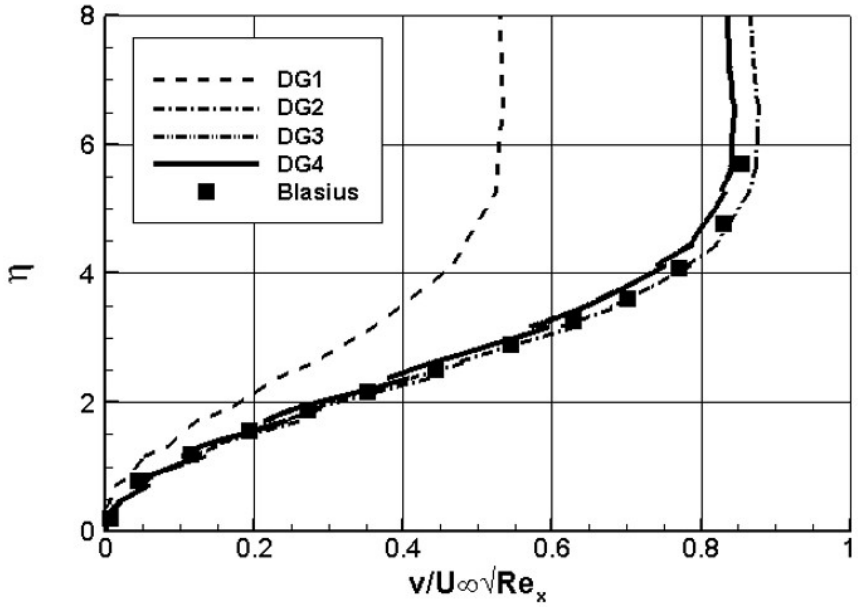


(b) x/L=51%

Figure 5.18: Comparison between computed and analytical normal velocity profiles at the 20% and 51% sections of plate



(a) x/L=77%



(b) x/L=95%

Figure 5.19: Comparison between computed and analytical normal velocity profiles at the 77% and 95% sections of plate

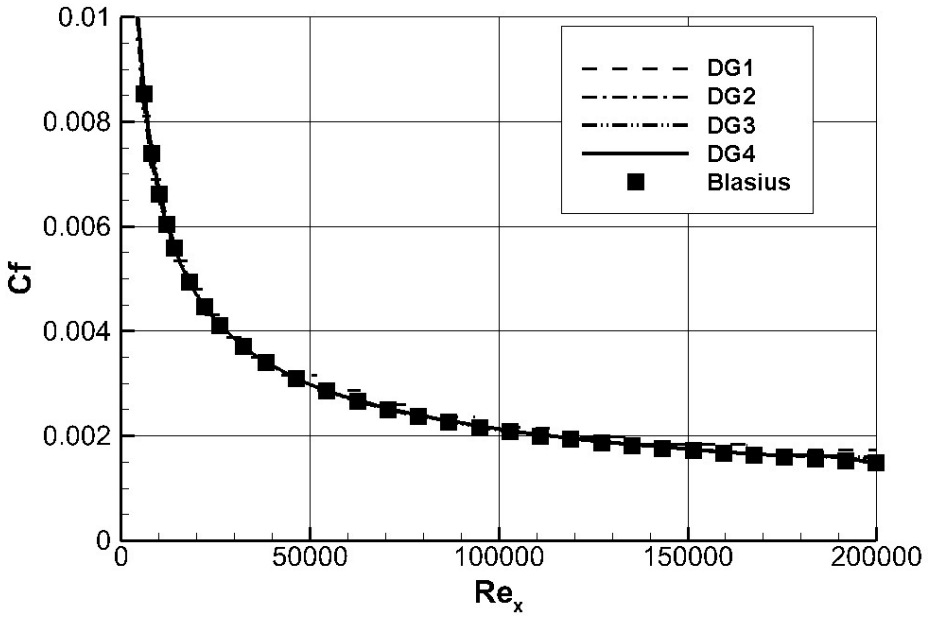


Figure 5.20: Computed skin friction coefficient along a flat plate

Overall, the excellent match between the DG results and the analytical Blasius solutions for the laminar boundary layer over a flat plate has validated the correct discretization and implementation of viscous terms for the DG scheme. It should be highlighted that the normal velocity profiles in the laminar boundary layer can be accurately predicted by the high-order DG solutions on a considerably coarse near wall mesh, attributed to the distinctive subdivision features of the DG scheme, and those from the low-order DG solutions, on the other hand, tend to be under predicted. In order to further assess the potential of the high-order DG scheme in resolving the boundary layer on the coarse mesh, a turbulent flow over a flat plate on an extraordinarily coarse near wall mesh is investigated as presented in the next section.

5.3 Turbulent Flow over a Flat Plate

For the turbulent flow studies, a fundamental test case of the turbulent boundary layer over a flat plate is examined for validating the turbulence modelling capability. The velocity profiles in the turbulent boundary layer can be described by the law of the wall by von Karman (1931). First, the logarithmic law of the wall at high Reynolds number is expressed as,

$$u^+ = \frac{1}{\kappa} \ln y^+ + C^+ \quad when \quad y^+ > 30 \tag{5.3.1}$$

where y^+ is a non-dimensional wall distance, u^+ is a dimensionless velocity, κ is a von Karman constant taken to be 0.41 and C^+ is a constant taken as 5.0 (see Schlichting, 1979). Before performing the dimensional analysis, a friction velocity, or called characteristic velocity, u_τ is introduced and defined as,

$$u_\tau = \sqrt{\frac{\tau_w}{\rho}} \tag{5.3.2}$$

where τ_w is the wall shear stress defined by Equation 5.2.5 in the previous section. Next, the dimensional analysis produces the two non-dimensional quantities,

$$\begin{aligned} y^+ &= \frac{y u_\tau}{\nu} \\ u^+ &= \frac{u}{u_\tau} \end{aligned} \tag{5.3.3}$$

where y is the distance to the wall, u is the velocity parallel to the wall and ν is the kinematic viscosity. Furthermore, there exists a small layer near the wall where the flow is essentially laminar and this viscous sublayer velocity profile is given by,

$$u^+ = y^+ \tag{5.3.4}$$

Overall, the law of the wall is applicable for describing the velocity profiles in a turbulent boundary layer over a smooth solid surface.

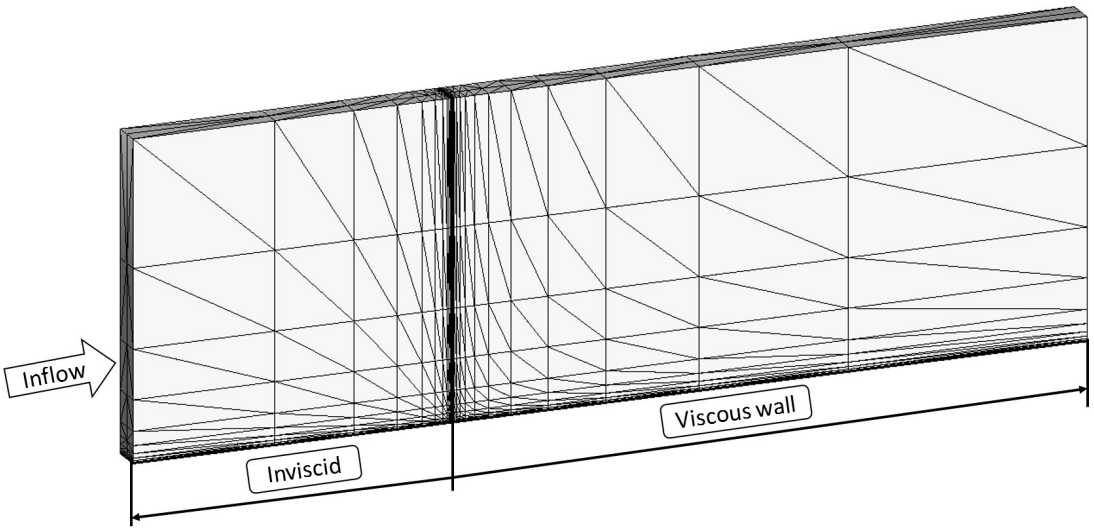


Figure 5.21: Flow past the flat plate

For the setup of this turbulent test case, the same inflow velocity for the laminar boundary layer over a flat plate in Section 5.2.2 is adopted and the Reynolds number is taken to be 6×10^6 based on the inflow velocity and the length of plate. The 3D computed mesh ($26 \times 15 \times 3$, the numbers of mesh points in x, y, z directions respectively) extruding from a 2D one with a periodic boundary condition in the third direction is shown in Figure 5.21. The first element space normal to the wall is $\Delta y/L = 1.2 \times 10^{-4}$ and a very high mesh spacing expansion ratio is chosen as 1.78. The first element along the wall is $\Delta x/L = 5.2 \times 10^{-4}$ and a high mesh spacing expansion ratio is taken as 1.6. The aspect ratio is a measure of the stretching of a mesh cell and is approximated to be a maximum of 3×10^3 in these given mesh cells. Note that the wall functions are not used in the present study and the no-slip walls are resolved by different orders of DG method. Moreover, this extraordinarily coarse and highly stretched near wall mesh, as shown in Figure 5.22(a), would not be applicable for a typical 2nd-order spatial discretization, but it can however be employed for the high-order DG simulations.

During the present numerical tests, the high-order DG computations with a standard SA turbulence model tend to be easily diverged due to the existence of the negative turbulence working variables. The computations with a modified SA model as detailed in Chapter 3, on the other hand, are fully converged, which is consistent with the conclusions in some recent work (see Burgess and Mavriplis, 2012a,b; Moro et al., 2011; Oliver, 2008). Thus, a modification of turbulence working variables is necessary to perform the high-order DG simulations for the turbulent flow.

The computed turbulent viscosity μ_t with units of Pa·s (pascal-second) from the 2nd-order DG1 to the 5th-order DG4 solutions over the flat plate are presented in Figure 5.22. It clearly shows that the flow region is better predicted as the order of accuracy increases.

In order to compare the near wall behaviour computed with different orders of accuracy, the non-dimensional velocity u^+ profiles against y^+ are plotted in Figure 5.23 for the DG solutions from the 2nd-order to 5th-order. The first element y^+ from the 2nd-order solution is markedly higher than that typically required for a direct no-slip wall condition. It is nearly 20 and u^+ is substantially over-predicted in the logarithmic layer. The computed results get closer to the theoretical law of wall as the order of accuracy increases. Overall, the 5th-order (DG4) results match very well with the theoretical velocity profiles in both the viscous sub layer and the log law layer. It should be noted that, for a even coarser near-wall mesh than the present one, the first element y^+ from DG1 solution can be as high as 30 so that the velocity profiles from DG4 solution can still be in agreement with the theoretical ones based on the present tests.

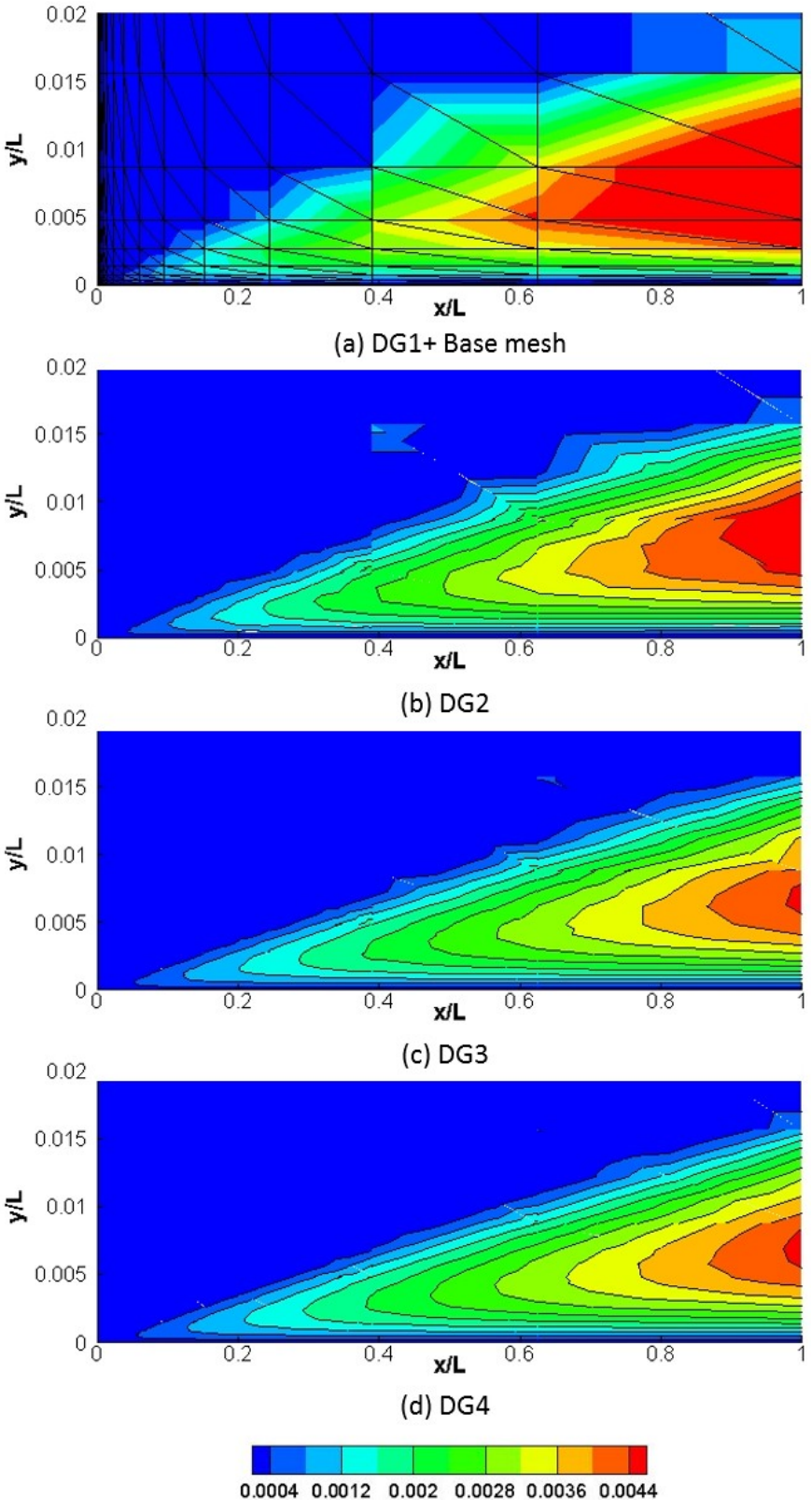


Figure 5.22: Computed turbulent viscosity over the flat plate

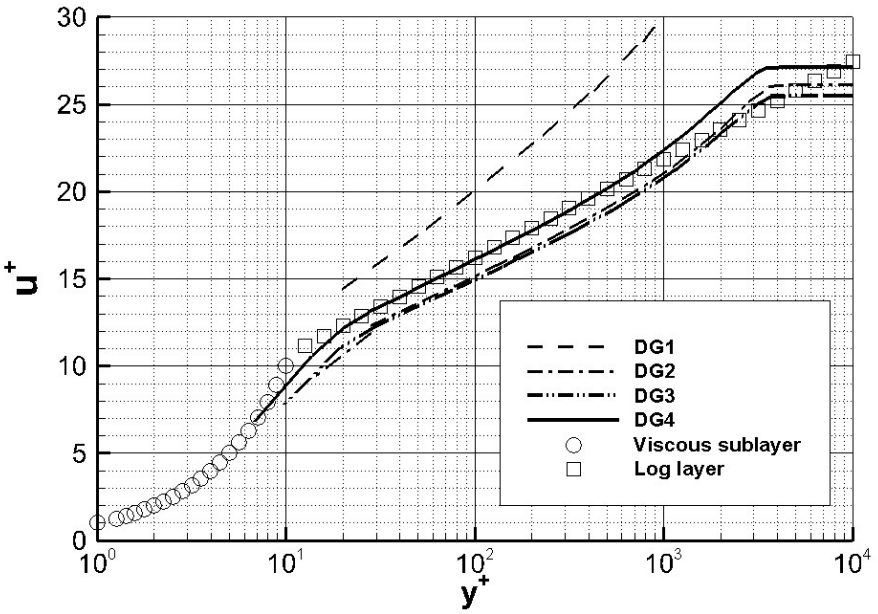


Figure 5.23: Computed velocity profiles

As presented in Figure 5.24, the skin friction coefficients over the flat plate from the DG1 to the DG4 solutions are compared to the theoretical approximation by Schlichting (1979). The theoretical skin fiction coefficient C_f over the flat plate is expressed as,

$$C_f = 0.0592 {Re_x}^{-\frac{1}{5}} \quad when \quad 5 \times 10^5 < Re_x < 10^7 \tag{5.3.5}$$

where Re_x is the Reynolds number at the location x over the flat plate.

As evident in Figure 5.24, the C_f distribution from the 2nd-order DG1 solutions is obviously under-predicted. The computed C_f distributions get closer to the theoretical distribution as the order of the piece-wise polynomial increases. The 5th-order DG4 results show an overall good agreement with the theoretical distribution.

Therefore, it is concluded that good results can be achieved by high-order DG solutions on extremely coarse meshes where a conventional 2nd-order scheme

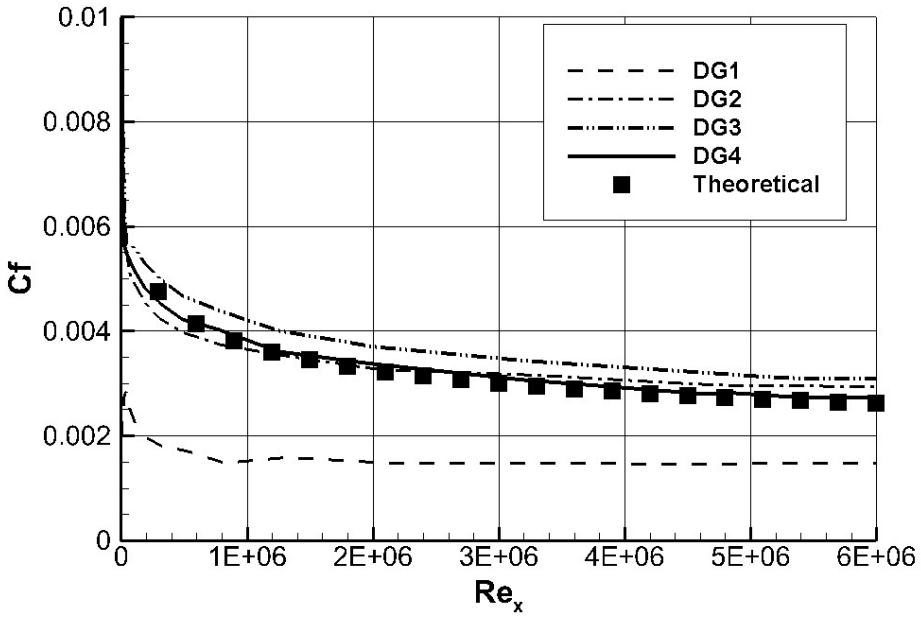


Figure 5.24: Computed skin friction coefficient along a flat plate, compared to the theoretical distribution of Schlichting (1979)

would struggle. The results also serve as a demonstration that the burden of generating high quality near wall fine meshes for complex geometries may be considerably alleviated by the high order methods for turbulent flow simulations without invoking the wall function.

Overall, the above good agreement between the high-order DG results and the theoretical data has validated the turbulence modelling capability by adopting a modified SA turbulence model in the current DG solver.

5.4 All-Speed Flow past an Airfoil

In order to validate the all-speed AUSM$^+$-up scheme adopted in the current DG solver, the test case of the laminar flow past an airfoil at a wide range of Mach numbers is examined. The symmetrical four digit NACA0012 airfoil, designed by the National Advisory Committee for Aeronautics (NACA), is chosen for this test case, which has been taken as a canonic test geometry for validating many CFD methods in the literature (see Bassi and Rebay, 1997a; Mavriplis and Jameson, 1990). The geometry of the NACA0012 airfoil is designed as (see Jacobs et al., 1933),

$$y_t = +- 0.6\Big[0.2969\sqrt{x} - 0.1260x - 0.3516x^2 + 0.2843x^3 - 0.1015x^4\Big] \quad (5.4.1)$$

where y_t is the half thickness of the airfoil at a given position of x along the chord from 0 to 1.

The 'C-type' mesh around the airfoil is generated, as seen in Figure 5.25, and only consists of 60×7 mesh points in the directions along and normal to the wall, which is relatively coarse for a typical 2nd-order spatial discretization. Hence, it is necessary to represent the curved boundary by the corresponding p-th order polynomials as taken in the spatial discretization. The overall mesh has been extended by 20 chords length away from the airfoil and the farfiled boundary condition is applied for the far fields. Likewise, a 3D computed mesh is generated from extruding the 2D one a layer (with 2 mesh cells) in the third direction with symmetry boundary conditions applied to accommodate the current 3D solver.

The simulations for the laminar flow past the NACA0012 airfoil have been performed from the 2nd-order DG1 with the BP1 boundary to the 4th-order DG3

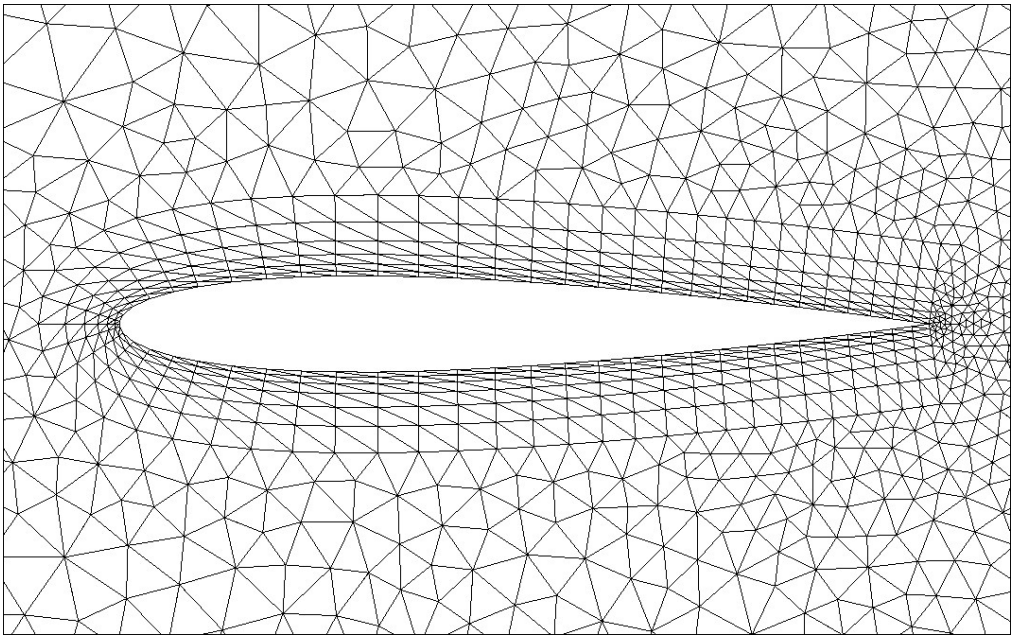


Figure 5.25: Mesh around the NACA0012 airfoil

with the BP3 boundary. The inflow free stream conditions are given at four different Mach numbers: 0.01, 0.5, 0.8 and 2. Detailed computational results will be described in the next four subsections.

5.4.1 Subsonic Flow with a Mach Number of 0.5

The first test case is a subsonic flow past a NACA0012 airfoil at an incidence of 0^0 with an inflow Mach number at 0.5. The Reynolds number, based on the inflow free stream velocity and the chord of airfoil, is taken as 5000, which is close to the upper limit for steady laminar flow (see Mavriplis and Jameson, 1990). As depicted in Figure 5.26(a), the base mesh in the proximity to the leading edge of the airfoil is fairly coarse. The computed static pressure coefficient contours around the leading edge are presented in Figure 5.26. The pressure field near the leading edge is poorly resolved by the 2nd-order DG1 solutions with a BP1 boundary, however, finer resolution of the pressure field is obtained from the higher-order DG solutions with corresponding orders of polynomials representing the boundary.

As presented in Figure 5.27, the computed Mach number contours from the DG1 to the DG3 solutions are compared with that of the reference 2nd-order FVM solution by Mavriplis and Jameson (1990). It should be noted that they adopted 192 mesh points to represent the geometry of airfoil, around 3 times greater than the number of mesh points in the present study, and significantly denser grids in the region far away from the airfoil. Except for the DG1, the Mach number field from higher than 3rd-order (DG2 and DG3) solutions are considerably smoother and better resolved than that of the reference 2nd-order solutions on the fine mesh. Note that the 2nd-order results from both the FVM by Mavriplis and Jameson (1990) and the present DG1 solutions indicate clearly some overshooting of the Mach numbers/velocities in the near wall regions. These seemingly numerical artifacts seem to have been eliminated by the higher order solutions.

The computed static pressure and skin friction coefficient on the airfoil surface from the DG3 solutions are plotted in Figure 5.28. The present DG3 results have agreed well with that of DG3 solutions by Bassi and Rebay (1997a), though the present skin friction coefficient near the leading edge is slightly under predicted.

Overall, the above validation results has demonstrated that the current DG solver with an AUSM$^+$-up scheme is capable of accurately simulating the compressible flow around an airfoil with a moderate speed.

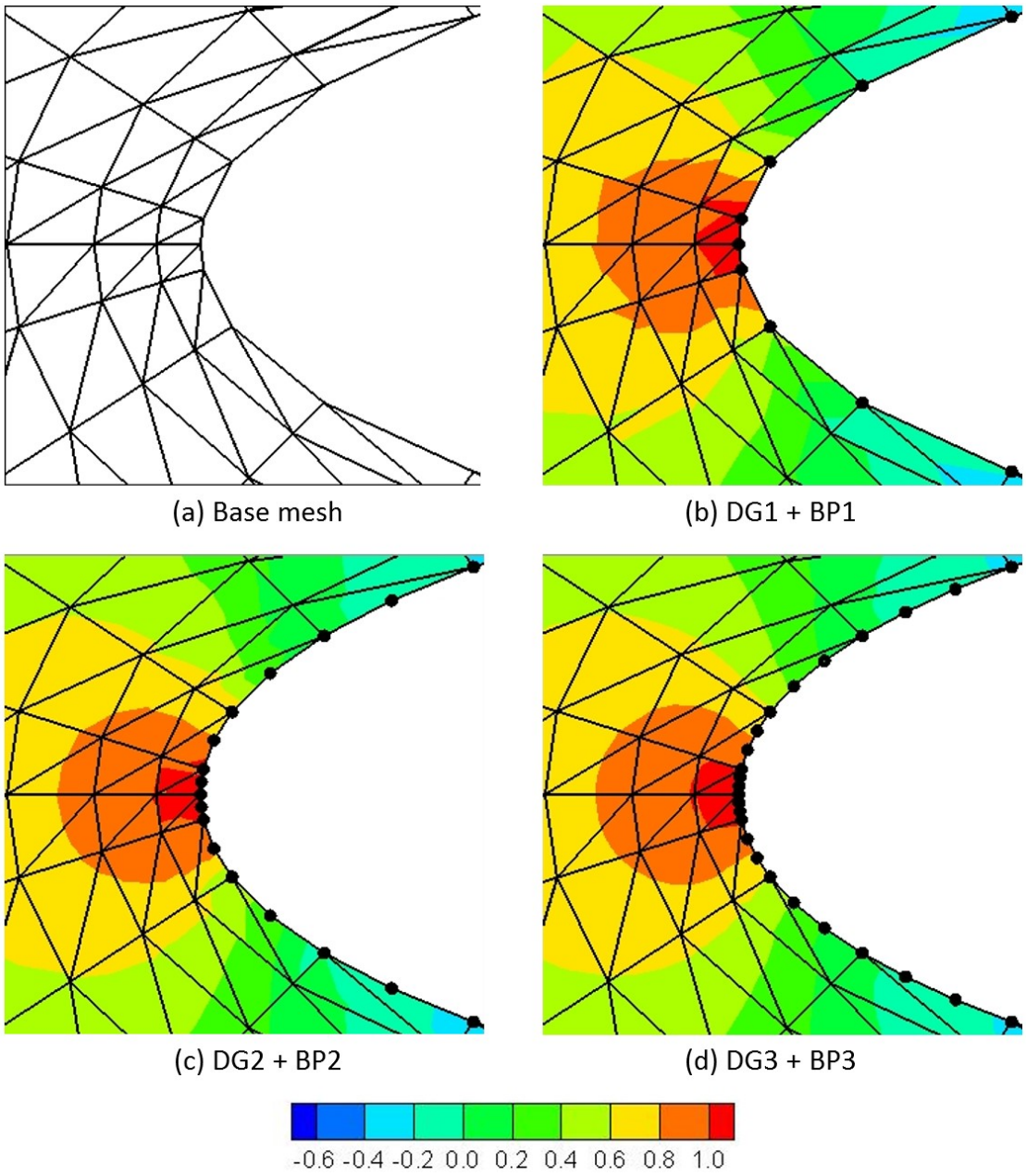


Figure 5.26: Static pressure coefficient contours for a subsonic flow near the leading edge of a NACA0012 airfoil of DG representations with corresponding orders of boundary geometrical representation (Mach=0.5, Re=5000, incidence = 0^0)

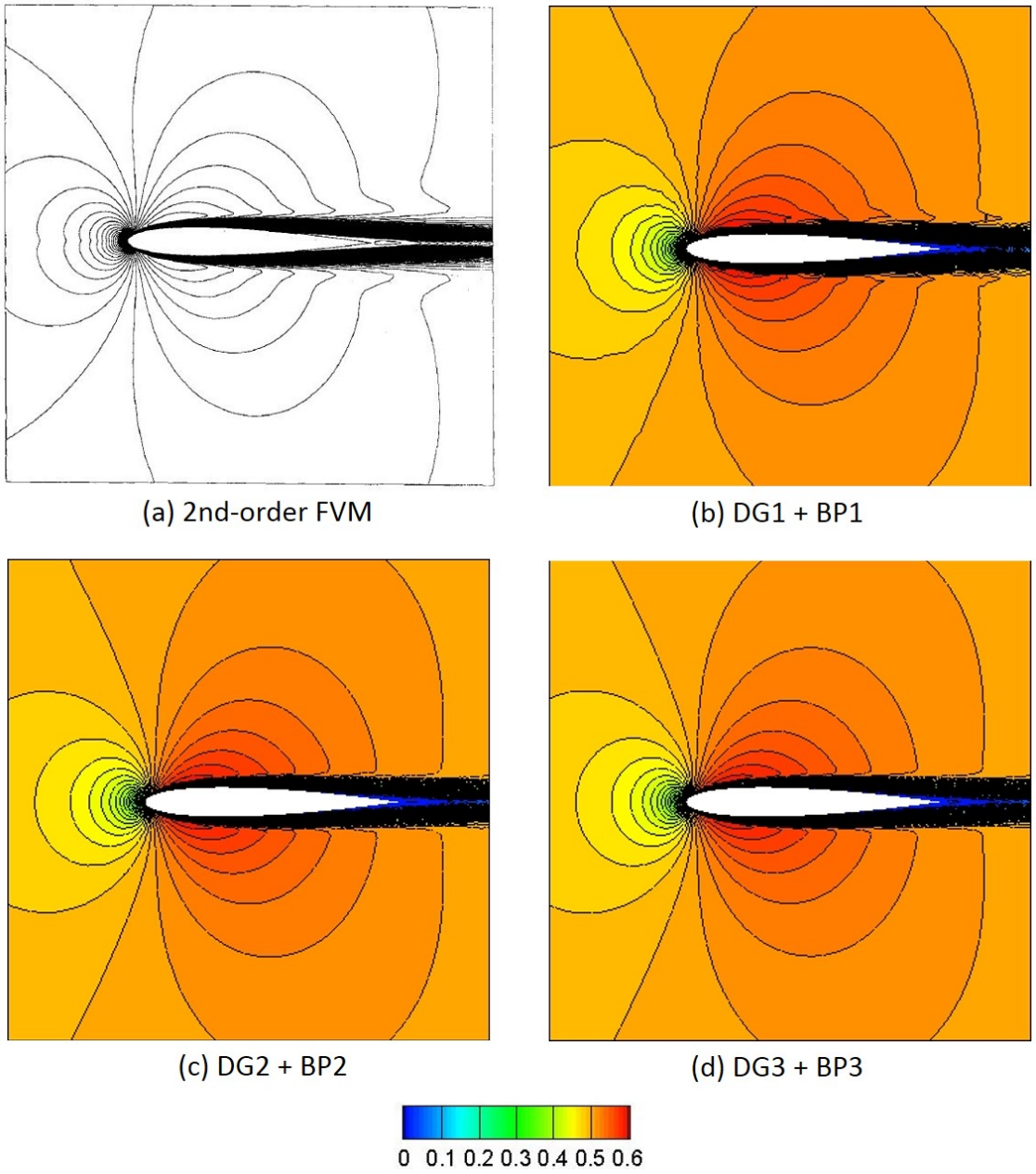
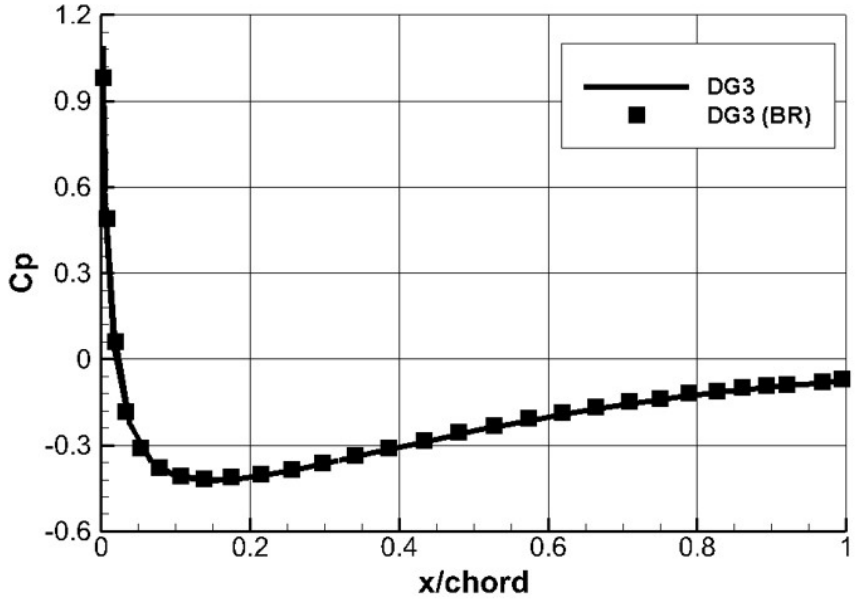
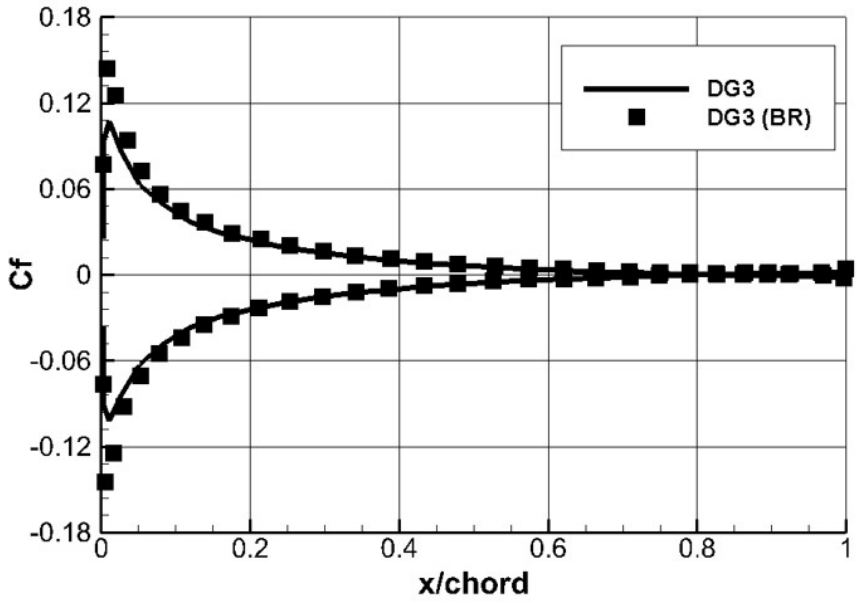


Figure 5.27: Mach number contours around the NACA0012 airfoil from the 2nd-order DG1 to the 4th-order DG3 solutions, compared to that of the 2nd-order FVM solution by Mavriplis and Jameson (1990) (Mach=0.5, Re=5000, incidence = 0^0)



(a) Static pressure coefficient



(b) Skin friction coefficient

Figure 5.28: Computed distributions on the NACA0012 airfoil surface from the DG3 solutions, compared to that of the DG3 solutions by Bassi and Rebay (1997a) (Mach=0.5, Re=5000, incidence = 0^0) (a) static pressure coefficient; (b) skin friction coefficient

5.4.2 Transonic Flow with a Mach Number of 0.8

In the second test case, the transonic inflow Mach number is 0.8, the Reynolds number is 73 and the incidence is taken to be 10^0. The inflow conditions are taken from the test case by Mavriplis and Jameson (1990). Here, the viscous dominated flow with extremely low Reynolds number can be applied for validating the implementation of the discretization of the viscous terms in the CFD solver. The computed static pressure coefficient contours around the airfoil with a close up near the leading edge are shown in Figure 5.29. For the flow region with low gradient (e.g. far field), the results from the DG1 to the DG3 solutions show overall good agreement. However, for the flow field with high gradient (e.g. leading and trailing edges, suction and pressure surfaces of the airfoil), the flow field from the 2nd-order solution with the linear boundary is poorly resolved whereas those from the higher-order solutions with high-order curved boundaries are better resolved.

A comparison between the present computed Mach number contours and those of the reference case is given in Figure 5.30. From both the present and reference results, the supersonic flow is obtained in a small region outside the viscous layer of the suction surface. However, the developed wake downstream of the airfoil from the DG1 solution is not well resolved. The overall resolution of the DG2 results are comparable to that of the reference one. Moreover, the flow region from the DG3 solutions is further smoother and more accurate, especially in the field with high gradient.

As presented in Figure 5.31(a), the static pressure coefficient distribution on the airfoil surface from the present DG3 solutions is in good agreement with the

reference one. The skin friction coefficient distribution from the current DG3 solutions, as seen in Figure 5.31(b), has matched the reference one well, though a slight under-prediction at the suction surface close to the leading edge is observed.

Overall, the above good match between the present DG results and reference ones has validated the current DG solver with a capability of simulating a transonic flow.

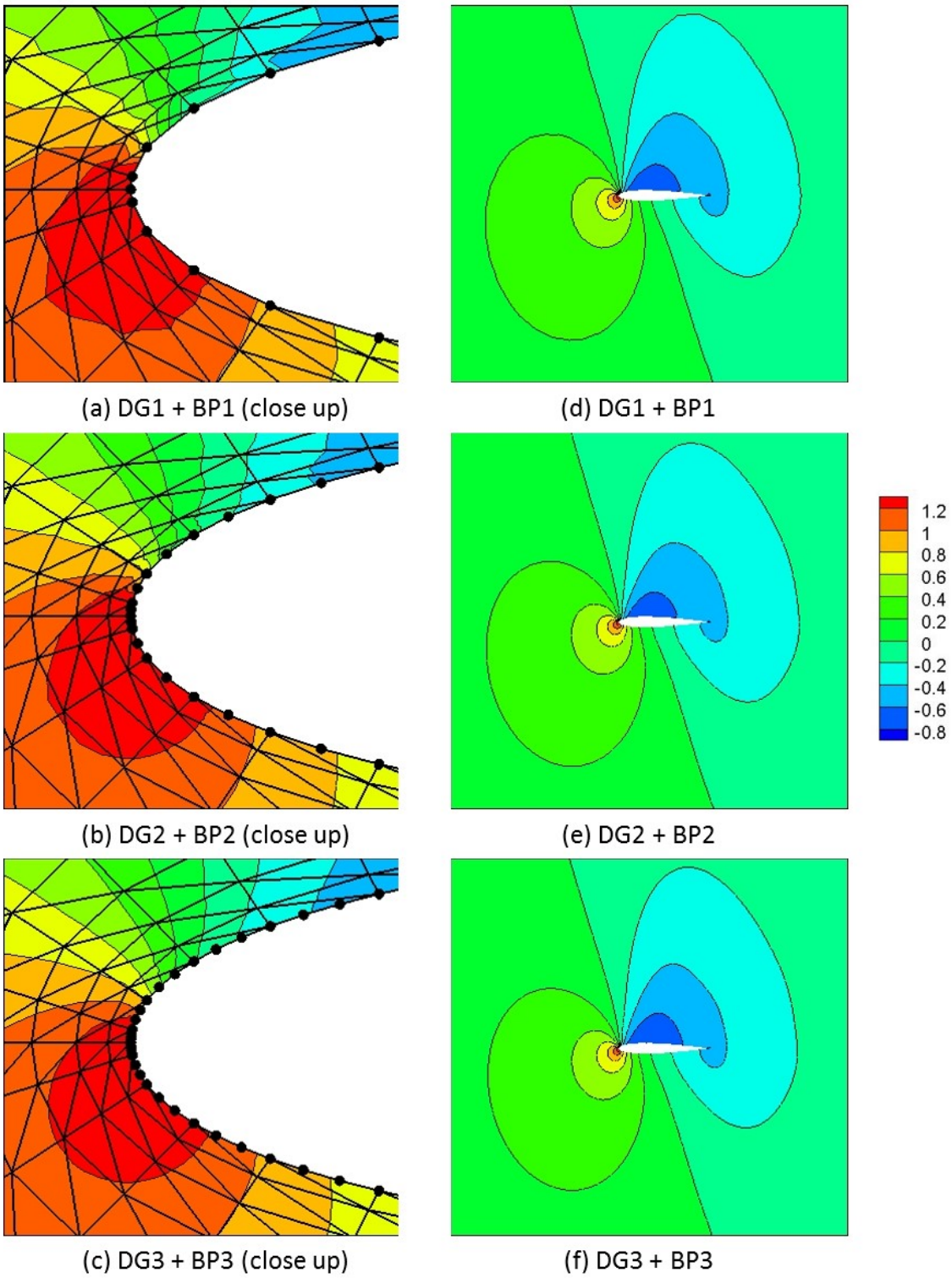


Figure 5.29: Static pressure coefficient contours around the NACA0012 airfoil with a close up near the leading edge (Mach=0.8, Re=73, incidence = 10^0)

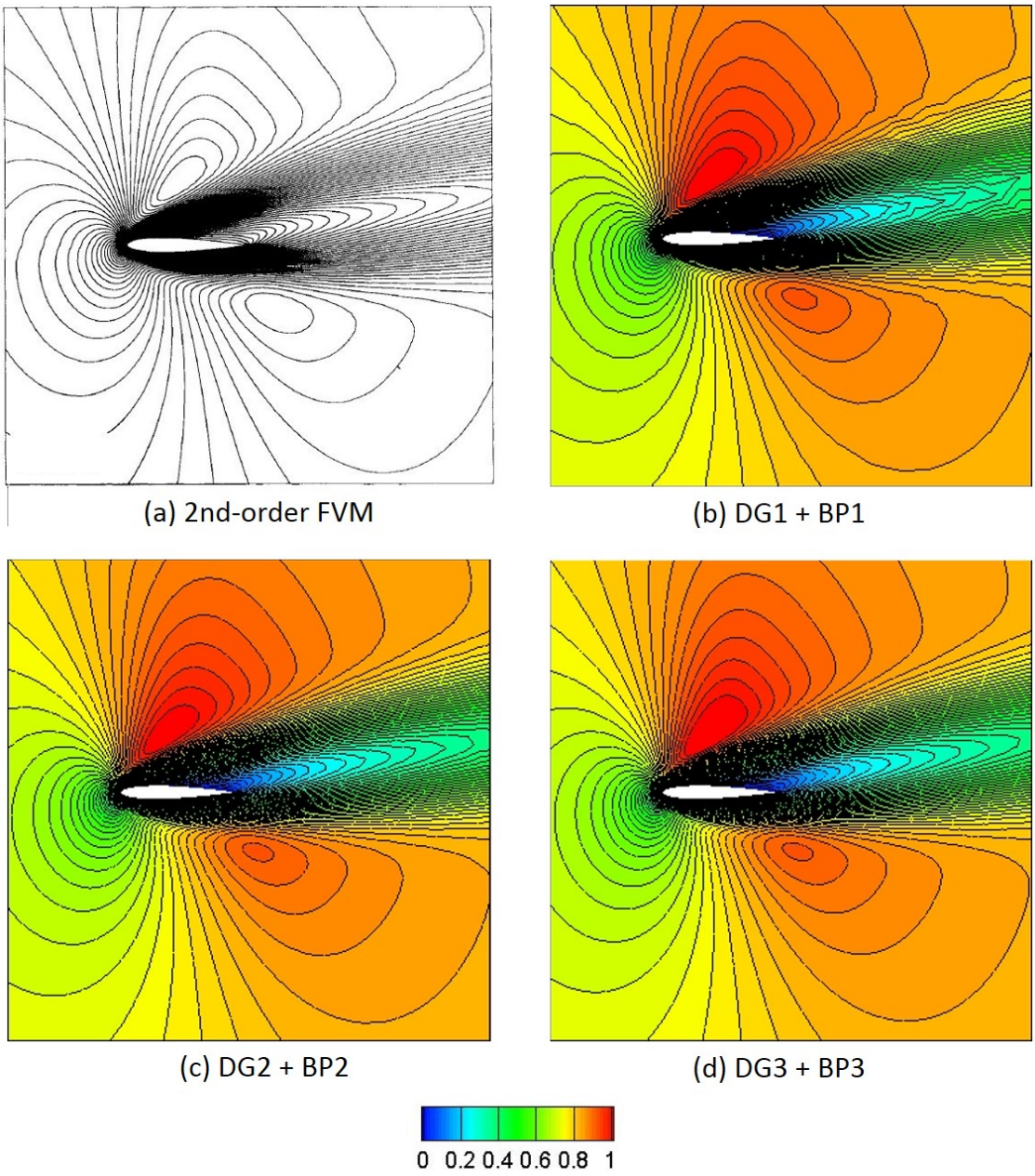
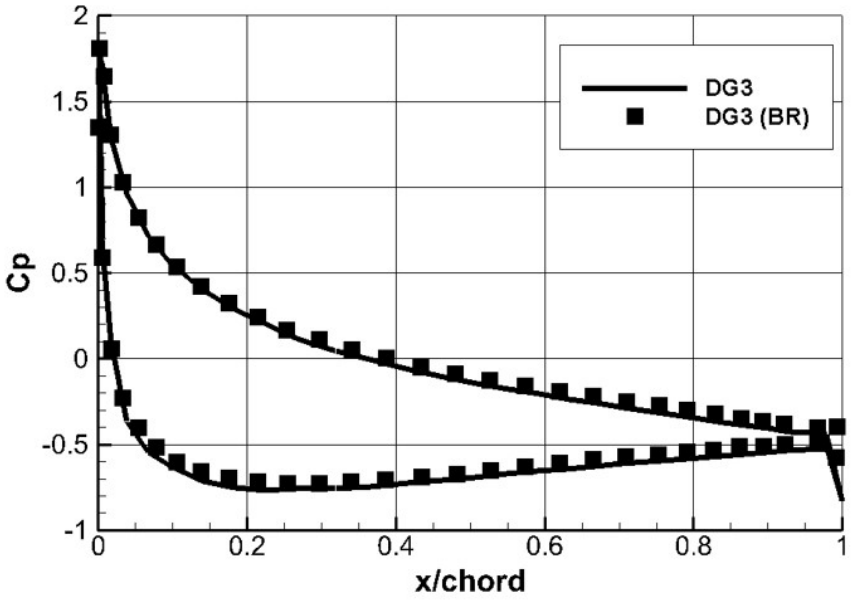
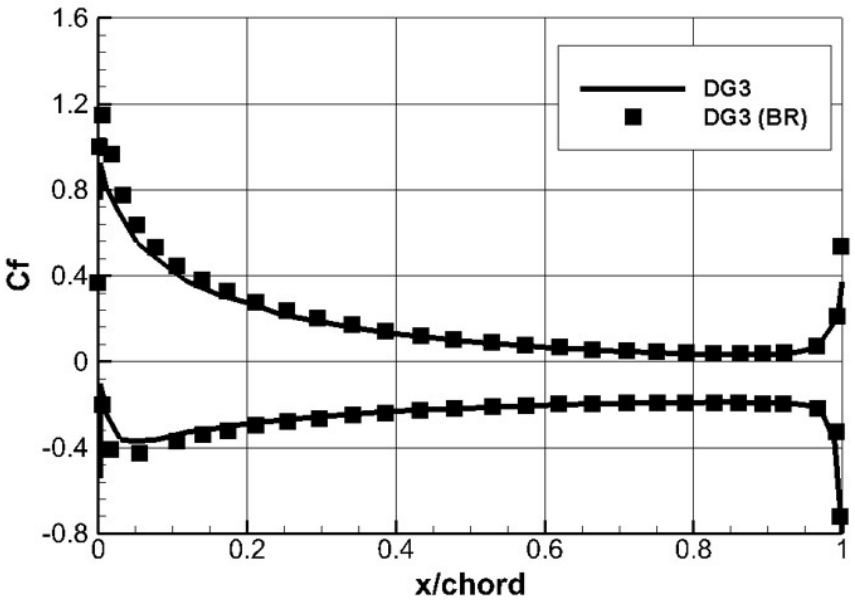


Figure 5.30: Mach number contours around the NACA0012 airfoil from the 2nd-order DG1 to the 4th-order DG3 solutions, compared to that of the 2nd-order FVM solution by Mavriplis and Jameson (1990) (Mach=0.8, Re=73, incidence = 10^0)



(a) Static pressure coefficient



(b) Skin friction coefficient

Figure 5.31: Computed distributions on the NACA0012 airfoil surface from the DG3 solutions, compared to that of the DG3 solutions by Bassi and Rebay (1997a) (a) static pressure coefficient; (b) skin friction coefficient (Mach=0.8, Re=73, incidence = 10^0)

5.4.3 Supersonic Flow with a Mach Number of 2

The third test case is a supersonic flow past a NACA0012 airfoil at an incidence of 10^0. The inflow free stream Mach number is 2 and the Reynolds number is taken to be 106, which are also taken from the validation case by Mavriplis and Jameson (1990). Figure 5.32 presents the computed static pressure coefficient contours around the airfoil with a close up near the leading edge. Note that the comments made for Figure 5.29 in the Subsection 5.4.2 also apply here.

As shown in Figure 5.33, the density contours around the airfoil from the DG solutions are compared to the reference one. The strong bow shock has been observed and tends to dissipate in the far field from both the present DG and reference results. Likewise, the shock wave from the DG1 solution are markedly oscillating and poorly resolved. It is evident from Figure 5.33 that the resolution of the shock wave tends to be distinctively improved as the order of piece-wise polynomials increases.

The computed static pressure and skin friction coefficient on the airfoil surface from the present DG3 solutions are compared to the reference distributions, as presented in Figure 5.34. Similarly, the comments made for Figure 5.31 in the Subsection 5.4.2 can be applied here as well.

Overall, provided the results discussed above, it is concluded that the current DG solver with the AUSM$^+$-up scheme has the capability of simulating the supersonic flow.

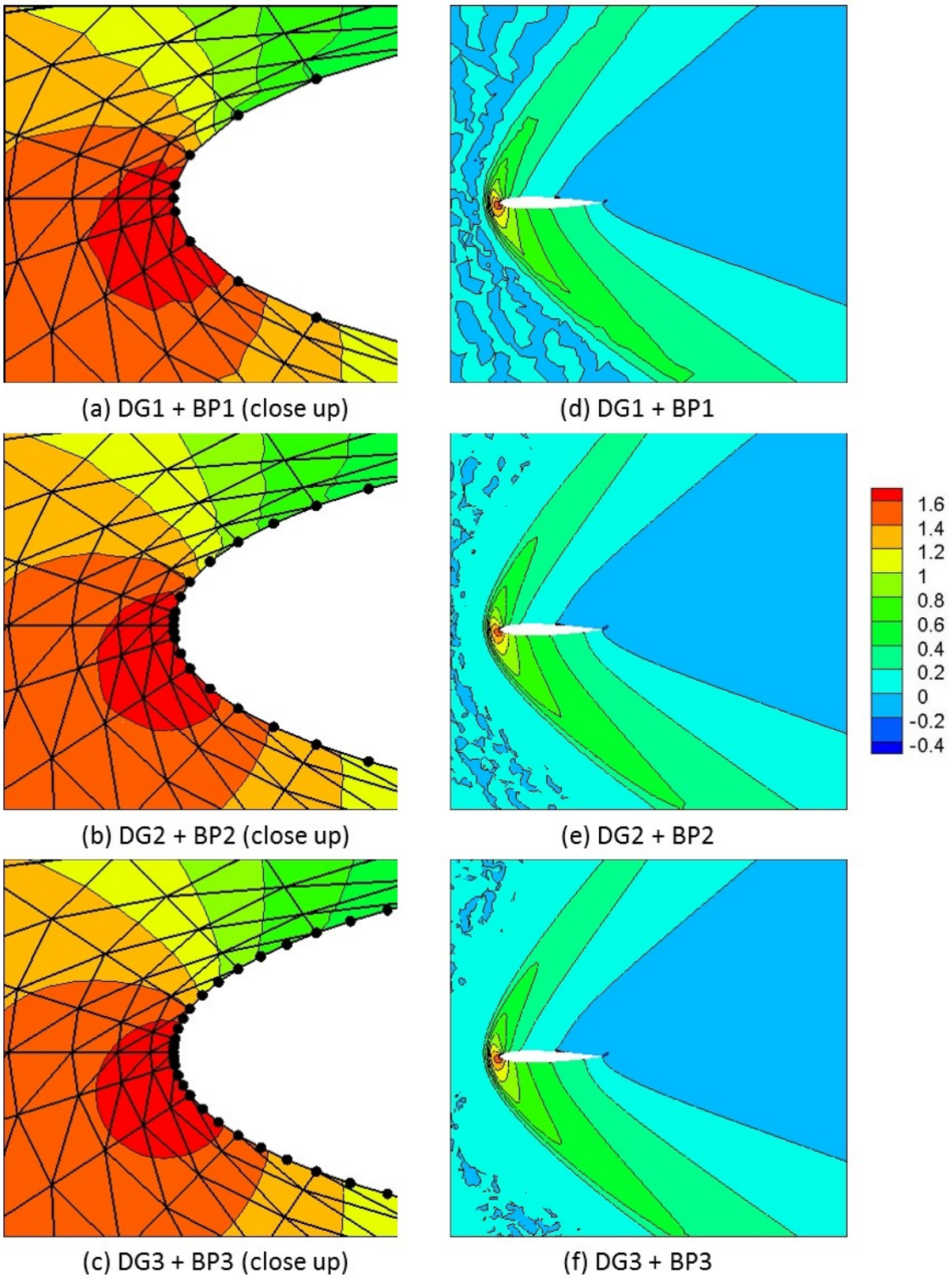


Figure 5.32: Static pressure coefficient contours around the NACA0012 airfoil with a close up near the leading edge (Mach=2, Re=106, incidence = 10^0)

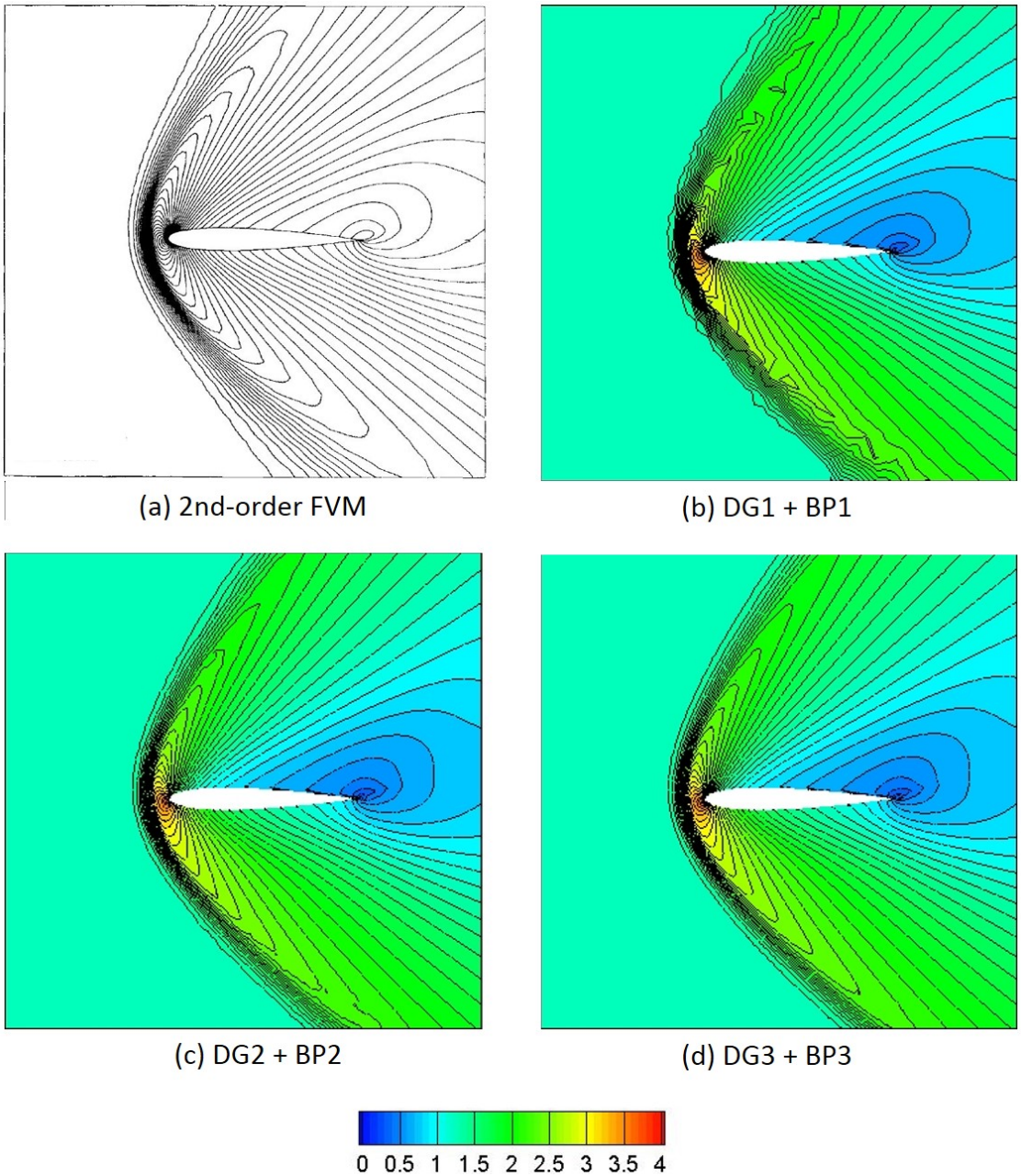
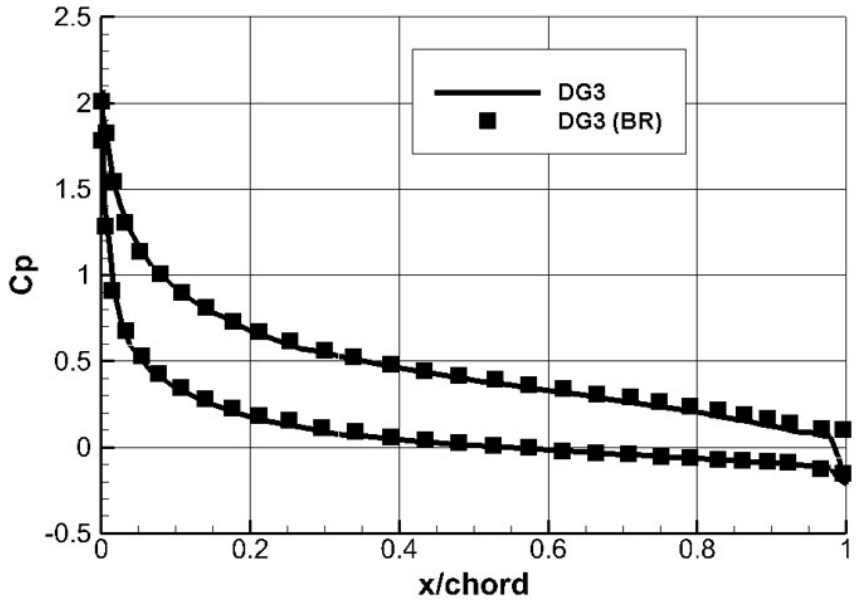
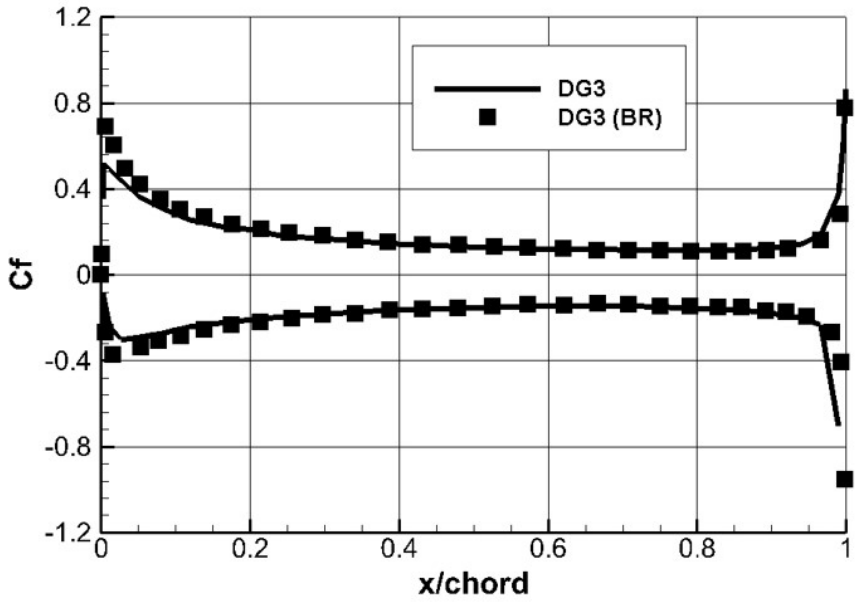


Figure 5.33: Density contours around the NACA0012 airfoil from the 2nd-order DG1 to the 4th-order DG3 solutions, compared to that of the 2nd-order FVM solution by Mavriplis and Jameson (1990) (Mach=2, Re=106, incidence = 10^0)



(a) Static pressure coefficient



(b) Skin friction coefficient

Figure 5.34: Computed distributions on the NACA0012 airfoil surface from the DG3 solutions, compared to that of the DG3 solutions by Bassi and Rebay (1997a) (a) static pressure coefficient; (b) skin friction coefficient (Mach=2, Re=106, incidence = 10^0)

5.4.4 Low-Speed Flow with a Mach Number of 0.01

For the final test case, an extremely low-speed inflow condition is taken. The Mach number is chosen as 0.01, the Reynolds number is 100 and the incidence is taken as 0^0. In order to further resolve the viscous layer for this extreme low-speed flow, the 'C-type' mesh around the airfoil is slightly refined, as shown in Figure 5.36(a), and now consists of of 64×9 mesh points. Moreover, Figure 5.35(a) depicts the refined mesh in the region of close proximity to the leading edge, however, this reined one is still considerably coarse for a typical 2nd-order spatial discretization.

Figure 5.35 presents the computed static pressure coefficient contours near the leading edge from the present DG solutions. Note that the remarks made for Figure 5.26 in Subsection 5.4.1 can also be applied here.

The Mach number contours around the airfoil from the DG1 to the DG3 solutions are shown in Figure 5.36. As to be expected, the flow region is better resolved as the order of piece-wise polynomial increases. The computed static pressure and skin friction coefficients on the airfoil surface from the 4th-order DG3 solution are plotted in Figure 5.37

Overall, the above results have demonstrated that the current DG solver with the AUSM$^+$-up scheme has the potential of simulating an extraordinarily low-speed flow. Note that this low speed solution can be achieved without any extra pre-conditioner in the current DG solver, attributed to the all-speed AUSM$^+$-up scheme, which is in clear contrast to the typical density-based time-marching flow solvers as widely applied to turbomachinery flows.

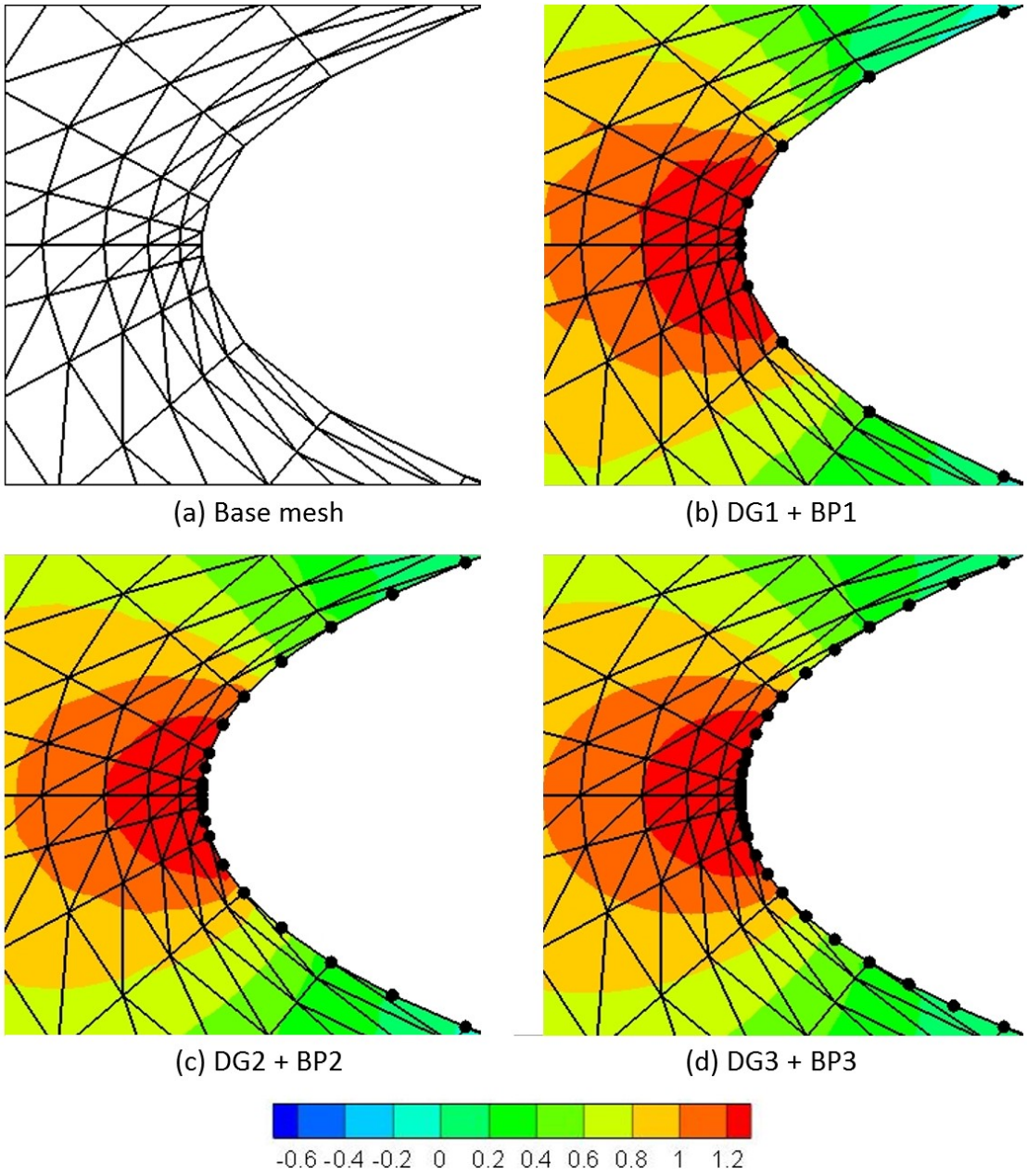


Figure 5.35: Static pressure coefficient contours for an incompressible flow around the leading edge of a NACA0012 airfoil of DG representations with corresponding orders of boundary geometrical representation (Mach=0.01, Re=100, incidence = 0^0)

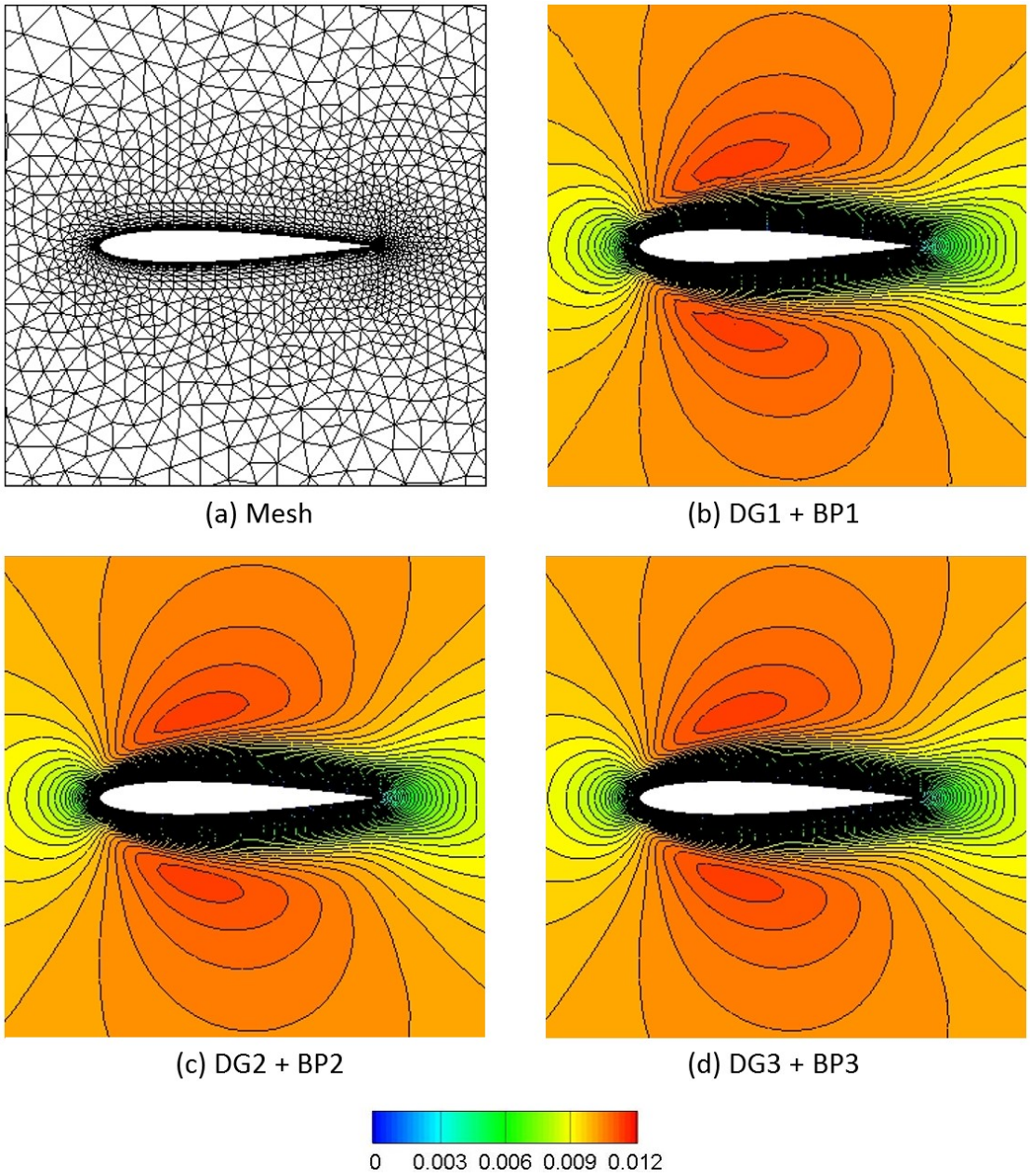
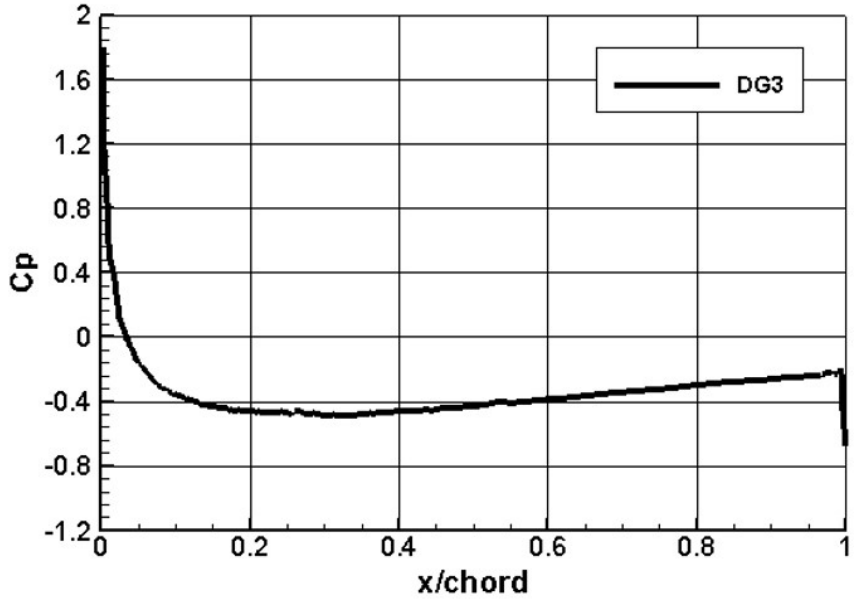
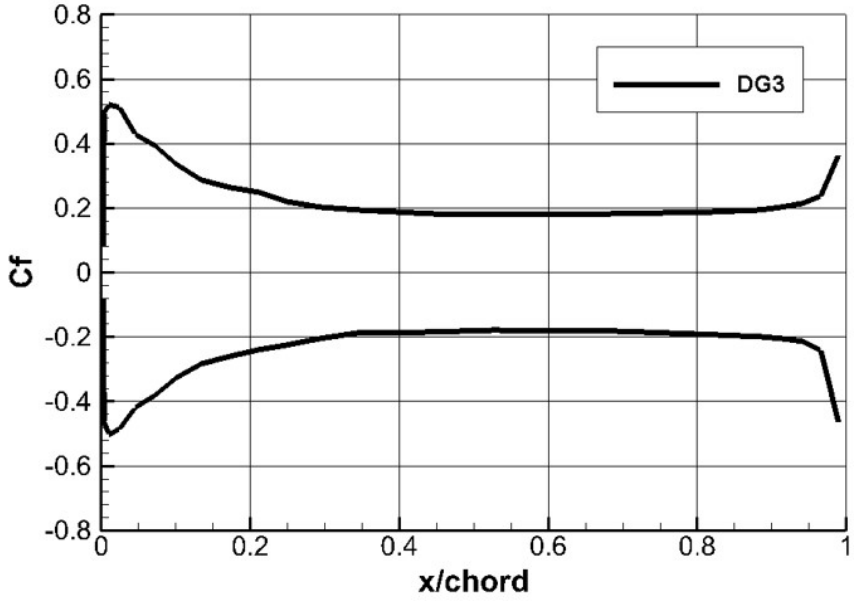


Figure 5.36: Mach number contours around the NACA0012 airfoil from the 2nd-order DG1 to the 4th-order DG3 solutions (Mach=0.01, Re=100, incidence = 0^0)



(a) Static pressure coefficient



(b) Skin friction coefficient

Figure 5.37: Computed distributions along the NACA0012 airfoil from the DG3 solutions (Mach=0.01, Re=100, incidence = 0^0)

5.5 Summary

The validation study for the current DG solver has been carried out through several tests, including the inviscid, viscous and turbulent ones as well as in a wide flow speed range. First, an inviscid flow around a cylinder has been simulated up to the 5th-order of accuracy with high-order curved boundary representation on an extremely coarse mesh. From these results, it is concluded that the flow field is better resolved as the order of accuracy increases with corresponding order of piece-wise polynomials representing the boundary. Note that the high-order results from the linear elements on the curved geometry might not be very meaningful without the proper curved boundary representation.

Next, two laminar flow simulations, one is the viscous flow around a cylinder and the other is the laminar boundary layer over a flat plate, have been performed. These computed results have shown overall good agreement with the reference data and validated the proper discretization and implementation of the viscous terms using the BR2 method, which also demonstrate that the current DG solver has both steady and unsteady viscous flow modelling capability accounting for the implicit time integration strategy using the preconditioned Newton-GMRES method.

A subsequent turbulent flow test case is the turbulent boundary layer over a flat plate on a nonstandard coarse near wall mesh. The good match between the computed high-order results and the reference one has validated the proper discretization and implementation of the RANS equations with a modified Spalart-Allmaras turbulent model. The results also highlight that the high-order methods might effectively alleviate the burden of generating high quality near wall meshes

for complex geometries.

Finally, a viscous flow past an airfoil has been simulated with a wide flow speed regimes, including the extremely low-speed incompressible flow, subsonic flow, transonic flow and supersonic flow. The results demonstrate consistently the great performance of the AUSM$^+$-up scheme for the high-order DG method.

For all the validation cases, the memory storage and computational time have been increased with the increased order of accuracy for the high-order DG simulations. Overall, an implicit solver using the DG discretization with an all-speed scheme on unstructured meshes has been validated.

6

RANS Solution for High Pressure Turbine Cascade

As stated in Chapter 2, the major source of flow losses in a blade passage is the endwall region dominated by the secondary flow (see Denton, 1993). To the best knowledge of the present author, the endwall secondary flow development has not yet been studied by using the high-order scheme. It is of the present interest to examine the predictability of aerodynamic performance of 3D turbine blades strongly influenced by endwall secondary flow using the current high-order DG solver. To this end, the high pressure turbine cascade experimentally studied at Durham University (commonly known as 'Durham Cascade', by Gregory-Smith et al. (1988)) is selected.

6.1 Durham HPT Cascade

Durham cascade has been used extensively in the past for studying secondary flow loss generation (see Gregory-Smith and Cleak, 1992; Gregory-Smith et al., 1988) and optimization of endwall geometry for loss reduction (see Hartland et al., 2000; Ingram

Table 6.1: Geometrical and flow parameters of Durham cascade

Inlet angle	42.75^0
Blade exit angle	68.7^0
Blade axial chord	181 mm
Pitch	191 mm
Blade half span	200 mm
Reynolds number	4×10^5
Exit Mach number	0.1

Table 6.2: Traverse slot locations

Slot number	Position ($\%C_{ax}$)	Position (mm)
Slot 1	-9	-197
Slot 6	71	-52
Slot 8	97	-5
Slot 10	128	51

et al., 2005), as well as a standard test case for validating turbomachinery CFD methods (see Cleak and Gregory-Smith, 1992; Moore and Gregory-Smith, 1996).

The main parameters of Durham cascade are given in Table 6.1. Durham HPT cascade has a high flow turning angle, approximately 110^0, typical for HPT rotor blades. The large secondary flow developed through the cascade has been comprehensively investigated experimentally, with various measurements, such as velocities, angles and total pressure losses, acquired with a five-hole probe at different traverse slots (see Hartland et al., 2000). The measurement slot locations taken in the present study are given in Table 6.2, where C_{ax} is the axial chord. Figure 6.1 plots the cascade with four traverse slot locations at the axial chord positions of C_{ax} = -9%, 71%, 97% and 128%. The computed results will be compared to the measured data of the experiment from Hartland (2001) at these positions.

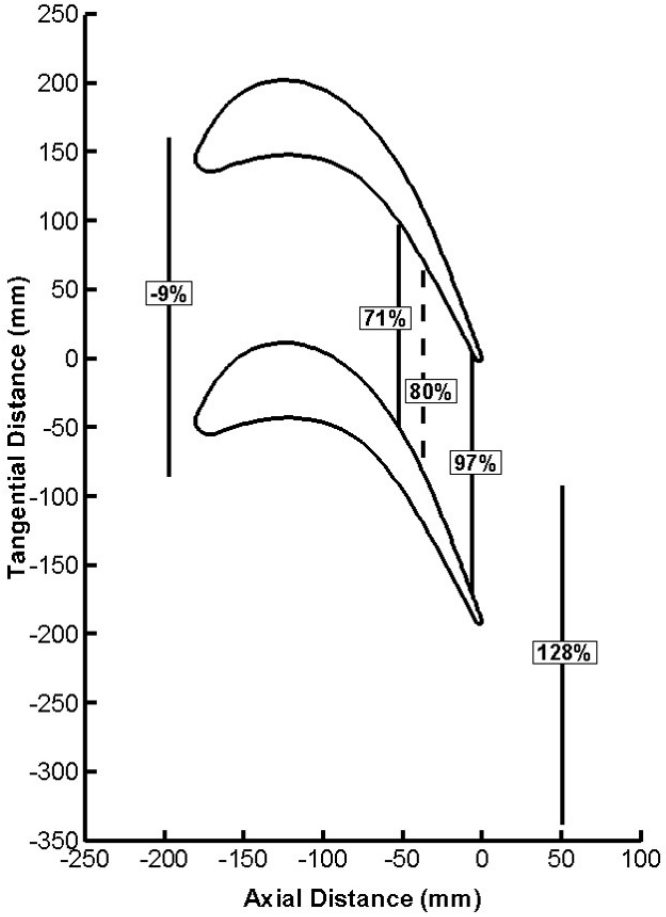


Figure 6.1: Axial positions of measurement for Durham cascade

At the experimental conditions with a Reynolds number of $4x10^5$, the flow in the passage is shown to be transitional subject to a bubble type separation (see Gregory-Smith and Cleak, 1992). The boundary layer at the endwall is largely laminar and transition to turbulent boundary layer occurs on the suction surface near the trailing edge, where a laminar separation bubble in the midspan region has been clearly observed at approximately 80% axial chord on the suction surface (see Cleak and Gregory-Smith, 1992). As indicated in Figure 6.2, the flow region from the leading edge to the 80% C_{ax} in the axial direction and from the 10% span length to the midspan in the radial direction can be assumed to be largely laminar.

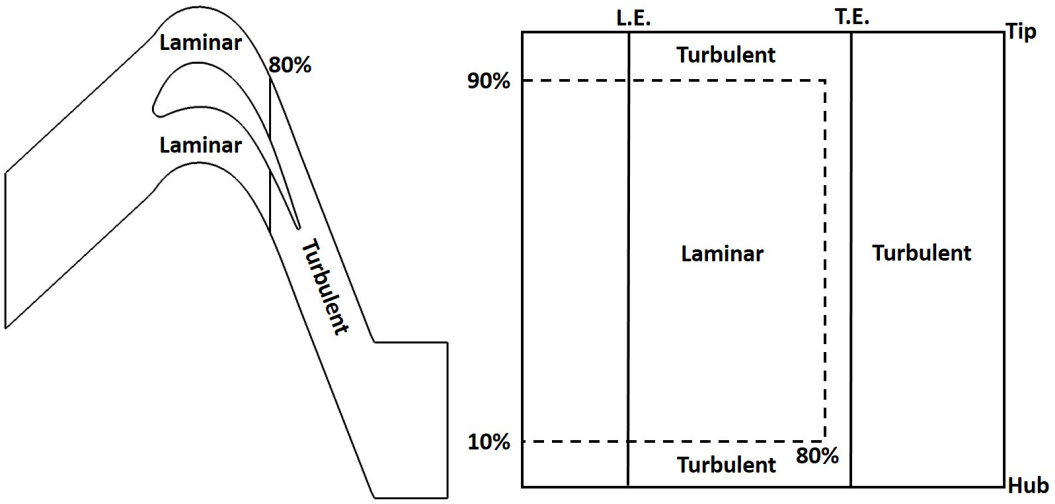


Figure 6.2: Schematic of flow regimes through the blade passage

To predict the secondary flow in this Durham HPT cascade, several turbulence models have been attempted but the transitional flow effects have been shown to be challenging (see Moore and Gregory-Smith, 1996).

6.2 Definition of Secondary Flow Quantities

The secondary velocity at any position in the flow region is obtained by resolving along and normal to the local midspan flow direction at that pitchwise position. Thus, there may be a significant variation across the pitch for the reference midspan yaw angle within the blade (see Ingram, 2003). The secondary velocity U_{sec} is defined by,

$$U_{sec} = \frac{u \sin(\beta - \beta_{mid})}{\cos(\beta)} \tag{6.2.1}$$

where u is the velocity component in the axial direction, β is the yaw angle and β_{mid} is the midspan yaw angle defined by,

$$\beta = \tan^{-1}\left(\frac{u}{v}\right) \tag{6.2.2}$$

where v is the velocity component in the circumferential direction.

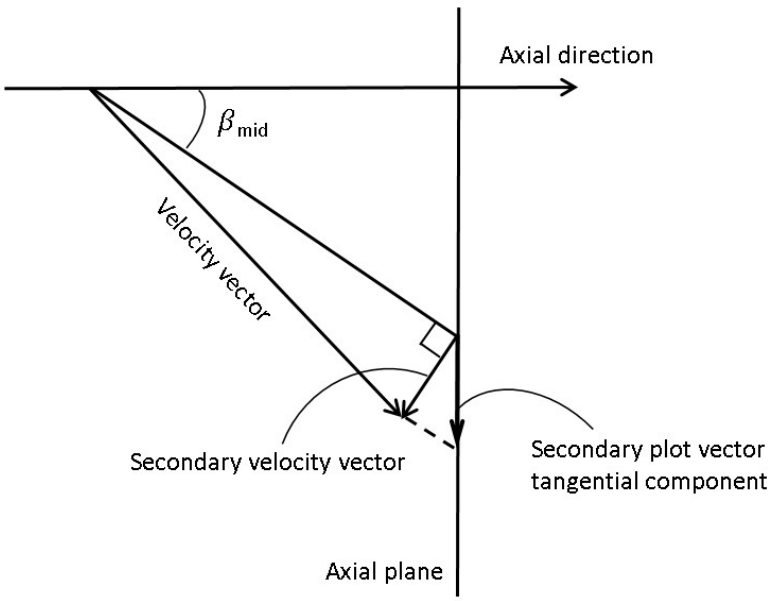


Figure 6.3: Secondary flow vectors

The secondary velocity vector is projected onto the axial plane, as shown in Figure 6.3. For the secondary vector plots that will be presented in the next section, the tangential component of the secondary plot vector is shown in Figure 6.3 and the radial velocity w is the normal component.

In addition, the secondary kinetic energy coefficient C_{ske} is defined by,

$$C_{ske} = \frac{U_{sec}^2 + w^2}{U_{inlet}^2} \tag{6.2.3}$$

where U_{inlet} is the inlet velocity. The total pressure loss coefficient Cp_0 is also defined as,

$$Cp_0 = \frac{p_{0inlet} - p_0}{\frac{1}{2}\rho U_{inlet}^2} \tag{6.2.4}$$

where the p_0 is the total pressure and p_{0inlet} is the inlet total pressure.

Note that the above definitions of the flow quantities and coefficients are consistent with those described by Hartland (2001) and Ingram (2003).

6.3 3D RANS Solution

The present DG solver in the RANS mode has been applied to predict the main flow and secondary losses of the cascade. The numerical simulations of this Durham cascade are conducted in a fully turbulent steady-state manner. In order to match the experimental boundary conditions, the outlet static pressure is gradually adjusted to obtain the required inlet velocity. To achieve the measured inlet boundary layer profile, total pressure variation is specified as the inlet boundary condition. Also, the turbulent working variable $\tilde{\nu}$ at inlet is calculated from the measured turbulence parameters (turbulence intensity and length scale) one axial chord upstream of the blade leading edge. Accordingly, the inlet flow angle is slightly higher than the design value due to the deflection of upstream turbulence, which is set as 43.5^0 in the following DG simulations, in line with that recommended for CFD by Hartland et al. (2000).

As shown in Figure 6.4(a), a 2D blade is firstly made and then extruded in the third direction, approximately only 5×10^4 node points and 3×10^5 tetrahedral cells are generated for RANS simulation of this half-span blade passage with one endwall, where $y^+ < 0.7$ at the blade surface and $z^+ < 0.5$ (the definition of z^+ is the same as that of y^+) at the endwall. In order to obtain the reasonable results of the fully turbulent Durham cascade from the 2nd-order DG1 solution, these first elements y^+ and z^+ are relatively small and locate within viscous sublayer. Note that for the near wall mesh, a mesh spacing ratio normal to the blade surface is chosen as 1.75 and another mesh spacing ratio normal to the endwall is taken as 1.8, which are significantly higher than that typically required for the 2nd-order scheme.

Figure 6.4(b) displays the 3D mesh employed for the Durham cascade, which is a reasonably coarse mesh with a refined wake region downstream of the blade passage.

6.3.1 Traverse Plots

The present RANS simulations for the Durham cascade have been performed up to the 3rd-order of accuracy due to the increased storage requirement for Jacobian matrix in the high-order DG solutions conflicting with the limit of the computer resources. The computed results of secondary vectors and traverse plots for total pressure loss coefficients Cp_0, yaw angles β and secondary kinetic energy coefficients C_{ske}, compared to the measured experiment data at the axial chord position of C_{ax} = -9%, 71%, 97% and 128%, are presented as follows. Note that the 'Experiment' legend shown in the remaining figures of this thesis represents the measured data of the experiment by Hartland (2001).

6.3.1.1 Slot 1: -9% C_{ax}

The comparisons between the computed contour plots and the measured ones of the experiment at plane -9% C_{ax} are shown in Figures 6.5, 6.6, 6.7 and 6.8. Results from both the computed and experimental data clearly reveal that the flow upstream of the blade leading edge is still considerably undisturbed. The computed secondary vectors, total pressure losses and yaw angles show overall good agreement with the experimental data, however, the yaw angles contours in Figure 6.7 indicate that the computed peak moves slightly closer to the suction side. The secondary kinetic energy coefficients from both the DG1 and DG2 solutions are obviously under-predicted when compared to the measured experiment ones, as

seen in Figure 6.8, though the computed coefficients are slightly better predicted when the order of the polynomials increases.

6.3.1.2 Slot 6: 71% C_{ax}

The computed secondary vectors compared to the measured ones at plane 71% C_{ax} are given in Figure 6.9. The passage vortex has been well formed close to the blade suction surface near the endwall and will move further away from the endwall, which has been described in detail by Gregory-Smith et al. (1988). The convection rate and the final position of this passage vortex indicates the strength of the secondary flow (see Hartland et al., 2000). In Figure 6.10, the total pressure loss contours from the present DG solutions match the measured experiment ones relatively well, though the computed loss cores tend to be slightly closer to the endwall. The present computed yaw angles and secondary kinetic energy coefficients are in agreement with the experimental ones, as shown in Figures 6.11 and 6.12 respectively. Overall, the flow fields from the DG2 solutions are better resolved than those from the DG1 solutions.

6.3.1.3 Slot 8: 97% C_{ax}

The comparison between the computational and experimental secondary vectors at plane 97% C_{ax}, just before the trailing edge, is presented in Figure 6.13. Both the computed and measured experiment plots show that the inlet boundary layer further rolls up and forms a strengthened passage vortex away from the endwall. As depicted in Figure 6.14, the total pressure loss cores from the DG1 solutions tend to move slightly closer to the suction surface, whereas the pitchwise location of the loss

cores from the DG2 solutions seem to match the experimental position relatively well. However, both DG1 and DG2 results tend to show the increased intensities of the loss cores with a slight movement toward the endwall. The computed yaw angles and secondary kinetic energy coefficients from the DG1 solutions are slightly under-resolved, as seen in Figures 6.15 and 6.16, but those from the DG2 solutions are better resolved and comparable to the experimental ones. Overall, the peaks of the computational flow parameters are located slightly closer to the blade suction surface compared to those of the experiment. Moreover, the over-predicted total pressure loss cores from the DG solutions tend to be closer to the endwall as well.

6.3.1.4 Slot 10: 128% C_{ax}

The computational secondary vectors at plane 128% C_{ax}, downstream of the trailing edge, compared to the measured data of the experiment are plotted in Figure 6.17. Both the computed and measured secondary vectors show that the passage vortex moves further away from the endwall with a counter vortex located above it (closer to the suction surface), which seems to be a shedding vortex initiated from the trailing edge of the blade (see Hartland et al., 2000). Furthermore, a small counter vortex is also observed in a crossflow region near the endwall. As shown in Figure 6.18, the double loss peaks in the loss cores are not well captured by the DG1 solutions, while the DG2 solutions distinctly predict the double loss peaks as well as the small counter vortex close to the endwall. However, both the DG1 and DG2 solutions have markedly over-predicted the intensities of the loss cores and shown a slight movement toward the suction side as well as the endwall. In Figure 6.19, the flow yaw angles from the DG2 solutions agree quite well with the measured experiment

ones, especially around the peak region, where the flow features from the DG1 solutions are considerably under-resolved. Similarly, the computed peak tends to move slightly closer to the endwall compared to that of the experiment. In Figure 6.20, the secondary kinetic energy coefficients from the DG1 solutions show a clear under-prediction of both the main features and the peak compared to the measured ones of the experiment, whereas the DG2 solutions capture the main features well and reasonably predict the peak. Overall, the computed loss cores downstream of the trailing edge are significantly over-predicted by the present DG solutions, though the computed flow fields show an enhanced resolution with increased order of accuracy. In addition, the positions of flow peaks are located further closer to both the suction surface and the endwall.

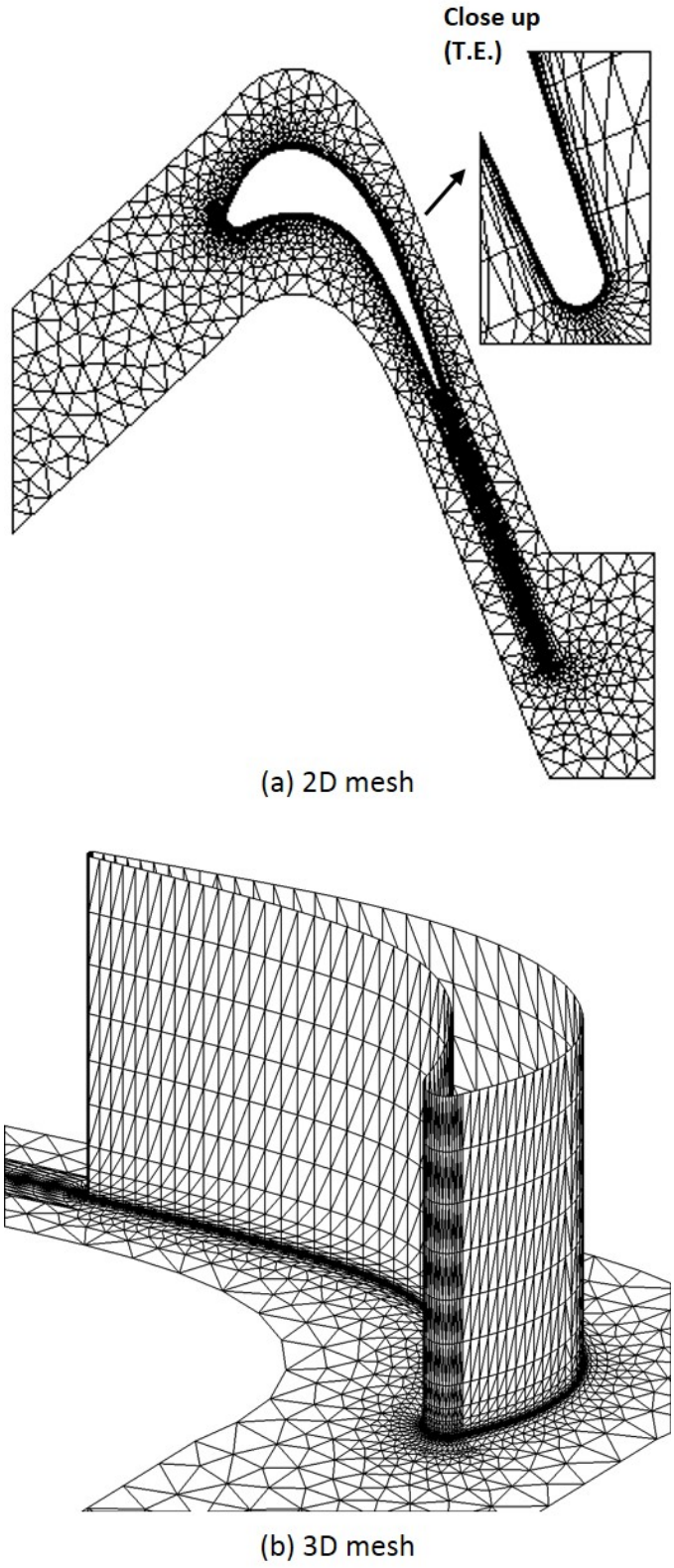


Figure 6.4: Mesh for RANS simulations

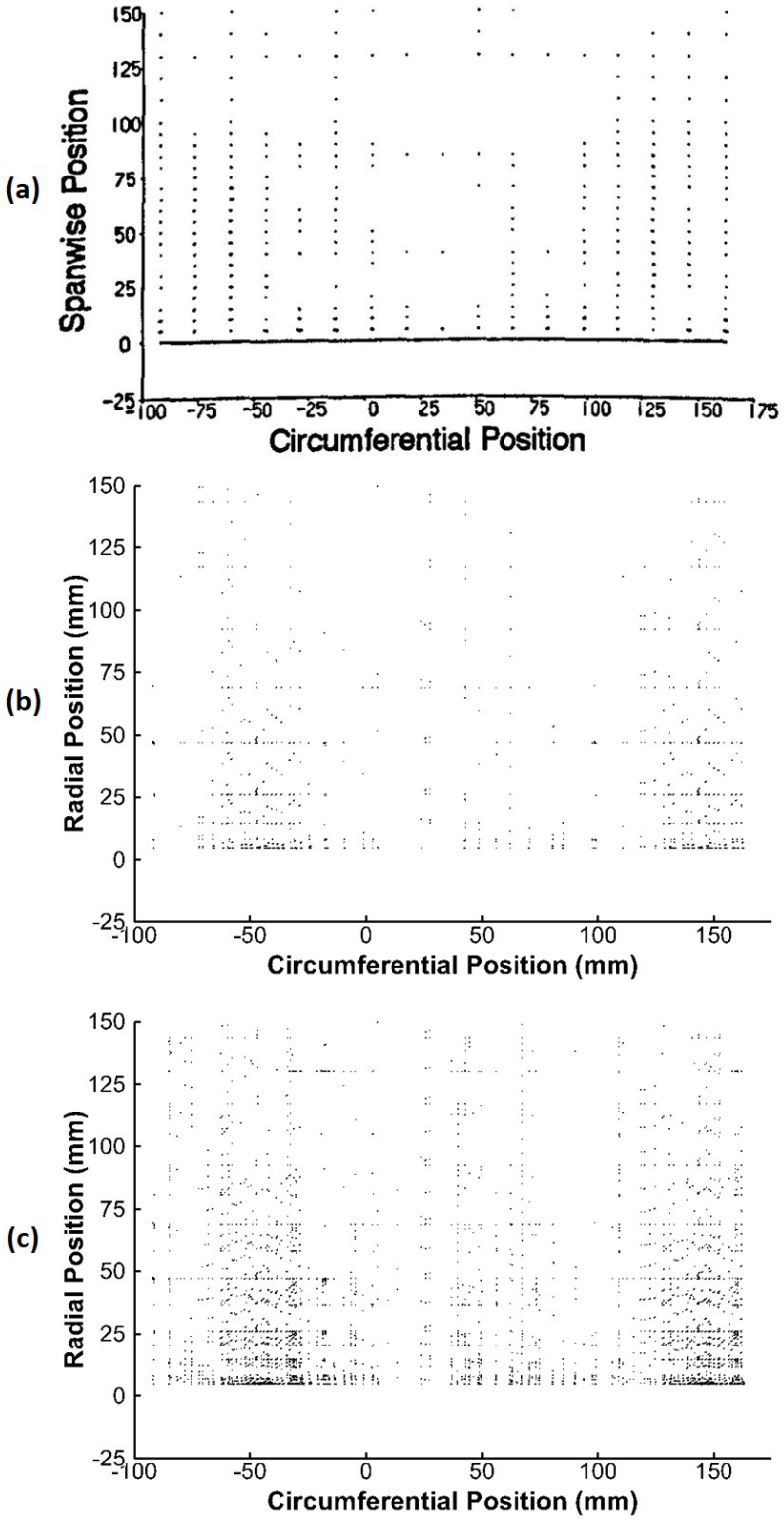


Figure 6.5: Secondary vectors at axial chord position of C_{ax}=-9% (a) Experiment by Hartland (2001); (b) RANS DG1; (c) RANS DG2

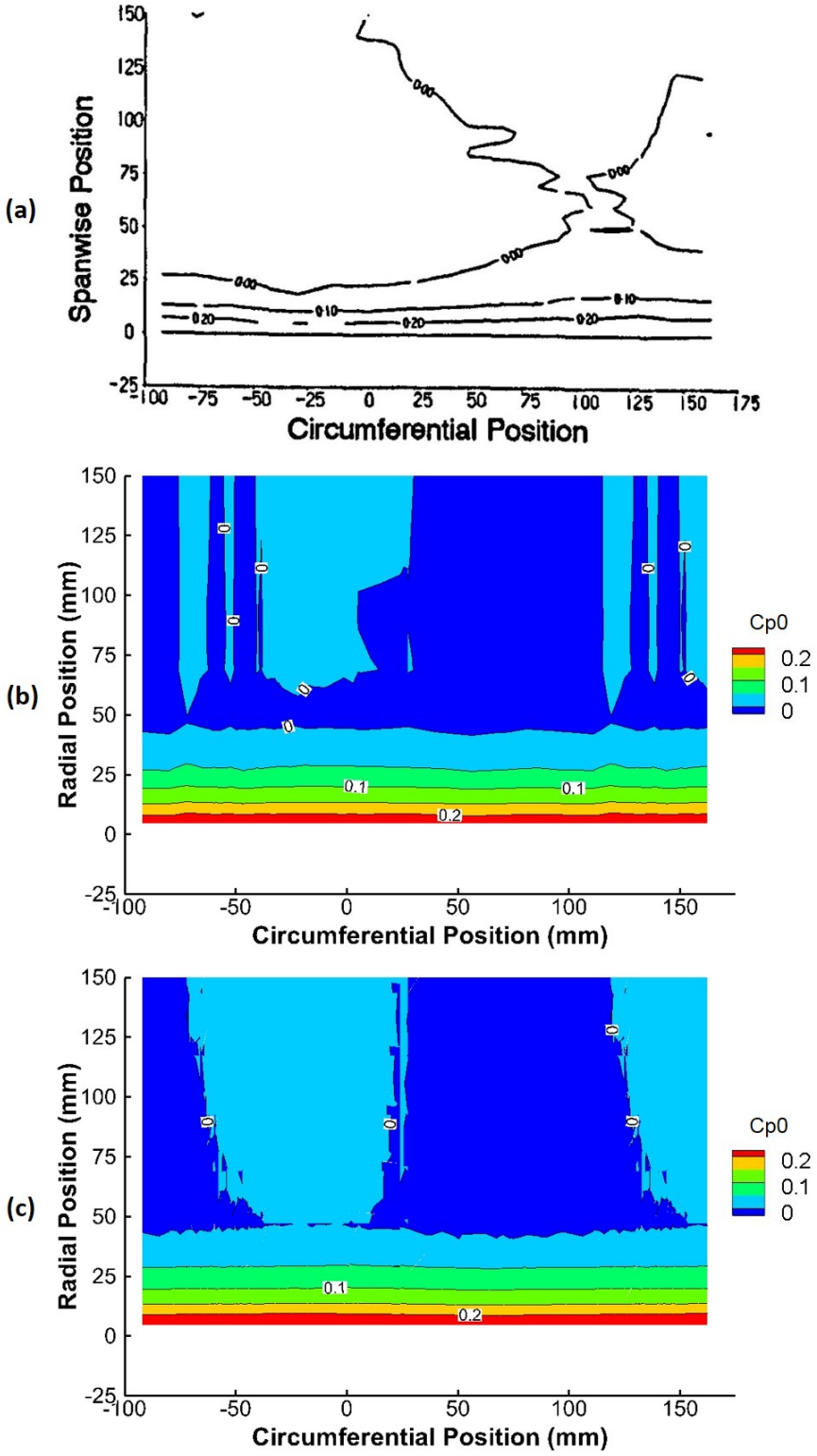


Figure 6.6: Total pressure loss coefficient contours at axial chord position of C_{ax}=-9% (a) Experiment by Hartland (2001); (b) RANS DG1; (c) RANS DG2

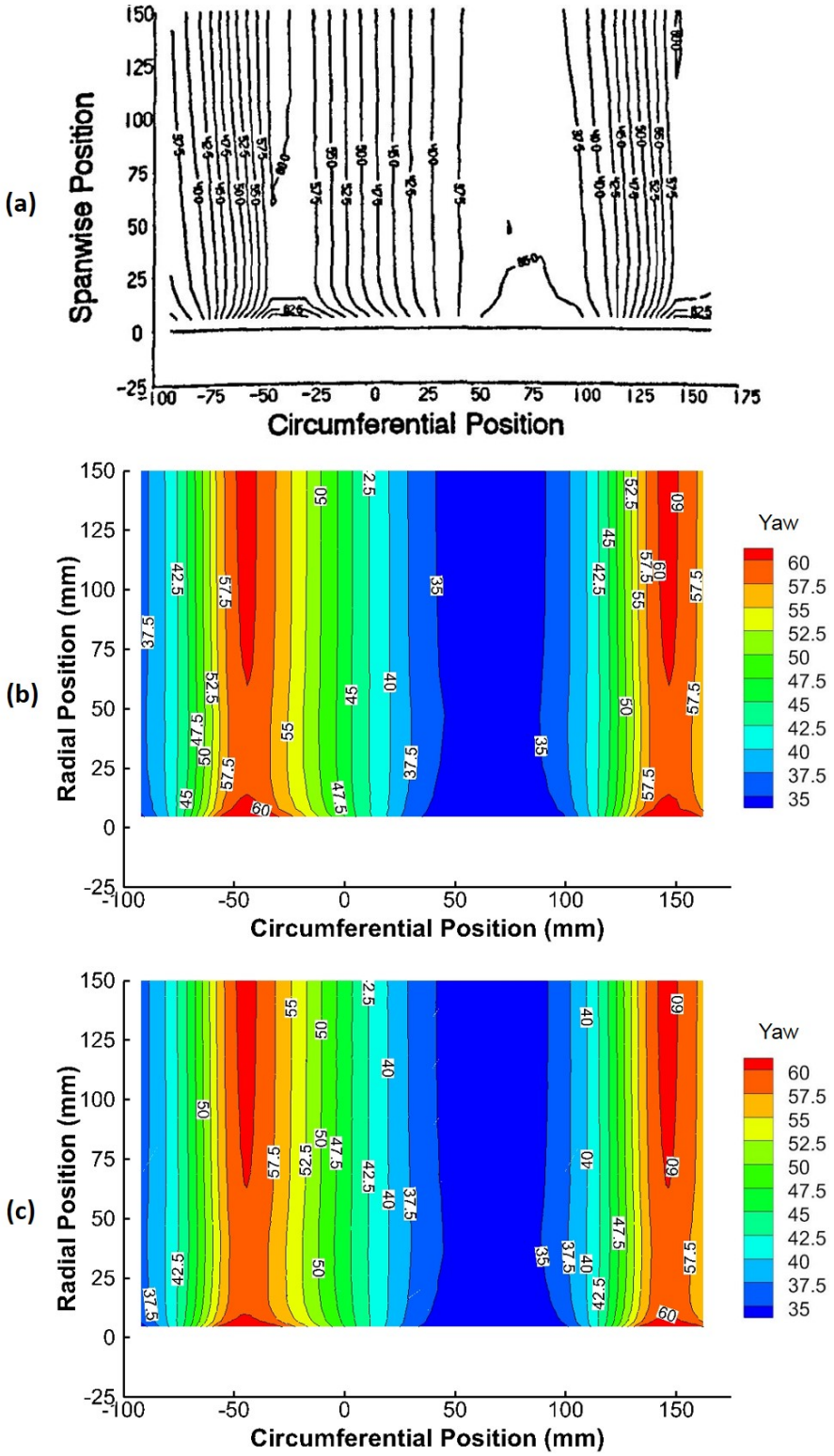


Figure 6.7: Yaw angles contours at axial chord position of C_{ax}=-9% (a) Experiment by Hartland (2001); (b) RANS DG1; (c) RANS DG2

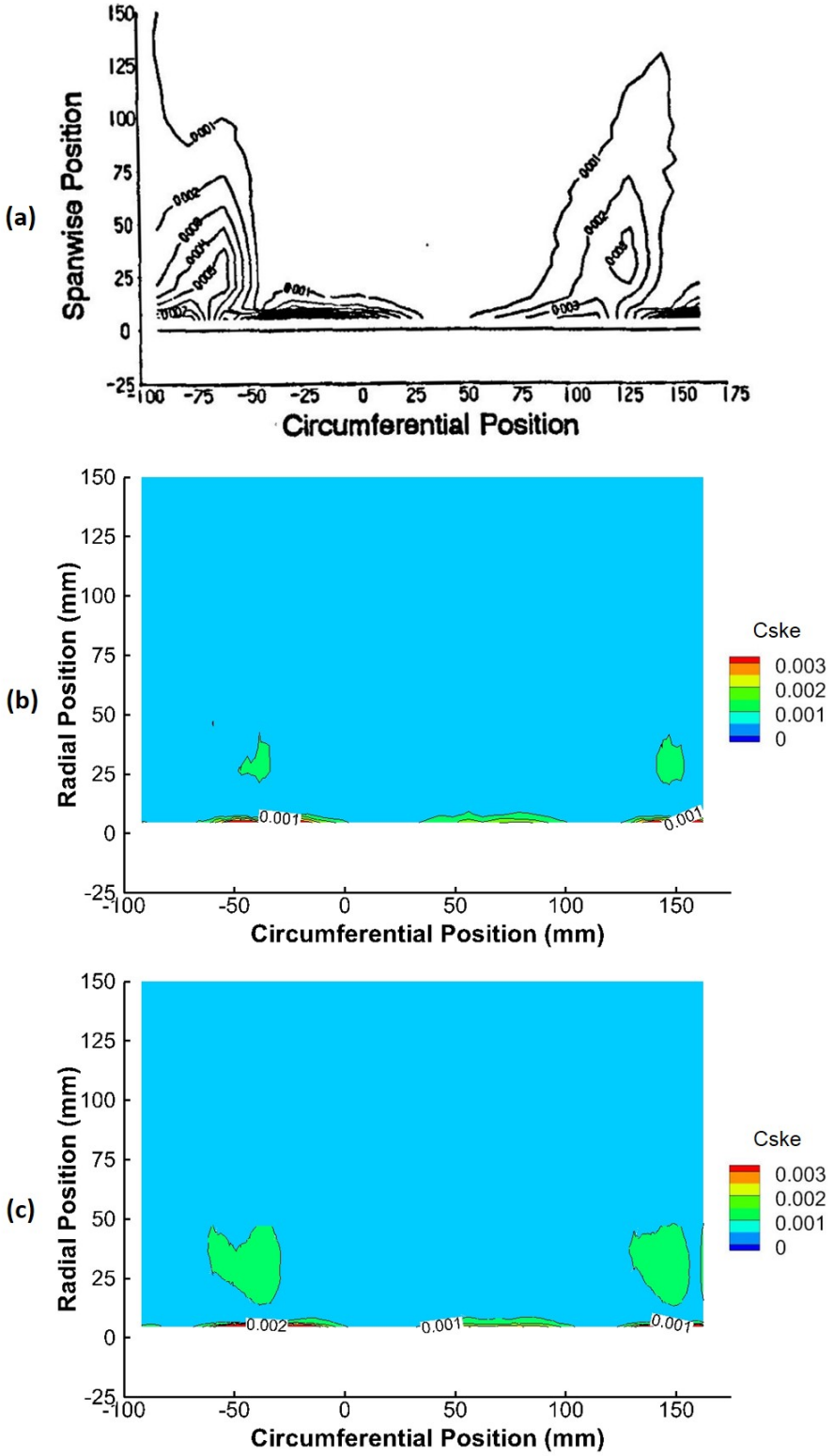


Figure 6.8: Secondary kinetic energy coefficient contours at axial chord position of C_{ax}=-9% (a) Experiment by Hartland (2001); (b) RANS DG1; (c) RANS DG2

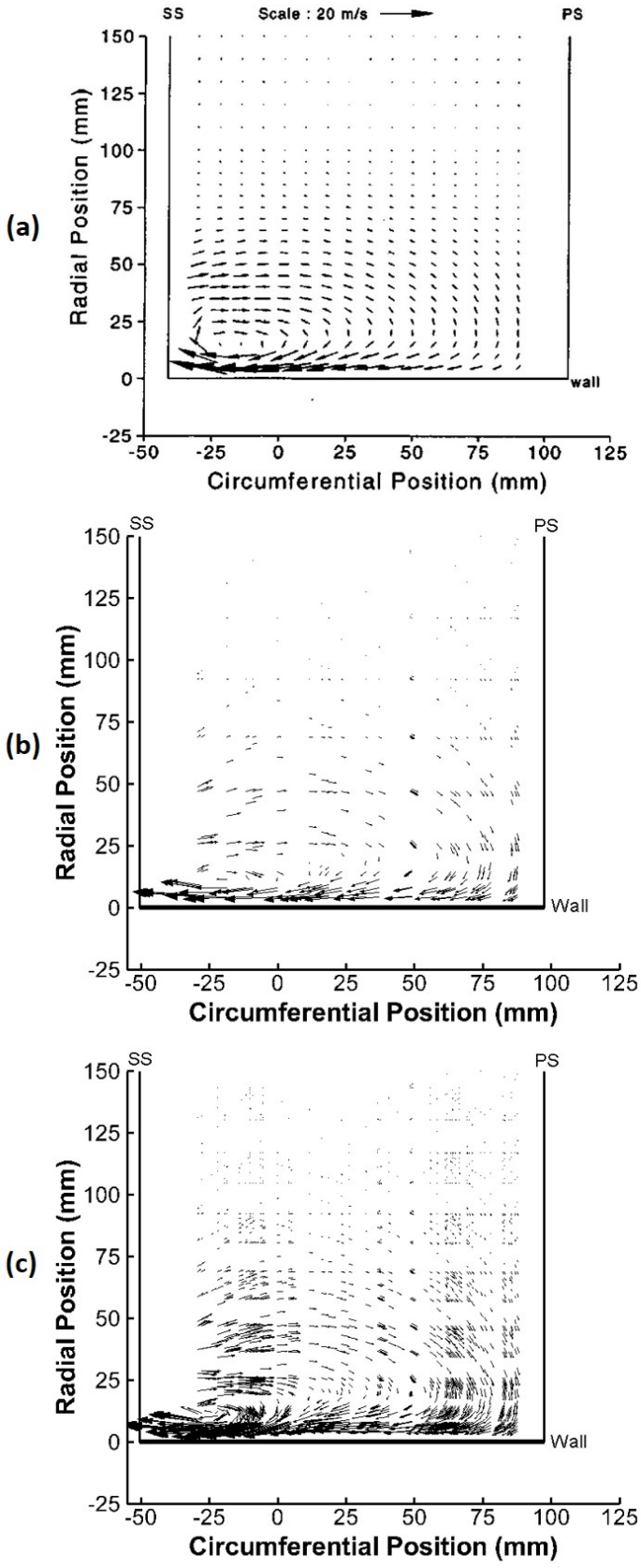


Figure 6.9: Secondary vectors at axial chord position of C_{ax}=71% (a) Experiment by Hartland et al. (2000); (b) RANS DG1; (c) RANS DG2

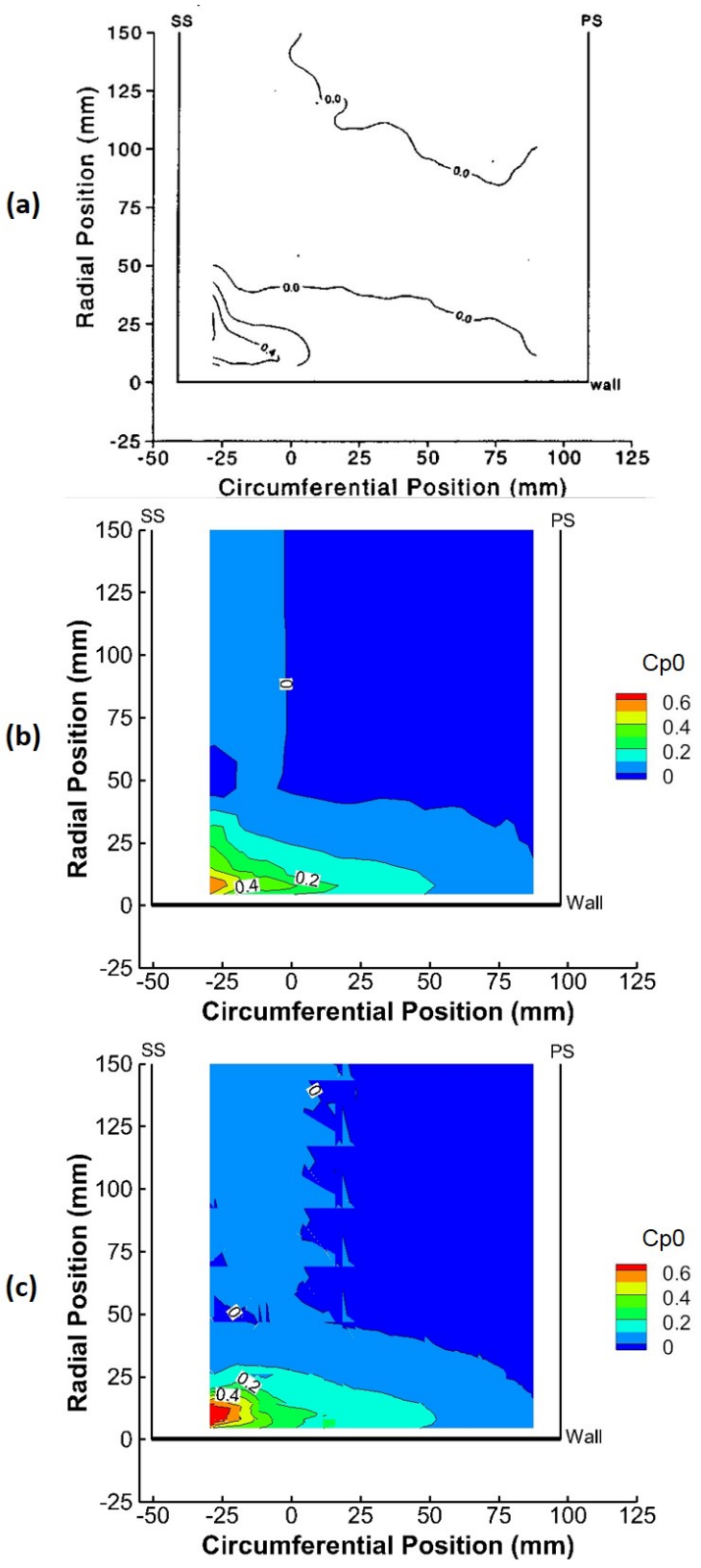


Figure 6.10: Total pressure loss coefficient contours at axial chord position of C_{ax}=71% (a) Experiment by Hartland et al. (2000); (b) RANS DG1; (c) RANS DG2

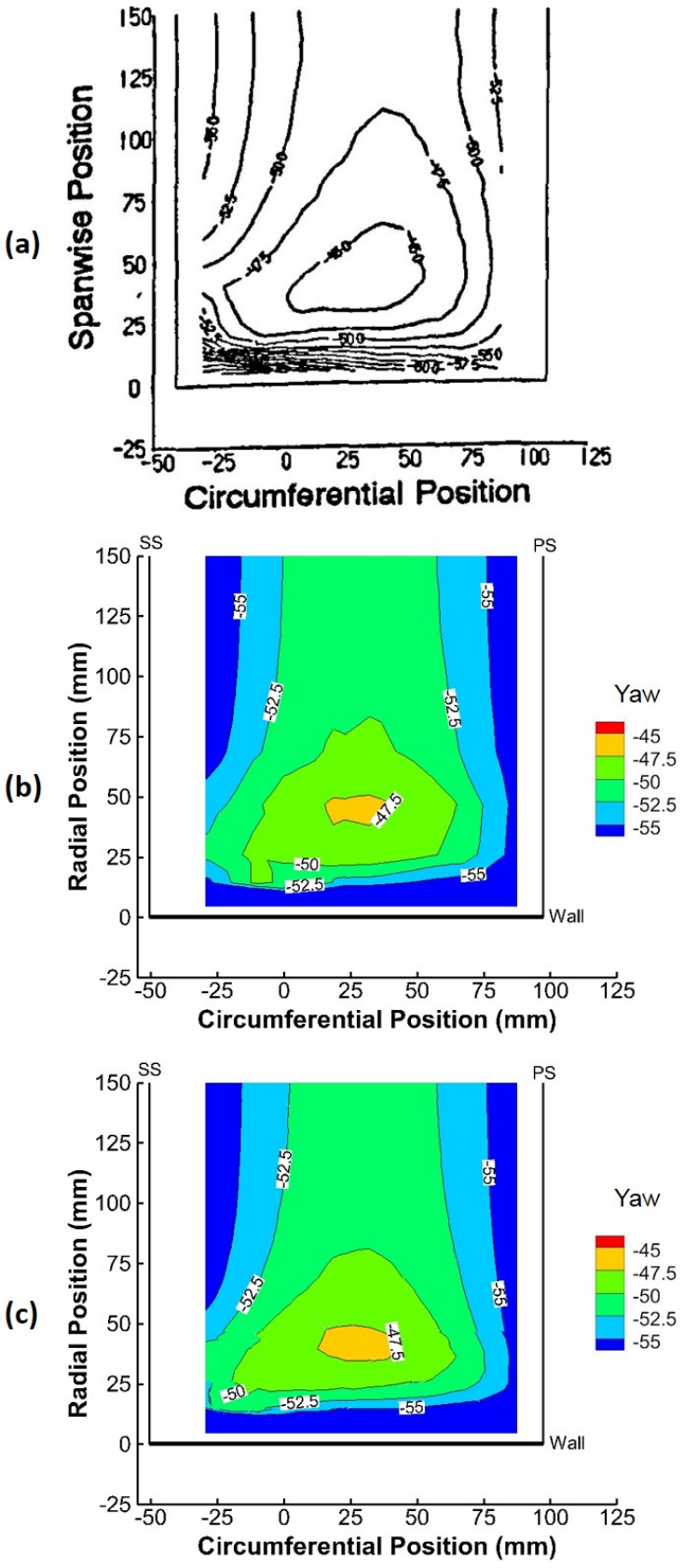


Figure 6.11: Yaw angles contours at axial chord position of C_{ax}=71% (a) Experiment by Hartland (2001); (b) RANS DG1; (c) RANS DG2

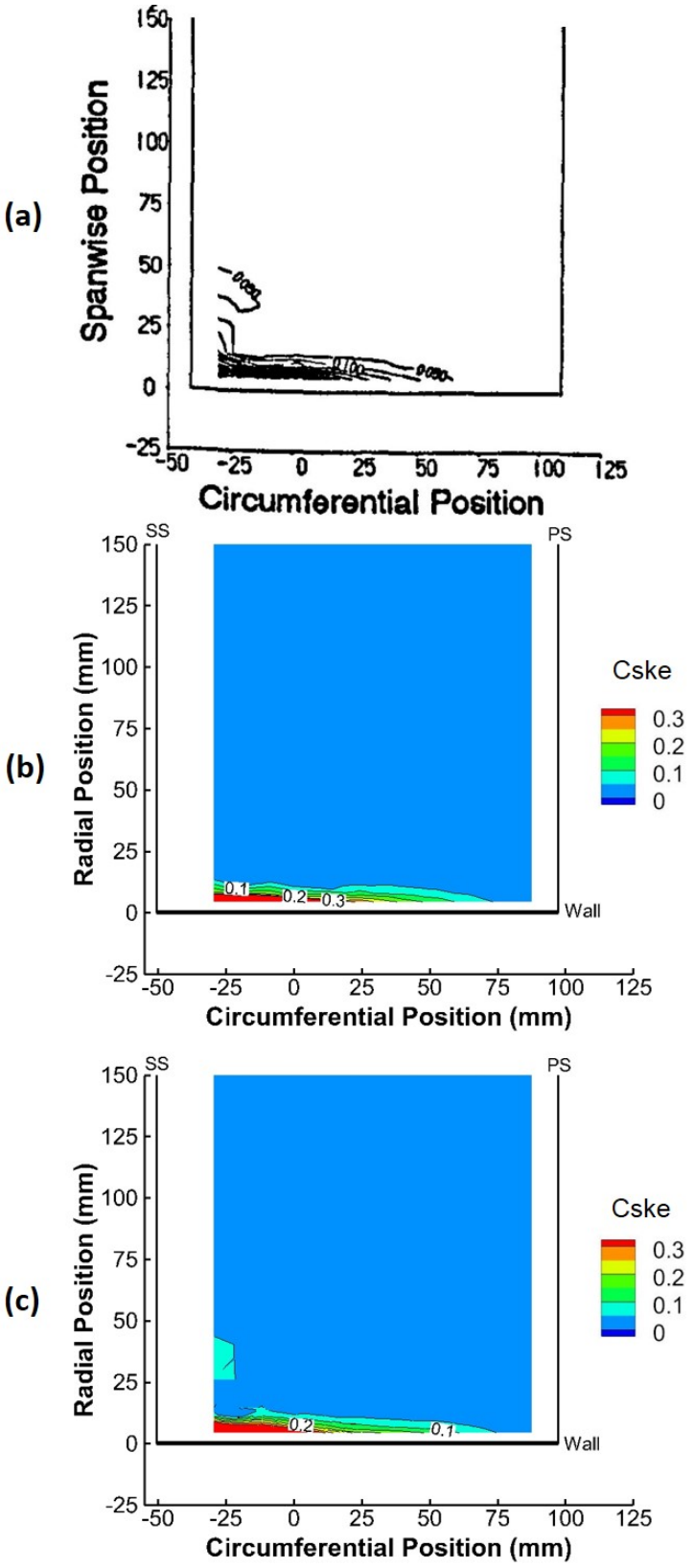


Figure 6.12: Secondary kinetic energy coefficient contours at axial chord position of C_{ax}=71% (a) Experiment by Hartland (2001); (b) RANS DG1; (c) RANS DG2

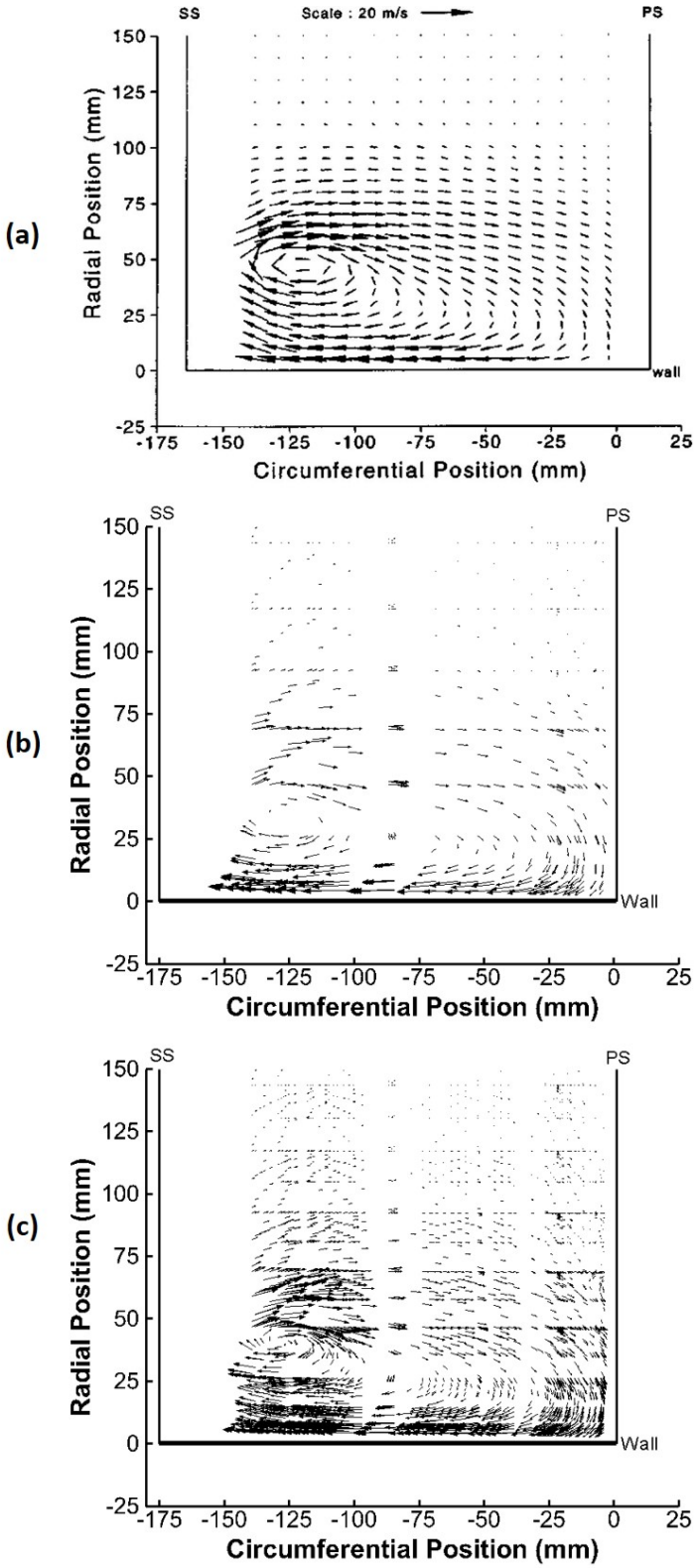


Figure 6.13: Secondary vectors at axial chord position of C_{ax}=97% (a) Experiment by Hartland et al. (2000); (b) RANS DG1; (c) RANS DG2

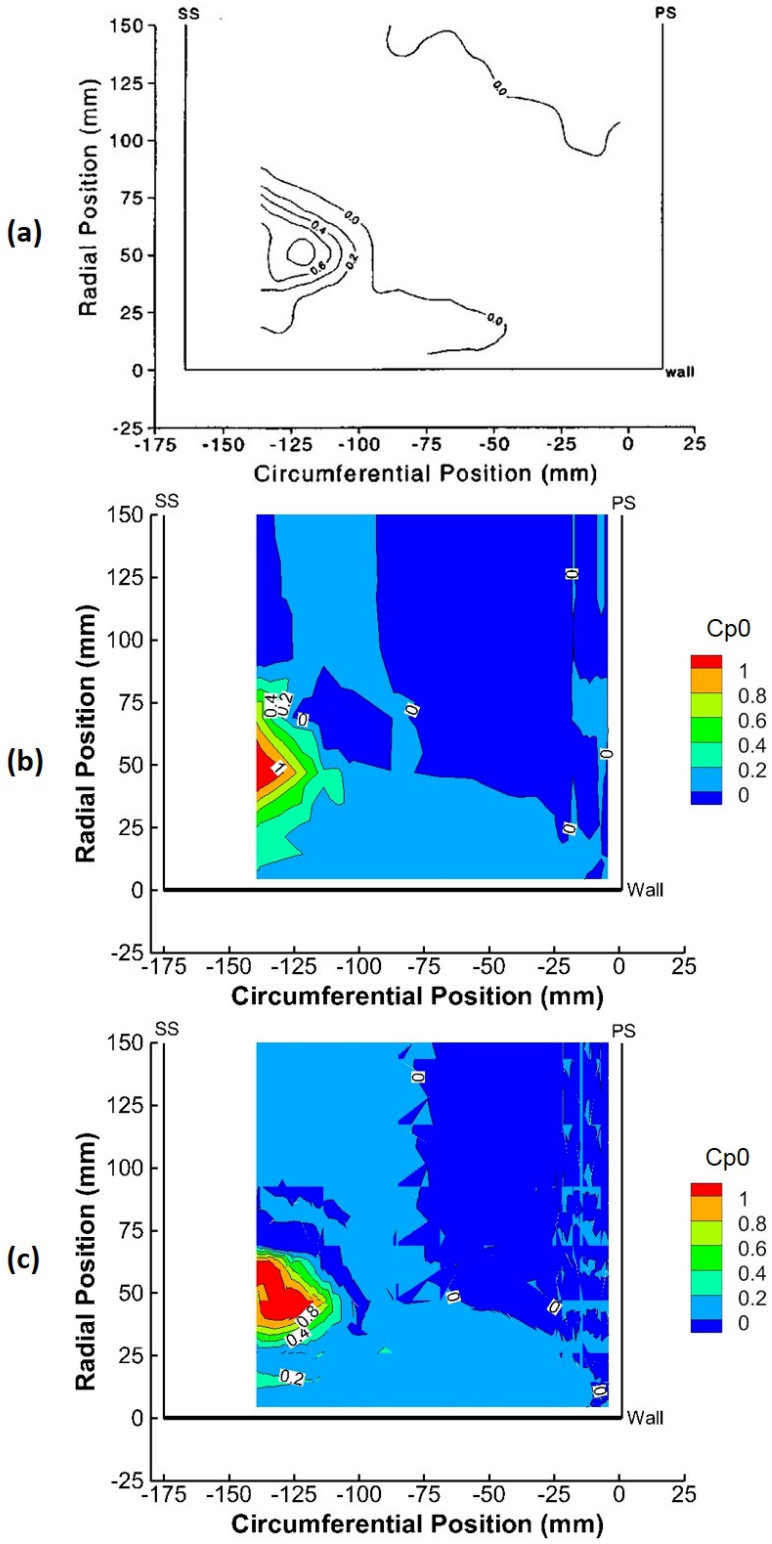


Figure 6.14: Total pressure loss coefficient contours at axial chord position of C_{ax}=97% (a) Experiment by Hartland et al. (2000); (b) RANS DG1; (c) RANS DG2

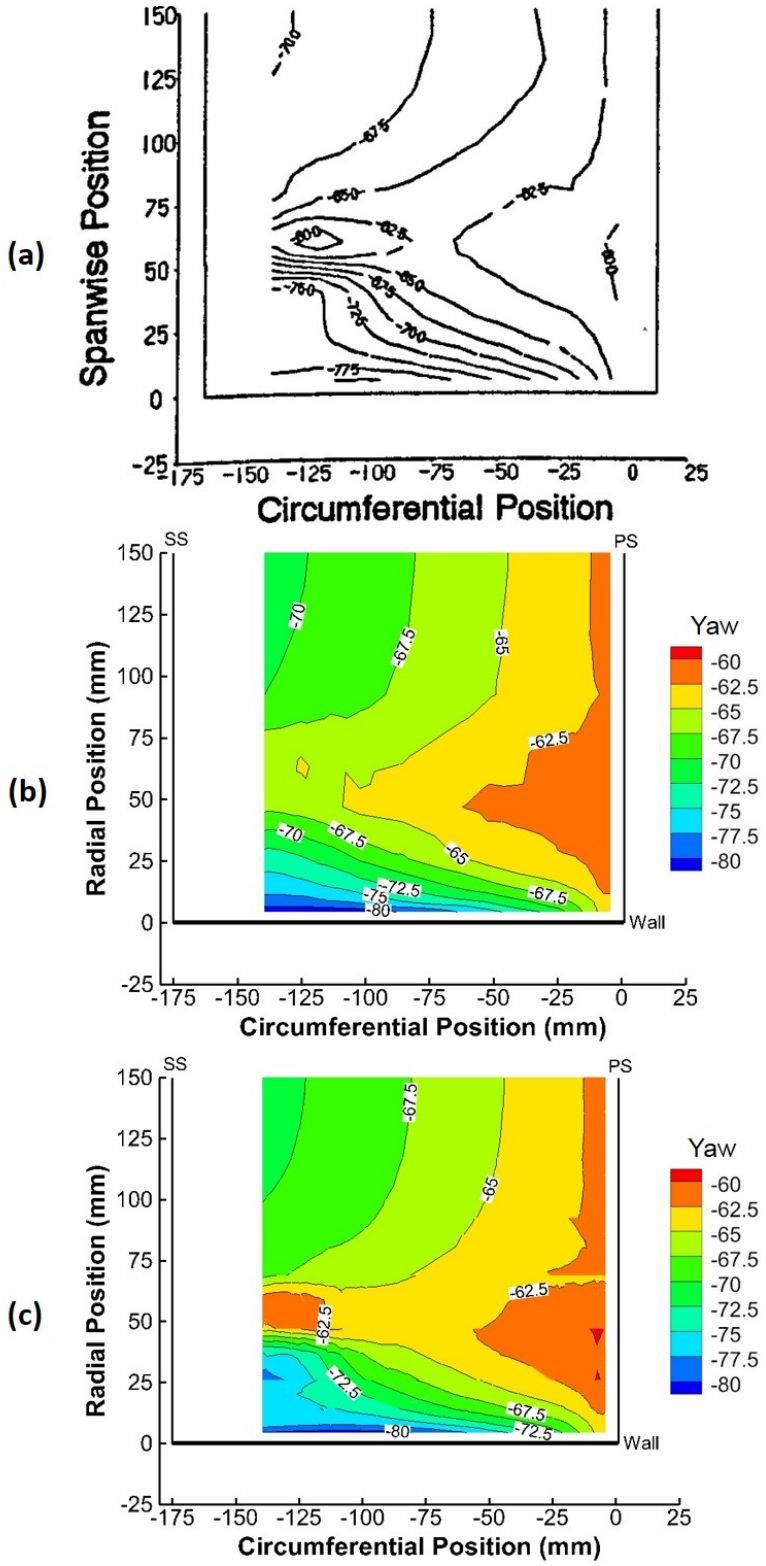


Figure 6.15: Yaw angles contours at axial chord position of C_{ax}=97% (a) Experiment by Hartland (2001); (b) RANS DG1; (c) RANS DG2

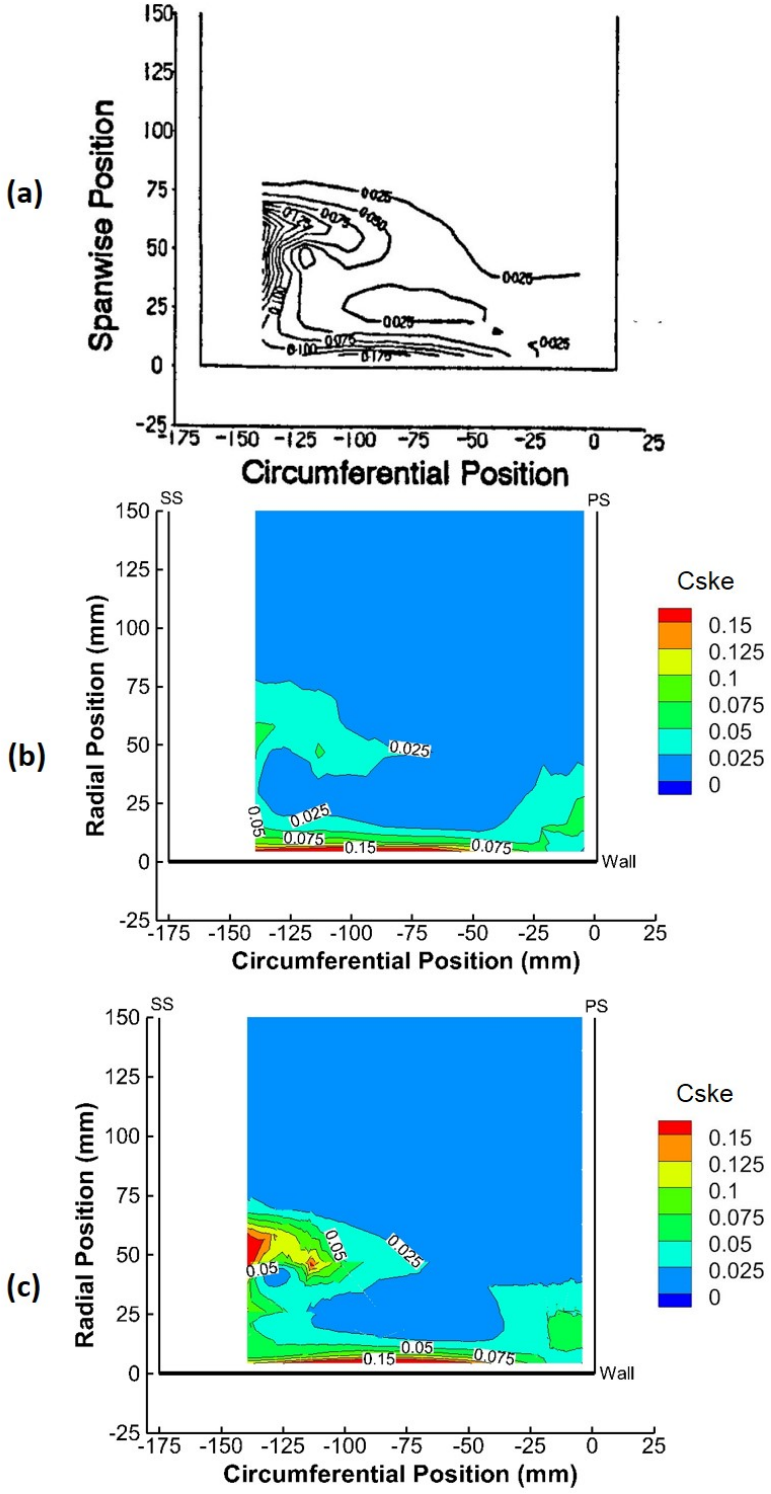


Figure 6.16: Secondary kinetic energy coefficient contours at axial chord position of C_{ax}=97% (a) Experiment by Hartland (2001); (b) RANS DG1; (c) RANS DG2

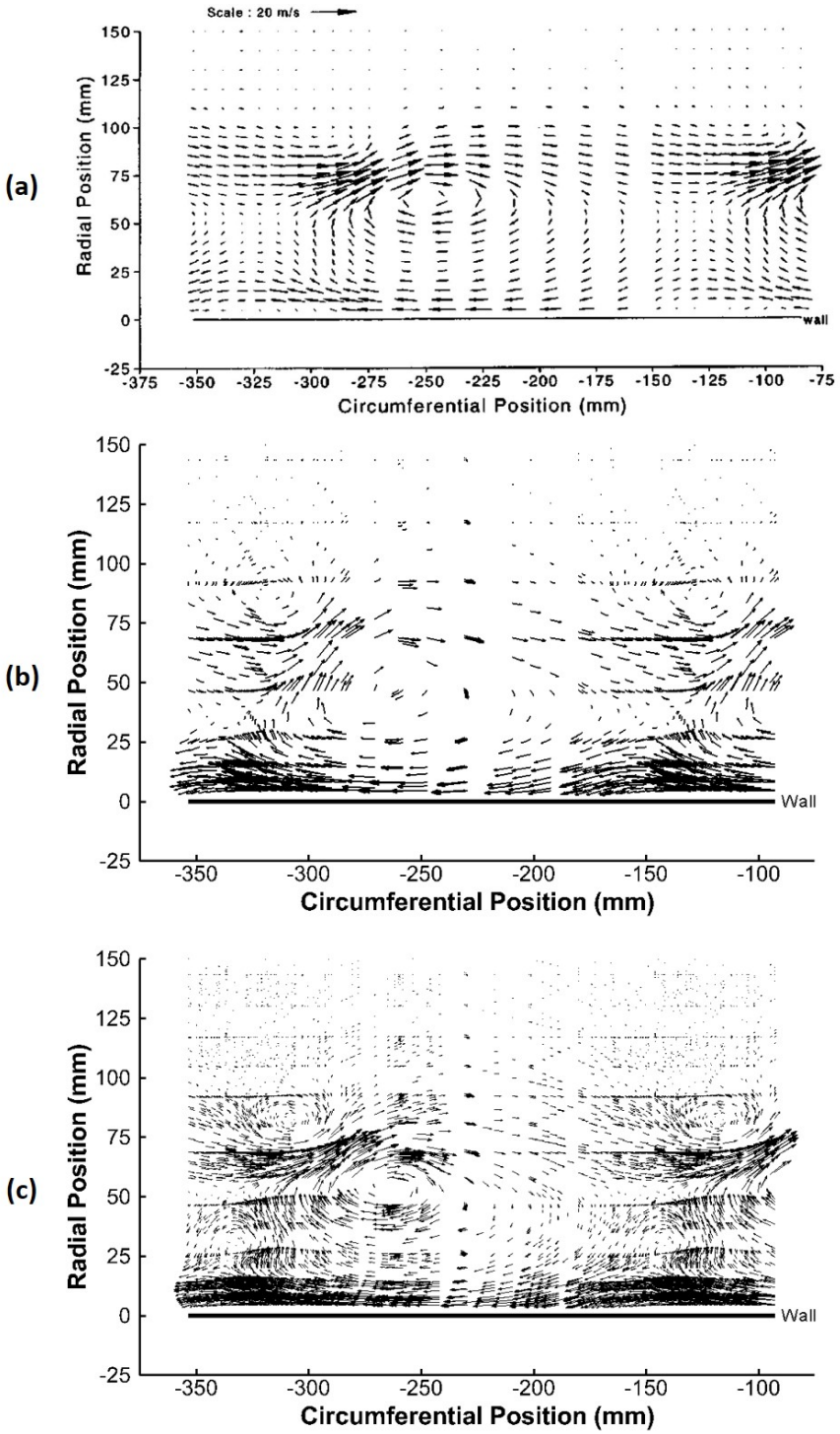


Figure 6.17: Secondary vectors at axial chord position of C_{ax}=128% (a) Experiment by Hartland et al. (2000); (b) RANS DG1; (c) RANS DG2

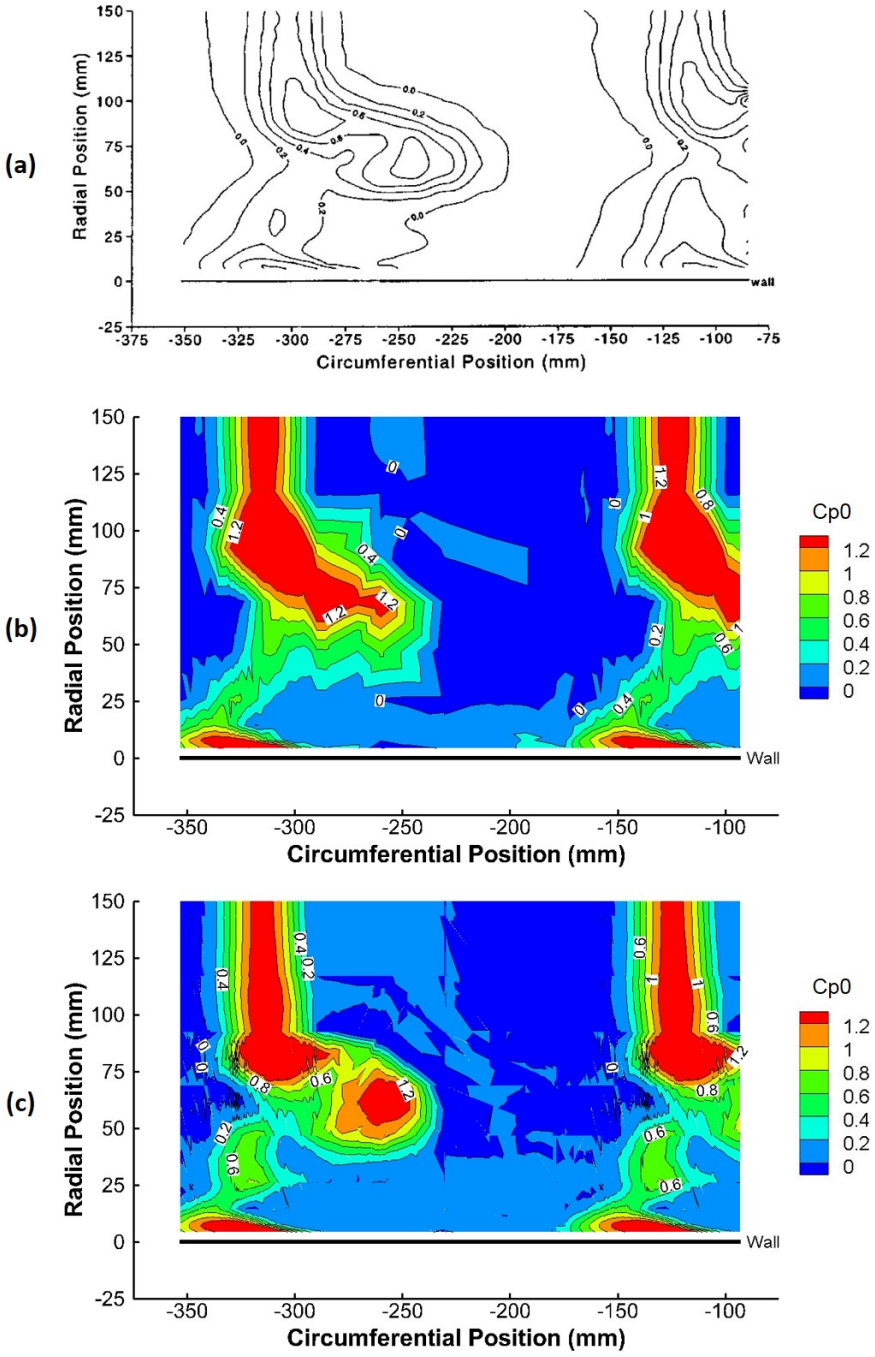


Figure 6.18: Total pressure loss coefficient contours at axial chord position of C_{ax}=128% (a) Experiment by Hartland et al. (2000); (b) RANS DG1; (c) RANS DG2

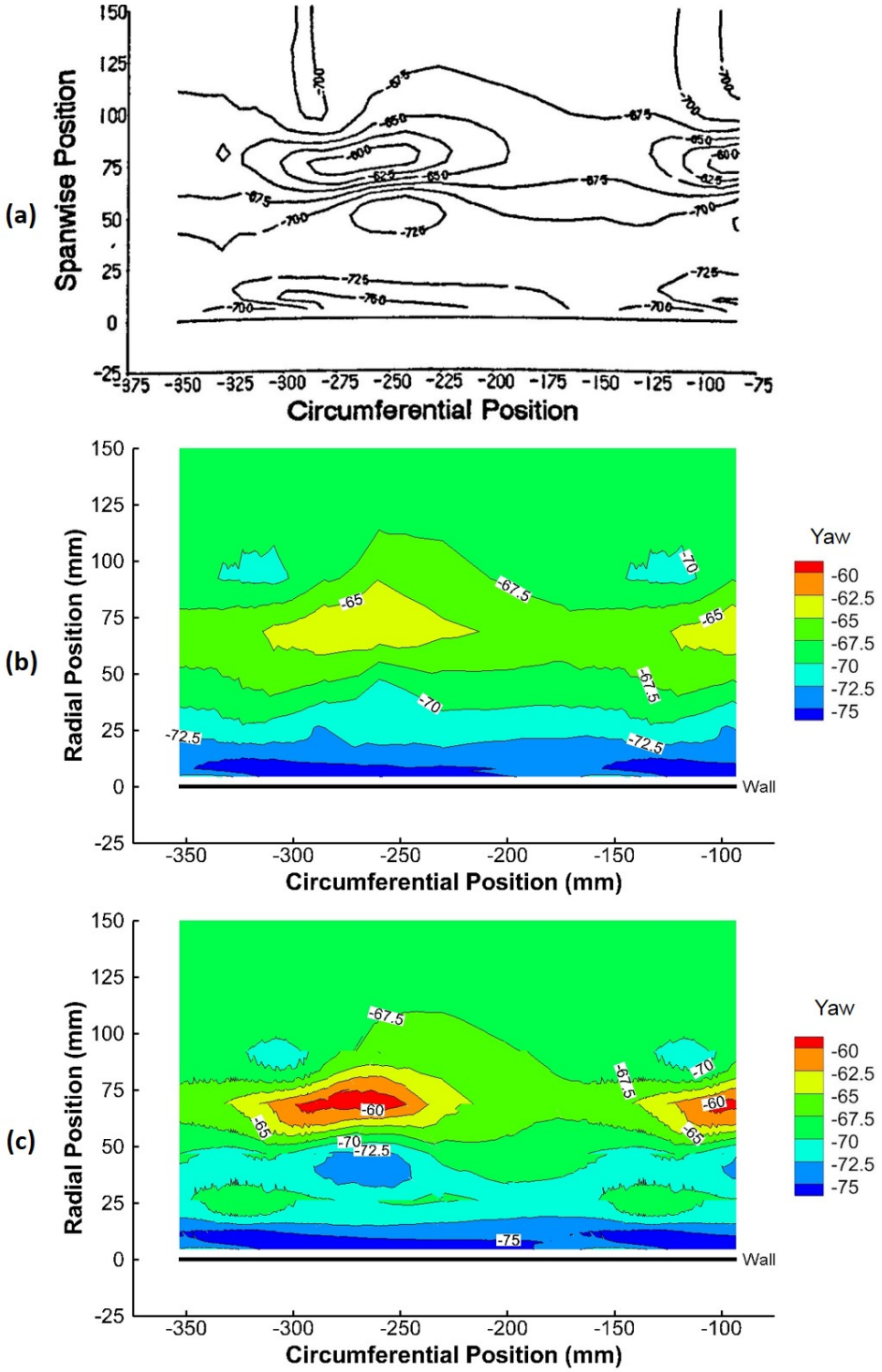


Figure 6.19: Yaw angles contours at axial chord position of C_{ax}=128% (a) Experiment by Hartland (2001); (b) RANS DG1; (c) RANS DG2

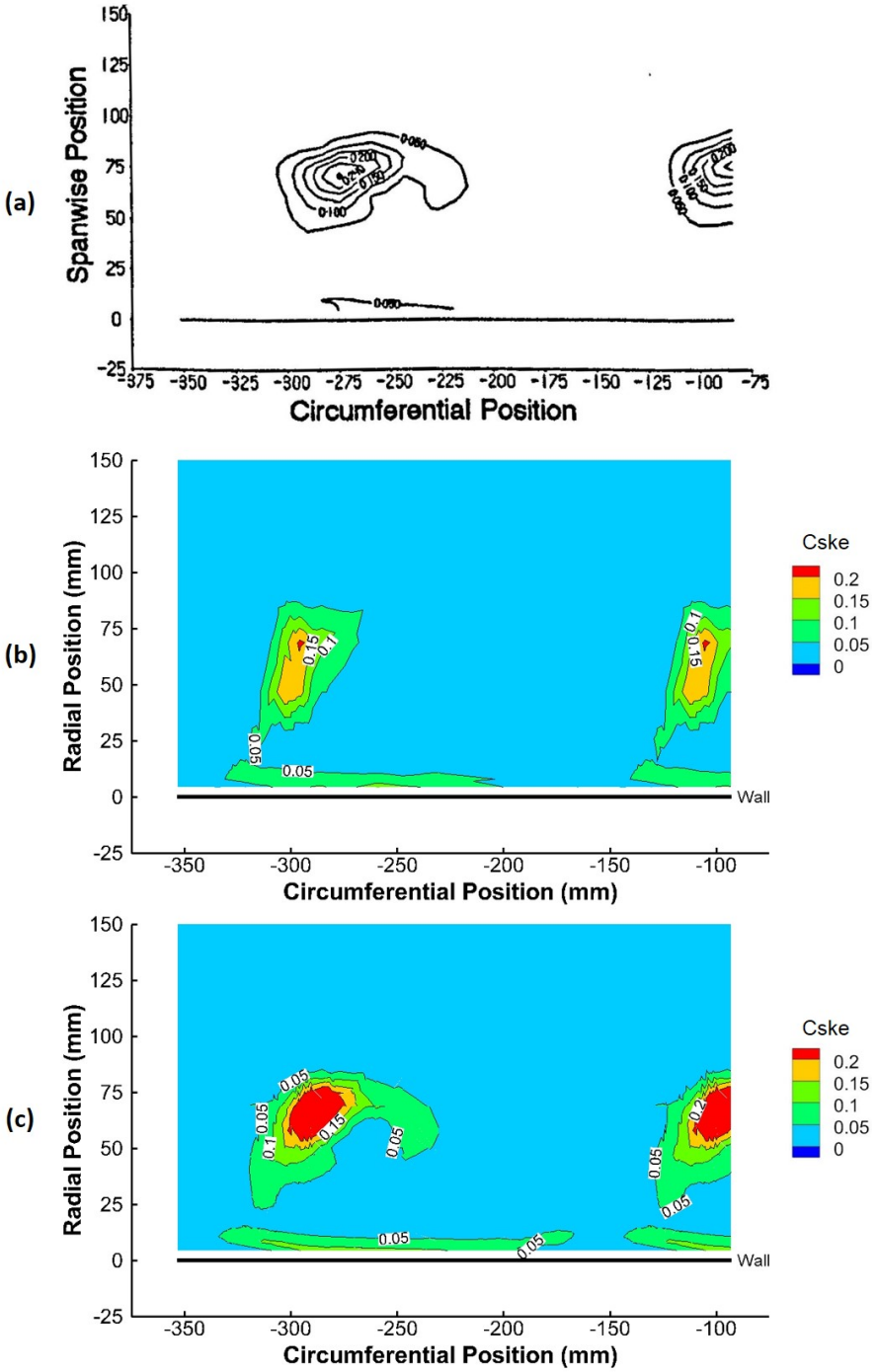


Figure 6.20: Secondary kinetic energy coefficient contours at axial chord position of C_{ax}=128% (a) Experiment by Hartland (2001); (b) RANS DG1; (c) RANS DG2

6.3.2 Pitch-Averaged Results

This section provides more detailed comparisons by means of the pitchwise mass-averaged flow performance parameters. The pitchwise mass-averaged results from both the computed and experimental data (see Hartland, 2001) at four axial chord positions of C_{ax}= -9%, 71%, 97% and 128% are presented in this section.

6.3.2.1 Slot 1: -9% C_{ax}

The pitchwise mass-averaged total pressure loss coefficients Cp_0, yaw angles β and secondary kinetic energy coefficients C_{ske} at plane -9% C_{ax} are plotted in Figures 6.21(a), 6.21(b) and 6.21(c), respectively. In Figure 6.21(a), there is no negative loss predicted by the computed solutions, since the negative loss found in the measured boundary layer profile of the experiment by Hartland (2001) has not been modelled in the present RANS simulations. As shown in Figure 6.21(b), the pitch-averaged yaw angles from the DG solutions agree quite well with the measured experiment ones, though slightly higher inflow angles are predicted near the endwall. The pitch-averaged secondary kinetic energy coefficients are obviously under-predicted by the computed solutions as presented in Figure 6.21(c). Overall, the agreement between the DG1 and the DG2 solutions shows a reasonable order of accuracy convergence.

6.3.2.2 Slot 6: 71% C_{ax}

The pitch-averaged total pressure loss coefficients are presented Figure 6.22(a). It is clearly indicated that the passage vortex loss cores predicted by the DG solutions are closer to the endwall, in line with the conclusions made for the traverse plots at

plane 71% C_{ax} in the previous section. In Figure 6.22(b), despite the slightly higher overturning of the flow near the midspan that is predicted by the DG solutions, a good agreement between the computed and experimental flow angles near the endwall is obtained. The pitch-averaged secondary kinetic energy coefficients from the DG solutions show overall good agreement with the measured ones of the experiment, as presented in Figure 6.22(c).

6.3.2.3 Slot 8: 97% C_{ax}

Figure 6.23(a) shows the overall increased pitch-averaged losses since the passage vortex are further strengthened, compared to the losses at plane 71% C_{ax} as presented in Figure 6.22(a). Though the loss peak from the DG solutions is considerably over-predicted and moves further closer to the endwall compared to that of the measured one, the DG results show an agreement with the experimental data in terms of the shape of the spanwise variation of the loss. The pitch-averaged yaw angles are presented in Figure 6.23(b), where the predicted peak moves toward the endwall by about 10mm and shows a reduction in the overturning compared to the experimental one. As shown in Figure 6.23(c), the computed DG solutions give much less secondary kinetic energy coefficients compared to the experimental data by Hartland (2001), but show reasonable agreement with the measured data by Moore (1995) near the endwall. Note that the reason for the distinctive differences between those two experimental data is not clearly known. These differences among the computed and experimental results might be attributed to the different pitchwise ranges taken for averaging.

6.3.2.4 Slot 10: 128% C_{ax}

The loss peak from the present DG solutions is clearly over-predicted, as given in Figure 6.24(a), and the computed values of the midspan losses are nearly twice than those of the experiment, which is consistent with previous RANS predictions by Moore and Gregory-Smith (1996) and Kiran and Anish (2017). The pitch-averaged yaw angles are presented in Figure 6.24(b), where a small deduction of the overturning is predicted and the computed peak moves slightly inward by about 10mm, consistent with the movement observed at plane 71% C_{ax}. In addition, the trends of the pitch-averaged yaw angles along the span from the DG2 solutions agree fairly well with that of the experiment. The peak of pitch-averaged secondary kinetic energy coefficient from the DG1 solutions is clearly under-predicted, as displayed in Figure 6.24(c), whereas that from the DG2 solutions show an improved prediction.

Table 6.3: RANS overall mass-averaged Cp_0 and C_{ske} at planes 97% and 128% C_{ax}

	97% C_{ax}		128% C_{ax}	
	Cp_0	C_{ske}	Cp_0	C_{ske}
DG1	0.036	0.0107	0.257	0.0145
DG2	0.041	0.0131	0.245	0.0177
Experiment	0.006	0.0115	0.136	0.0192

The overall mass-averaged total pressure loss coefficients Cp_0 and the secondary energy coefficients C_{ske} at planes 97% and 128% C_{ax} are presented in Table 6.3. Clearly the agreement between the DG1 and the DG2 solutions shows a reasonable order of accuracy convergence, and both show a clear over-prediction of overall flow losses.

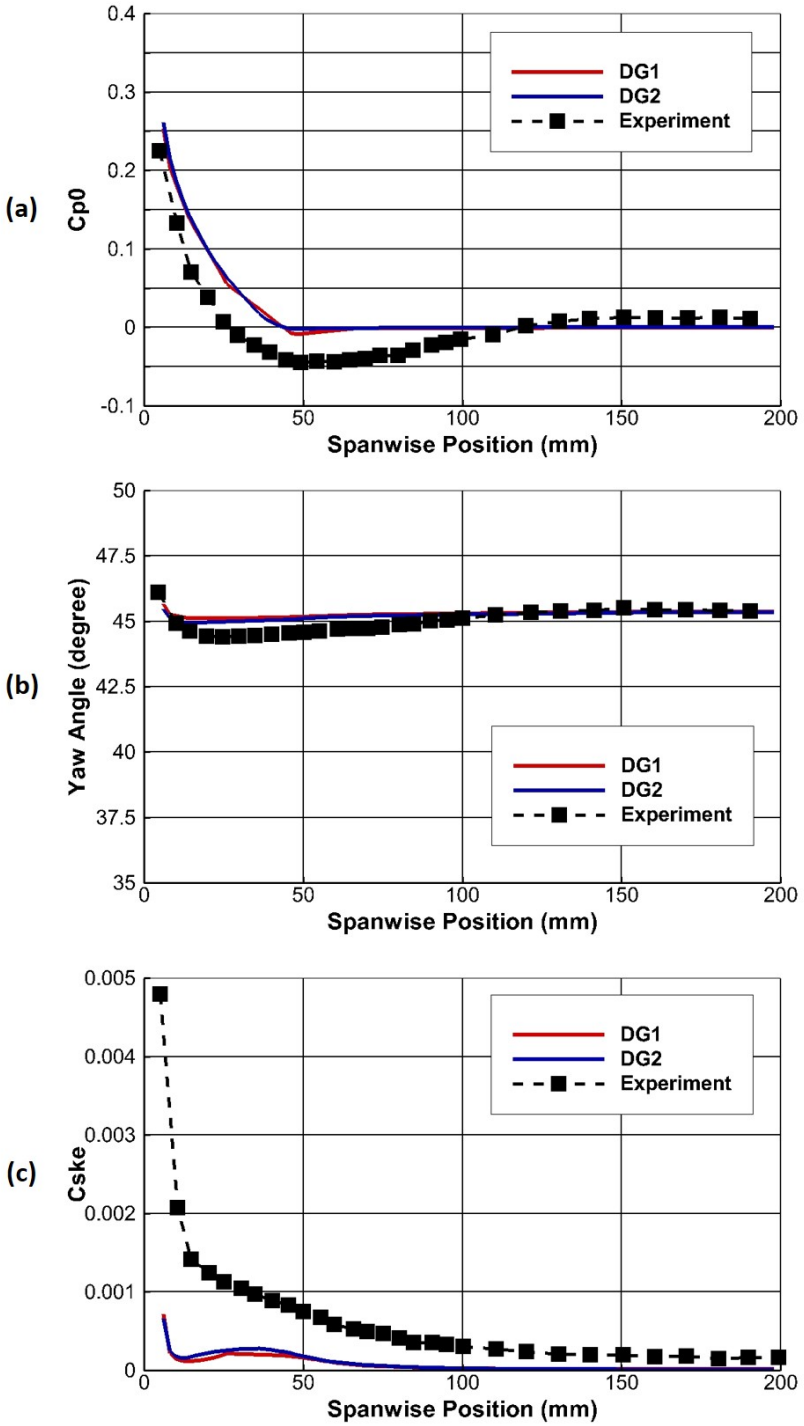


Figure 6.21: Pitch-averaged data at axial chord position of C_{ax}=-9% (a) Total pressure loss coefficient; (b) Yaw angle; (c) Secondary kinetic energy coefficient (Experiment denotes the measured data by Hartland, 2001)

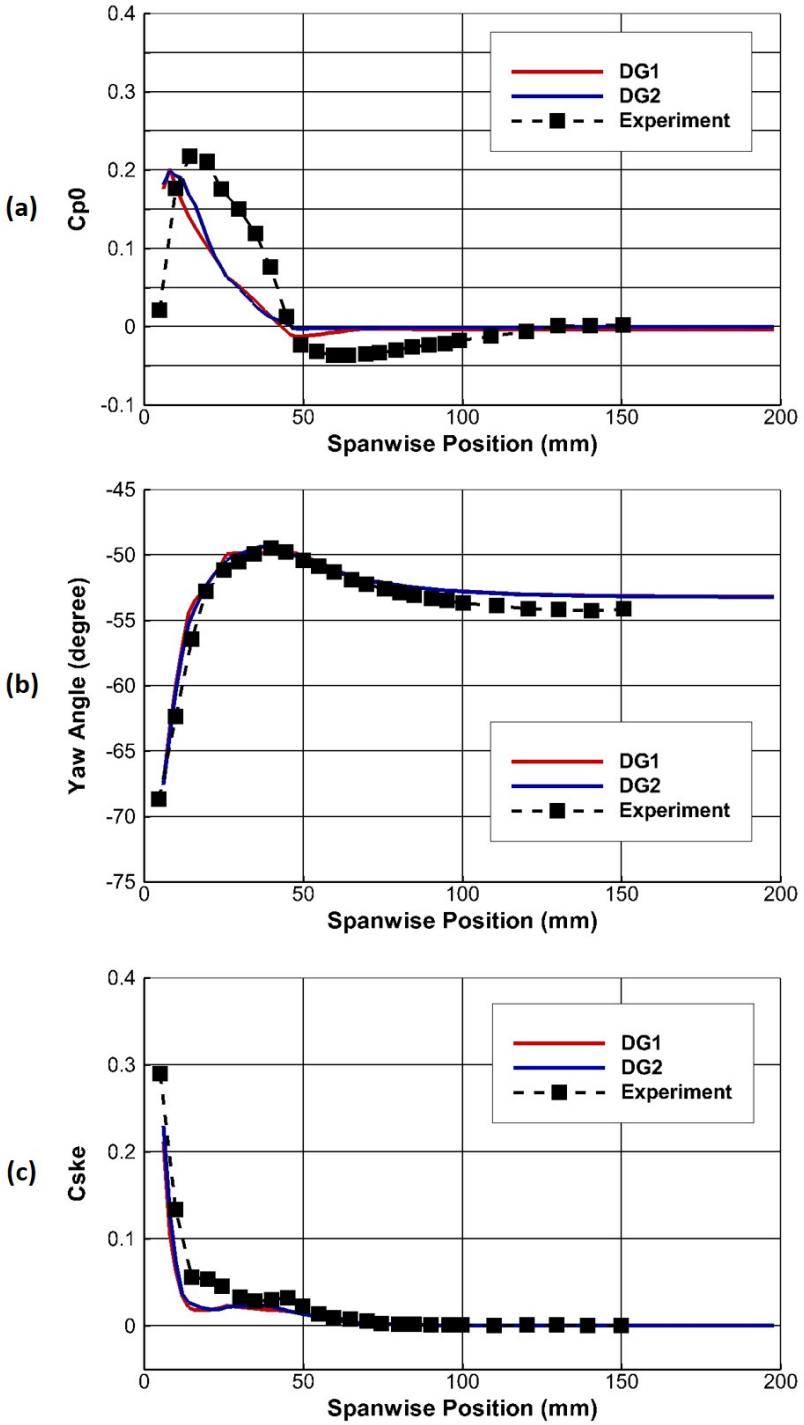


Figure 6.22: Pitch-averaged data at axial chord position of C_{ax}=71% (a) Total pressure loss coefficient; (b) Yaw angle; (c) Secondary kinetic energy coefficient (Experiment denotes the measured data by Hartland, 2001)

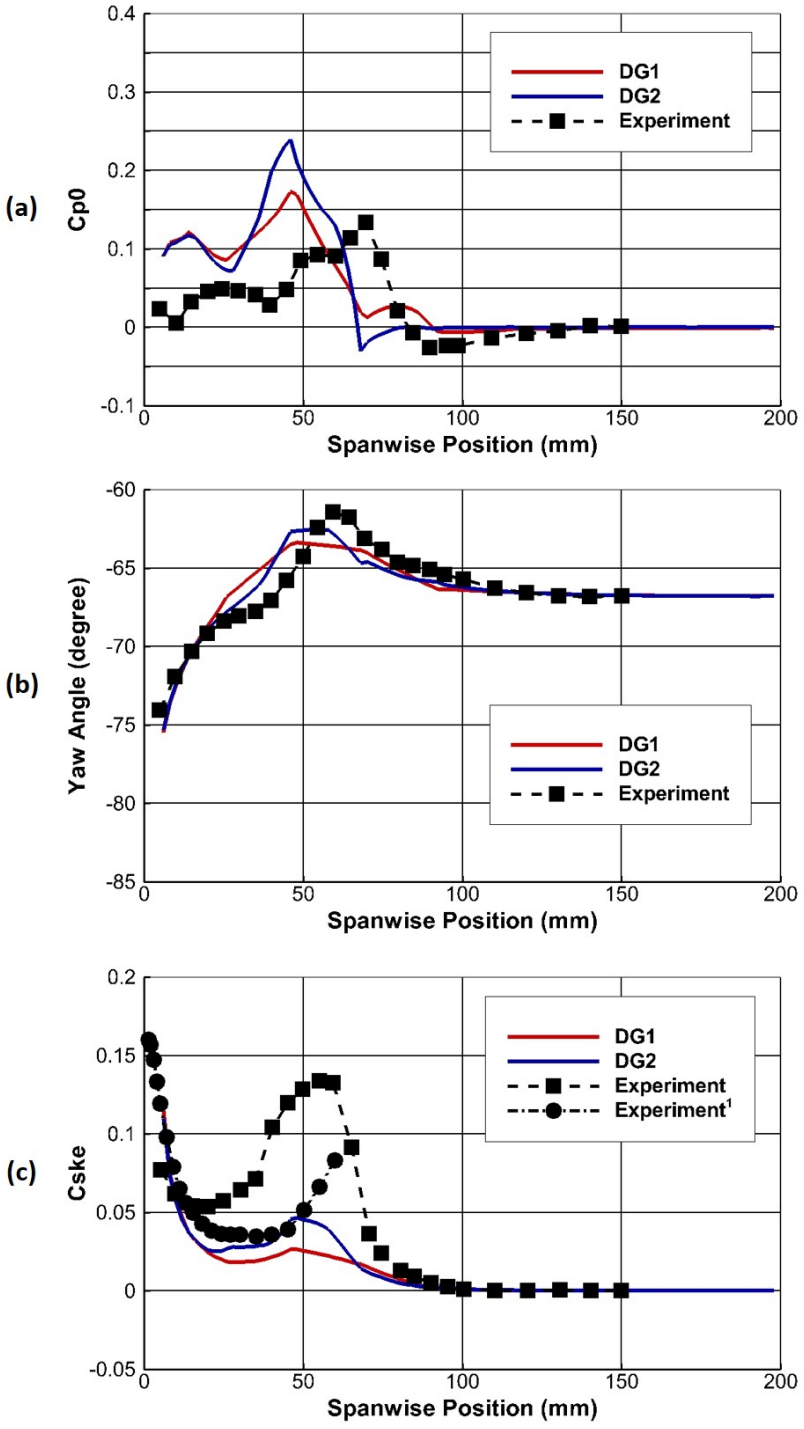


Figure 6.23: Pitch-averaged data at axial chord position of C_{ax}=97% (a) Total pressure loss coefficient; (b) Yaw angle; (c) Secondary kinetic energy coefficient (Experiment denotes the measured data by Hartland, 2001; Experiment[1] denotes the measured data by Moore, 1995)

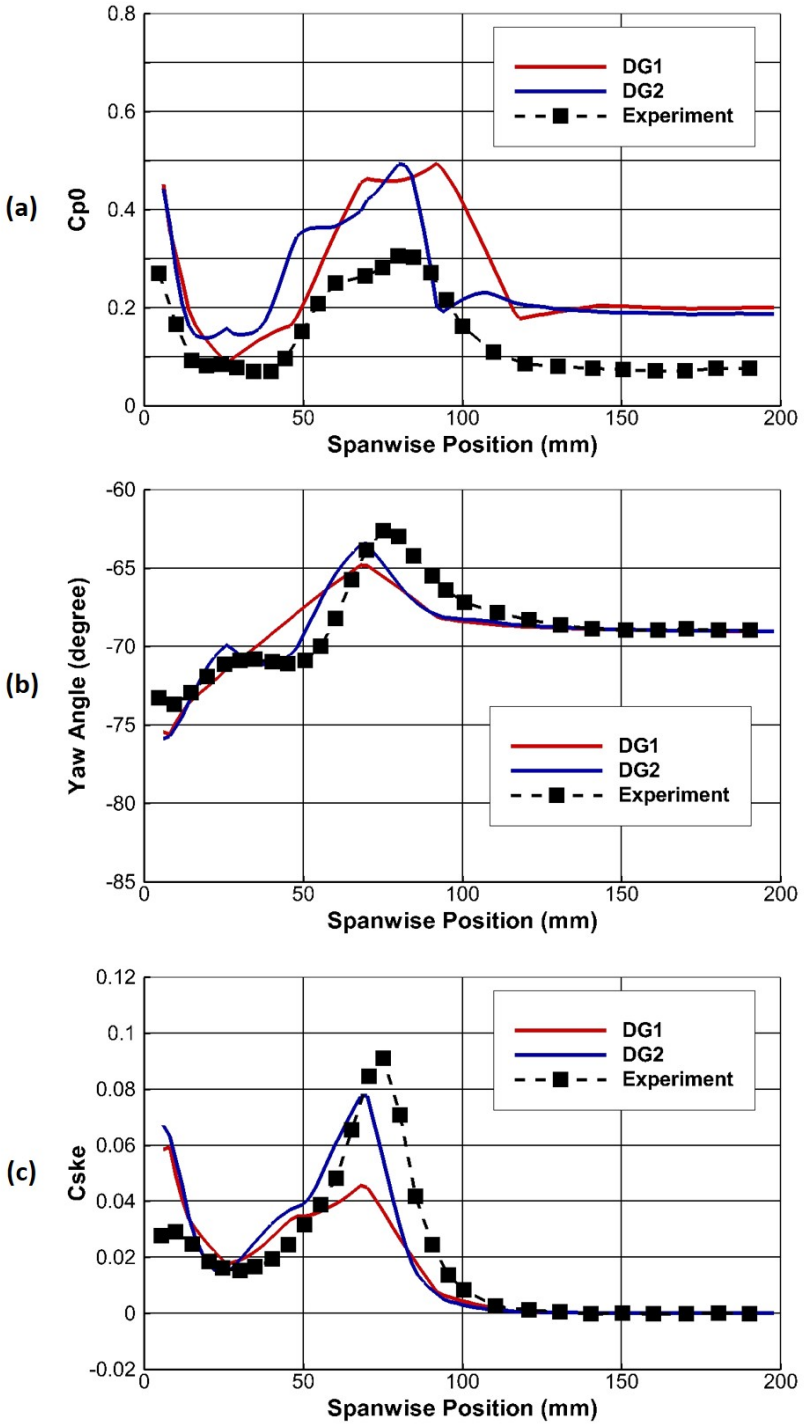


Figure 6.24: Pitch-averaged data at axial chord position of C_{ax}=128% (a) Total pressure loss coefficient; (b) Yaw angle; (c) Secondary kinetic energy coefficient (Experiment denotes the measured data by Hartland, 2001)

6.4 Summary and Discussion

For the Durham cascade, the development of the secondary flow in the endwall region has been predicted using the current DG solver and the computed results compared to the measured data of the experiment are shown in the above detailed traverse plots and pitch-averaged results through the blade passage (from upstream of the leading edge to downstream of the trailing edge). The computed results show that the passage vortex is formed near the endwall/suction surface upstream of the trailing edge, strengthened away from the endwall and further developed toward the midspan, downstream of the trailing edge, which are consistent with the experimental observations. The computed total pressure loss cores show reasonable agreement with the measured ones of the experiment upstream of the trailing edge. The main features of the flow yaw angles and secondary kinetic energy coefficients are better predicted as the order of accuracy increases.

However, the DG results show much higher loss cores downstream of the trailing edge due to the higher midspan losses regardless of the order of the piece-wise polynomials. Additionally, the position of loss cores are located slightly closer to the endwall/suction surface. The similar results were also observed by previous CFD works by Cleak and Gregory-Smith (1992) and Moore and Gregory-Smith (1996).

It is known that, except for the endwall region, the flow near the midspan in a blade passage can be seen as a two-dimensional flow, where the flow upstream of the blade leading edge is largely laminar accounting for a moderate Reynolds number adopted for this Durham cascade, followed by a laminar separation at approximate 80% C_{ax} on the suction surface as observed in the experiments, and

the flow downstream of the blade trailing edge is developed into fully turbulent. However, the RANS simulations assume that the flow in a blade passage is fully turbulent. This brings to a question that whether the steady RANS solutions can accurately predict the flow losses influenced by both the endwall secondary flow and the laminar separation on the blade suction surface? This question will be further addressed and answered in the remaining part of this thesis.

7 Unsteady Laminar Solution for High Pressure Turbine Cascade

7.1 Some Further Modelling Considerations

The consistent over-predictions of the flow losses by the steady RANS solutions lead to further modelling considerations. The most basic issue of interest is whether or not a steady flow model is adequate. A steady laminar flow solution is firstly attempted and the DG1 solution is shown in Figure 7.1. The steady solution struggles to converge to a steady state, but the results reveal two distinctive potential sources of the problem of the convergence, firstly a laminar bubble type separation starts at about 80 % suction surface, and secondly vortices shed from the blunt trailing edge. Therefore, there are two parts of the flow where the role of unsteadiness needs to be considered:

a) Oscillatory shear layer of the laminar separation;

b) Unsteady vortex shedding from the blade trailing edge.

Although both can be captured by a full LES, the corresponding mesh re-

quirement would typically be by a factor of $O(10^2)$ larger than that required for a RANS. It is recognized that the bubble type separation can be captured by a certain transition models by Langtry and Menter (2009), however the behavior of a boundary layer based transition model in a 3D secondary flow strongly influenced by the endwall is rather unknown. Furthermore, a RANS model, even with a properly captured transition on the blade surface, will be ultimately limited by the unknown interplay between the modeled turbulence unsteadiness (via an eddy viscosity) and the resolved unsteady shed vortices, thus the risk of 'double counting' turbulence & unsteadiness. The trailing edge vortex shedding is shown to be crucial to the trailing edge base pressure and thus the losses e.g. Ning and He (2001) and He and Yi (2017). Given these influential unsteady flow mechanisms, a modeling question is then put forward: is there any reasonable alternative to either a full LES or a RANS?

A further modeling consideration in the present work stems from a recent work by He and Yi (2017), in which the computation of a laminar separation has been contrasted between steady and unsteady laminar solutions. It was shown that an unsteady laminar solution, even at seemingly much coarser temporal and spatial resolutions than a typical LES, can predict an effectively reattached separation bubble, in agreement with the experiment. The key requirement seems to be an unsteady laminar solution with sufficient temporal resolution to capture the evolution of the large scale unsteady vortices in the separated shear layer. For the present case, a direct fully laminar flow model is thus attempted. Accordingly, a consistent numerical constraint in this present case is that the temporal and spatial resolution should be sufficiently fine to resolve both the evolution of the

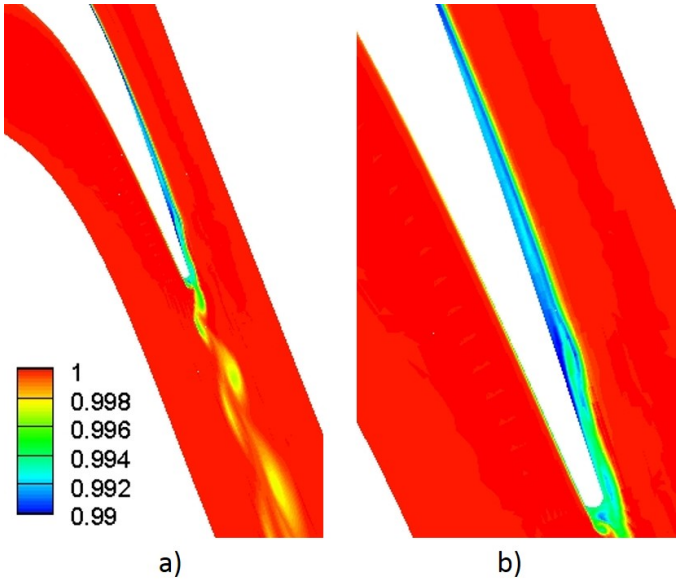


Figure 7.1: Entropy contour of the steady laminar solution from DG1: (a) overall domain and (b) close-up of suction surface near trailing edge

unstable laminar separated shear layer on the blade suction surface as well as that of the trailing edge vortex shedding.

7.2 Sensitivity Study on Temporal Resolution of Unsteady Laminar Solution

Given the above modelling consideration and intent, it will be illustratively helpful to first get some guide on the corresponding temporal resolution adequately required for a unsteady laminar solution. A finer mesh has been generated to ensure that the spatial scales of the shear layer instability and the trailing edge vortex shedding are adequately captured, as shown in Figure 7.2. For the shear layer instability, a typical RANS boundary layer mesh can only provide a reasonable resolution in the wall normal direction, so further refinement in the streamwise is added as indicated in Figure 7.2 with a close up around the suction surface separation region. Similarly around the trailing edge and in the wake region, a sufficiently fine mesh is required to support the local resolution to capture the initiation and development of the vortex shedding as illustrated in Figure 7.2 for the close up around the T.E. and wake. The total mesh cells for the half turbine passage is 1.2 million with 2×10^5 node points and this mesh resolution is still much coarser than one for a LES for the half passage domain. It's also pointed out that high-order DG simulations are equivalent to subdividing mesh points and increasing the DG order for a given mesh and it thus should have a similar effect to that of a mesh refinement.

Temporal resolution requirement can then be examined by the comparative study in terms of number of time steps in one period of the unsteady shed vortices to be resolved, corresponding to a maximum Courant-Friedrichs-Lewy (CFL) number. Here, the calculations are conducted for the 2D turbine cascade based on the midspan flow conditions. Four time steps corresponding to four maximum CFL

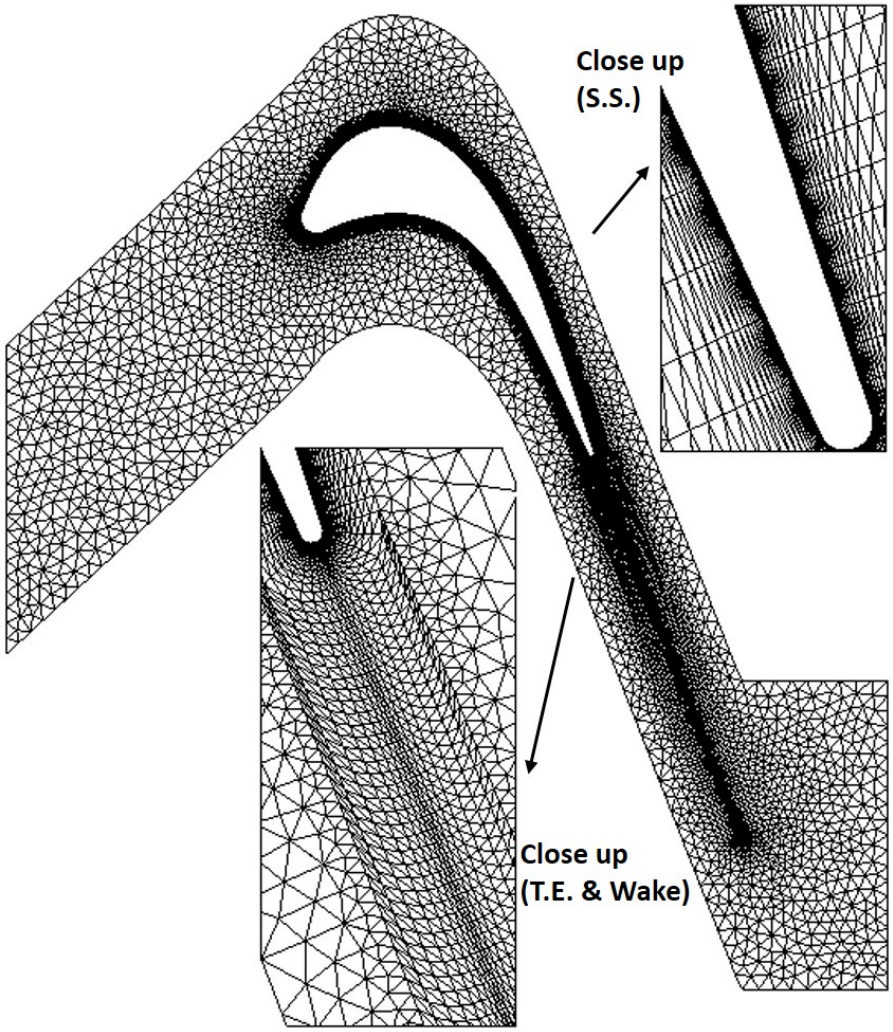


Figure 7.2: Mesh for direct unsteady laminar simulations

numbers of 2000, 1000, 500 and 250 are examined. For this Durham cascade, only are the DG1 (2nd-order) and DG2 (3rd-order) computations carried out. Figure 7.3 and Figure 7.5 show the instantaneous entropy contours in the near trailing edge region from the DG1 and the DG2 solutions on four different maximum CFL numbers (CFL_m= 2000, 1000, 500 and 250). Also, Figure 7.4 and Figure 7.6 give more details at close up of suction surface near trailing edge from the DG1 and the DG2 solutions on the four different maximum CFL numbers.

Apart from the large time steps case (CFL_m=2000 and 1000), both the DG1 and

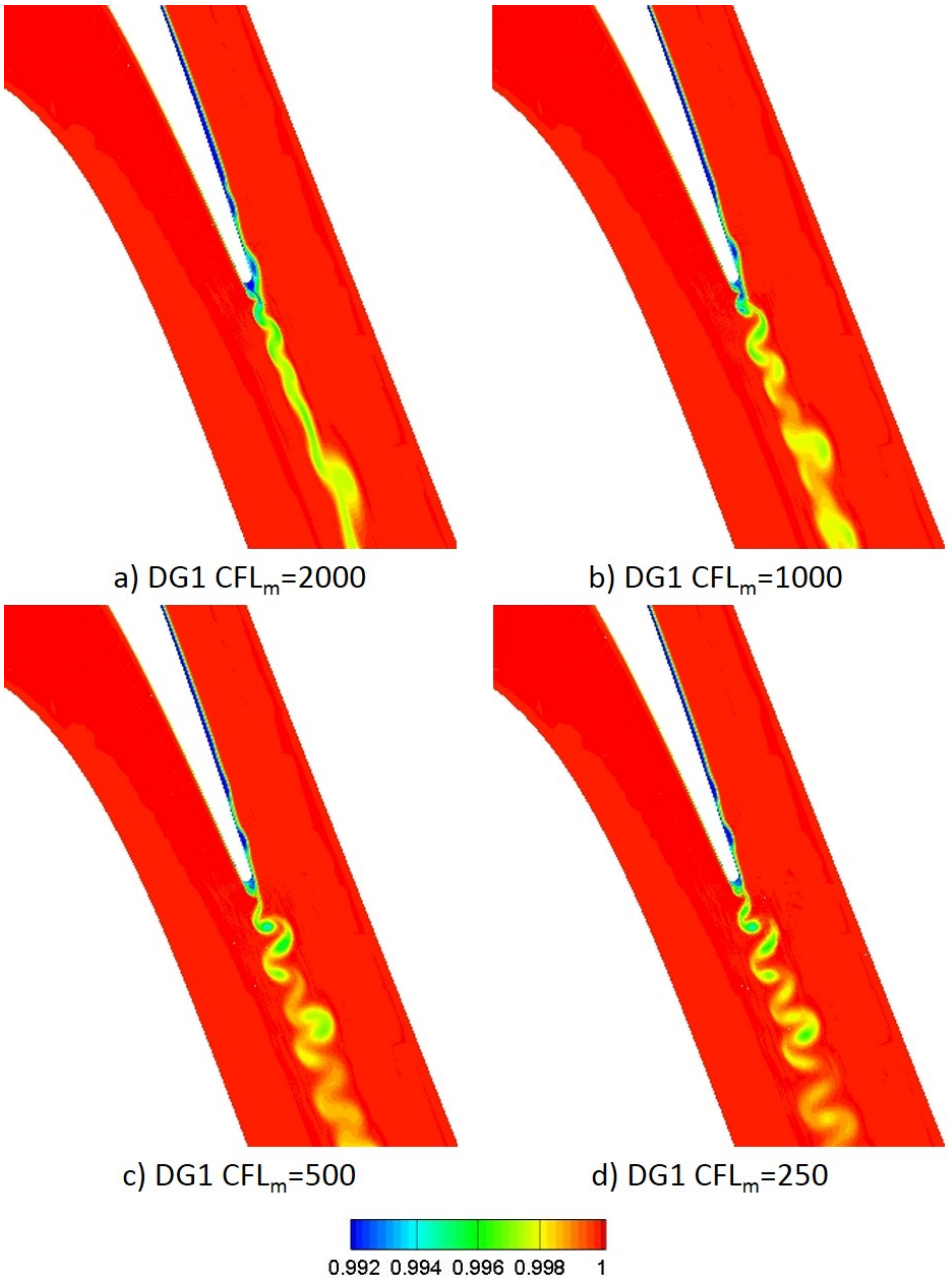


Figure 7.3: Instantaneous entropy contours from DG1 on CFL_m = 2000, 1000, 500 and 250

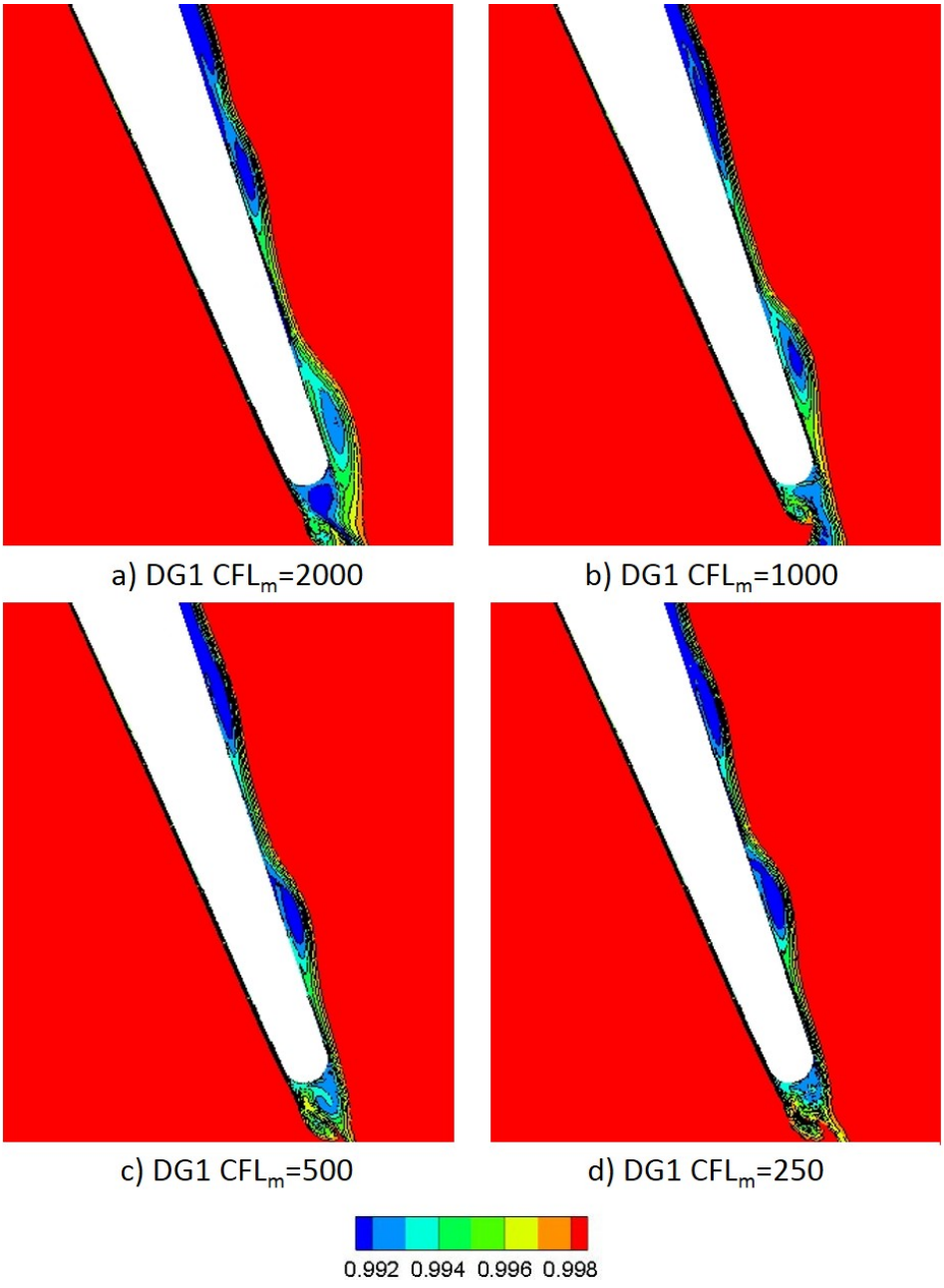


Figure 7.4: Instantaneous entropy contours from DG1 on CFL_m = 2000, 1000, 500 and 250 close-up of suction surface and trailing edge

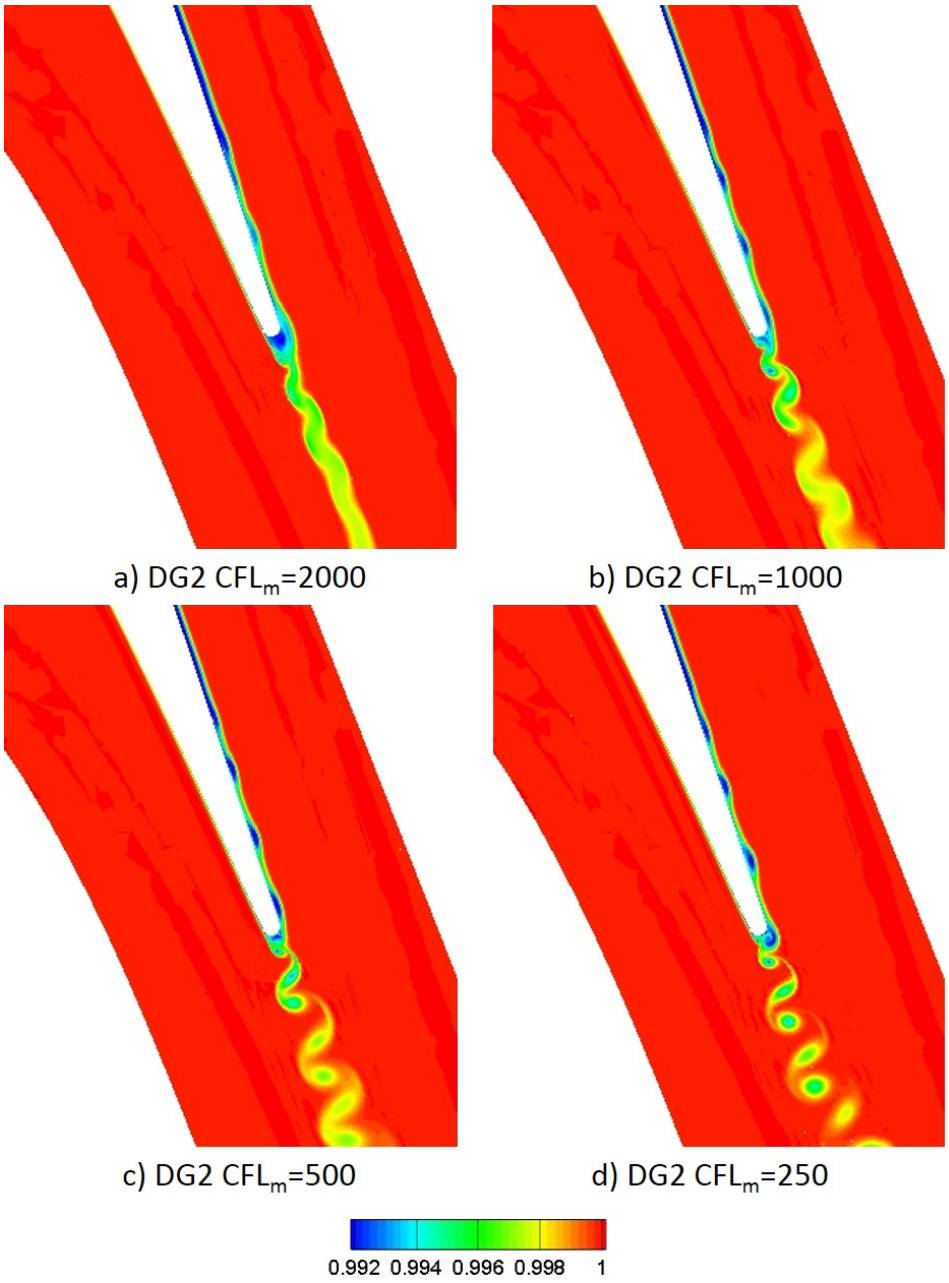


Figure 7.5: Instantaneous entropy contours from DG2 on CFL_m = 2000, 1000, 500 and 250

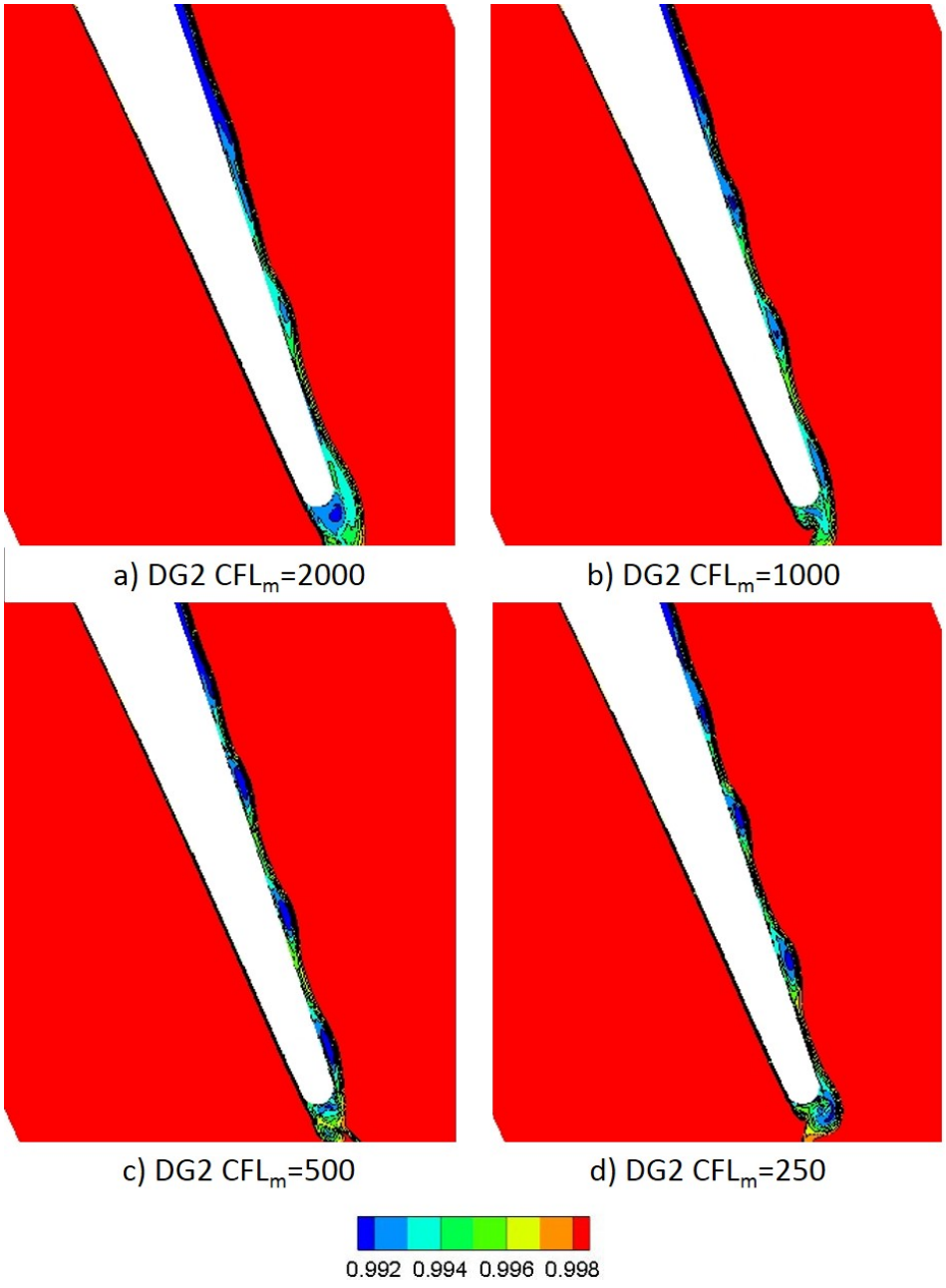


Figure 7.6: Instantaneous entropy contours from DG2 on CFL_m = 2000, 1000, 500 and 250, close-up of suction surface and trailing edge

DG2 solutions for CFL_m=500 and 250 have captured shear layer instabilities and constant propagation of unsteady disturbances to downstream. More specifically, the DG2 shows better resolved vortical structures than the DG1, since the higher-order discretization results in less numerical dissipation. The number of time steps per period and Strouhal numbers for trailing edge shedding vortices are compared in Table 7.1. The computed time steps per one period and Strouhal numbers for DG1 and DG2 at CFL_m=500 and 250 are very consistent. Note that the present predicted HP turbine cascade vortex shedding Strouhal number is close to the value of 0.235 in the VKI turbine blade as computed by Ning and He (2001).

Table 7.1: Number of time steps per period and calculated Strouhal numbers for trailing edge vortex shedding

	Time steps		Strouhal number	
CFL_m	DG1	DG2	DG1	DG2
2000	18	17	0.238	0.252
1000	39	37	0.220	0.233
500	78	78	0.219	0.221
250	151	151	0.226	0.228

It is observed that the unsteady behaviour will be largely consistent once that the number of time steps for the one period of vortex shedding after the trailing edge is about 80. The shed vortices from the separated shear layer of the suction surface separation has a nearly twice longer period so the number of time steps per period of the suction surface unsteady separation is approximately 180, corresponding to a DG1 result of $CFL_m = 500$. Overall, the number of time steps for a blade passage domain through-flow time is about 4800. It must be recognized that both the mesh counts and the time step sizes taken here are by about two orders of

magnitude less than those typical for LES.

The unsteady solutions are time averaged over a passage through-flow time to obtain the time-averaged parameters. Given the importance of base pressure in loss generation around a trailing edge, it is relevant to look at the local time-averaged static pressure contours from the DG1 and DG2 solutions at CFL_m=2000, 1000, 500 and 250, as shown in Figure 7.7 and 7.8. The steady laminar solutions are also presented in Figures 7.7(a) and 7.8(a) for comparison. Both the steady solutions and the unsteady solutions at CFL_m=2000 miss the vortex shedding, as clearly observed, so only predict a high pressure region, resulting from the flow reattachment from both suction and pressure surfaces, thus a clearly higher base pressure. The unsteady time-averaged solutions even at a large time step (CFL_m=1000, Figures 7.7(c) and 7.8(c)), still qualitatively capture the vortex shedding, leading to apparently different results from the steady one. Moreover, the solutions with increased temporal resolution at CFL_m=500 and CFL_m=250 (Figures 7.7(d), 7.7(e), 7.8(d) and 7.8(e)) show that the pressure fields around the trailing edge are considerably more consistent. The results confirming the time-step independent time mean solution can be reached when the maximum CFL number is less than 500 in this case. Additionally, the time-averaged DG2 results are shown to give a better resolved flow field than that of the DG1 at the same CFL_m number.

As stated earlier, it is of interest to see if the large scale resolved unsteady shed vortices from the suction surface separation (e.g. shown in Figures 7.3, 7.4 and 7.5 and 7.6) would effectively 'reattach' the separated shear layer, to lead a reattached boundary layer like a turbulent boundary layer, as suggested in the previously

results of He and Yi (2017). Figure 7.9 displays the time-averaged Mach number contours from the steady and unsteady solutions at CFL_m=500.

A clearly unrealistic large laminar separation is predicted by the steady laminar solution given in Figures 7.9(a) and 7.9(b). The consistent steady results by both DG1 and DG2 also suggest that the separation flow behavior would be erroneously predicted by a steady model regardless of spatial resolution. On the other hand, the time-averaged unsteady laminar solutions with the well resolved large scale unsteadiness (Figures 7.9(c) and 7.9(d)), clearly show an effectively reattached boundary layer. The striking difference between the steady and unsteady laminar solution underlines the marked importance of unsteadiness in the present case and other similar cases.

Based on the findings of the present sensitivity study on the temporal resolution, all the subsequent 3D unsteady laminar calculations of the Durham HPT cascade will be carried out with the time-step size corresponding to that of CFL_m=500 for this 2D case.

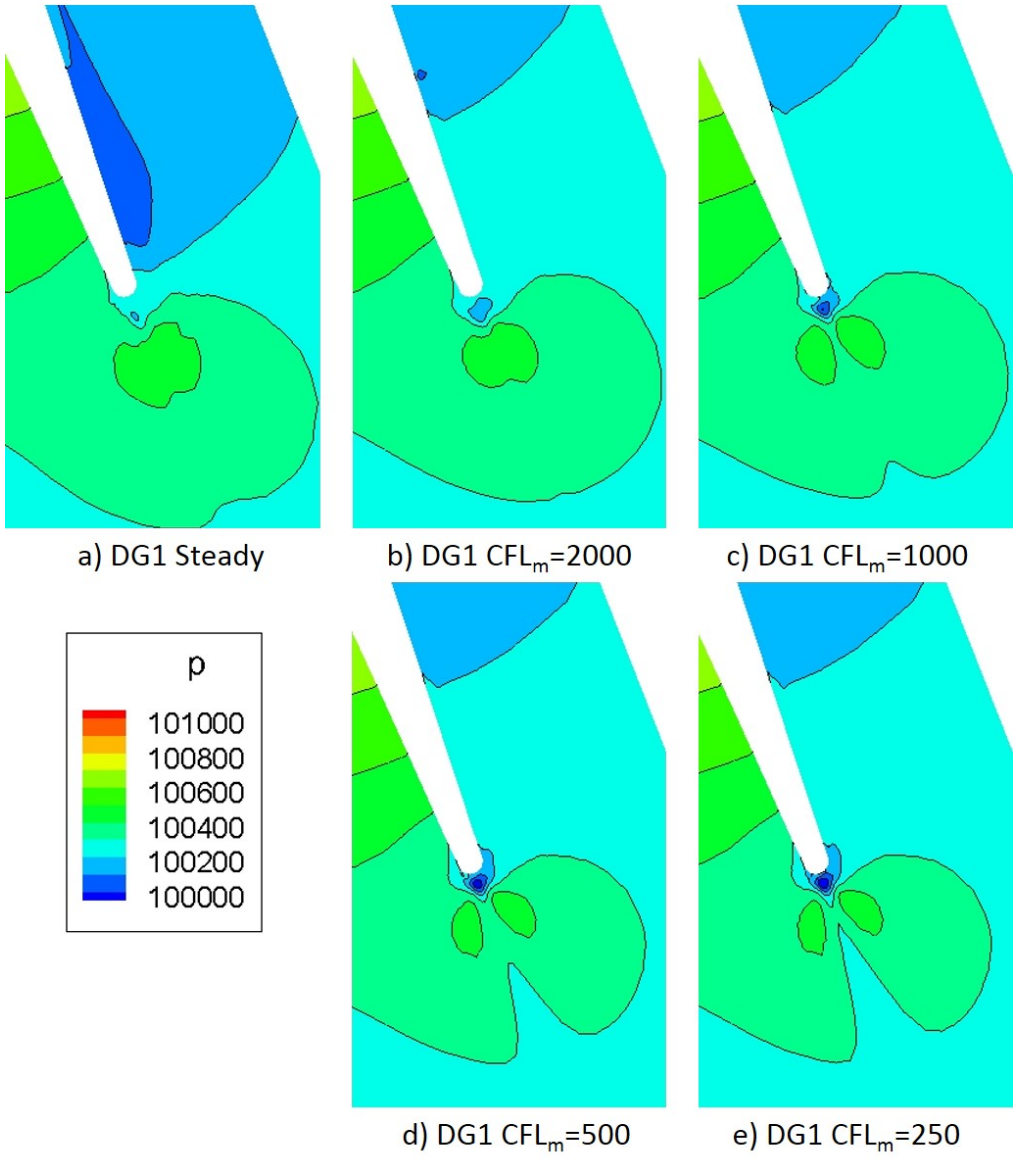


Figure 7.7: Comparison of steady and unsteady time-averaged static pressure contours around trailing edge from DG1

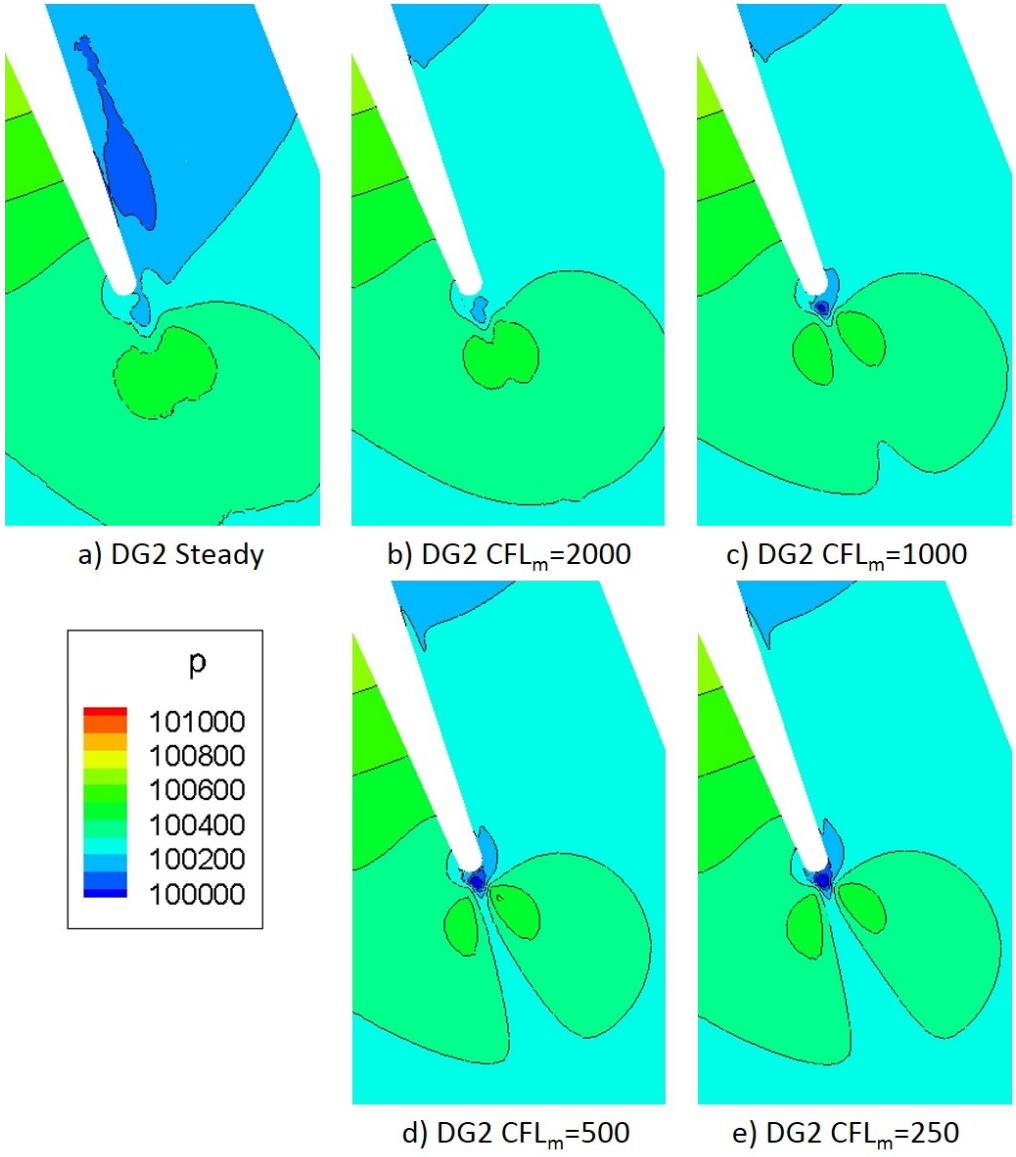


Figure 7.8: Comparison of steady and unsteady time-averaged static pressure contours around trailing edge from DG2

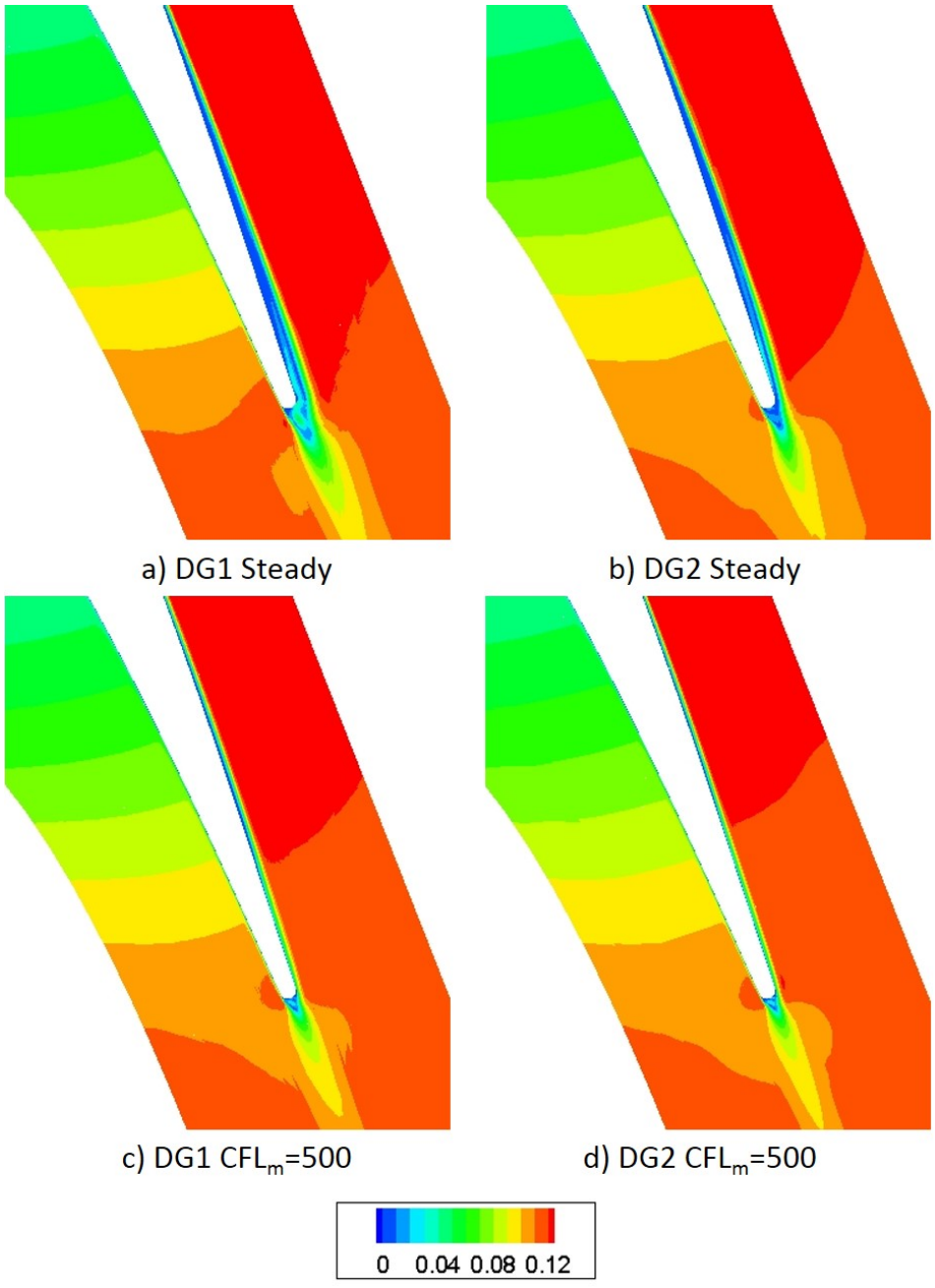


Figure 7.9: Time-averaged Mach contours from steady and unsteady on CFL$_m$=500

7.3 3D Unsteady Laminar Solution of Durham Cascade

The 3D unsteady laminar calculations of the Durham HPT cascade using the DG method have been conducted. The time-averaged solutions are obtained over time steps to cover at least one passage through-flow time.

7.3.1 Traverse Plots

The time-averaged results of secondary vectors, total pressure loss coefficients, yaw angles and secondary energy loss coefficients from the DG1 and DG2 solutions will be studied in detail at the planes of -9%, 71%, 97% and 128% C_{ax} in this section. The measured data by Hartland (2001) is chosen as the reference data for comparison. In addition, it is of interest to qualitatively compare plots from the unsteady laminar solutions with those of the RANS solutions in Section 6.3.1 in Chapter 6, which will be also carried out in this section.

7.3.1.1 Slot 1: -9%C_{ax}

The time-averaged secondary flow velocity vectors upstream of the leading edge at plane -9% C_{ax} are presented in Figure 7.10, which indicates that there is no obvious flow disturbance before the blade leading edge, consistent with the conclusions made for Figure 6.5 in Chapter 6. The time-averaged loss and yaw angles show good agreement with the experimental ones, as depicted in Figures 7.11 and 7.12 respectively, and the agreement between the time-averaged DG1 and DG2 solutions shows a reasonable convergence with respect to the order of accuracy. As shown in Figure 7.13, the strength of the secondary flow from the laminar solutions matches

the experimental one relatively well, on the other hand, that of the RANS solutions in Figure 6.8 in Chapter 6 presents a clear mismatch. Note that the secondary flow upstream of the leading edge is largely caused by the horseshoe vortex (see Moore, 1995), which might indicate that the unsteady laminar solutions better resolve the horseshoe vortex upstream of the leading edge than the RANS solutions.

7.3.1.2 Slot 6: 71%C_{ax}

In Figure 7.14, the passage vortex near the endwall region at plane 71% C_{ax} is well predicted by the laminar solutions, though seemingly closer to the endwall, which might be attributed to the lack of turbulence diffusion of the endwall flow. As the passage vortex is formed near the endwall/suction surface region, the loss cores in this region are strengthened, where the laminar solutions agree well with the experimental ones as shown in Figure 7.15 but the position of loss cores tends to be closer to the endwall as well.

The time-averaged flow yaw angles, as presented in Figure 7.16, show agreement with the measured experiment ones, however, the peak seems to be slightly closer to the blade suction surface and higher strength of the peak indicates a higher overturning of the flow, consistent with the RANS results in Figure 6.11 in Chapter 6. The time-averaged secondary kinetic energy coefficients show fairly good agreement with the measured one of the experiment as presented in Figure 7.17. The secondary flow region from the laminar solution is clearly much better resolved than that from the RANS solution as presented in Figure 6.12 in Chapter 6.

7.3.1.3 Slot 8: 97%C_{ax}

The time-averaged secondary vectors show that the passage vortex loss cores are moved further away from the endwall, as depicted in Figure 7.18, but are located slightly closer to the endwall as well as the suction surface compared to the position of the passage vortex in the experiment. Though the loss cores are slightly closer to the suction surface, the overall time-averaged total pressure loss coefficients contours agree quite well with the experimental ones in Figure 7.19. On the other hand, the loss cores predicted by the RANS solutions, shown in Figure 6.14 in Chapter 6, are considerably over-predicted. This might indicate that the direct unsteady laminar approach is more capable of predicting the flow losses influenced by both the endwall boundary layer and a laminar separation on the blade surface.

As shown in Figure 7.20, the time-averaged flow yaw angles from both the DG1 and DG2 solutions show good agreement with the experimental ones, though a slight movement inward the suction surface is consistently observed. The time-averaged secondary kinetic energy coefficients are in good agreement with the measured experiment ones as presented in Figure 7.21. On the contrary, the RANS solutions show a clear under-predict of the coefficients, as depicted in Figure 6.16 in Chapter 6.

7.3.1.4 Slot 10: 128% C_{ax}

As presented in Figure 7.22, the time-averaged secondary vectors show that the passage vortex travels further toward the midspan with a counter vortex sitting above it to the left. However, the passage vortex position tends to be still closer to both the endwall and the suction side, possibly resulting from the lower diffusion

near the wall by the laminar flow model. The time-averaged total pressure loss coefficients are shown in Figure 7.23, where the double loss peaks as well as the counter vortex near the endwall are captured by both the DG1 and DG2 solutions. For the loss cores near the midspan, the DG2 solutions give slightly lower values than the DG1 solutions, though both are slightly over-predicted compared to the measured ones of the experiment. On the other hand, the RANS loss cores, as shown in Figure 6.18 in Chapter 6, are more markedly over-predicted.

In Figure 7.24, the main features of the time-averaged yaw angles contours match those of the experiment quite well, however, the peaks are still moved slightly inward. The time-averaged secondary kinetic energy coefficients, as presented in Figure 7.25, show good agreement with the measured ones in terms of both flow contour values and shapes. Note that the DG2 solutions provide slightly higher resolution of the cores accounting for the increased order of spatial accuracy.

Overall, the loss cores near the midspan downstream of the trailing edge are less over-predicted by the unsteady laminar solutions, whereas the RANS solutions show a significant over-prediction. Hence, it demonstrates that the unsteady laminar approach has a good predictability of flow losses affected by both the endwall secondary flow and a blade surface bubble type separation. In addition, the development of the secondary flow through the blade passage is well captured by the unsteady laminar solutions. Finally, the agreement between the DG1 and DG2 traverse plots clearly indicates a reasonable order of accuracy convergence for the unsteady laminar solutions.

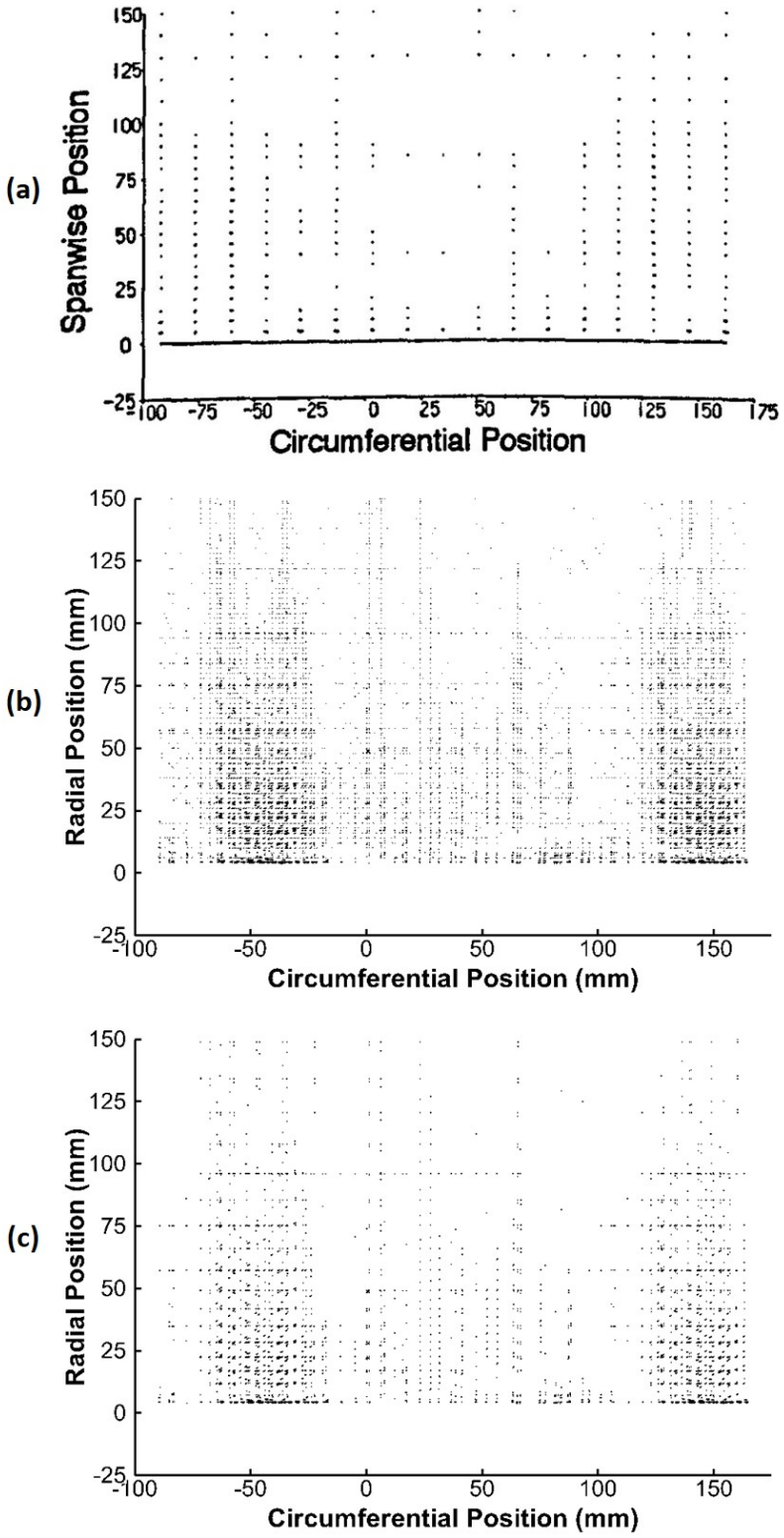


Figure 7.10: Secondary vectors at axial chord position of C_{ax}=-9% (a) Experiment by Hartland (2001); (b) Time-averaged unsteady laminar DG1; (c) Time-averaged unsteady laminar DG2

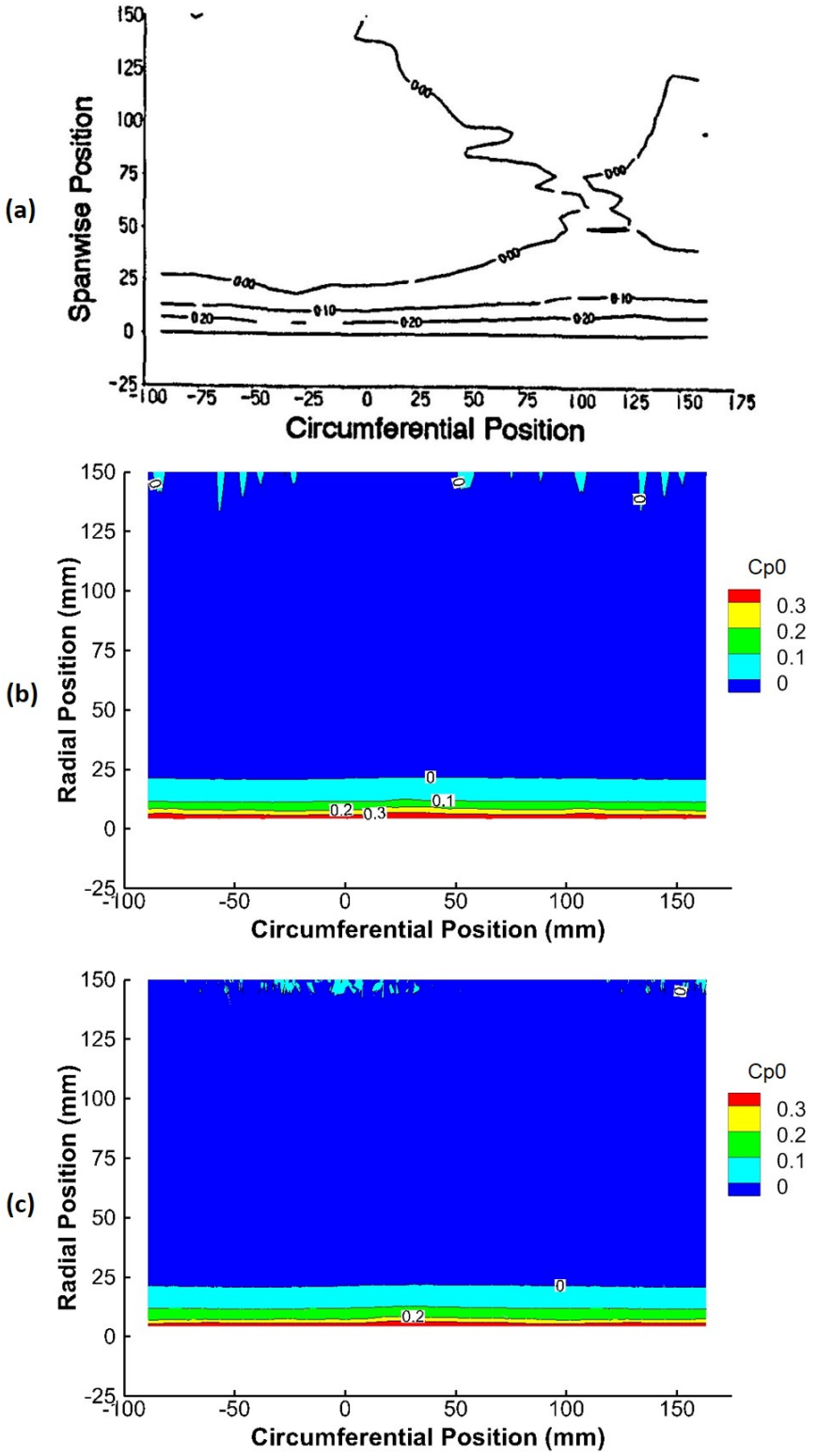


Figure 7.11: Total pressure loss coefficient contours at axial chord position of C_{ax}=-9% (a) Experiment by Hartland (2001); (b) Time-averaged unsteady laminar DG1; (c) Time-averaged unsteady laminar DG2

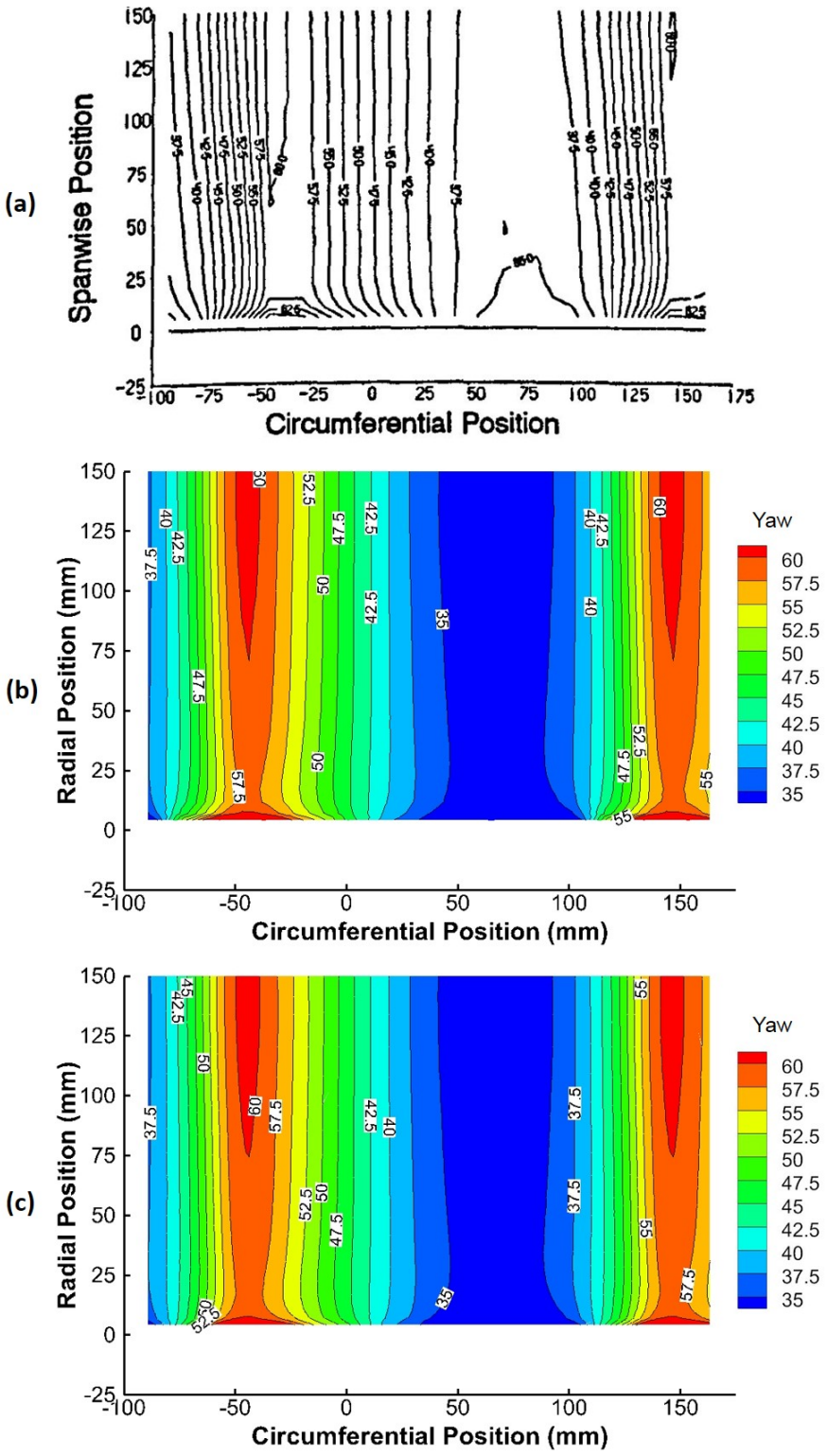


Figure 7.12: Yaw angles contours at axial chord position of C_{ax}=-9% (a) Experiment by Hartland (2001); (b) Time-averaged unsteady laminar DG1; (c) Time-averaged unsteady laminar DG2

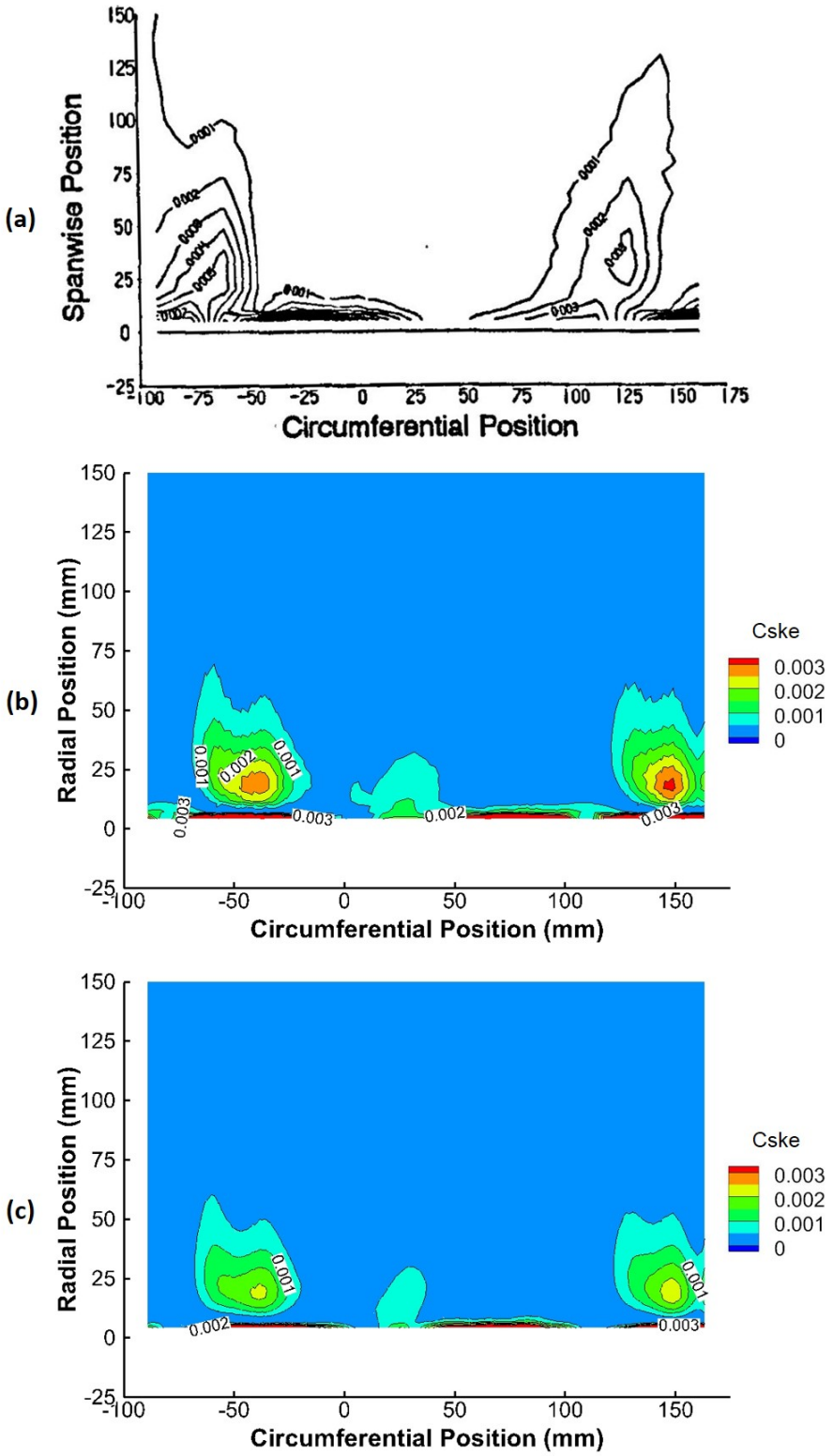


Figure 7.13: Secondary kinetic energy coefficient contours at axial chord position of C_{ax}=-9% (a) Experiment by Hartland (2001); (b) Time-averaged unsteady laminar DG1; (c) Time-averaged unsteady laminar DG2

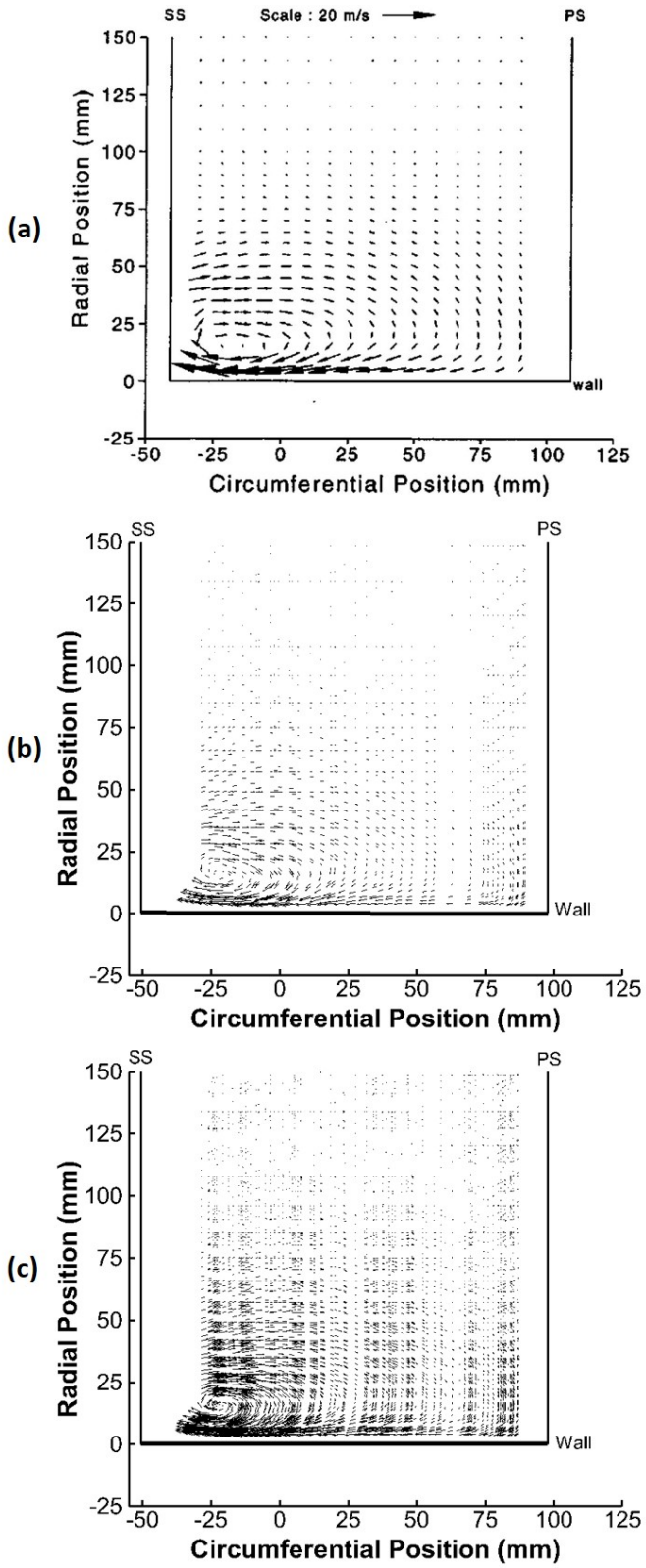


Figure 7.14: Secondary vectors at axial chord position of C_{ax}=71% (a) Experiment by Hartland et al. (2000); (b) Time-averaged unsteady laminar DG1; (c) Time-averaged unsteady laminar DG2

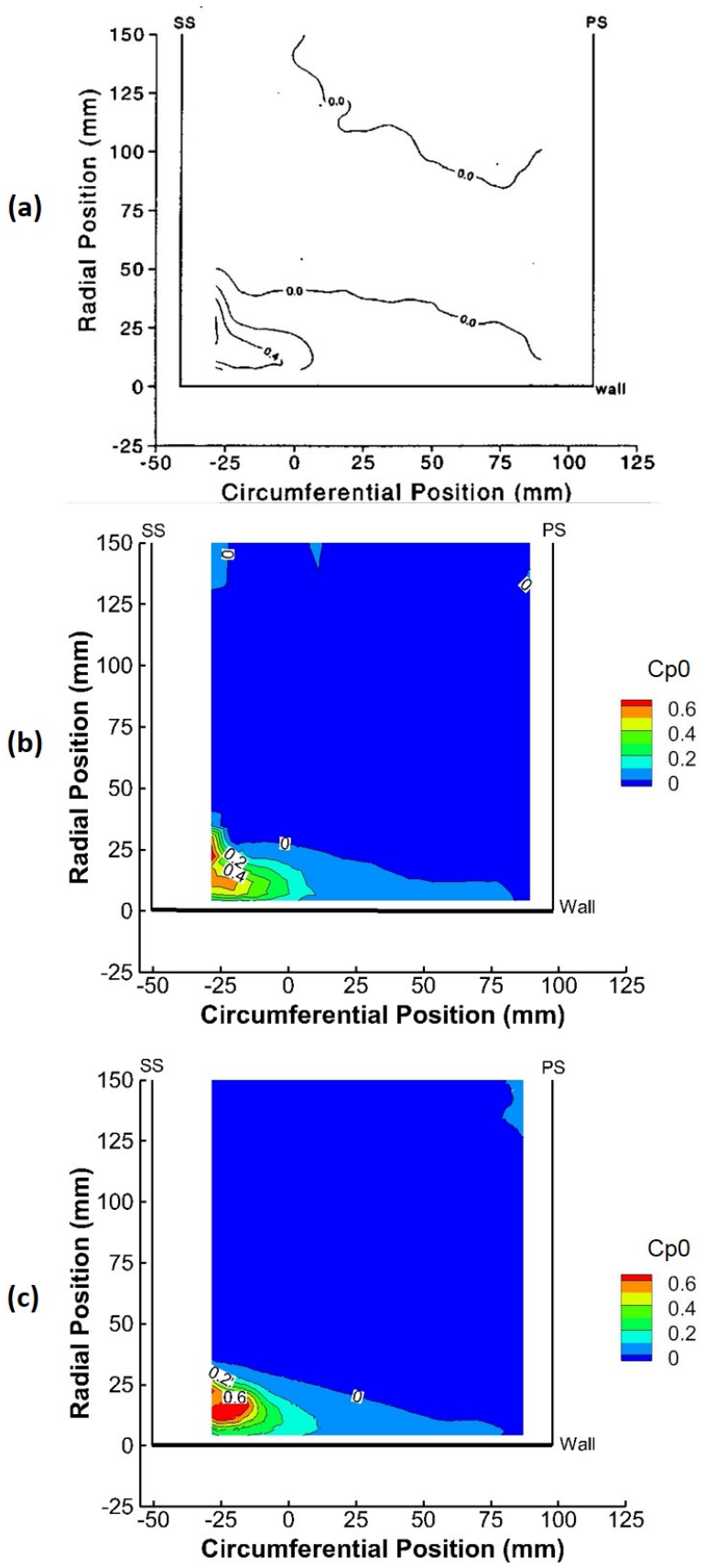


Figure 7.15: Total pressure loss coefficient contours at axial chord position of C_{ax}=71% (a) Experiment by Hartland et al. (2000); (b) Time-averaged unsteady laminar DG1; (c) Time-averaged unsteady laminar DG2

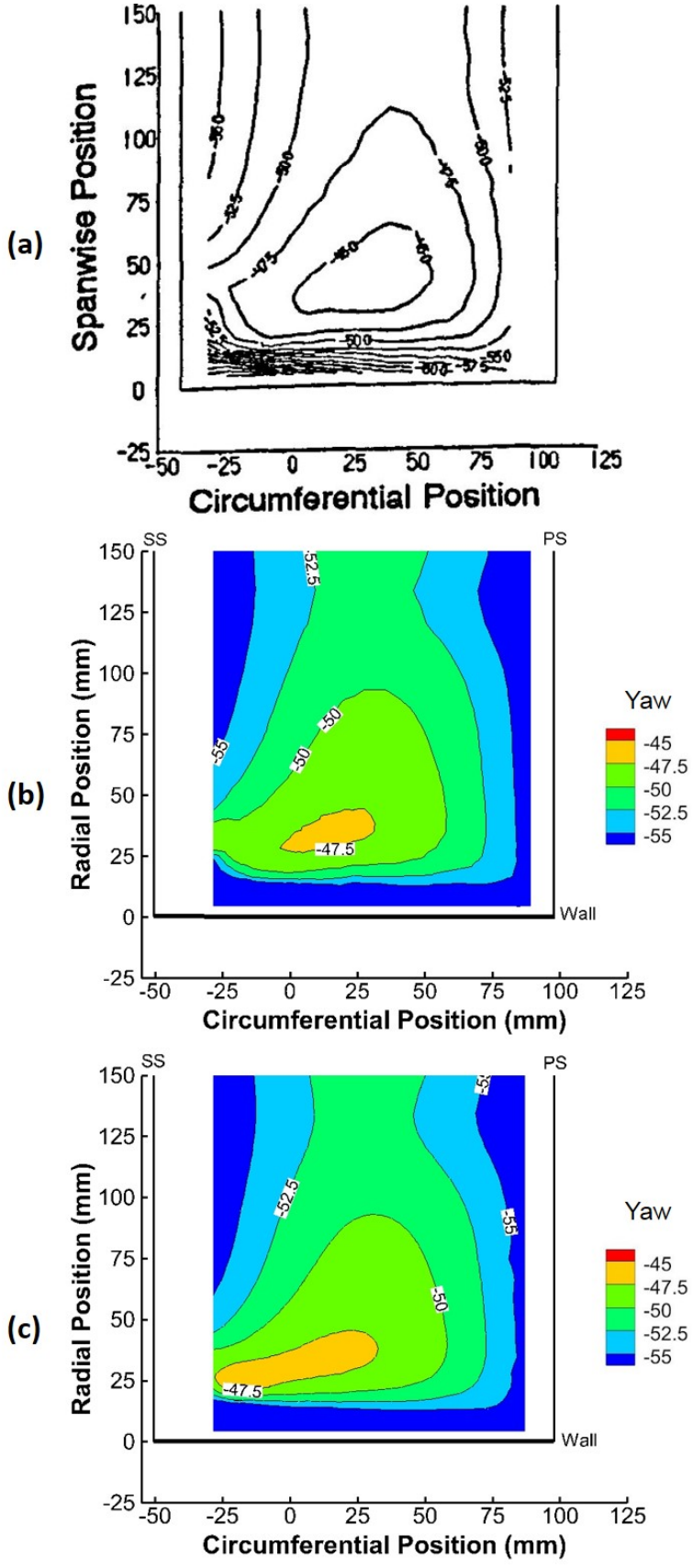


Figure 7.16: Yaw angles contours at axial chord position of C_{ax}=71% (a) Experiment by Hartland (2001); (b) Time-averaged unsteady laminar DG1; (c) Time-averaged unsteady laminar DG2

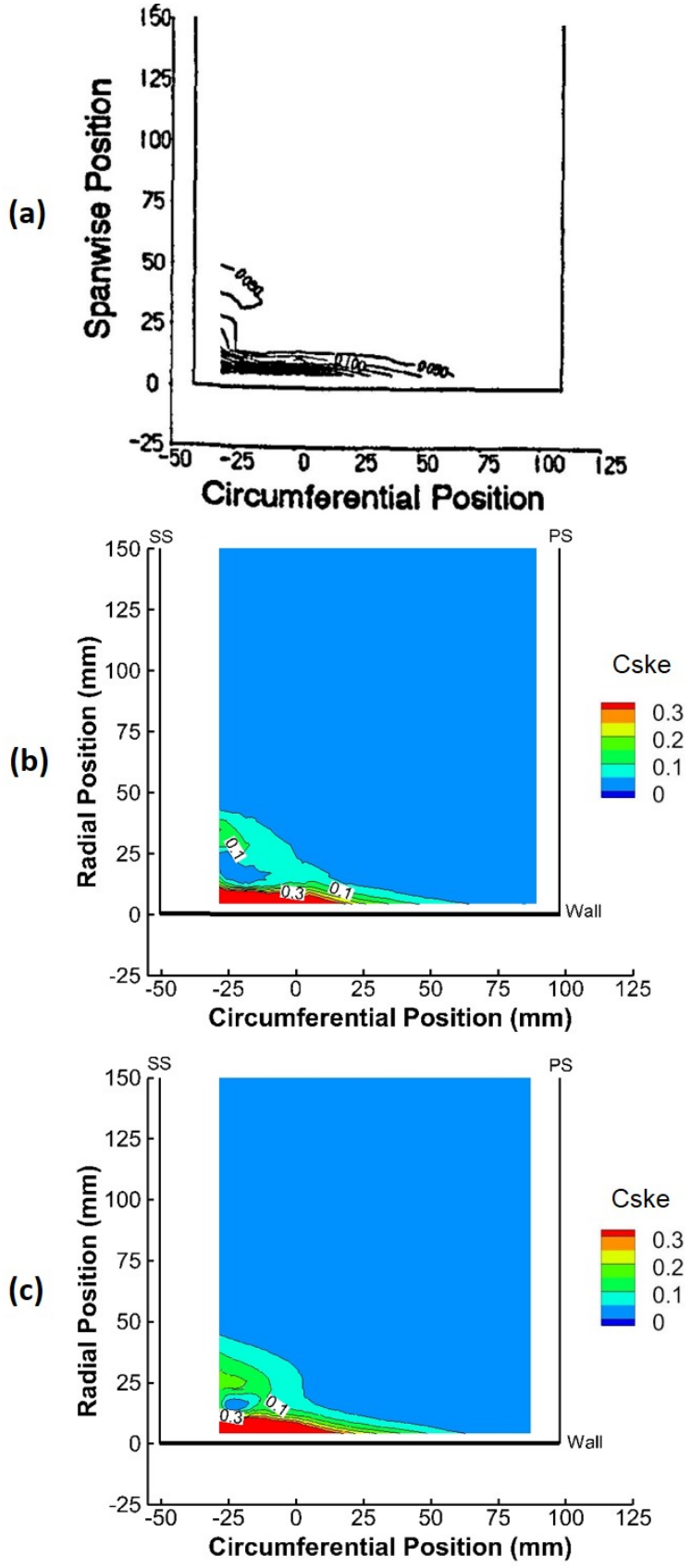


Figure 7.17: Secondary kinetic energy coefficient contours at axial chord position of C_{ax}=71% (a) Experiment by Hartland (2001); (b) Time-averaged unsteady laminar DG1; (c) Time-averaged unsteady laminar DG2

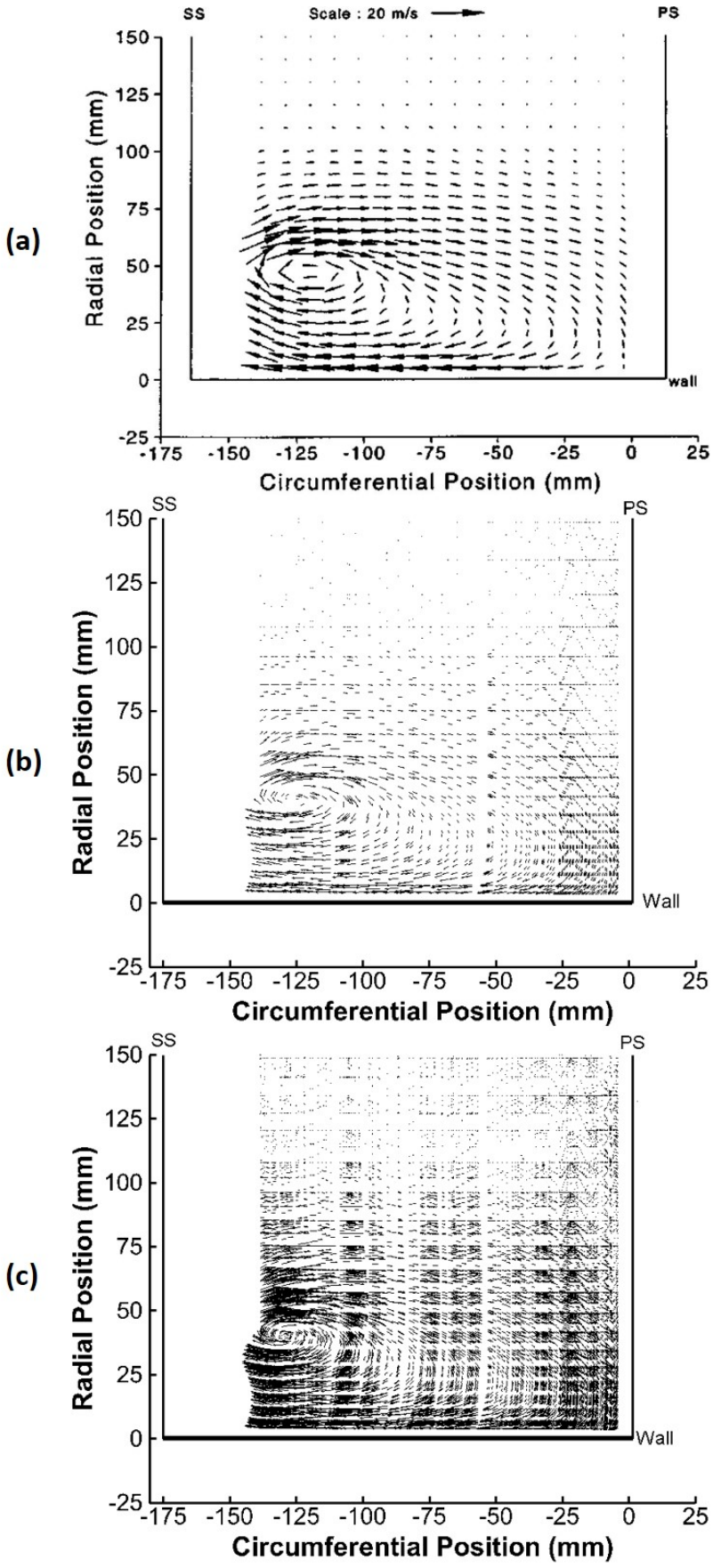


Figure 7.18: Secondary vectors at axial chord position of C_{ax}=97% (a) Experiment by Hartland et al. (2000); (b) Time-averaged unsteady laminar DG1; (c) Time-averaged unsteady laminar DG2

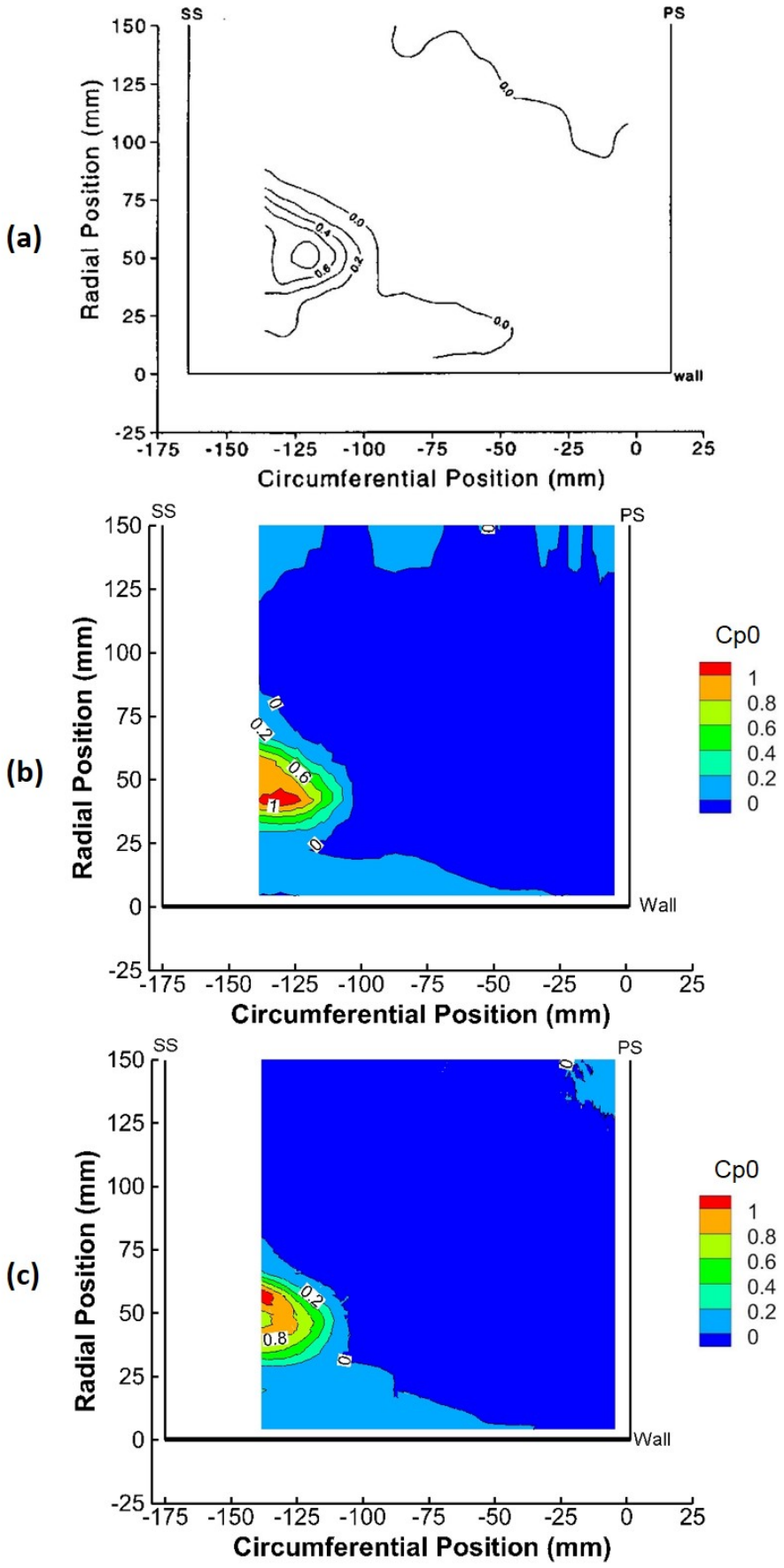


Figure 7.19: Total pressure loss coefficient contours at axial chord position of C_{ax}=97% (a) Experiment by Hartland et al. (2000); (b) Time-averaged unsteady laminar DG1; (c) Time-averaged unsteady laminar DG2

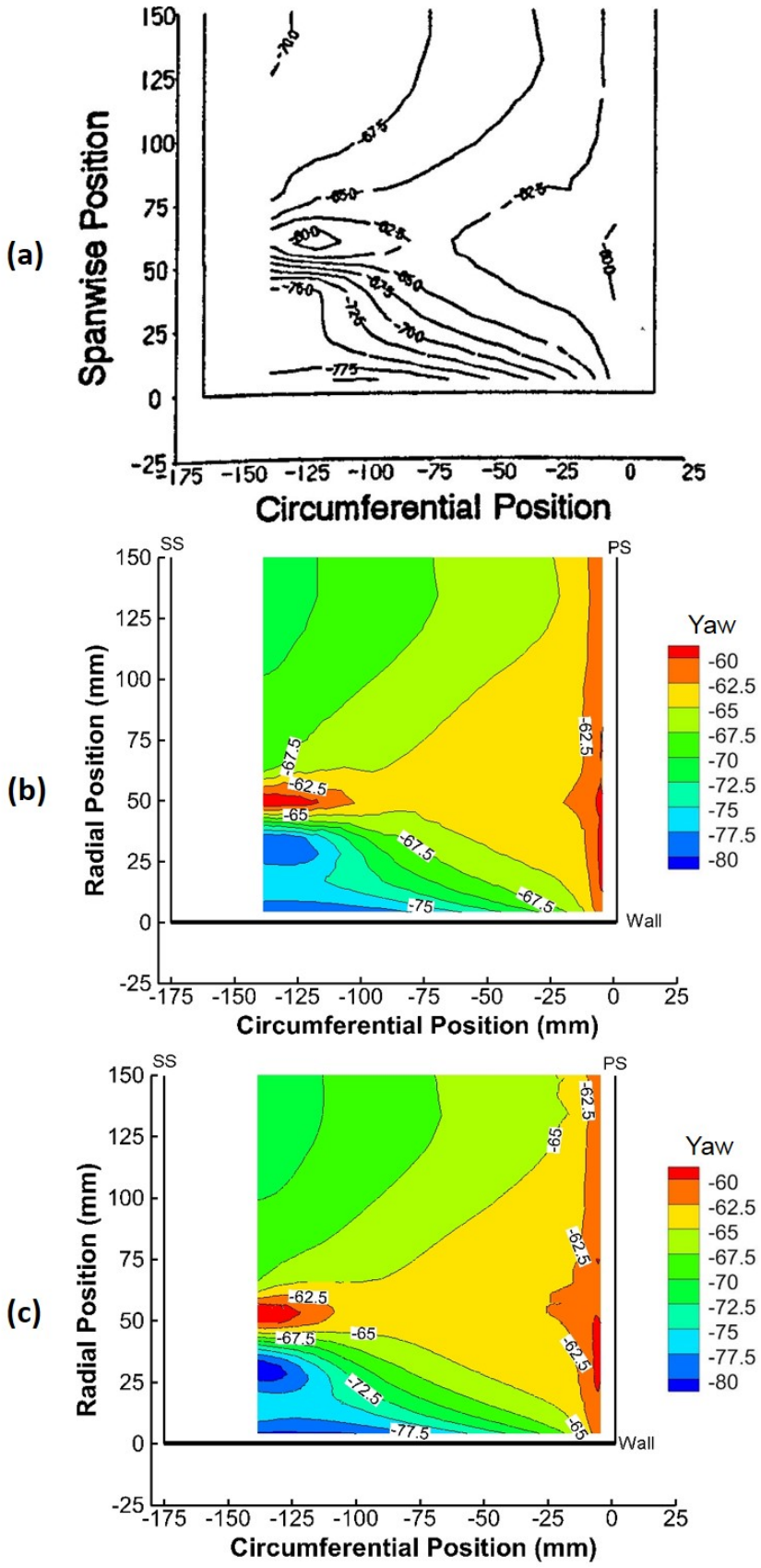


Figure 7.20: Yaw angles contours at axial chord position of C_{ax}=97% (a) Experiment by Hartland (2001); (b) Time-averaged unsteady laminar DG1; (c) Time-averaged unsteady laminar DG2

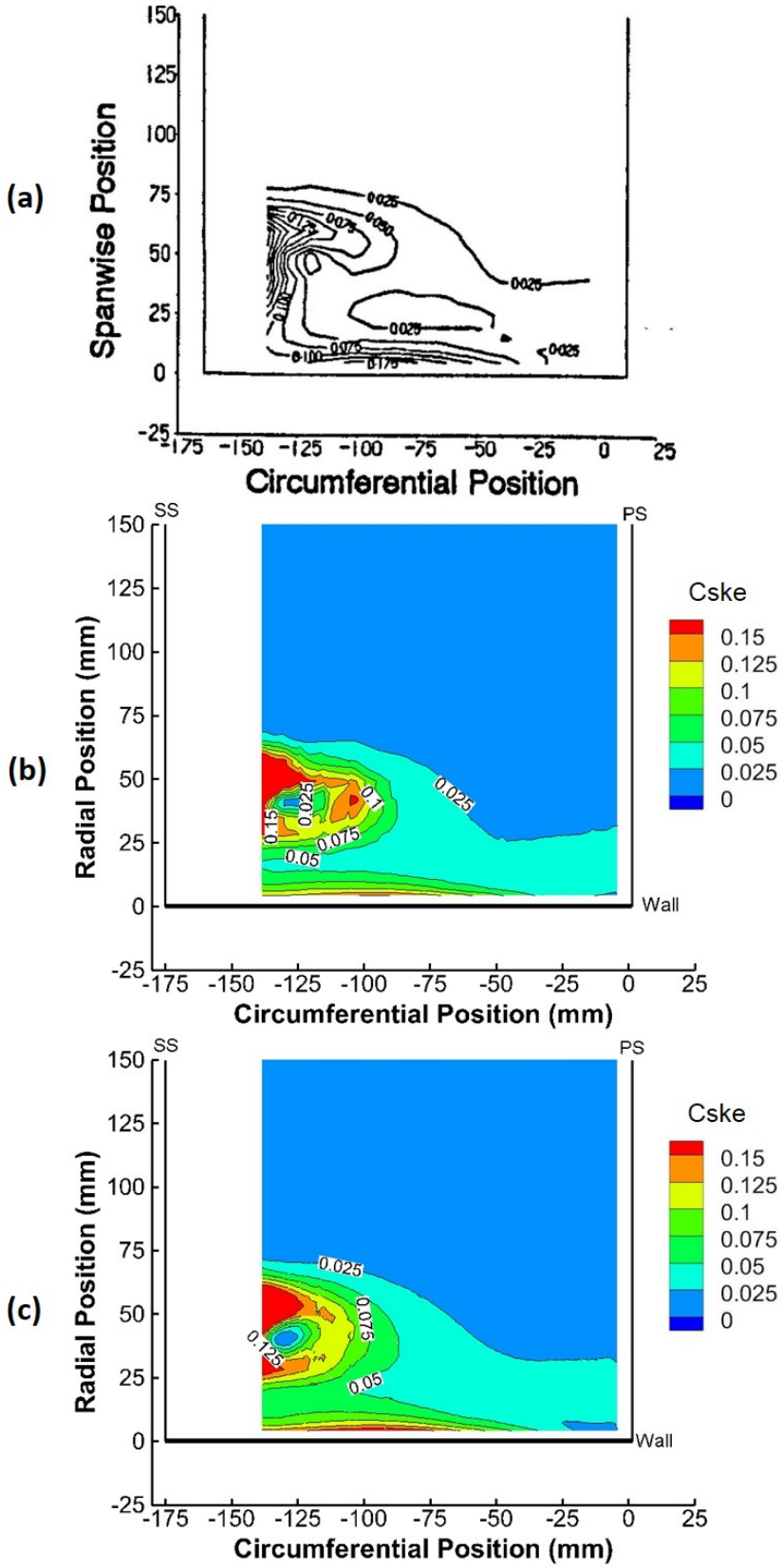


Figure 7.21: Secondary kinetic energy coefficient contours at axial chord position of C_{ax}=97% (a) Experiment by Hartland (2001); (b) Time-averaged unsteady laminar DG1; (c) Time-averaged unsteady laminar DG2

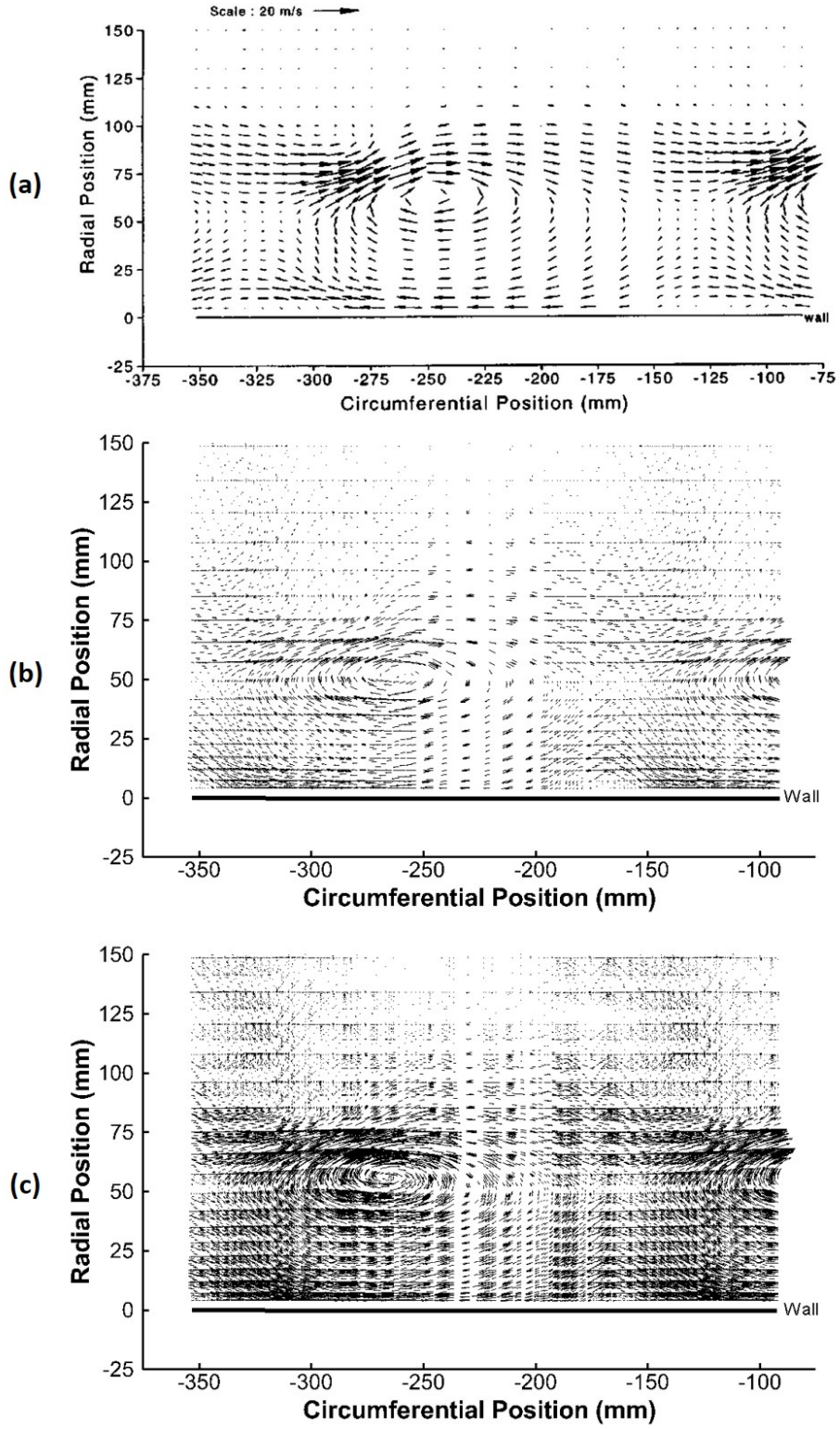


Figure 7.22: Secondary vectors at axial chord position of C_{ax}=128% (a) Experiment by Hartland et al. (2000); (b) Time-averaged unsteady laminar DG1; (c) Time-averaged unsteady laminar DG2

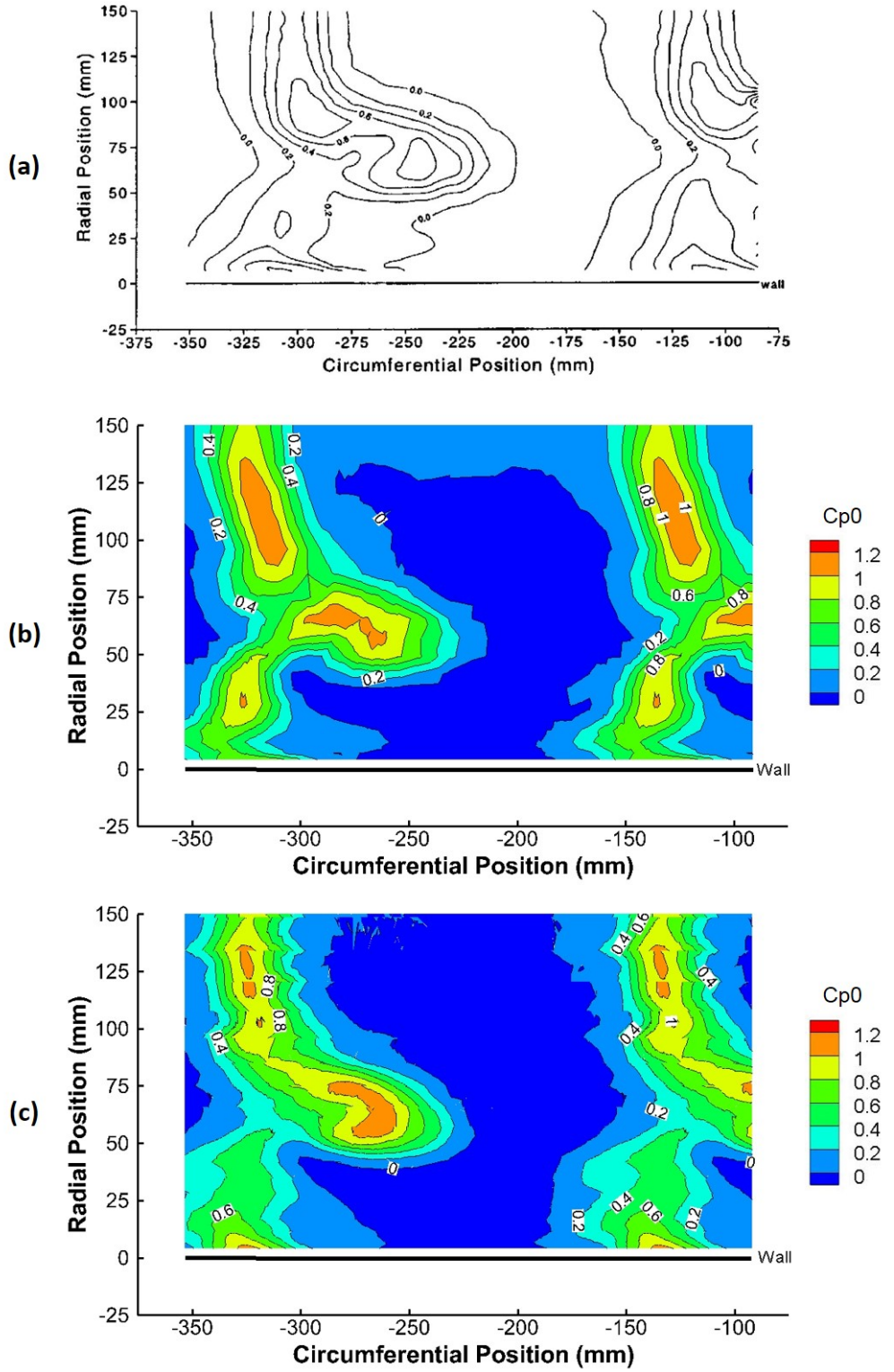


Figure 7.23: Total pressure loss coefficient contours at axial chord position of C_{ax}=128% (a) Experiment by Hartland et al. (2000); (b) Time-averaged unsteady laminar DG1; (c) Time-averaged unsteady laminar DG2

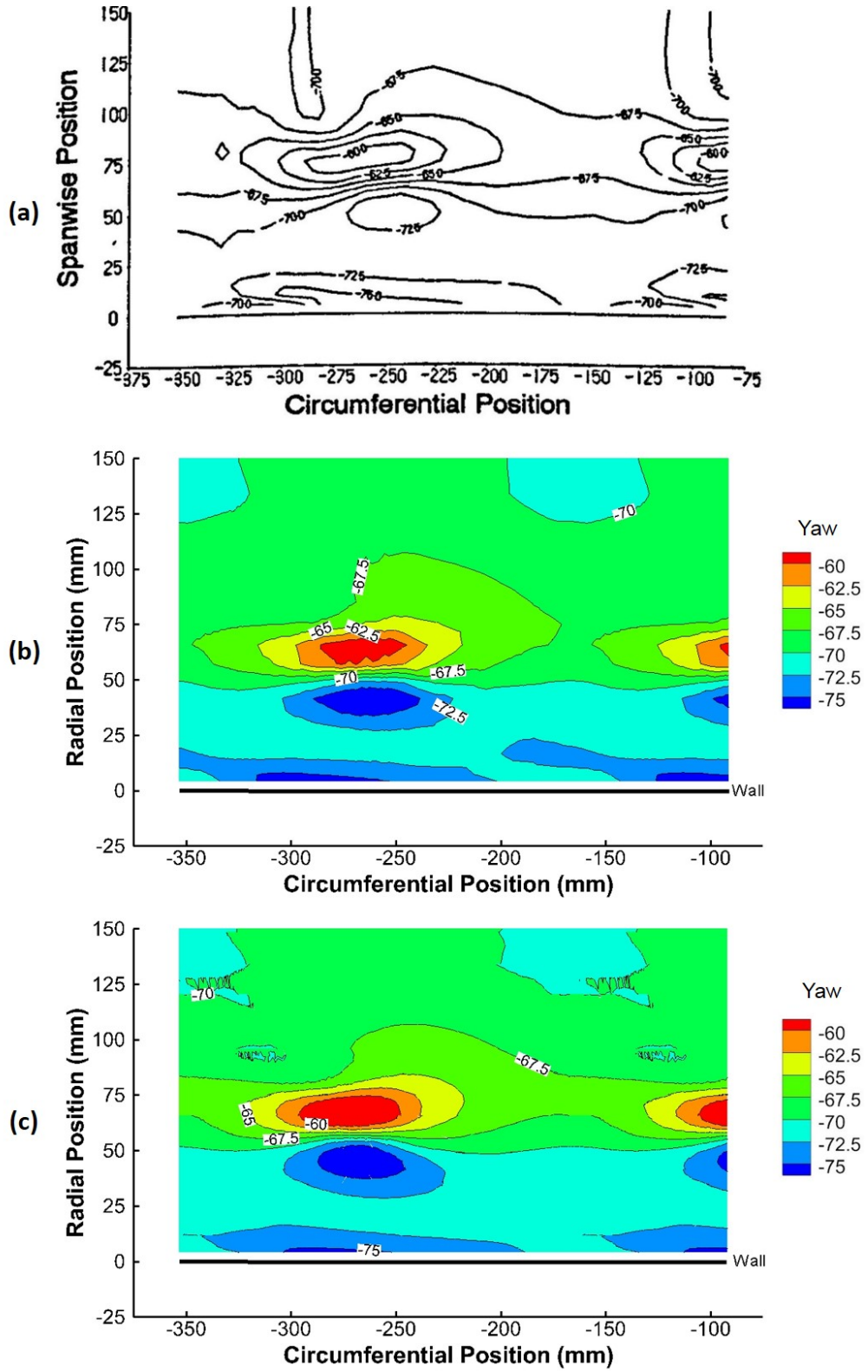


Figure 7.24: Yaw angles contours at axial chord position of C_{ax}=128% (a) Experiment by Hartland (2001); (b) Time-averaged unsteady laminar DG1; (c) Time-averaged unsteady laminar DG2

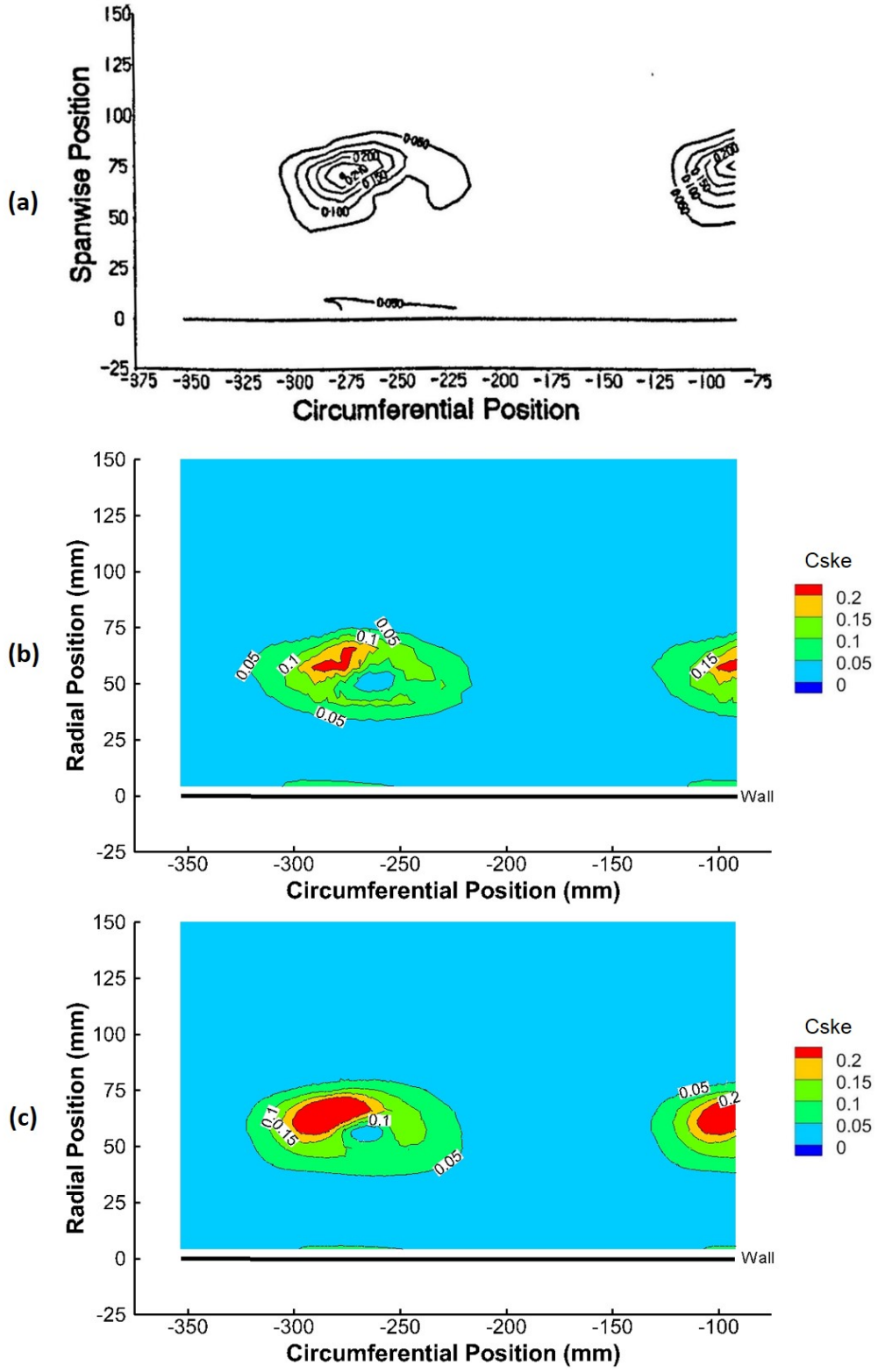


Figure 7.25: Secondary kinetic energy coefficient contours at axial chord position of C_{ax}=128% (a) Experiment by Hartland (2001); (b) Time-averaged unsteady laminar DG1; (c) Time-averaged unsteady laminar DG2

7.3.2 Pitch-Averaged Results

Furthermore, the pitchwise mass-averaged results from both the time-averaged and experimental solutions (see Hartland, 2001) at the corresponding axial chord positions will be presented in this section.

7.3.2.1 Slot 1: -9% C_{ax}

The pitch-averaged total pressure loss coefficients from the time-averaged unsteady laminar solutions show good agreement with the measured experiment one as seen in Figure 7.26(a). Note that the reference inlet boundary layer reported by Hartland (2001) has been modelled in the present unsteady laminar simulations, thus the laminar results match the upstream loss profile fairly well.

Figure 7.26(b) and Figure 7.26(c) give the pitch-averaged yaw angles and secondary kinetic energy coefficients along the span, respectively. The pitch-averaged yaw angles from the unsteady laminar solutions are in good agreement with the experimental data, whereas the secondary kinetic energy coefficients close to the endwall are slightly under-predicted.

7.3.2.2 Slot 6: 71% C_{ax}

As shown in Figure 7.27(a), the unsteady laminar solutions give an under-prediction of the pitch-averaged total pressure loss coefficients close to the endwall but show an improved prediction away from the endwall. The pitch-averaged yaw angles from the laminar solutions are in good agreement with the experimental data in Figure 7.27(b). In addition, the pitch-averaged secondary kinetic energy coefficients from both the DG solutions agree fairly well with the ones from the experiment,

as presented in Figure 7.27(c).

7.3.2.3 Slot 8: 97% C_{ax}

The pitch-averaged loss coefficients from the laminar solutions are in agreement with the experimental ones in terms of the shape of the spanwise variation as presented in Figure 7.28(a), but the position of the predicted loss peak is shown to be closer to the endwall compared to that of the experiment.

In Figure 7.28(b), the pitch-averaged yaw angles from the laminar solutions show overall agreement with the measured experiment ones, though the peak moves toward the endwall by approximately 5mm.

As shown in Figure 7.28(c), the time-averaged unsteady laminar solutions give a clear under-prediction of the pitch-averaged secondary kinetic energy coefficients near the endwall. To the present author's knowledge, this difference between the predicted and experimental pitch-averaged distributions could be attributed to the fact that the predicted secondary flow cores tend to move slightly closer to the suction surface, as seen in the time-averaged secondary coefficients contours at the same axial chord position in Figure 7.21. Thus, a less effective pitchwise range of the computed results is taken for pitch-averaging that leads to a much lower pitch-averaged distribution near the endwall.

7.3.2.4 Slot 10: 128% C_{ax}

The pitch-averaged results downstream of the trailing edge from the unsteady laminar solutions compared to the experimental data are presented in Figure 7.29. The loss peak near the endwall from the time-averaged DG1 solution is slightly over-

predicted, whereas the peak from the DG2 solution agrees with the experimental one relatively well, and both move slightly toward the endwall, as shown in Figure 7.29(a), this might be attributed to lower diffusion introduced by the laminar model. The midspan losses from the time-averaged solutions are slightly higher than the measured experiment ones. Note that the oscillations of pitch-averaged loss coefficients near the midspan might be due to lack of sufficient time steps for time-averaging.

The pitch-averaged yaw angles are presented in Figure 7.29(b), where the overturning peak from the time-averaged solution moves inward by about 5mm as well. The secondary kinetic energy coefficients from the DG2 solutions show good agreement with the experimental ones, whereas the secondary loss peak from the DG1 solutions is slightly under-predicted as illustrated in Figure 7.29(c).

Table 7.2: Laminar overall mass-averaged Cp_0 and C_{ske} at planes 97% and 128% C_{ax}

	C_{ax}=97%		C_{ax}=128%	
	Cp_0	C_{ske}	Cp_0	C_{ske}
DG1	0.005	0.0163	0.178	0.0154
DG2	0.002	0.0174	0.166	0.0181
Experiment	0.006	0.0115	0.136	0.0192

Table 7.2 gives the overall mass-averaged total pressure loss coefficients Cp_0 and secondary kinetic energy coefficients C_{ske} at planes 97% and 128% C_{ax}. Clearly the unsteady laminar solutions show reasonable agreement with the measured experiment ones in both overall and secondary losses, and a better prediction can be obtained as the order of accuracy increases.

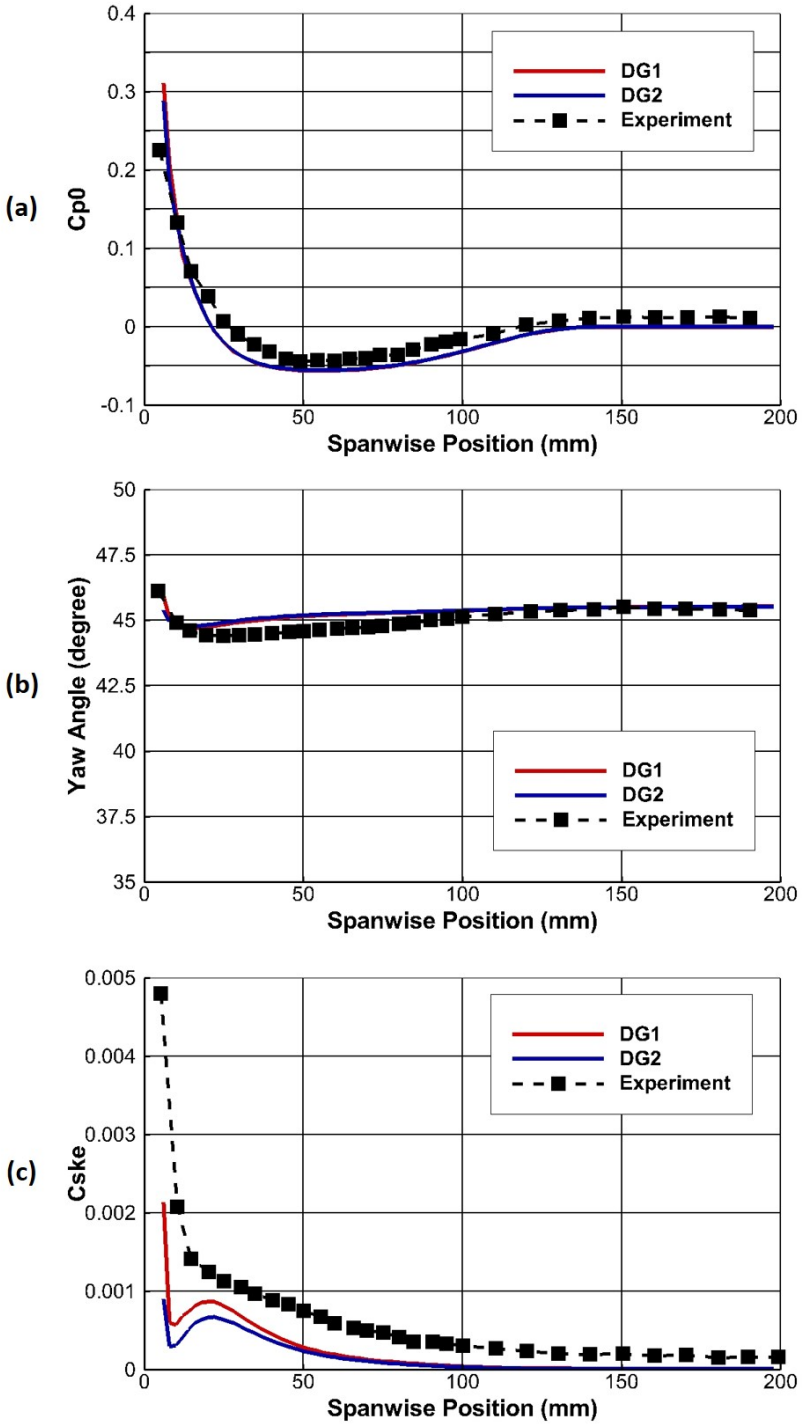


Figure 7.26: Pitch-averaged data at axial chord position of C_{ax}=-9% (a) Total pressure loss coefficient; (b) Yaw angle; (c) Secondary kinetic energy coefficient (Experiment denotes the measured data by Hartland, 2001)

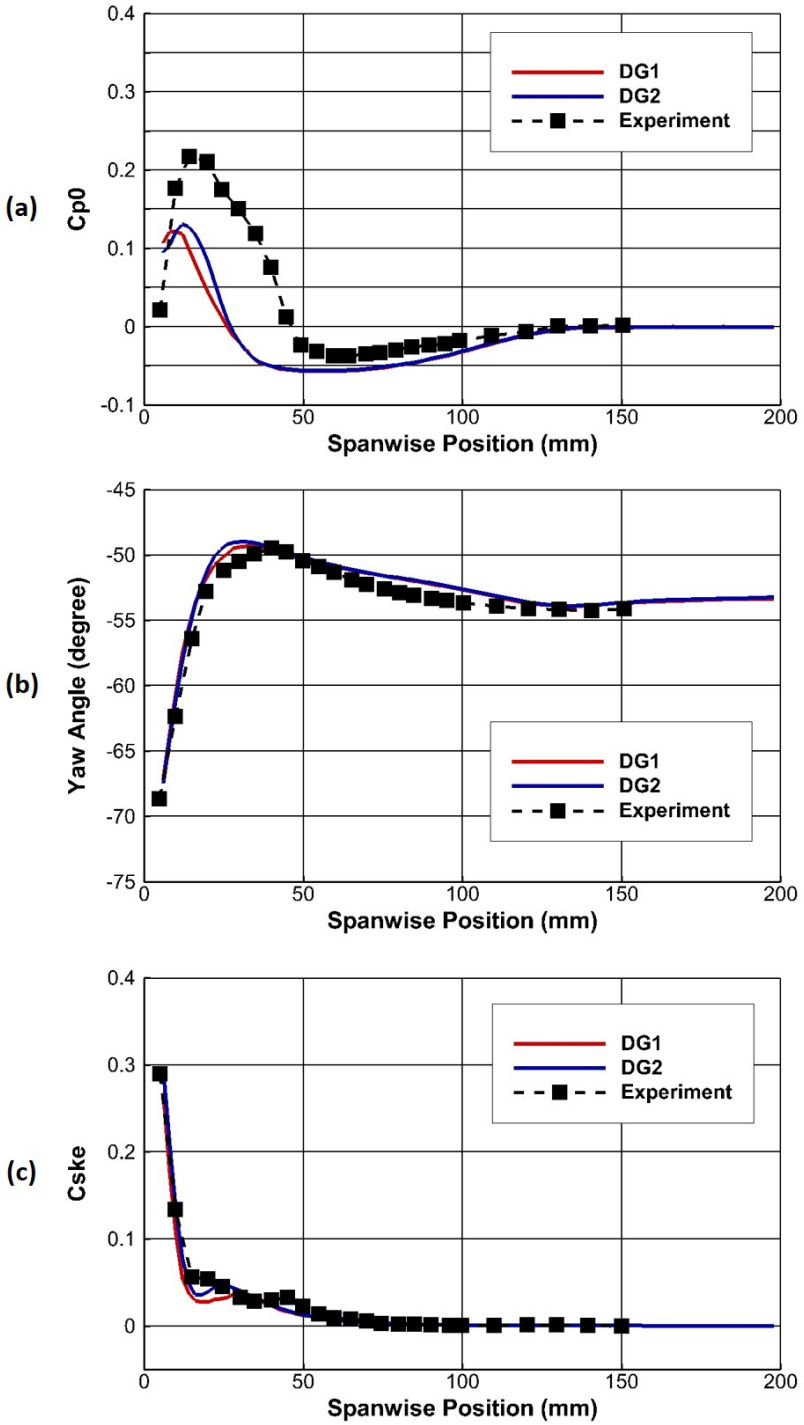


Figure 7.27: Pitch-averaged data at axial chord position of C_{ax}=71% (a) Total pressure loss coefficient; (b) Yaw angle; (c) Secondary kinetic energy coefficient (Experiment denotes the measured data by Hartland, 2001)

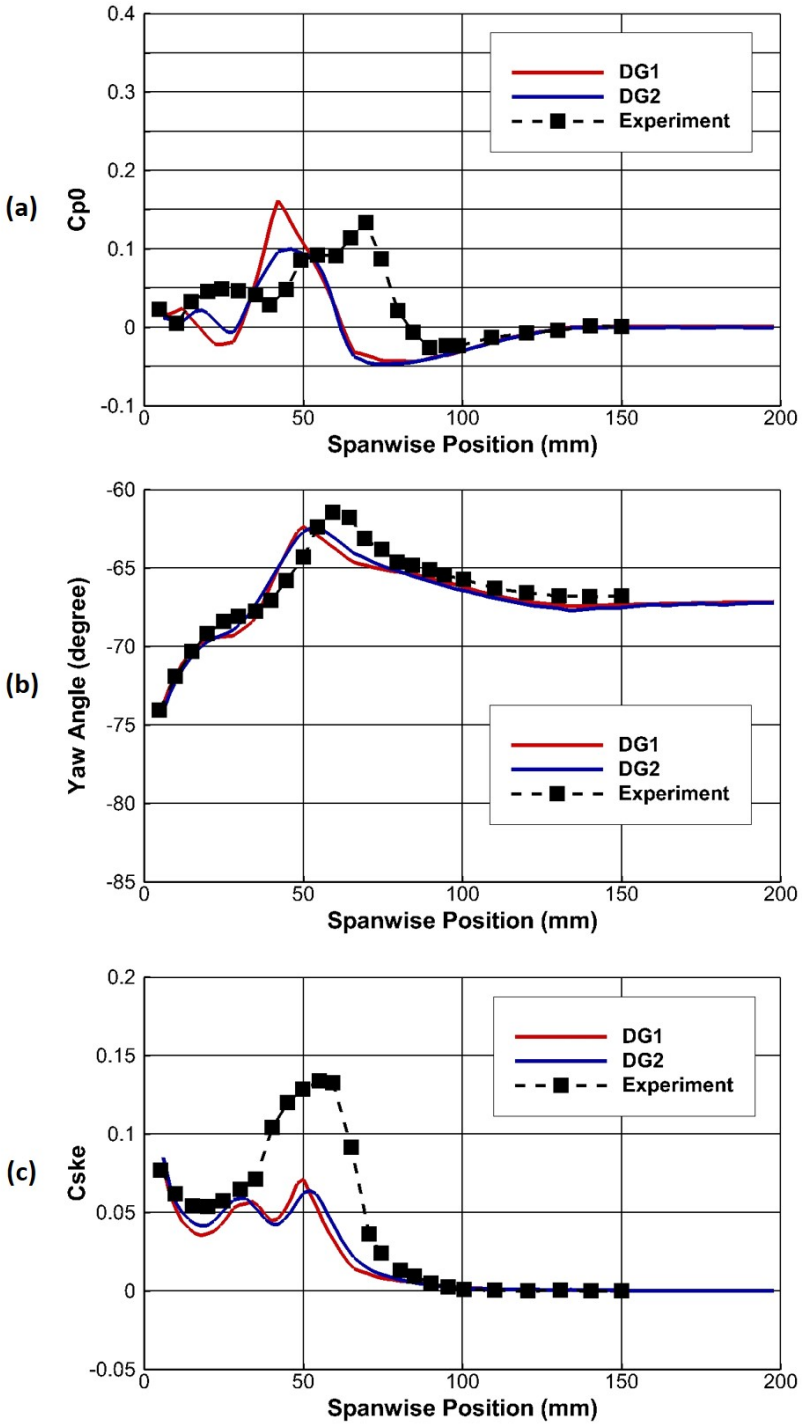


Figure 7.28: Pitch-averaged data at axial chord position of C_{ax}=97% (a) Total pressure loss coefficient; (b) Yaw angle; (c) Secondary kinetic energy coefficient (Experiment denotes the measured data by Hartland, 2001)

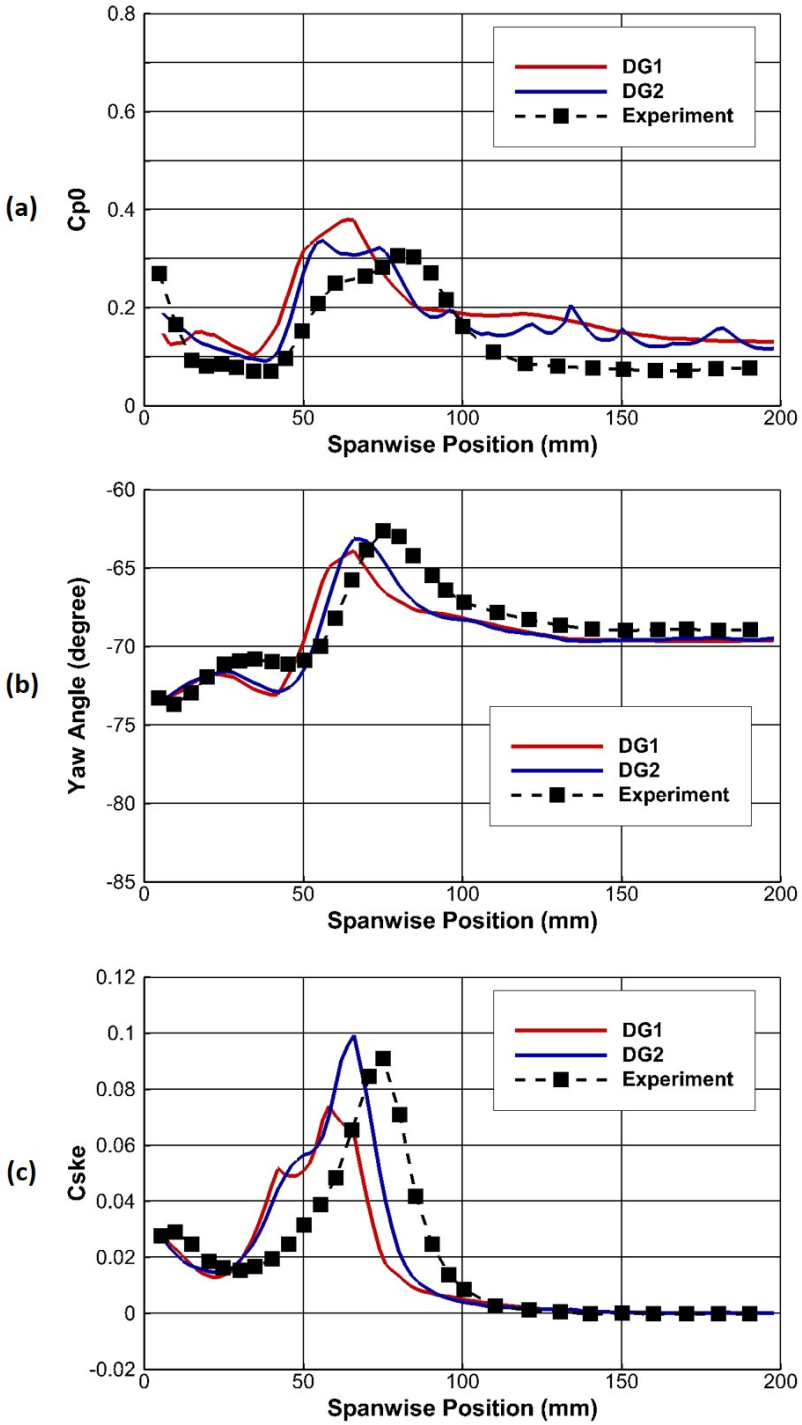


Figure 7.29: Pitch-averaged data at axial chord position of C_{ax}=128% (a) Total pressure loss coefficient; (b) Yaw angle; (c) Secondary kinetic energy coefficient (Experiment denotes the measured data by Hartland, 2001)

7.3.3 Further Comparison between Unsteady Laminar and RANS

In order to further assess the predictability of aerodynamic performance of 3D blades influenced by both endwall secondary flow and blade surface bubble type separation, a comparison study between the unsteady laminar and the RANS results will be carried out in this section.

The 3rd-order accurate (DG2) results of total pressure loss coefficients Cp_0 from the time-averaged unsteady laminar and the RANS solutions compared to the measured experiment data by Hartland et al. (2000) are presented in Figure 7.30. The measured data of the experiment illustrated in Figure 7.30(a) show a passage vortex, a main counter vortex sits farther from the endwall while a small counter vortex is located in a crossflow region near the endwall. Next, the time-averaged unsteady laminar and the RANS results of the computations are shown in Figures 7.30(b) and 7.30(c) respectively. The RANS solution significantly over-predicts the passage vortex core, in line with the over-predictions of loss cores from previous RANS results by Cleak and Gregory-Smith (1992), Moore and Gregory-Smith (1996) and Kiran and Anish (2017), whereas the laminar solution distinctively predicts this loss peak as well as the counter vortex located farther above the passage vortex. Moreover, the losses near the midspan are clearly over-predicted by the RANS solutions but are reasonably well predicted by the unsteady laminar solution. Both the RANS and laminar solutions capture the small counter vortex close to the endwall. Overall, the total pressure losses of the laminar solution are much better predicted than that of the RANS solution.

Furthermore, a more detailed comparison is made by means of the pitchwise mass-averaged flow performance parameters. The pitchwise mass-averaged Cp_0 at planes 97% and 128% C_{ax} are shown in Figures 7.31(a) and 7.31(b) respectively. Compared to the RANS solution, the loss peak predicted by the present unsteady laminar solution shows a significant reduction, thus is much closer to the experimental value. Yet the peak moves slightly towards the endwall, this might be attributed to lack of turbulence diffusion of the endwall flow as predicted by the laminar flow model. Near the midspan, the losses from the direct laminar are comparable to the experimental one, though still slightly higher at plane 128% C_{ax} as shown in Figure 7.31(b).

Table 7.3: Overall mass-averaged Cp_0 at planes 97% and 128% C_{ax}

	97% C_{ax}	128% C_{ax}
DG2 RANS	0.041	0.245
DG2 Laminar	0.002	0.166
Experiment	0.006	0.136

The overall mass-averaged total pressure loss values at planes 97% and 128% C_{ax} are given in Table 7.3. The unsteady laminar solution shows a significantly loss reduction comparing to the RANS solution and agrees reasonably well with the experimental one.

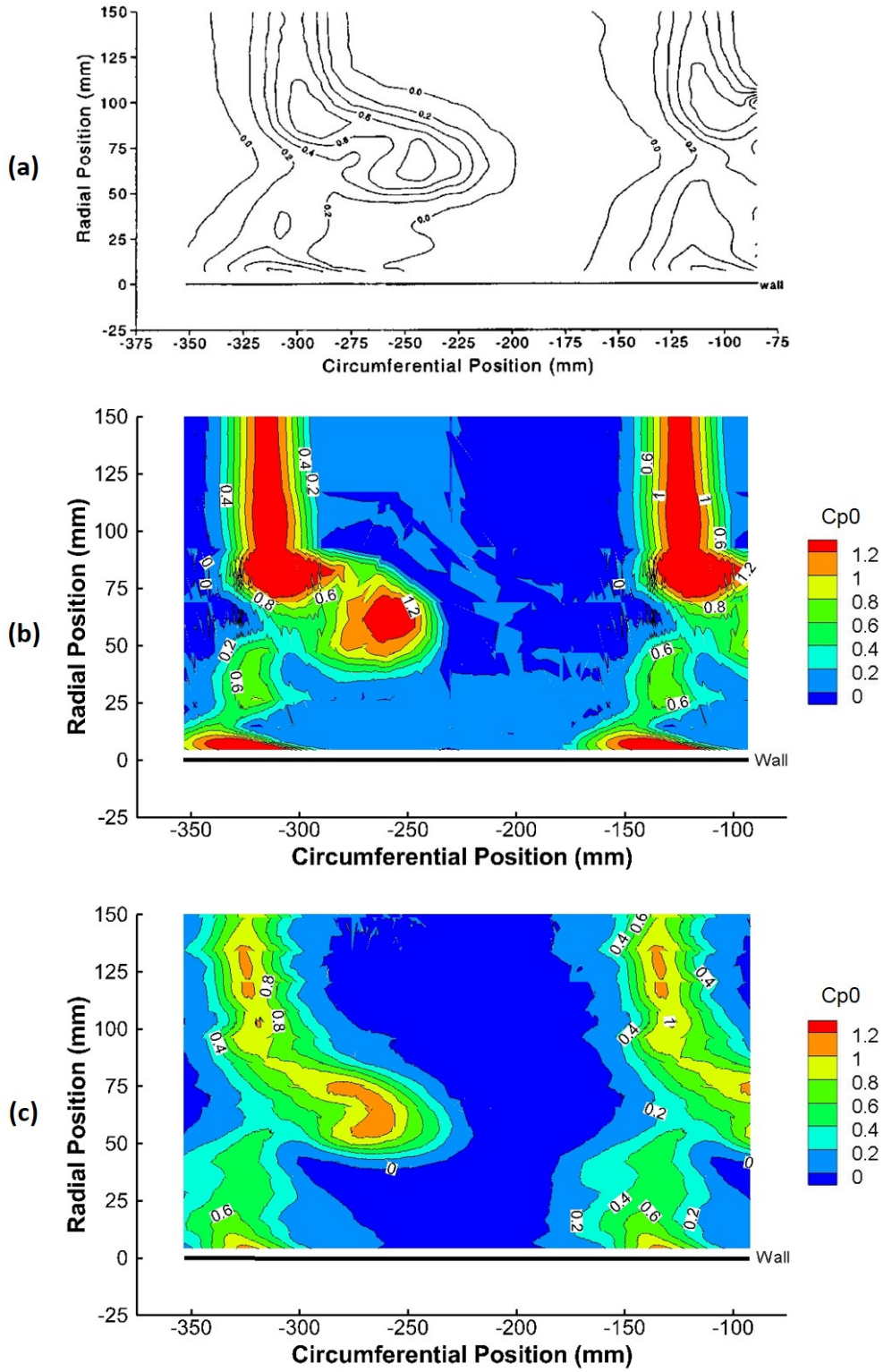
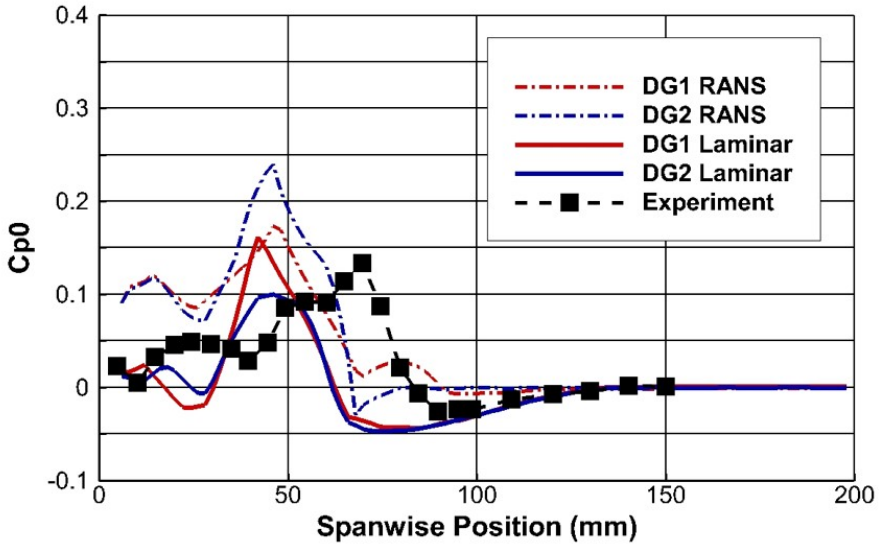
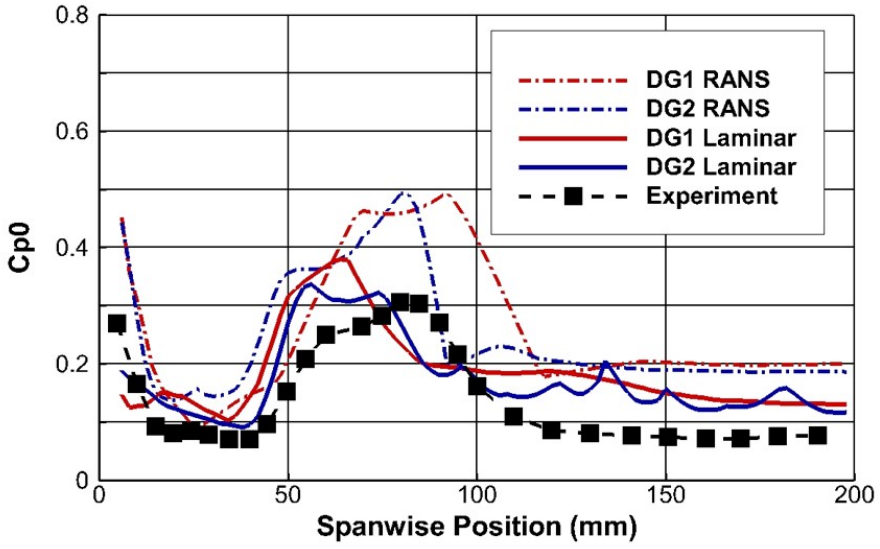


Figure 7.30: Comparison of total pressure loss coefficient contours at axial chord position of C_{ax}=128% (a) Experiment by Hartland et al. (2000); (b) DG2 RANS; (c) DG2 time-averaged unsteady laminar



(a) 97% C_{ax}



(b) 128% C_{ax}

Figure 7.31: Comparison of pitch-averaged total pressure loss coefficient at axial chord positions of (a) C_{ax}=97% (b) C_{ax}=128% (Experiment denotes the measured data by Hartland, 2001)

7.4 Summary

Due to the consistent over-prediction of flow losses by the RANS solutions, further considerations on whether the flow with a shear layer instability and a trailing edge vortex shedding can be modelled by the RANS model lead to a direct unsteady laminar approach for this Durham cascade.

The sensitivity study on the temporal resolution for the unsteady laminar solution on a 2D blade has been first performed. The unsteady laminar results show that the flow behaviour is largely consistent once the time step size reaches a certain point, where the shed vortices from both the separated shear layer and trailing edge vortex shedding can be largely resolved. A following time-averaged solution shows that the separated shear layer is effectively reattached to the boundary layer with well resolved large unsteadiness. The time step size found for this 2D time-consistent solution is applied for the subsequent 3D simulations. Note that the mesh resolution for the unsteady laminar approach is far more coarser than that for a typical LES, though slightly finer than that for the RANS simulations.

Next, the comparison between the 3D time-averaged unsteady laminar results and the experimental data has been presented through the traverse plots and pitch-averaged distributions in detail. The time-averaged unsteady laminar results show a distinctively better prediction of the flow losses through the blade passage. This might lead to an answer to the question put forward in Section 6.4 in Chapter 6. The flow losses influenced by both the endwall secondary flow and the laminar separation on the suction surface have been and will be consistently over-predicted by the RANS solution, however, the present unsteady laminar approach seems

to provide a useful alternative solution for the turbine blade flows, similar to the one presently tested, instead of the full-scale LES.

8 Conclusions and Recommendations

This final chapter will present the conclusions of the present study, followed by the recommendations for the future work.

8.1 Conclusions

In this present work, an implicit solver using the Discontinuous Galerkin (DG) discretization on unstructured meshes has been developed, validated and applied for analysis of the turbine blade flows. The DG scheme is distinctive in that a higher order accuracy is achieved by simple internal sub-divisions of a given mesh cell. This, in combination with the implicit time-integration formulation as well as an all-speed flux scheme, is well suited for an unstructured mesh solver.

8.1.1 Method Implementation

The DG discretization of the Navier-Stokes equation has been performed on a 3D computational domain consisting of unstructured tetrahedra elements. The inviscid flux across the element interfaces are computed using the upwind flux scheme called

AUSM$^+$-up flux. The discretization of the viscous terms are conducted using the BR2 method, which includes a local lifting operator instead of a global one to ensure that, for each single element, only information from neighbouring elements are needed, thus there is no need to construct extended stencils for high-order simulations. In addition, the Jacobian of both the inviscid and viscous terms are also calculated and implemented in the present DG solver. There are various boundary conditions implemented, including subsonic inflow, subsonic outflow, no-slip wall, slip wall, characteristic farfield and periodic boundary conditions.

For the implicit time integration strategy, the preconditioned Newton-GMRES method is adopted and implemented with three preconditioned methods, including block ILU0, block Jacobi and block GS. Furthermore, the local time stepping is adopted in the steady simulations with increased convergence while constant time stepping can also be applied for unsteady simulations.

The DG discretization of the RANS equations with one equation SA model is also implemented in a tightly coupled manner, of which all the five conservatives variable with the turbulence working variable are solved together in the system equations. Furthermore, a modified version of the SA model preventing the negative working values is also implemented for high-order simulations for turbulent flow.

8.1.2 Validation Work

The preliminary test for a flow around cylinder up to 5th-oder of accuracy is conducted to verify the method implementation, and also illustrate the importance of a higher-order geometrical representation. It is concluded that the flow field is

better resolved as the order of accuracy increases with the corresponding order of polynomials representing the curved boundary. It should be highlighted that the high-order simulations might not be meaningful without proper curved boundary representations for those coarse linear boundary meshes.

A laminar vortex shedding has been performed to validate the unsteady viscous flow modelling capability and another laminar flat boundary layer has been validated against the analytical Blasius solution. Those laminar validation studies demonstrate the proper discretization of viscous flux using the BR2 scheme and the robust steady and unsteady modelling capabilities owing to the implicit time marching with the preconditioned Newton-GMRES method.

A test for a flat plate turbulent boundary layer shows the good performance of modified SA turbulence in terms of both accuracy and robustness. The results also highlight advantage of the simple internal sub-division of a mesh cell in relaxing the fine near wall mesh generation as required by a conventional low-order scheme.

A final test for the all-speed flow past an airfoil demonstrates the great capability of AUSM$^+$-up scheme in solving the flow with a wide speed range. To the best knowledge of the present author, this novel approach of combining the implicit high-order DG method with all-speed AUSM$^+$-up scheme on unstructured mesh for the turbomachinery flow has not been reported by others yet.

8.1.3 Turbomachinery Application

The developed DG solver is then applied to a high pressure turbine cascade (Durham cascade) for which flow losses are strongly influenced by the boundary layer transition

on the blade surface and the secondary flow development in the endwall region. The validation studies using the 2nd and 3rd order DG schemes based on the RANS with a one-equation turbulence model show consistent over-predictions of the flow losses, in line with previous RANS solutions.

The more interesting and remarkable observation is that the flow losses predicted by a direct unsteady laminar solution are consistently better than those produced by the RANS solution. Noting that the present unsteady laminar solutions are produced on a much coarser spatial and temporal resolutions than those typically required for a full scale LES, the results seem to indicate that a coarse mesh unsteady laminar solution may be further explored as a possible option for turbine blading aerodynamics analyses.

8.2 Recommendations for Future work

This section will provide some recommendations for the future work based on the findings from the present author. The recommendations for both methodology development and turbomachinery applications are listed as following.

8.2.1 Further Methodology Development

- It would be of practical interest to further develop the solver to accommodate more types of mesh, including the hexahedron and pyramid, for further applications with complex geometry;

- For high Reynolds turbulent flows, more layers of near wall meshes need to be curved for predicting the thin boundary layer; Thus, the preprocessing of

the mesh need to be reconstructed to accommodate the multi-layer curved boundary meshes;

- The burden of requiring large amount of computer memory to store the Jacobian matrix for the implicit high-order simulation could be alleviated by adopting a matrix-free scheme for the present solver;

- It would be of great interest to include the hp-adaptation in the present solver to give more adaptability in the practical applications.

8.2.2 Future Applications

- The all-speed turbomachinery cases could be adopted for high-order DG simulations, such as coolant flows, cavity flows and leakage flows;

- The high-order DG simulations of the rotor blade rows in multiple rotor-stator stages could be carried out with the mixing plane concept across the interface and the replacement of the Cartesian coordinates with the cylindrical coordinates in the solver could be better for the simulations of rotor-stator blade row interactions;

- The performance of direct unsteady laminar approach need to be further assessed in another case, similar to the present one; In addition, the minimum requirement of mesh counts and time step size for the unsteady laminar approach could be further explored, which should give some basic guidance on future work using this method;

- The LES or DNS approach for the present Durham cascade could be carried

out. For the sake of saving the computational resources, the hybrid LES-RANS method could be firstly implemented and examined.

Bibliography

[1] A. Arnone. “Viscous analysis of 3-d rotor flow using a multigrid method”. In: *ASME J. Turbomach* 116.3 (1994), 435–445.

[2] A. Arnone, M. S. Liou, and L. A. Povinelli. “Integration of Navier–Stokes Equations Using Dual Time Stepping and a Multigrid Method”. In: *AIAA J.* 33.6 (1995), 985–990.

[3] I. Babuska, B. A. Szabo, and I. N. Katz. “The P-Version of the Finite Element Method”. In: *SIAM J. Numer. Anal.* 18.3 (1981), pp. 515–545.

[4] G. E. Barter. “Shock Capturing with PDE-Based Artificial Viscosity for an Adaptive, Higher-Order Discontinuous Galerkin Finite Element Method”. PhD thesis. Massachusetts Institute of Technology, 2008.

[5] T. J. Barth. “Recent Developments in High Order K-Exact Reconstruction on Unstructured Meshes”. In: 31st AIAA Aerospace Sciences Meeting and Exhibit. Reno, NV, U.S.A., 1993.

[6] F. Bassi and S. Rebay. “A High-order Accurate Discontinuous Finite Element Method for the Numerical Solution of the Compressible Navier-Stokes Equations”. In: *Journal of Computational Physics* 131 (1997), pp. 267–279.

[7] F. Bassi and S. Rebay. “High-Order Accurate Discontinuous Finite Element Solution of the 2D Euler Equations”. In: *Journal of Computational Physics* 138 (1997), pp. 251–285.

[8] F. Bassi and S. Rebay. “GMRES Discontinuous Galerkin Solution of the Compressible Navier-Stokes Equations”. In: *Discontinuous Galerkin Methods*. Ed. by B. Cockburn, G. E. Karniadakis, and C.-W. Shu. Berlin, Heidelberg: Springer Berlin Heidelberg, 2000, pp. 197–208.

[9] F. Bassi and S. Rebay. “Numerical evaluation of two discontinuous Galerkin methods for the compressible Navier–Stokes equations”. In: *International Journal for Numerical Methods in Fluids* 40.1-2 (2002), 197–207.

[10] F. Bassi et al. “Discontinuous Galerkin solution of the Reynolds-averaged Navier-Stokes and k-ω turbulence model equations”. In: *Computers and Fluids* 34 (2005), pp. 507–540.

[11] F. Bassi et al. “An implicit high-order discontinuous Galerkin method for steady and unsteady incompressible flows”. In: *Computers and Fluids* 36.10 (2007), pp. 1529–1546.

[12] F. Bassi et al. "High-Order Discontinuous Galerkin Discretization of Transonic Turbulent Flows". In: 47th AIAA Aerospace Sciences Meeting. Orlando, Florida, 2009.

[13] F. Bassi et al. "Assessment of a high-order accurate discontinuous Galerkin method for turbomachinery flows". In: *International Journal of Computational Fluid Dynamics* 30.4 (2016), 307–328.

[14] G. Batchelor. *An Introduction to Fluid Dynamics*. Cambridge University Press, 2000.

[15] H. Blasius. *The Boundary Layers in Fluids With Little Friction*. NACA-TM-1256. National Advisory Committee for Aeronautics, 1950.

[16] N. Burgess and D. Mavriplis. "High-order Discontinuous Galerkin Methods for Turbulent High-lift Flows". In: Seventh International Conference on Computational Fluid Dynamics (ICCFD7). Big Island, Hawaii, 2012.

[17] N. Burgess and D. Mavriplis. "Robust Computation of Turbulent Flows Using a Discontinuous Galerkin Method". In: 50th AIAA Aerospace Sciences Meeting. Nashville, Tennessee, 2012.

[18] J.-R. Carlson. *Inflow/Outflow Boundary Conditions with Application to FUN3D*. NASA/TM–2011-217181. NASA, 2011.

[19] Cast. *Fundamentals of Gas Turbine Engines*. 1997. URL: `http://cast-safety.org/pdf/3_engine_fundamentals.pdf`.

[20] J. E. Castillo. *Mathematical Aspects of Numerical Grid Generation*. Ed. by J. E. Castillo. Society for Industrial and Applied Mathematics, 1991.

[21] P. Castonguay, P. E. Vincent, and A. Jameson. "A New Class of High-Order Energy Stable Flux Reconstruction Schemes for Triangular Elements". In: *Journal of Scientific Computing* 51.1 (2012), 224–256.

[22] J. G. E. Cleak and D. G. Gregory-Smith. "Turbulence Modeling for Secondary Flow Prediction in a Turbine Cascade". In: *ASME J. Turbomach* 114.3 (1992), pp. 590–598.

[23] B. Cockburn and C. W. Shu. "TVD Runge-Kutta Local Projection Discontinuous Galerkin Finite Element Method for Scalar Conservation Laws II: General Framework". In: *Mathematics of Computation* 52 (1989), pp. 411–435.

[24] B. Cockburn and C. W. Shu. "The Runge-Kutta Local Projection p1-Discontinuous Galerkin Method for Scalar Conservation Laws". In: *M2AN* 25 (1991), pp. 337–361.

[25] B. Cockburn and C. W. Shu. "The Runge-Kutta Discontinuous Galerkin Finite Element Method for Conservation Laws V: Multidimensional Systems". In: *Journal of Computational Physics* 141 (1998), pp. 199–224.

[26] B. Cockburn and C. Shu. "The Local Discontinuous Galerkin Method for Time-Dependent Convection-Diffusion Systems". In: *SIAM Journal of Numerical Analysis* 35 (1998), 2440–2463.

[27] B. Cockburn and C. Shu. "Runge–Kutta Discontinuous Galerkin Methods for Convection-Dominated Problems". In: *Journal of Scientific Computing* 16.3 (2001), pp. 173–261.

[28] B. Cockburn, S. Y. Lin, and C. W. Shu. "TVD Runge-Kutta Local Projection Discontinuous Galerkin Finite Element Method for Conservation Laws III: One Dimensional Systems". In: *Journal of Computational Physics* 84 (1989), pp. 90–113.

[29] B. Cockburn, S. Hou, and C. W. Shu. "TVD Runge-Kutta Local Projection Discontinuous Galerkin Finite Element Method for Conservation Laws IV: The Multidimensional Case". In: *Mathematics of Computation* 54 (1990), pp. 545–581.

[30] B. Cockburn et al. "Local Discontinuous Galerkin Methods for the Stokes System". In: *SIAM Journal of Numerical Analysis* 40.1 (2002), 319–343.

[31] B. Cockburn, G. Kanschat, and D. Schötzau. "A locally conservative LDG method for the incompressible Navier-Stokes equations". In: *Math. Comp.* 74.251 (2005), pp. 1067–1095.

[32] A. Crivellini and F. Bassi. "An implicit matrix-free Discontinuous Galerkin solver for viscous and turbulent aerodynamic simulations". In: *Computers and Fluids* 50.1 (2011), pp. 81–93.

[33] W. Dawes. "Development of a 3D Navier–Stokes solver for application to all types of turbomachinery". In: *ASME Paper No. 88-GT-70* (1988).

[34] W. Dawes. "Toward improved throughflow capability: the use of three-dimensional viscous flow solvers in a multistage environment". In: *ASME J. Turbomach* 114.1 (1992).

[35] C. C. de Wiart, K. Hillewaert, and P. Geuzaine. "DNS of a Low Pressure Turbine Blade Computed with the Discontinuous Galerkin Method". In: ASME Turbo Expo 2012: Turbine Technical Conference and Exposition. Copenhagen, Denmark, 2012.

[36] C. C. de Wiart et al. "Development of a Discontinuous Galerkin Solver for High-Quality Wall-Resolved/Moddelled DNS and LES for Practical Turbomachinery Flows on Fully Unstructured Meshes". In: ASME Turbo Expo 2015: Turbine Technical Conference and Exposition. Montreal, Quebec, Canada, 2015.

[37] J. D. Denton. *A time marching method for two and three dimensional blade to blade flows*. Tech. rep. ARC R M 3775, 1975.

[38] J. D. Denton. "An improved time-marching method for turbomachinery flow calculation". In: *Journal of Engineering for Power* 105.3 (1983), 514–521.

[39] J. D. Denton. "The calculation of three-dimensional viscous flow through multistage turbomachine". In: *ASME J. Turbomach* 114.1 (1992), pp. 18–26.

[40] J. D. Denton. "Loss mechanisms in turbomachines". In: *ASME J. Turbomach* 115.4 (1993), pp. 621–656.

[41] L. T. Diosady and D. L. Darmofal. "Preconditioning methods for discontinuous Galerkin solutions of the Navier–Stokes equations". In: *Journal of Computational Physics* 228.11 (2009), pp. 3917–3935.

[42] S. Elnaz Naghibi et al. "Fast spectral solutions of the double-gyre problem in a turbulent flow regime". In: *Applied Mathematical Modelling* 66 (2019), pp. 745–767.

[43] G. A. Faranosov et al. "CABARET method on unstructured hexahedral grids for jet noise computation". In: *Computers and Fluids* 88.15 (2013), pp. 165–179.

[44] A. Garai et al. "DNS of Flow in a Low-Pressure Turbine Cascade Using a Discontinuous-Galerkin Spectral-Element Method". In: ASME Turbo Expo 2015: Turbine Technical Conference and Exposition. Montreal, Quebec, Canada, 2015.

[45] A. Garai et al. "DNS of Low-Pressure Turbine Cascade Flows With Elevated Inflow Turbulence Using a Discontinuous-Galerkin Spectral-Element Method". In: ASME Turbo Expo 2016: Turbine Technical Conference and Exposition. Seoul, South Korea, 2016.

[46] P. L. George, F. Hecht, and E. Saltel. "Automatic mesh generator with specified boundary". In: *Computer Methods in Applied Mechanics and Engineering* 92.3 (1991), pp. 269–288.

[47] P. L. George. *Automatic mesh generation : application to finite element methods*. Chichester; New York : J. Wiley; Paris : Masson, 1991.

[48] A. Ghidoni et al. "Simulation of the transitional flow in a low pressure gas turbine cascade with a high-order discontinuous Galerkin method". In: *ASME J. Fluids Eng.* 135.7 (2013), p. 071101.

[49] M. Giles. "An Approach for Multi-Stage Calculations Incorporating Unsteadiness". In: *ASME Paper 92-GT-282* (1992).

[50] M. B. Giles. "Calculation of unsteady wake/rotor interaction". In: *Journal of Propulsion and Power* 4.4 (1988), pp. 356–362.

[51] M. B. Giles. "Stator/rotor interaction in a transonic turbine". In: *Journal of Propulsion and Power* 6.5 (1990), pp. 621–627.

[52] D. G. Gregory-Smith and J. G. E. Cleak. "Secondary Flow Measurements in a Turbine Cascade With High Inlet Turbulence". In: *ASME J. Turbomach* 114.1 (1992), pp. 173–183.

[53] D. G. Gregory-Smith, C. P. Graves, and J. A. Walsh. "Growth of Secondary Losses and Vorticity in an Axial Turbine Cascade". In: *ASME J. Turbomach* 110.1 (1988), pp. 1–8.

[54] C. Hah. "Calculation of three-dimensional viscous flows in turbomachinery with an implicit relaxation method". In: *Journal of Propulsion and Power* 3.5 (1987), pp. 415–422.

[55] J. C. Hartland. "Secondary loss reduction in rotor blades by non-axisymmetric end-wall profiling". PhD thesis. University of Durham, 2001.

[56] J. C. Hartland et al. "Nonaxisymmetric Turbine End Wall Design: Part II—Experimental Validation". In: *ASME J. Turbomach* 122.2 (2000), pp. 286–293.

[57] R. Hartmann. *Numerical Analysis of Higher Order Discontinuous Galerkin Finite Element Methods*. Ed. by H. Deconinck. 2008.

[58] R. Hartmann. "Higher-order and adaptive discontinuous Galerkin methods with shock-capturing applied to transonic turbulent delta wing flow". In: *International Journal for Numerical Methods in Fluids* 72.8 (2013), pp. 883–894.

[59] R. Hartmann, J. Held, and T. Leicht. "Adjoint-based error estimation and adaptive mesh refinement for the RANS and k-ω turbulence model equations". In: *Journal of Computational Physics* 230.11 (2011), pp. 4268–4284.

[60] L. He. "New Two-Grid Acceleration Method for Unsteady Navier-Stokes Calculations". In: *AIAA Journal of Propulsion and Power* 9.2 (1993), pp. 272–280.

[61] L. He. "Unsteady Flow in Oscillating Turbine Cascades: Part 2—Computational Study". In: *ASME J. Turbomach* 120.2 (1998), pp. 269–275.

[62] L. He. "Three-dimensional unsteady Navier—Stokes analysis of stator—rotor interaction in axial-flow turbines". In: *Proceedings of the Institution of Mechanical Engineers, Part A: Journal of Power and Energy* 214.1 (2000), 13–22.

[63] L. He. "Fourier methods for turbomachinery applications". In: *Progress in Aerospace Sciences* 46.8 (2010), pp. 329–341.

[64] L. He. "Multiscale block spectral solution for unsteady flows". In: *Int J Numer Meth Fluids.* 86.10 (2018), pp. 655–678.

[65] L. He and J. D. Denton. "Three-Dimensional Time-Marching Inviscid and Viscous Solutions for Unsteady Flows Around Vibrating Blades". In: *ASME J. Turbomach* 116.3 (1994), pp. 469–476.

[66] L. He and W. Ning. "Efficient Approach for Analysis of Unsteady Viscous Flows in Turbomachines". In: *AIAA Journal* 36.11 (1998), pp. 2005–2012.

[67] L. He and J. Yi. "Two-Scale Methodology for URANS/Large Eddy Simulation Solutions of Unsteady Turbomachinery Flows". In: *ASME J. Turbomach* 139.10 (2017), p. 101012.

[68] K. Hillewaert et al. "Assessment of a High-Order Discontinuous Galerkin Method for the Direct Numerical Simulation of Transition at Low-Reynolds number in the T106C High-Lift Low Pressure Turbine Cascade". In: ASME Turbo Expo 2014: Turbine Technical Conference and Exposition. Düsseldorf, Germany, 2014.

[69] H. Hoheisel. "Entwicklung Neuer Entwurfskonzepte Fur Zwei Turbinengitter, Teil III, Ergebnisse T106". In: *Technical report* (1981).

[70] T. J. Hughes, L. P. Franca, and M. Balestra. "A new finite element formulation for computational fluid dynamics: V. Circumventing the babuška-brezzi condition: a stable Petrov-Galerkin formulation of the stokes problem accommodating equal-order interpolations". In: *Computer Methods in Applied Mechanics and Engineering* 59.1 (1986), pp. 85–99.

[71] T. J. Hughes, L. P. Franca, and G. M. Hulbert. "A new finite element formulation for computational fluid dynamics: VIII. The galerkin/least-squares method for advective-diffusive equations". In: *Computer Methods in Applied Mechanics and Engineering* 73.2 (1989), pp. 173–189.

[72] H. T. Huynh. "A Flux Reconstruction Approach to High-Order Schemes Including Discontinuous Galerkin Methods". In: 18th AIAA Computational Fluid Dynamics Conference. Miami, Florida, 2007.

[73] G. Ingram, D. Gregory-Smith, and N. Harvey. "Investigation of a Novel Secondary Flow Feature in a Turbine Cascade With End Wall Profiling". In: *ASME J. Turbomach* 127.1 (2005), pp. 209–214.

[74] G. L. Ingram. "Endwall Profiling for the Reduction of Secondary Flow in Turbines". PhD thesis. University of Durham, 2003.

[75] E. N. Jacobs, K. E. Ward, and R. M. Pinkerton. *The characteristics of 78 related airfoil sections from tests in the variable-density wind tunnel*. NACA-TR-460, PB-177874. National Advisory Committee for Aeronautics, 1933.

[76] A. Jameson, P. E. Vincent, and P. Castonguay. "On the Non-linear Stability of Flux Reconstruction Schemes". In: *Journal of Scientific Computing* 50.2 (2012), 434–445.

[77] A. Jameson, W. Schmidt, and E. Turkel. "Numerical solution of the Euler equations by finite volume methods using Runge Kutta time stepping schemes". In: 14th AIAA Fluid and Plasma Dynamics Conference. Palo, Alto, CA, 1981.

[78] T. Jimbo, D. Biswas, and Y. Niizeki. "Studies on unsteady flow characteristics in a high pressure turbine cascade based on a high-order large eddy simulation turbulence model". In: *ASME J. Turbomach* 134.5 (2012), p. 051018.

[79] C. Johnson and J. Saranen. "Streamline Diffusion Methods for the Incompressible Euler and Navier-Stokes Equations". In: *MATHEMATICS OF COMPUTATION* 47.175 (1986), pp. 1–18.

[80] S. A. Karabasov and V. M. Goloviznin. "New Efficient High-Resolution Method for Nonlinear Problems in Aeroacoustics". In: *AIAA Journal* 45.12 (2007), pp. 2861–2871.

[81] S. A. Karabasov and V. M. Goloviznin. "Compact Accurately Boundary-Adjusting high-REsolution Technique for fluid dynamics". In: *Journal of Computational Physics* 228 (2009), pp. 7426–7451.

[82] S. A. Karabasov et al. "Jet Noise: Acoustic Analogy informed by Large Eddy Simulation". In: *AIAA Journal* 48.7 (2010), pp. 1312–1325.

[83] G. Karniadakis and S. Sherwin. *Spectral/hp Element Methods for Computational Fluid Dynamics*. Oxford, UK: Oxford University Press, 1999.

[84] I. J. Keshtiban, F. Belblidia, and M. F. Webster. *Compressible Flow Solvers for Low Mach Number Flows - A Review*. Technical Report CSR2. Institute of Non-Newtonian Fluid Mechanics, University of Wales, 2004.

[85] K. N. Kiran and S. Anish. "An investigation on the effect of Pitchwise Endwall design in a turbine cascade at different incidence angles". In: *Aerospace Science and Technology* 71 (2017), pp. 382–391.

[86] K. R. Laflin et al. "Data Summary from Second AIAA Computational Fluid Dynamics Drag Prediction Workshop". In: *Journal of Aircraft* 42.5 (2005), pp. 1165–1178.

[87] B. Landmann. "A Parallel Discontinuous Galerkin Code for the Navier-Stokes and Reynolds-Averaged Navier-Stokes Equations". PhD thesis. University of Stuttgart, 2008.

[88] R. B. Langtry and F. R. Menter. "Correlation-Based Transition Modelling for Unstructured Parallelized Computational Fluid Dynamics Codes". In: *AIAA J.* 214.1 (2009), pp. 137–170.

[89] P. LaSaint and P. A. Raviart. "On a Finite Element Method for Solving the Neutron Transport Equation". In: *Mathematical Aspects of Finite Elements in Partial Differential Equations*. Mathematics Research Center, the University of Wisconsin–Madison, US: Academic Press, 1974, pp. 89–123.

[90] S. K. Lele. "Compact Finite Difference Schemes with Spectral-like resolution". In: *Journal of Computational Physics* 103.1 (1992), pp. 16–42.

[91] D. W. Levy et al. "Data Summary from the First AIAA Computational Fluid Dynamics Drag Prediction Workshop". In: *Journal of Aircraft* 40.5 (2003), pp. 875–882.

[92] D. W. Levy et al. "Summary of Data from the Fifth Computational Fluid Dynamics Drag Prediction Workshop". In: *Journal of Aircraft* 51.4 (2014), pp. 1194–1213.

[93] M. S. Liou. "A Sequel to AUSM: AUSM+". In: *Journal of Computational Physics* 129.2 (1996), pp. 364–382.

[94] M. S. Liou. "A sequel to AUSM, part II: AUSM+-Up for All Speeds". In: *Journal of Computational Physics* 214.1 (2006), pp. 137–170.

[95] M. S. Liou and C. J. Steffen. "A New Flux Splitting Scheme". In: *Journal of Computational Physics* 107.1 (1993), pp. 23–39.

[96] H. Luo et al. "A Reconstructed Discontinuous Galerkin Method for the Compressible Navier-Stokes Equations on Arbitrary Grids". In: *Journal of Computational Physics* 229 (2010), pp. 6961–6978.

[97] H. Luo et al. "A Parallel, Reconstructed Discontinuous Galerkin Method for the Compressible Flows on Arbitrary Grids". In: *Communications in Computational Physics* 9.2 (2011), pp. 363–389.

[98] J. Marty et al. "LES and hybrid RANS/LES simulations of turbomachinery flows using high order methods". In: ASME Turbo Expo 2015: Turbine Technical Conference and Exposition. Montreal, Quebec, Canada, 2015.

[99] A. Masud and R. A. Khurram. "A multiscale/stabilized finite element method for the advection–diffusion equation". In: *Computer Methods in Applied Mechanics and Engineering* 193.21-22 (2004), pp. 1997–2018.

[100] D. J. Mavriplis. *Unstructured mesh generation and adaptivity*. Tech. rep. 1995.

[101] D. J. Mavriplis and A. Jameson. "Multigrid solution of the Navier-Stokes equations on triangular meshes". In: *AIAA Journal* 28.8 (1990), pp. 1415–1425.

[102] D. J. Mavriplis et al. "Grid quality and Resolution Issues from the Drag Prediction Workshop Series". In: *Journal of Aircraft* 46.3 (2009), pp. 935–950.

[103] H. Moore. "Experiments in a turbine cascade for the validation of turbulence and transition models". PhD thesis. University of Durham, 1995.

[104] H. Moore and D. G. Gregory-Smith. "Transition Effects on Secondary Flows in a Turbine Cascade". In: ASME 1996 International Gas Turbine, Aeroengine Congress, and Exhibition. Birmingham, UK, 1996.

[105] R. D. Moore and L. Reid. *Performance of singlestage axial flow transonic compressor with rotor and stator aspect ratios of 1.19 and 1.26, respectively, and with design pressure ratio of 2.05*. NASA Technical Paper 1659. NASA, 1980.

[106] D. Moro, N. C. Nguyen, and J. Peraire. "Navier-Stokes Solution Using Hybridizable Discontinuous Galerkin Methods". In: 20th AIAA Computational Fluid Dynamics Conference. Honolulu, Hawaii, 2011.

[107] N. C. Nguyen, P. O. Persson, and J. Peraire. "RANS Solutions Using High-Order Discontinuous Galerkin Methods". In: 45th AIAA Aerospace Sciences Meeting and Exhibit. Reno, Nevada, 2007.

[108] N. C. Nguyen, J. Peraire, and B. Cockburn. "An implicit high-order hybridizable discontinuous Galerkin method for nonlinear convection–diffusion equations". In: *Journal of Computational Physics* 228.23 (2009), pp. 8841–8855.

[109] N. C. Nguyen, J. Peraire, and B. Cockburn. "An implicit high-order hybridizable discontinuous Galerkin method for the incompressible Navier–Stokes equations". In: *Journal of Computational Physics* 230.4 (2011), pp. 1147–1170.

[110] W. Ning and L. He. "Some Modeling Issues on Trailing-Edge Vortex Shedding". In: *AIAA J.* 39.5 (2001), pp. 787–793.

[111] T. A. Oliver. "A High-Order, Adaptive, Discontinuous Galerkin Finite Element Method for the Reynolds-Averaged Navier-Stokes Equations". PhD thesis. Massachusetts Institute of Technology, 2008.

[112] J. Peraire and P. O. Persson. "The Compact Discontinuous Galerkin (CDG) Method for Elliptic Problems". In: *SIAM Journal on Scientific Computing* 30 (2008), pp. 1806–1824.

[113] J. Peraire, N. C. Nguyen, and B. Cockburn. "A Hybridizable Discontinuous Galerkin Method for the Compressible Euler and Navier-Stokes Equations". In: (2010).

[114] P. O. Persson and J. Peraire. "Newton-GMRES Preconditioning for Discontinuous Galerkin Discretizations of the Navier–Stokes Equations". In: *SIAM J. Sci. Comput.* 30.6 (2008), pp. 2709–2733.

[115] E. S. Politis and K. C. Giannakoglou. "A Pressure-Based Algorithm for High-Speed Turbomachinery Flows". In: *International Journal for Numerical Methods in Fluids* 25 (1997), pp. 63–80.

[116] W. H. Press et al. *Numerical Recipes 3rd Edition: The Art of Scientific Computing*. 3rd ed. New York, NY, USA: Cambridge University Press, 2007.

[117] W. H. Reed and T. R. Hill. "Triangular Mesh Methods for the Neutron Transport Equations". In: *Tech. Report LA-UR-73-479* (1973).

[118] P. L. Roe. "Approximate Riemann Solvers, Parameter Vectors, and Difference Schemes". In: *Journal of Computational Physics* 43 (1981), pp. 357–372.

[119] A. Scandaliato and M.-S. Liou. "AUSM-Based High-Order Solution for Euler Equations". In: 48th AIAA Aerospace Sciences Meeting. Orlando, Florida, 2010.

[120] H. Schlichting. *Boundary-layer theory*. McGraw-Hill Book Company, 1979.

[121] F. Shakib, T. J. Hughes, and Z. Johan. "A new finite element formulation for computational fluid dynamics: X. The compressible Euler and Navier-Stokes equations". In: *Computer Methods in Applied Mechanics and Engineering* 89.1-3 (1991), pp. 141–219.

[122] C. W. Shu and S. Osher. "Efficient Implementation of Essentially Non-Oscillatory Shock-Capturing Schemes". In: *Journal of Computational Physics* 77 (1988), pp. 439–471.

[123] P. Solin, K. Segeth, and I. Dolezel. *Higher-Order Finite Element Methods*. 3rd. Chapman and Hall/CRC, 2003.

[124] P. Spalart and S. Allmaras. "A one-equation turbulence model for aerodynamic flows". In: 30th Aerospace Sciences Meeting and Exhibit. Reno, NV, 1992.

[125] A. Thom. "The flow past circular cylinders at low speeds". In: *Proc. R. Soc. Lond., Ser A.* 141.845 (1933), pp. 651–669.

[126] J. F. Thompson, Z. Warsi, and C. W. Mastin. *Numerical Grid Generation: Foundations and Applications*. New York, NY, USA: Elsevier North-Holland, Inc., 1985.

[127] E. N. Tinoco et al. "Summary Data from the Sixth AIAA CFD Drag Prediction Workshop: CRM Cases". In: *Journal of Aircraft* 55.4 (2018), pp. 1352–1379.

[128] E. Turkel, R. Radespiel, and N. Kroll. "Assessment of Preconditioning Methods for Multidimensional Aerodynamics". In: *Computers and Fluids* 26.6 (1997), pp. 613–634.

[129] B. van Leer. "Flux-vector splitting for the Euler equations". In: ed. by E. Krause. Vol. 170. Eighth International Conference on Numerical Methods in Fluid Dynamics. Lecture Notes in Physics. Berlin, Heidelberg: Springer, 1982, p. 507.

[130] B. van Leer, W. Lee, and P. Roe. "Characteristic Time-Stepping or Local Preconditioning of the Euler Equations". In: 10th AIAA Computational Fluid Dynamics Conference. Honolulu, HI, 1991.

[131] J. C. Vassberg et al. "Summery of the Third AIAA CFD Drag Prediction Workshop". In: 45th AIAA Aerospace Sciences Meeting and Exhibit. Reno, Nevada, 2007.

[132] J. C. Vassberg et al. "Summary of the Fourth AIAA Computational Fluid Dynamics Drag Prediction Workshop". In: *Journal of Aircraft* 51.4 (2014), pp. 1070–1089.

[133] P. E. Vincent, P. Castonguay, and A. Jameson. "A New Class of High-order Energy Stable Flux Reconstruction Schemes". In: *Journal of Scientific Computing* 47.1 (2011), pp. 50–72.

[134] M. R. Visbal and D. V. Gaitonde. "On the Use of High-Order Finite-Difference Schemes on Curvilinear and Deforming Meshes". In: *Journal of Computational Physics* 181.1 (2002), pp. 155–185.

[135] T. v. von Karman. *Mechanical similitude and turbulence*. NACA-TM-611. National Advisory Committee for Aeronautics, 1931.

[136] Z. Wang. "High-order computational fluid dynamics tools for aircraft design". In: *Phil. Trans. R. Soc.* A.372 (2014), p. 20130318.

[137] Z. Wang et al. "High-order CFD methods: current status and perspective". In: *International Journal for Numerical Methods in Fluids* 72.8 (2013), pp. 811–845.

[138] D. C. Wilcox. "Reassessment of the scale-determining equation for advanced turbulence models". In: *AIAA Journal* 26.11 (1988), pp. 1299–1310.

[139] D. M. Williams and A. Jameson. "Energy Stable Flux Reconstruction Schemes for Advection–Diffusion Problems on Tetrahedra". In: *Journal of Scientific Computing* 59.3 (2014), 721–759.

[140] D. M. Williams et al. “Energy stable flux reconstruction schemes for advection–diffusion problems on triangles”. In: *Journal of Computational Physics* 250 (2013), pp. 53–76.

[141] Y. Xia et al. “A set of parallel, implicit methods for a reconstructed discontinuous Galerkin method for compressible flows on 3D hybrid grids”. In: *Computers and Fluids* 98 (2014), pp. 134–151.

[142] Y. Zheng and L. He. “Multigrid upwind Euler/Navier-Stokes computation on adaptive unstructured meshes”. In: *The Aeronautical Journal* 105.1046 (2001), 173–184.